

**Photophysics of Prototype Anticancer Drugs
Sanguinarine and Chelerythrine on Plasmonic, Magnetic
and Magnetoplasmonic Nano Surface: A Transient
Absorption Study**

By

Sudeshna Das Chakraborty

<CHEM05201504002>

Saha Institute of Nuclear Physics, HBNI, Kolkata, India

*A thesis submitted to the
Board of Studies in Chemical Sciences*

*In partial fulfilment of requirements
for the Degree of*

DOCTOR OF PHILOSOPHY

of

HOMI BHABHA NATIONAL INSTITUTE



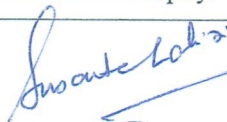
February 2019

Homi Bhabha National Institute

Recommendations of the Viva Voce Committee

As members of the Viva Voce Committee, we certify that we have read the dissertation prepared by **Sudeshna Das Chakraborty** (CHEM05201504002) entitled "**Photophysics of Prototype Anticancer Drugs Sanguinarine and Chelerythrine on Plasmonic, Magnetic and Magnetoplasmonic Nano Surface: A Transient Absorption Study**" and recommend that it may be accepted as fulfilling the thesis requirement for the award of Degree of Doctor of Philosophy.

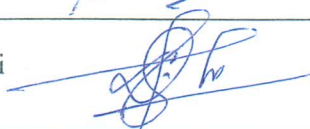
Chairman - Prof. Susanta Lahiri



date

22.04.2019

Guide / Convener - Dr. Dulal Senapati



date

22.04.2019

Examiner - Prof. Amitava Patra



date

22.4.2019

Member 1- Dr. Padmaja P Mishra



date

22/04/19

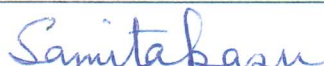
Member 2- Dr. Manabendra Chandra



date

22.04.2019

Member 3- Prof. Samita Basu



date

22.04.2019.

Final approval and acceptance of this thesis is contingent upon the candidate's submission of the final copies of the thesis to HBNI.

I/We hereby certify that I/we have read this thesis prepared under my/our direction and recommend that it may be accepted as fulfilling the thesis requirement.

Date: 22.04.2019

Place: SINP, Kolkata



Dulal Senapati

Guide

STATEMENT BY AUTHOR

This dissertation has been submitted in partial fulfilment of requirements for an advanced degree at Homi Bhabha National Institute (HBNI) and is deposited in the Library to be made available to borrowers under rules of the HBNI.

Brief quotations from this dissertation are allowable without special permission, provided that accurate acknowledgement of the source is made. Requests for permission for extended quotation from or reproduction of this manuscript in whole or in part may be granted by the Competent Authority of HBNI when in his or her judgment the proposed use of the material is in the interests of scholarship. In all other instances, however, permission must be obtained from the author.

Sudeshna Das Chakraborty

Sudeshna Das Chakraborty

DECLARATION

I, hereby declare that the investigation presented in the thesis has been carried out by me.
The work is original and has not been submitted earlier as a whole or in part for a degree/diploma at this or any other Institution / University.

Sudeshna Das Chakraborty.

Sudeshna Das Chakraborty

List of Publications arising from the thesis

Journal

1. Development of a Triplet-Triplet Absorption Ruler: DNA- and Chromatin-Mediated Drug Molecule Release from a Nanosurface. **Das Chakraborty, S.**; Sau, A.; Kuznetsov, D. V.; Banerjee, A.; Bardhan, M.; Bhattacharya, M.; Dasgupta, D.; Basu, S^{*}; Senapati, D^{*}. *J. Phys. Chem. B*, 2016, 120 (27), 6872–6881.
2. Low Magnetic Field Induced Surface Enhanced Transient Spin-Trajectory Modulation of a Prototype Anticancer Drug Sanguinarine on a Single Domain Superparamagnetic Nanosurface. **Das Chakraborty, S.**; Sau, A; Maity, A.; Sengupta, C; Bhattacharya, M; Bhattacharjee, G; Banik, S; Satpati, B; Basu, S^{*}; Senapati, D^{*}. *J. Phys. Chem. C*, 2018, 122 (36), 20619–20631.
3. Differential photophysical behaviour of the iminium and alkanolamine form of chelerythrine and sanguinarine on superparamagnetic nano surface. **Das Chakraborty, S.**; Pal, U.; Kumar, S.; Pathak. B.; Basu, S^{*}; Senapati, D^{*}.(Manuscript under preparation)
4. Designing engineered crystal mismatched differentially frosted magneto plasmonic nanostructures and exploration of the role of magnetoplasmonic field on the excited state photophysical pathways of naturally occurring common alkaloid anticancer drugs. **Das Chakraborty, S.**; Basu, S.; Senapati, D. (Manuscript under preparation).

Sudeshna Das Chakraborty
Sudeshna Das Chakraborty

Conference Attended:

- (1) Presented a Talk in the 255th ACS National Meeting and Exposition: Nexus of Food, Energy & Water – 18th-22nd March 2018, New Orleans, Louisiana, USA.
- (2) Presented a Poster in the 5th International Symposium on Advanced Biological Inorganic Chemistry (SABIC) 7th-11th January 2017, IACS, Kolkata, India.
- (3) Presented a Poster in the International Conference of Optics within Life Sciences (OWLS) 16th-19th March 2016, TIFR, Mumbai, India.
- (4) Attended the “SCM 2015 – 14th International Symposium on Spin and Magnetic Field Effects in Chemistry and Related Phenomena”- Saha Institute of Nuclear Physics, Kolkata, 15th-20th March 2015.

Others:

- (1) Attended a Workshop on AFM organized by Bruker and Forevision Instruments on 1st-2nd December 2017, Bangalore, INDIA.

Sudeshna Das Chakraborty
Sudeshna Das Chakraborty

Dedicated to,

Baba, Ma, Mama, Bunu

&

My Husband Saurabh

ACKNOWLEDGEMENTS

At this juncture of my career, I take this opportunity to look back and place on record my sincere gratitude to a number of people, without whose active support and encouragement this thesis would not have been possible.

First and foremost, I wish to express my deep sense of gratitude and sincere thanks to my PhD supervisor Dr Dulal Senapati, for his profuse guidance, continuous support, and constant encouragement throughout this tenure. Due to his illuminating guidance, assistance, and patience on me, I can able myself feel motivated in the area of research throughout.

I feel short of words in expressing my sincere gratitude and whole-hearted respect to Prof. Samita Basu, head of chemical sciences division, SINP. Her continuous guidance, patience, endless support and lots of very useful discussions helped me greatly to understand the field of excited state dynamics properly.

The doctoral committee members Dr P.P Mishra, Dr Manabendra Chandra and the former and present dean academy of CI Prof. Avijit Chakraborty and Prof Partha Saha are gratefully acknowledged for their review and suggestions during progress review and pre-synopsis viva-voce. I am thankful to Dr Biswasrup Satpati for TEM analysis and Dr Montu K. Hazra for several helpful discussions on quantum mechanics. I sincerely acknowledge the support of Prof. Krishnakumar S.R. Menon & Mr. Sukanta Barman, SPMS, SINP for the XPS facility, Anish K. Mahapatra for XRD and Dr Pintu Sen from VECC for magnetization measurements. I thank all my lab members, all faculty members and supporting staff members of the Chemical Sciences Division, all the collaborators, Divisional seniors and juniors, all my friends and all my teachers since childhood. I would like to thank all my family members (Baba, Ma, Mama, Rupan, my beloved husband Saurabh, Buru, Sumana, Bebi, Nilu, Mala masi, Kaka, kakima, all sisters and brothers, boudi, didivai, daduvai, dadu, thamma, my father in law and mother in law).

Table of contents

Title	Page No
SUMMARY	v
List of figures	vi
List of tables	xv
CHAPTER-1	1
Introduction	1
1.2 Types of Photoinduced reactions:.....	9
1.2.1 Photoelectron transfer process (PET).....	9
1.2.2 Excited State Proton Transfer (ESPT)	15
1.2.3 Proton-Coupled Electron Transfer	16
1.3 Magnetic Field Effect: Link between charge transfer and spin dynamics:.....	17
1.3.1 Vectorial Representation of Singlet and Triplet RIPS	18
1.3.2 S-T intersystem crossing (ISC) and mechanism of MF effect	21
1.4 Nanoparticles: An Overview	24
1.4.1 Plasmonic nanomaterials and their Interesting properties.....	27
1.4.2 AuNP as a drug carrier	28
1.4.3 Magnetic Materials.....	29
1.4.4 Magneto-plasmonic nanomaterials	35
1.5 Biomolecules (Ct-DNA and Chromatin):	36
1.6 Anticancer Drugs:	36
1.6.1 Anticancer Drug and Reactive Oxygen Species Generation.....	37

1.6.2 Sanguinarine and Chelerythrine as prototype anticancer drugs	38
1.7 Principle of Photodynamic Therapy:	40
CHAPTER-2	42
Methodology and Experimental Set Up	42
2.2 Methods:	43
2.2.1 Ultraviolet-Visible (UV–Vis) Absorption Spectroscopy	43
2.2.2 Fluorescence Spectroscopy	43
2.2.3 Time-resolved Spectra (Time-Correlated Single Photon Counting Technique)	43
2.2.4 Femtosecond (fs) fluorescence up-conversion measurements	44
2.2.5 Laser Flash Photolysis (Excited State Transient Absorption Technique)	46
2.2.6 Surface Enhanced Raman Spectroscopy (SERS)	48
2.2.7 Preparation of Plasmonic Spherical AuNPs	49
2.2.8 Synthetic protocol of magnetic nanoparticle Fe ₃ O ₄	50
2.2.9 Transmission Electron Microscopy (TEM)	51
2.2.10 X-Ray Diffraction (XRD) Technique	51
2.2.11 Magnetization Measurements	52
2.2.12 Molecular Docking and Dynamics	52
2.2.13 Preparation of ctDNA	52
2.2.14 Isolation of Chromatin from Chicken Liver	53
CHAPTER-3	54
Development of a Triplet-Triplet Absorption Ruler: DNA and Chromatin-Mediated Drug Molecule Release from a Plasmonic Nanosurface	54
3.1 Introduction:	55

3.2 Results and Discussion:	57
3.3 Conclusions:.....	73
CHAPTER-4	75
Low Magnetic Field Induced Surface Enhanced Transient Spin-Trajectory Modulation of a Prototype Anticancer Drug Sanguinarine on a Single Domain Superparamagnetic Nanosurface	75
4.1 Introduction.....	76
4.2 Results and Discussion:	80
4.2.1 Portrayal of the nanoparticle by Transmission Electron Microscopy (TEM)....	80
4.2.2 The measurement of magnetization of the nanoparticle (Isothermal Magnetization and the Equivalent Langevin Function Fit.).....	81
4.2.3 Structural Characterization by XRD method.	83
4.2.4 The Ground State Complex Formation between Sgr and Superparamagnetic FeNPs and its Stability to Govern the Transient Spin-Trajectory Followed by Photoexcitation.....	84
4.2.5 The Influence of Nanosurface, Donor-Acceptor Proximity, Surface Charge and Hydration Dynamics for Transient Spin-Trajectory Modulation.....	85
4.2.6 Efficient Transient Spin-Trajectory Modulation by Single-Domain Superparamagnetic Moment-Driven Spin Interconversion.....	93
4.3. Conclusions:.....	105
CHAPTER-5	106
Differential Photophysical Behaviour of the Iminium and Alkanolamine form of Chelerythrine and Sanguinarine on Superparamagnetic Nano surface	106
5.1 Introduction:.....	107

5.2 Results and Discussion:	109
5.2.1 Complex formation between Chel and superparamagnetic Fe ₃ O ₄ nanosurface and its stability to govern the transient spin-trajectory followed by photoexcitation	113
5.2.2 MD Simulation to understand the role of difference in geometry between the molecules on the extent of S ↔ T interconversion	116
5.3 Conclusion:	123
CHAPTER-6	124
6.1 Introduction:.....	125
6.2 Result and Discussion:.....	127
6.2.1 Sonochemical Synthesis of Magneto-plasmonic material	127
6.2.1.1 Ground state UV-vis absorption spectra	127
6.2.2 Characterization of magnetoplasmonic nanomaterial	128
6.2.3 Magnetization of the magnetoplasmonic material in presence of an external magnetic field.....	131
6.2.4 The complex formation between Sgr and Au@Fe ₃ O ₄	131
6.2.5: Influence of Au@Fe ₃ O ₄ Nanosurface on the Transient Spin-Trajectory Modulation of surface adsorbed Sgr	134
6.2.6: Transient Spin-Trajectory Modulation by Au@Fe ₃ O ₄ surface with ultra-high efficiency in presence of a low external magnetic field.....	135
6.2.7: Triplet lifetime of Sgr in presence of Au@Fe ₃ O ₄ nanosurface.....	137
References	140

SUMMARY

Both photophysics and photochemistry are the branches of science dealing with the interaction between incident photons and molecules or materials. Photoinduced reactions are concerned with the changes initiated in the electronically excited molecules after absorption of suitable radiation in the UV-visible and near-infrared (NIR) region of the spectrum. Photon driven processes (physical or chemical) are the basic to the world we live in. In this thesis, I have discussed the photophysics of a class of prototype anticancer drugs which include sanguinarine (Sgr) and chelerythrine on (Chel) on metal nanoparticle's surface. By light absorption when molecules excite to the higher energy electronic states, several transients or short-lived intermediates with unpaired spin are formed. Excited state transient absorption is a spectroscopic tool to detect those transients, to gather the information related to the intersystem crossing (ISC) during electronic transitions, the nature of the spin state of the transients, stability and time scale of generation of the transients, excited state electron transfer property, the mode of reaction in the photoexcited state and the nature of the complex generated with reaction between the photoexcited electron donor and acceptor molecules.

Nanoparticles are very interesting materials due to their great nanotechnological potential, unique and strongly size and shape-dependent electronic, chemical, optical and magnetic properties. I have discussed how the transient absorption technique can be used as a sensory tool for the detection of drug release (prototype anticancer drug sanguinarine) from a nano surface in presence of cellular components like (DNA and Chromatin) upon laser irradiation. The influence of the plasmonic and magnetic field of a nano surface on the modulation of intersystem crossing (ISC) i.e., singlet-triplet interconversion has also been discussed. The role of nanoparticle as external stimuli on the overall spin statistics in the excited electronic states of the small molecule anticancer drugs (sanguinarine and chelerythrine) which are adsorbed on the nano surface has been explained in details in this thesis.

List of figures

Figure 1.1: The Jablonski diagram ²⁶ which explains not only the relative energy spacing among different energy (electronic and vibrational) states but also shows possible photoinduced processes may initiate from the photoexcited molecular state.	4
Figure 1.2: The Oxidative and reductive electron transfer process.....	10
Figure 1.3: Solvent polarity dependent excited state intermediate formation.....	12
Figure 1.4: Variation of stability of the intermediates as we modulate the solvent polarity ⁸⁵	13
Figure 1.5: Potential energy curves for the electron transfer complexes in different solvent polarity as a function of intermolecular separation. ⁸³	14
Figure 1.6: Slices of the free energy surfaces for the ground state reactant (I) and product (II) vibronic states along the solvent coordinate. ¹²¹	17
Figure 1.7: Vector representation of electron spin moment in presence of external magnetic field (up) and the Singlet and Triplet spin states (bottom) of a RIP. ¹³²	19
Figure 1.8: Energies of Singlet and triplet RIPS and their pathways in solutaion. ¹³³	20
Figure.1.9: Magnetic Field effect due to hyperfine mechanism. ¹³²	22
Figure1.10: Vector cones of total angular momentum.....	23
Figure1.11: Metal nanoparticles with different shape and sizes.	24
Figure1.12: Nanomaterials with different shape and size."Reprinted (adapted) with permission from Self-assembly of noble metal nanocrystals: Fabrication, optical property, and application, Nano Today (2012) 7, 564-585, DOI.org/10.1016/j.nantod.2012.10.008, Elsevier, Copyright year (2012)."	26
Figure 1.13: Schematic of plasmon oscillation in spherical plasmonic nanoparticle showing the displacement of the conduction electron charge cloud relative to the nuclei."Reprinted (adapted) with permission from Metal nanoparticle photocatalysts:	

emerging processes for green-organic synthesis, Catal. Sci. Technol., 2015, DOI: 10.1039/C5CY02048D, Copyright (2016)	28
Figure 1.14: (A) Change of magnetic susceptibility with temperature for different magnetic materials (B) Ensemble orientation of the magnetic dipoles in different materials (C) Magnetization vs H plot of different types of bulk magnetic materials.....	32
Figure 1.15: Magnetization behaviours of ferromagnetic and superparamagnetic NPs in the presence and absence of an external magnetic field (b) Relationship between nanoparticle size and the magnetic domain structures. D_s and D_c are the 'superparamagnetism' and 'critical' size thresholds. ¹⁷⁷	33
Figure 1.16: Schematic illustration of the coercivity-size relations of small magnetic particles. ¹⁷⁷	34
Figure 1.17: Schematic illustration of the magnetoplasmonic material	35
Figure 1.18: Schematic illustration of DNA and Chromatin.....	36
Figure 1.19. Mechanism of tumour destruction by PDT. "Reprinted (adapted) with permission from (Role of Reactive Oxygen Species (ROS) in Therapeutics and Drug Resistance in Cancer and Bacteria Allimuthu T. Dharmaraja Journal of Medicinal Chemistry 2017 60 (8), 3221-3240DOI:10.1021/acs.jmedchem.6b01243).Copyright (2017)."	37
Figure 1.20: Schematic representation of photodynamic therapy	40
Figure 2.2.1: Block diagram of TCSPC Set up	45
Figure 2.2.2: Block diagram of femtosecond upconversion technique. ²⁴⁰	46
Figure 2.2.3 Schematic diagram of laser flash photolysis set-up	47
Figure 2.2.4: Schematic diagram of the experimental SERS set up.....	49
Figure 2.2.5: Schematic diagram of the AuNP synthesis set up.	50
Figure 2.2.6: Schematic diagram of the FeNP synthesis set up.	51

Figure 3.1: Absorption profile of Sgr (black), citrate-capped gold nanoparticle (blue) and Sgr-AuNP complex (red).....	58
Figure 3.2: TEM images of (A) AuNP (10 nM), (B) AuNP (10 nM)-Sgr (10 μ M) complex, (C) AuNP-Sgr complex, with 0.05 μ M ctDNA, (D) AuNP-Sgr complex, with 0.15 μ M ctDNA, and (E) AuNP-Sgr complex, with 0.25 μ M ctDNA.	59
Figure 3.3: T-T absorption spectra of Sgr [100 μ M] (A) with AuNP [100 nM], ctDNA [2.5 μ M], and AuNP followed by ctDNA; and (B) with AuNP [100 nM], chromatin [2.5 μ M], and AuNP followed by chromatin in tris-NaCl buffer (pH: 7.4 \pm 0.2) after 1 μ s laser flash of λ_{ex} = 355 nm.	60
Figure 3.4: Time-resolved T-T absorption spectra of Sgr [100 μ M] show an overall decrease in optical density (Δ OD) from 560 to 650 nm with a gradual increase in time, which indicates that all of these peaks are of the same origin.....	61
Figure 3.5: T-T absorption titration by varying the concentrations of ctDNA and chromatin and keeping the Sgr [100 μ M] concentration constant.....	63
Figure 3.6: Correlation between intercalator concentration and efficiency of drug release (%) which shows a linear plot for both ctDNA (A) and chromatin (B).	64
Figure 3.7: Decay profile of Sgr at 360 nm (A) with AuNP [100 nM], ctDNA [2.5 μ M], and AuNP followed by ctDNA and (B) with AuNP [100 nM], chromatin [2.5 μ M], and AuNP followed by chromatin in tris-NaCl (pH: 7.4 \pm 0.2) buffer after 1 μ s of laser flash with λ_{ex} = 355 nm.	65
Figure 3.8: (A) Gradual reduction in fluorescence intensity as a function of the increasing amount of AuNPs for 10 μ M Sgr and release of Sgr from the AuNP surface as a function of gradually increasing amount of (B) ctDNA and (C) chromatin.....	67
Figure 3.9: Variation of fluorescence quenching with the concentration of quencher (0.4-7.1 nM). Here 20-25 nm TSC stabilized AuNPs acts as a quencher and Sgr as the fluorophore.	68

Figure 3.10: Variation of fluorescence intensity, obtained from Sgr-AuNP complex, with time without the addition of ctDNA and chromatin as active bio-scaffolds.	69
Figure 3.11: (A) The gradual increment of SERS intensity as a function of the increasing amount of AuNPs (0-10 nM) for 10 μ M Sgr and release of Sgr from the AuNP surface as a function of gradually increasing amount of (B) ctDNA and (C) chromatin.	72
Figure 4.1: (A) Direction of precession of an electron, with the large arrow indicating the external magnetic field and the small arrow showing the spin angular momentum of the electron; (B) synthesized FeNP (TEM images); (B ₁) Individual FeNP (HRTEM image) ; (B ₂) Diffraction Pattern (Acquired Selected Area) of the nanoparticles and the different crystal planes present in the nanoparticles; (C) EDX spectra of nanoparticles acquired in STEM mode from TEM. (D) Electron energy loss spectra (EELS) of the nanoparticles. .	81
Figure 4.2: (A) The plot of Normalized magnetization (M/M_S) as a function of H/T at 200K and 300K; (B) Magnetization vs applied magnetic field dependence at 300K. The red line depicts the Langevin function fit on to the M-H data, and (C ₁ & C ₂) shows XRD pattern of FeNP and FeNP-Sgr complex respectively.	83
Figure 4.3: (A and B) The plot of differential absorption spectra of Sgr in the presence of superparamagnetic FeNP in CH ₃ CN and H ₂ O respectively (insets shows their respective isosbestic points); (C) Plot of UV-vis absorption spectra of the synthesized FeNP.	84
Figure 4.4: (A ₁ and B ₁) Plot of fluorescence decay profile of surface adsorbed Sgr on increasing concentrations of FeNP in CH ₃ CN and H ₂ O respectively; (A ₂ and B ₂) Plot of FeNP concentration-dependent T-T absorption spectra of surface adsorbed Sgr in CH ₃ CN and H ₂ O respectively; (A ₃ and B ₃) Plot showing the Trend and extent of fluorescence quenching from S ₁ state of Sgr in presence of varying concentrations of FeNP in CH ₃ CN and H ₂ O respectively; (A ₄ and B ₄) Stern-Volmer plot of Sgr-FeNP complex as a function of increasing concentration of FeNP for CH ₃ CN and H ₂ O respectively; (C) Linear and	

nonlinear Stern-Volmer plot of Sgr-FeNP complex as a function of low concentration FeNP in CH ₃ CN and H ₂ O respectively.	86
Figure 4.5: (A ₁ and B ₁) Decay profile of fluorescence lifetime of Sgr molecule in absence and presence of increasing concentration of the FeNPs in CH ₃ CN and H ₂ O medium respectively; (A ₂ and A ₃) biexponential decay profile of the excited triplet state of Sgr-FeNPs complex in the absence and presence of an external magnetic field in CH ₃ CN and (B ₂ and B ₃) in H ₂ O medium respectively.	91
Figure 4.6: The plot of biexponential decay profiles of the excited triplet state of Sgr-FeNP in absence and presence of magnetic field (0.08T) at 360 nm (A) and 410 nm (B). 92	
Figure 4.7: (A and C) The plot of T-T absorption spectra and the respective modulation of the transient spin state of Sgr molecule in presence of variable FeNPs concentration in presence of constant low external magnetic field (0.08T) in CH ₃ CN and H ₂ O respectively;	93
Figure 4.8: Plot of (A) Triplet absorbance (O.D.) as a function of externally applied low magnetic field (in Tesla unit) in CH ₃ CN and (B) Induced magnetic moment vs external magnetic field (in Tesla unit) in vacuum at 300K.	94
Figure 4.9. The plot of excited state T-T absorption spectra of Sgr-AuNP composite in the presence (red-line) and absence (black-line) of a magnetic field of magnitude 0.08T.	95
Figure 4.10: Fluorescence quenching trend and extent from the S ₁ state of Sgr molecule with variable concentration of (A) FeNPs and (B) AuNPs in H ₂ O medium. (A ₁ and B ₁) The corresponding Stern-Volmer plot of Sgr-FeNP complex (red) and Sgr-AuNP (black) complex with the concentration of FeNPs and AuNPs. (A ₂ and B ₂) Shows the corresponding quenching constants in presence of a lower concentration of FeNPs and AuNPs respectively.	96

Figure 4.11: The plot of excited state T-T absorption spectra of Sgr molecule in (A) H ₂ O and (B) CH ₃ CN medium in the presence (red-line) and absence (black-line) of an external magnetic field of 0.08T.	97
Figure 4.12: The plot of time-delayed transient (excited triplet state) absorption spectra of Sgr. The time delay between pump and probe pulse ranges between 0.5 to 4.9μs.	98
Figure 4.13: (A) The plot of low-resolution, i.e 10 nm data point and (B) high-resolution, i.e 5 nm data point, T-T absorption spectra of Sgr molecule in absence of magnetic field in H ₂ O medium with noticeable humps in the 400 nm region.	99
Figure 4.14: The plot of FeNP concentration-dependent T-T absorption spectra of surface adsorbed Sgr molecule in Ethanol medium.	100
Figure 4.15: The plot of MD simulation to know the contribution from (A ₁) van der Waals, (A ₂) Coulombic, (A ₃) total electrostatic and non-electrostatic forces in the solvation of Sgr molecule in different solvents, (B) Hydrogen bonding tendencies of Sgr molecule with the different solvents.	102
Figure 4.16: Solvent cage formation around Sgr in (A ₁ -A ₃) H ₂ O, (B ₁ -B ₃) EtOH and (C ₁ -C ₃) CH ₃ CN medium 0, 600 and 1200 ps time frame.	103
Figure 5.1: The iminium and alkanolamine form of Chel in H ₂ O and EtOH medium respectively.	109
Figure 5.2: UV-Vis absorption spectra (A) of the iminium and the alkanolamine form of Chelerythrine (Chel) in H ₂ O and EtOH medium (B) with increasing concentration of the drug in EtOH medium.	110
Figure 5.3: The fluorescence spectra of Chel in H ₂ O and EtOH medium at lower concentration (5μM).	111
Figure 5.4: Change of fluorescence spectra on increasing the concentration of Chel from 5μM to 60μM in EtOH medium.	111

Figure 5.5: The triplet-triplet absorption spectra of Chel in (A) H ₂ O and (B) EtOH medium respectively in presence and absence of external magnetic field.	112
Figure 5.6: Changes in the number of H bonds with solvents (H ₂ O and EtOH) over time.	113
Figure 5.7: Quenching of fluorescence intensity on gradual addition of FeNP in (A) H ₂ O and (B) EtOH medium respectively.	114
Figure 5.8: FeNP concentration-dependent T–T absorption spectra of surface adsorbed Chel in (A) H ₂ O and (B) EtOH respectively.	114
Figure 5.9: Excited state transient absorption spectra of Chel on FeNP nanosurface in (A) H ₂ O and (B) EtOH medium respectively	115
Figure 5.10: Excited state transient absorption spectra of (A) Sgr in ethanol medium, Sgr on FeNP surface at (B ₁) 5nM (B ₂) 10nM and (B ₃) 15nM concentration.	116
Figure 5.11: Optimized geometries of Chel (left) and Sgr (right).....	117
Figure 5.12. Optimized geometry of the alkanolamine form of Chel (top view in the left and side view in the right). The dipole vector is shown with the red arrow.....	117
Figure 5.13. Root mean square deviations of Chel (black) and Sgr (red) dimers in H ₂ O (A) and EtOH (B) during MD simulation. In H ₂ O Chel and Sgr is in iminium form whereas, in EtOH, Chel and Sgr are in alkanolamine form.....	118
Figure 5.14. Structural changes of the Chel iminium dimer (A1-A3) and Sgr iminium dimer (B1-B3) in H ₂ O medium at 0, 600 and 1200 ps time frame.....	118
Figure 5.15. (A) Coulombic energy for Chel and Sgr (iminium) dimer formation in H ₂ O medium, (B) Coulombic energy for Chel and Sgr (alkanolamine) dimer formation in EtOH medium. Energy converges to zero as the dimer eventually breaks down. (C) Coulombic energy for the interaction of Chel and Sgr (iminium) with solvent H ₂ O, (D) Coulombic energy for the interaction of Chel and Sgr (iminium) with solvent EtOH.	119

Figure 5.16: (A) van der Waals energy for Chel and Sgr (iminium) dimer formation in H ₂ O medium. (B) van der Waals energy for Chel and Sgr (alkanolamine) dimer formation in EtOH medium, Energy converges to zero as the dimer eventually breaks down. (C) van der Waals energy for the interaction of Chel and Sgr (iminium) with solvent H ₂ O. (D) van der Waals energy for the interaction of Chel and Sgr (iminium) with solvent EtOH.	120
Figure 5.17. Chel alkanolamine (A ₁ -A ₃) dimers and Sgr alkanolamine (B ₁ -B ₃) dimer in ethanol medium at 0, 600 and 1200 ps time frame.....	122
Figure 6.1. The ground state absorption spectra of the Au@Fe ₃ O ₄ nanoparticle	128
Figure 6.2. (A), (B), (C) Bright field TEM images of Au@Fe ₃ O ₄ nanoparticle(D) Selected area electron diffraction (SAED) image from the nanoparticlespresented at the inset. ...	129
Figure 6.3. (A), (B) High-resolution TEM (HRTEM) images of Au@Fe ₃ O ₄ (C) FFT image from the area shown in Fig (B), (D) Fourier filtered image of Fig (C)	129
Figure 6.4. (A) STEM-HAADF image of the Au@Fe ₃ O ₄ , (B) EDX spectra acquired from the selected area 1 in Fig (A), (C) Au-L map, (D) Fe-K map, (E) Composite map.	130
Figure 6.5. (A) STEM-HAADF image of the Au@Fe ₃ O ₄ , (B) Line scan profile of the NP along the line shown in Fig (A).	130
Figure 6.6: Magnetic field dependent magnetization at 300 K for (A) Au@Fe ₃ O ₄ and (B) comparison of the extent of magnetization between Fe ₃ O ₄ and Au@Fe ₃ O ₄	131
Figure 6.7. UV-vis absorption spectra of Sgr on gradual addition of Au@Fe ₃ O ₄	132
Figure 6.8. Trend and extent of fluorescence quenching from the S ₁ state of Sgr in presence of a variable concentration of Au@Fe ₃ O ₄	133
Figure 6.9. (A) The stern-volmer plot of Sgr-Au@Fe ₃ O ₄ complex as a function of increasing concentration of Au@Fe ₃ O ₄ . (B) Linear Stern-Volmer plot of Sgr-Au@Fe ₃ O ₄ complex at low concentration Au@Fe ₃ O ₄	133

Figure 6.10. T-T absorption spectra of Sgr upon the addition of different concentration of Au@Fe₃O₄. 135

Figure 6.11. T-T absorption spectra and the corresponding modulation of the transient spin state of Sgr in presence of variable FeNP concentration under the influence of a constant low external magnetic field (0.08 T). 137

List of tables

Table 3.1: Average Lifetime of Triplet-State Sgr, Sgr-AuNP Complex, Sgr-ctDNA/Chromatin and Sgr-AuNP-ctDNA/ Chromatin, recorded at 360 nm after the Laser Flash at 355 nm.	66
Table 4.1: (A and B) Represents the details about the lifetime components of Sgr as a result of adsorption on magnetic nanosurface in CH ₃ CN and H ₂ O medium respectively.	88
Table 4.2: (A and B) The lifetime components of Sgr due to the adsorption on nanosurface in CH ₃ CN and H ₂ O respectively.	90
Table 4.3: Components of the biexponential decay profiles at (A) 360 nm and (B) 400 nm in C ₂ H ₅ OH medium.	93
Table 4.4: Table showing the time-averaged energetics for different electrostatic and non-electrostatic forces in different solvents.	102
Table 5.1: Fluorescence lifetime of Chel on increasing the concentration of the drug in EtOH medium.	112
Table 5.2: Solute-solute and solute-solvent interaction energies for Chel and Sgr in H ₂ O (iminium forms).	121
Table 5.3: Solute-solute and solute-solvent interaction energies for Chel and Sgr in EtOH (alkanolamine forms).	121
Table 6.1. The Lifetime Components of Sgr as a result of adsorption on Nanosurface.	134
Table 6.2. Excited state triplet lifetime of Sgr on plasmonic (AuNP), magnetic (FeNP) and magnetoplasmonic (Au@Fe ₃ O ₄) nanosurface in presence and absence of magnetic field.	138

CHAPTER-1

Introduction

OUTLINE: What does the chapter brief?

- Different types of photophysical processes
- The basic theory behind the photophysical processes
- Role of solvent polarity on the photoinduced reaction
- Effect of external magnetic field on the photophysics of a molecule
- Overview of nanoparticle
- Influence of nanosurface on the photophysics of the prototype anticancer drug molecules in a transient absorption perspective.
- Anticancer drugs
- Photodynamic therapy

Both photophysics and photochemistry are the branches of science dealing with the interaction between incident photons and molecules or materials. Photoinduced reactions are concerned with the changes initiated in the electronically excited molecules after absorption of suitable radiation in the UV-visible and near-infrared (NIR) region of the spectrum. Photophysics deals with physical changes of molecules caused by the interacting photons while photochemistry mainly focuses on the chemistry involved after the interaction of molecules with photons.¹ According to the Brhad-Devata, I:61 “All that exists was born from the Sun” or in other words ‘photon driven processes (physical or chemical) are the basic to the world we live in’.^{2,3} The origin of life is also a photochemical act.² All the photobiological machinery for the production of food and for the propagation of life are run by the utilization of solar energy. This developing field of science is the key to understand many natural phenomena of photosynthesis, atmospheric chemistry, bioluminescence, vitamin D synthesis and so on.^{4, 5,6,7,8} The vision process is also a result of a series of photophysical and photochemical changes in our eyes.^{9,10} The relevance of photochemistry also lies in the cutting edge research areas like solar cell,¹¹ water splitting reactions,¹² synthesis of natural products like vitamin D₂ from ergosterol, production of anti-viral agents (Cubans),¹³ generation of antioxidants by photosulphonation¹⁴ and green synthesis of some polymer like caprolactam from Nylon 6¹⁵ or polyvinyl pyrrolidone (PVP) from vinyl pyrrolidone.¹⁶ Along with these the photophysical phenomena of fluorescence and phosphorescence are used widely in bioimaging and sensing.^{17,18}

As photophysics deals with the exciting molecular system on light irradiation, the understanding and application of electronically excited molecular systems has got a new horizon of interest after the advancement in laser technology. Advancement of photon source provides us with the opportunity to fabricate powerful tools or help us in generating newer concepts to study different biological and chemical phenomena with

different timescale (from *ms* to *fs*) and energy regime. There are different types of the laser such as diode laser with low energy to detect the rotational and vibrational transition¹⁹ of a molecule and pulsed laser to detect the faster phenomena like transient absorption, femtosecond fluorescence lifetime measurement etc.²⁰ Considering the following frequency-time uncertainty relation²¹ for a photon pulse of interest

$$\Delta \nu \Delta t \geq 1/4\pi \dots\dots\dots (1.1)$$

where $\Delta \nu$ is the frequency spread (uncertainty in frequency) and Δt is the time spread (uncertainty in time). Hence, we can generate a shorter pulse by broadening the frequency spread or a longer pulse by contracting the frequency spread or in other words by using a shorter pulse (suitable for dynamical studies) we cannot do a better spectroscopy and by using a longer pulse (suitable for spectroscopy) we cannot perform a dynamics study.

The reality of energy crisis in this modern era increases the relevance of research on photoinduced reactions, conversion and storage of solar energy²² The crisis of energy can be solved worldwide if the suitable photochemical reaction can be discovered and devices for the storage of this abundant source of light can be designed. The use of photochemistry in therapy is worth to mention too e.g., in photodynamic therapy²³ the photosensitizer is first excited by laser then the photoexcited sensitizer molecule react with the surrounding triplet oxygen (³O₂, ground state) to produce singlet oxygen (¹O₂, excited state) or react with the solvent medium or associated molecules in the system to generate free radicals. These generated free radicals then destroy the toxic cells, tumours or cancer cells through H-abstraction based DNA cleavage method²⁴. However to understand any complex photo-induced reaction pathway it is very important to understand the photophysics and photochemistry of small molecules. In this thesis, I have discussed the photophysics of two small molecule prototype anticancer drugs i.e.,

sanguinarine (Sgr) and chelerythrine (Chel) on the metal nanoparticle surface. For the sake of basic research, the fundamental study of the photoexcited molecule is essential in the field of photophysics as well as an understanding of the actual photophysical and photochemical pathway of a molecule is exciting by itself. In addition, photoinduced electron and energy transfer in the faster time scale (in the order of *ns* to *fs* second) have allowed us the proper understanding of energy landscaping among electronic and spin states of short-lived transients or intermediates in a photoexcited molecular system, modes of energy transfer, and complex reaction pathways.²⁵

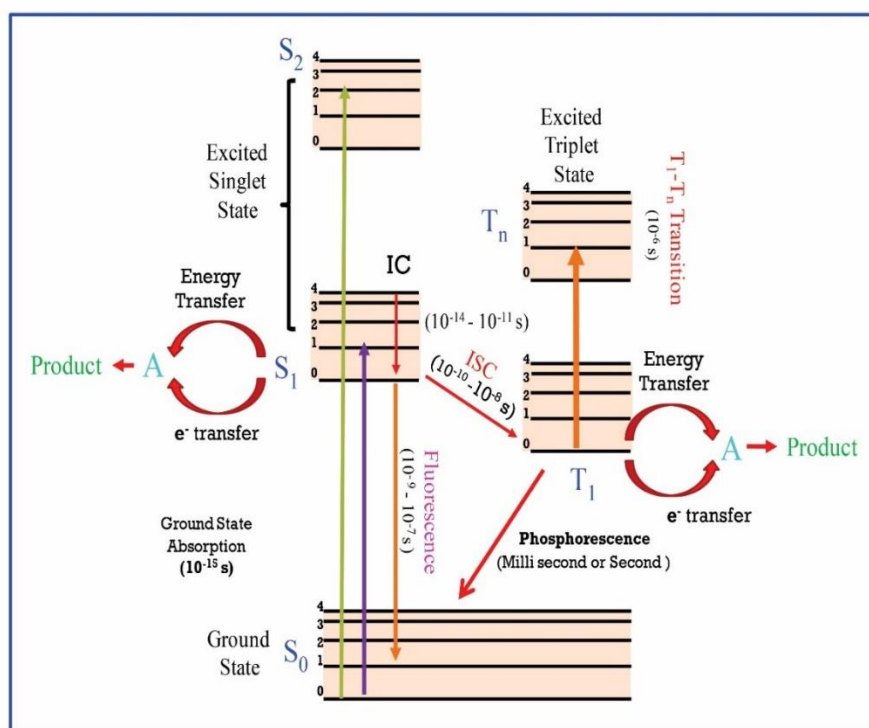


Figure 1.1: The Jablonski diagram²⁶ which explains not only the relative energy spacing among different energy (electronic and vibrational) states but also shows possible photoinduced processes may initiate from the photoexcited molecular state.

The photoexcitation of a molecule and the subsequent fate of the molecule after photoexcitation can be better understood by a Jablonski diagram²⁷ as shown in **Figure**

1.1. By absorbing a photon, a molecule may initiate an electronic transition from ground electronic S_0 state to higher energy S_1 (1st excited electronic state) or S_n (where $n = 2, 3, \dots$) state. Energy relaxation of the excited state may happen through either radiative or non-radiative pathways.^{28, 29} For simplicity and relevant to my thesis work I will consider only the 1st excited singlet state throughout the discussion. With this restriction, the higher energy vibrational state ($v=n, n \neq 0$) of S_1 electron can go to the lowest vibrational state ($v=0, S_1$) through vibronic coupling.³⁰ From the $v=0, S_n = S_1$ state, electron can come back to the S_0 state through a radiative transition we define the process as fluorescence. On the other hand, vibrationally cooled ($v=0$) excited electron ($S_n = S_1$) can relax to the ground state ($S_n = S_0$) via non-radiative heat transfer also familiarly known as collisional quenching. From the S_1 state, there is another possibility by which the excited state electrons may pass on to the triple degenerate T_1 state. According to the spin selection rule (in any allowed electronic transition, the overall spin angular momentum of the system should not change),³¹ this S_1 to T_1 interconversion is a forbidden transition. Since the spin multiplicity ($2S+1$) of the S_1 state is 1 whereas the spin multiplicity of the T_1 state is 3 the transition from S_1 to T_1 is not allowed as $\Delta S \neq 0$. Since S_1 to T_1 interconversion is not an allowed process, this type of electronic transition can take place only by the enforcement of spin-spin coupling or spin-orbit coupling.³² The process of S_1 to T_1 interconversion is called intersystem crossing (ISC). From T_1 state, an electron can go to the next higher energy triplet states (T_n) if the required amount of energy is provided during excitation. The process of T_1 to T_n transition is called the transient absorption. Flash photolysis or pulsed laser photolysis is the spectroscopic tools generally used for the study of higher energy triplet states.³³ The corresponding spectroscopy is called the excited state transient absorption spectroscopy and the experimental technique used is called the excited state transient absorption technique. The T_1 to T_n transition is interrelated with the ISC process and any change in

the ISC will change the probability of T_1 to T_n transition.³⁴ So, from the excited state transient absorption spectroscopy study we can gather the information related to the ISC, the nature of the spin state of the photon excitation, generated transients or intermediates, stability and time scale of generation of the transients, excited state electron transfer property, the mode of reaction in the photoexcited state and the nature of the complex generated with reaction between the photoexcited electron donor and acceptor molecules.³⁵ The electronic transition from the S_0 to S_1 state requires the time of the order of a femtosecond (fs) as shown in **Figure 1.1**. The relaxation of excited electron from S_1 to S_0 transition requires nearly nanosecond time but when electron goes to the T_1 state, T_1 to T_n transition takes place in the microsecond (μs) range and relaxation of a triplet electron requires microsecond to millisecond (ms) or even longer to sec (s) time to come back to the ground state (S_0) depending on the pathway (**Figure 1.1**) they relax. Phosphorescence based pathway is slower (in the millisecond to sec order).³⁶ The electron of a photoexcited molecule can react with another molecule from the S_1 state or from the T_1 state. As the energy relaxation of an initial triplet electron is slower than an initial singlet electron to the final S_0 state, the mode of reactions with another analyte molecule is different from that in S_1 state.^{37,38,39} If the S_1 to T_1 population or pathway can be perturbed by external factors the mode of reaction or the yield of reaction can be changed accordingly.^{40,41}

Nanoparticles are very interesting materials due to their great nanotechnological potential, unique and strongly size and shape-dependent electronic, chemical, optical and magnetic properties.^{42,43,44,45} For metal nanoparticles the degenerate energy bands of bulk metal split into discrete energy levels with increasing band gaps when their size goes smaller than the exciton Bohr radius (An exciton Bohr radius is a distance in an electron-hole pair. For example quantum dot (QD). A QD is a very small sized (2-10 nm) semiconductor generally formed by 10 to 50 atoms and the size of the crystal is on

the same order as the size of the exciton Bohr radius. This unique size-dependent property causes the “band” of energies to turn into discrete energy levels. The exciton Bohr or Bohr Exciton radius can be mathematically expressed as: $r_B = \frac{\hbar^2 \epsilon}{e^2} \left(\frac{1}{m_e} + \frac{1}{m_h} \right)$ where m_e and m_h are the effective mass of hole and electron respectively. For example, the exciton Bohr radius for ZnO is about 2.34 nm and makes the nano-configurations more similar to molecules than bulk materials.⁴⁶ Moreover, due to the unique nature of the nanosurface they can be used as an efficient drug delivery vehicle^{47, 48, 49}, as well as a very good transmitter/receiver antenna for programmed molecular interactions.⁵⁰ Nanosurface has an interesting role to enhance the intensity of fluorescence emission, Raman signals, Faraday rotation,^{51, 52, 53} Surface enhanced photothermal activity,⁵³ photo dynamic therapy,⁵⁴ etc. The role of nanosurface in the surface enhanced ground state absorption spectra, Raman spectra (SERS) and surface enhanced fluorescence spectra (nanosurface induced fluorescence enhancement and quenching) has been studied extensively but the role of nanosurface on the excited state transient absorption spectra is a very cutting-edge research area and needs to explore in details. A report by Tony E. Karam on “Enhanced Photothermal Effects and Excited-State Dynamics of Plasmonic Size-Controlled Gold–Silver–Gold Core–Shell–Shell Nanoparticles” where the excited-state dynamics of the plasmonic nanoparticles are thoroughly studied using pump–probe transient absorption spectroscopy and the lifetime related with phonon–phonon scattering in core–shell–shell nanoparticles is compared with that of gold nanospheres and nanorods.⁵⁵ Wen Yang, Kunhui Liu in their article “Aggregation-Induced Enhancement Effect of Gold Nanoparticles on Triplet Excited State” has explained that gold nanoparticles (AuNPs) by the excitation of localized surface plasmon resonances, affect strongly both the ground state as well as the excited state of adjacent organic molecules.⁵⁶ They have also explained how the enhancement effect on triplet excited state formation results from the aggregation of gold nanoparticles and depend on the

aggregation size. These findings confirm the aggregation induced plasmon field interaction of AuNPs with excited state population dynamics. There are also recent reports on the evolution in excited-state properties of the metal nano clusters⁵⁷ which offers new insight into the structure-dependent properties of the nanoclusters, and shows their great impact on the optical energy harvesting and photocatalytic applications.⁵⁸ A molecule irradiated close to a metal nanoparticle can be viewed as undergoing transmitter/receiver antenna interactions.^{59,60,50} Natalia L. Pacioniet al. has shown that the ground state and the excited state dynamics as well as the triplet yield of methylene blue (MB) changes significantly as a result of the MB-AuNP interaction. Besides the plasmonic materials, magnetic nano structures are also drawing great interest in the field of excited state dynamics. Adam E. Cohen has put forward a theory on the role of magnetic nanosurface on the intersystem crossing process (ISC) of a surface adsorbed molecule.⁶¹ There are also recent reports on “Correlation between Spin-Orbital Coupling and the Superparamagnetic Properties in Magnetite and Cobalt Ferrite Spinel Nanocrystals”.³² Zhiyuan Zhao *et al.* have studied the effect of interparticle interactions on the magnetization dynamics and related energy dissipation rates of spherical single-domain magnetically blocked nanoparticles in static and alternating magnetic fields (AMFs) using Brownian dynamics simulations.⁶²

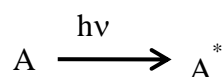
In this thesis the role of a nanosurface on the transient absorption (T_1 to T_n transition) spectra of photoexcited molecules has been discussed along with how the transient absorption technique can be used as a sensory tool for the detection of drug release (prototype anticancer drug Sanguinarine) from a nanosurface in the presence of cellular components like (DNA and Chromatin) has been explained in details. The role of plasmonic and magnetic field of a nanosurface on the modulation of intersystem crossing (ISC) i.e., singlet-triplet interconversion has also been discussed and this is perhaps the first experimental application of the theory for the modulation of radical pair

dynamics by magnetic nanoparticles originally given by Cohen,⁵⁶ for the specific case of a superparamagnetic system.⁶³⁻⁶⁸ The role of a nanoparticle as external stimuli on the overall spin statistics of the small molecule anticancer drugs (Sanguinarine and Chelerythrine) which are adsorbed on the nanosurface has been explained in details later in the subsequent chapters. Since the transient absorption phenomenon is inherently an absorption technique, this technique can be used as a universal sensory tool unlike the conventional fluorescence and SERS based technique^{69,70,71,72,73,74,75} as the transient absorption technique follows a linear relation between the O.D. of a molecule with its concentration which is not the case for fluorescence and SERS. Only a select number of molecules in a selective arrangement or in selective condition can show enhanced (or inherent) fluorescence and Raman activity. Following sections will be devoted to explaining different type of photoinduced reactions in details.

1.2 Types of Photoinduced reactions:

1.2.1 Photoelectron transfer process (PET)

For the photoinduced electron transfer process, the basic concept lies in the understanding of electron donors and an electron acceptor. The electron transfer may be either be an oxidative or reductive type.⁷⁶ In the case of oxidative electron transfer, one molecule (donor) gets excited from HOMO to LUMO by absorbing a photon and transfers the excited electron to the LUMO of another molecule (acceptor). In case of reductive electron transfer, one molecule (acceptor) gets excited from HOMO to LUMO (**Figure 1.2**) by absorbing a photon and then takes an electron to its HOMO from the HOMO of another molecule (donor).⁷⁷



Oxidative photoelectron transfer: $A^* + B \rightarrow A^+ + B^-$ (A: Donor, B: Acceptor)

Reductive photoelectron transfer: $A^* + B \rightarrow A^- + B^+$ (A: Acceptor, B: Donor)

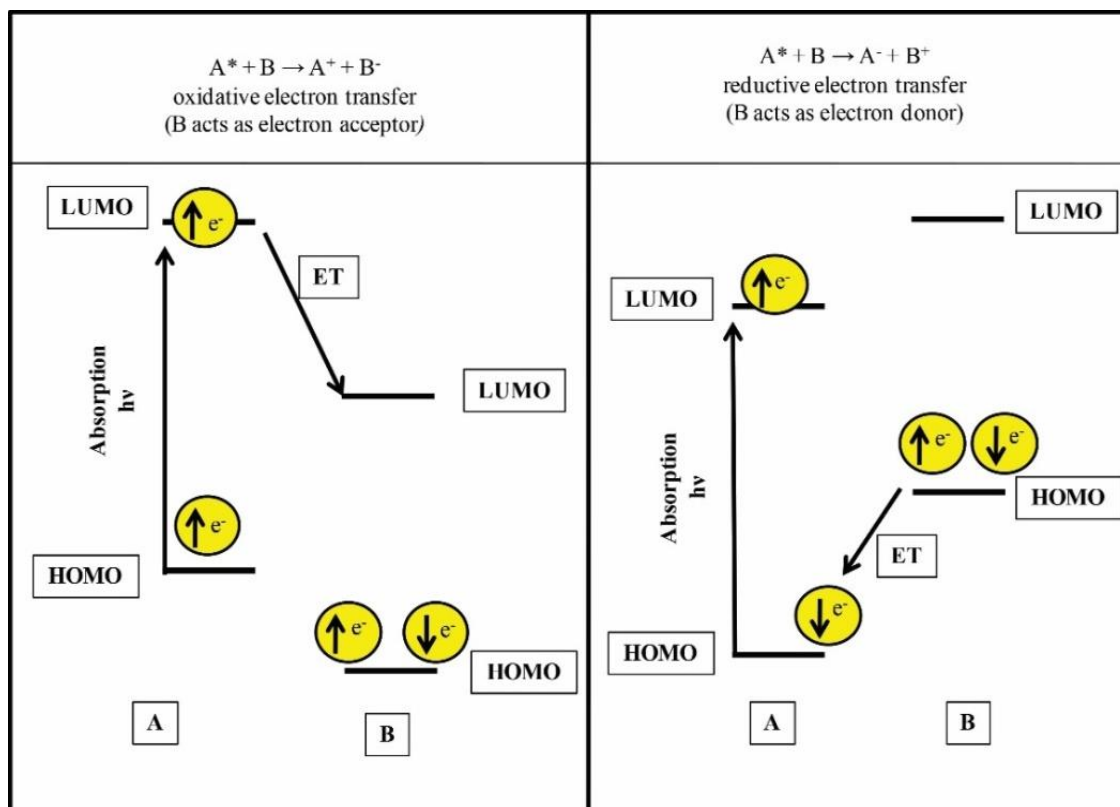


Figure 1.2: The Oxidative and reductive electron transfer process.

1.2.1.1 Encounter Complex Formation

After photoexcitation of a molecule in the liquid medium, an encounter complex may be formed. An encounter complex is like an intermolecular ensemble of excited state and ground state molecules (acts as donor and acceptor respectively) separated by a small distance and in case of a homogeneous mixture, there is a layer of solvents in between these donors and acceptor molecules. The structure of the encounter complex is determined by their size, shape, charge distribution on the reactants and their interactions with the solvent cage. The formation of the encounter complex can be explained by the ‘random walk’ hypothesis.⁷⁸ According to this hypothesis, the molecular diffusion follows a series of one dimensional randomized zigzag steps. During this random walk, the photoexcited molecules may collide, separate or undergo further collisions. A typical collision for uncharged small organic molecule takes about 10^{-9} – 10^{-10} s.⁷⁹ Quenching (deactivation of excited molecules) of the photoexcited

molecule may take place within the encounter complex depending on the nature of the reactants. Inside the encounter complex, the reactant molecules may undergo structural as well as electronic changes. The vibrational fluctuations determine the nuclear barrier of the pathways and have a frequency⁸⁰ of the order of 10^{12}s^{-1} . The lifetime of an encounter complex is sufficiently long enough for allowing the nuclear changes to take place. The nuclear reorganization is a very important aspect for successful electron transfer and it is the rate-limiting step of the quenching pathways.

1.2.1.2 Role of Solvent polarity: Contact ion pair (CIP) and the solvent separated ion pair (SSIP) Formation

During electron transfer between molecules (donor and acceptor) two types of intermediates may be formed: one is contact ion pair (CIP) and another is solvent-separated ion pair (SSIP) (**Figure 1.3**) depending on the polarity of a medium. In more polar solvent the formation of the SSIP is endothermic whereas the formation of the CIP is exothermic due to a difference in solvent stabilization⁸¹. The extent of formation of CIP and SIP also changes depending on the amount of solvent stabilization. The electronic coupling in CIP between the donor and acceptor is much more compared to that in SSIP the partners of photoelectron transfer remain in close proximity.⁸²

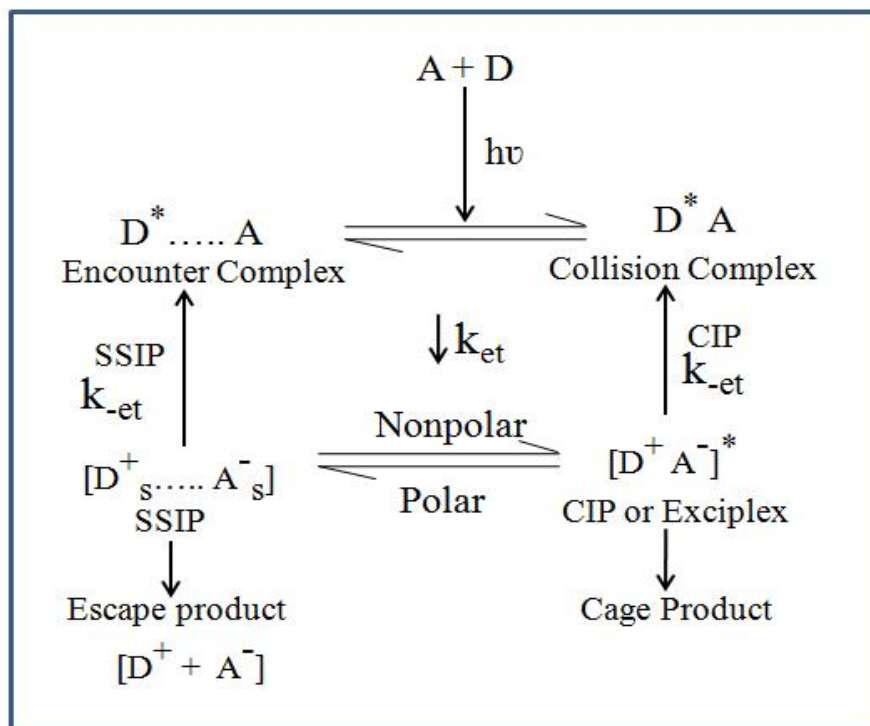


Figure 1.3: Solvent polarity dependent excited state intermediate formation

As CIP and SSIP are descendent of the same parental pair, they are called as ‘geminate’ ion pair. When SSIP are separated by the intervening solvent layer and separates them to a large distance, they are called free ions or solvated ions. These ionic species are totally independent of one another. They are analogous to stable free radicals or distinct, randomized, solvated long-lived species. When the interaction between the reactants is strong inside an encounter complex, an intermediate with a sufficiently long lifetime will be formed, which can undergo light emission. Such intermediates are called exciplex and have binding energy in the order of -5 to -20 kcal/mol. Inside the exciplex, reactant molecules show partial charge transfer character and depending on their magnitude of dipole moment their extent of charge transfer varies. In simplicity, an exciplex is an electronically structured, relatively stable and long-lived excited species. The electronic interaction in an exciplex is represented by the molecular orbital wave function as

$$\Psi = C_1\Psi (D^*A) + C_2 \Psi (DA^*) + C_3\Psi (D^+A^-) + C_4\Psi (DA) \dots \dots \dots (1.2)$$

where the coefficients (C_i) represents the relative contribution of each state or wave functions. In this expression, the first two terms come from the oxidative and reductive reactant pairs respectively, the third term represents the contribution for the electron transfer pair and the fourth term is for the ground state interaction. If $C_3 \gg C_2$ or C_1 , the exciplex will have CT character and there will be a tendency to dissociate into radical ion pairs (RIPs) or “cage products” mainly in polar solvents. In the ground and excited states, the stability of the intermediates has been shown by the potential energy curves for a D-A pair as a function of D-A distances (R). The deeper minimum of D-A in the excited state corresponds to the considerable binding energy between the D and A in the excited states.^{83,84} The binding energy of the excited state includes the ionization potential of D, electron affinity of A and the differential solvation energy of the charge transfer states arises from the difference in their dipole moments. The polarity dependence of such reaction is shown in the (Figure 1.4).⁸⁵

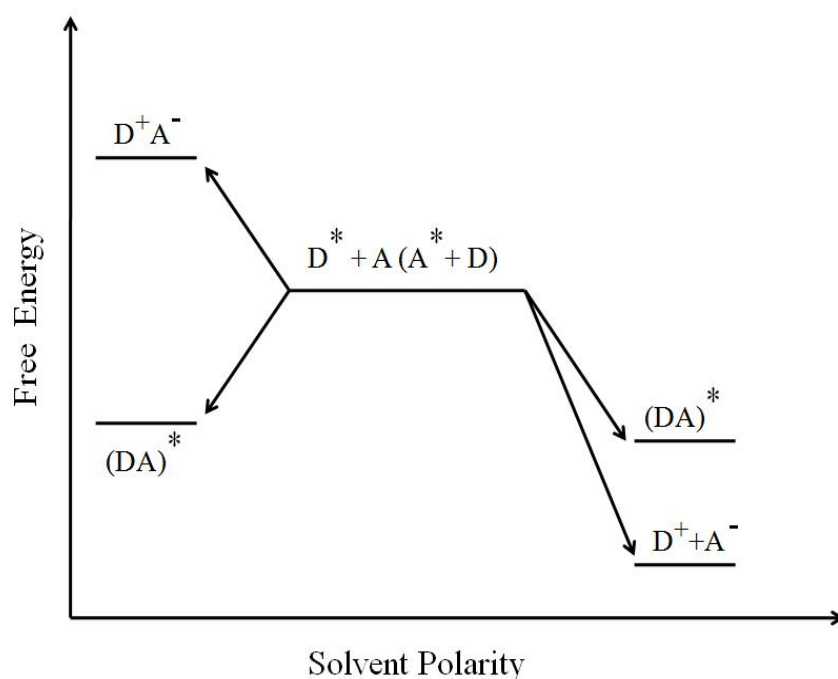


Figure 1.4: Variation of stability of the intermediates as we modulate the solvent polarity⁸⁵

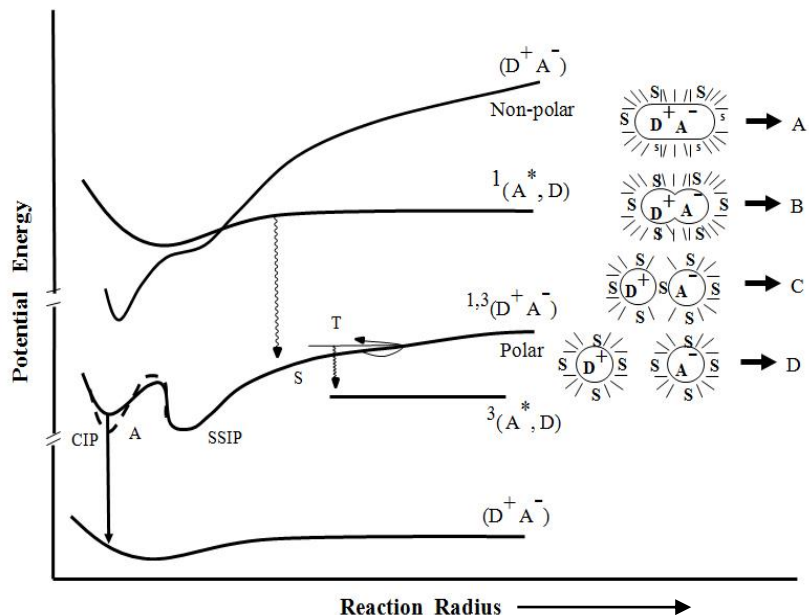


Figure 1.5: Potential energy curves for the electron transfer complexes in different solvent polarity as a function of intermolecular separation.⁸³

It is clearly visible from the above figure that the potential energy curve of the charge transfer state in a non-polar solvent is deeper (or steep) compared to that in a polar solvent (**Figure 1.5**). In polar solvent usually, there are two minima corresponding to the SSIP and CIP respectively. During the conversion from the SSIP to CIP, some of the solvent molecules have to be forced out and that makes an energy difference between the two states. The barrier height is difficult to obtain either theoretically or experimentally as it is likely to be dependent not only on the dielectric constant of the medium as well as on the specific interactions, like H-bonding of the solvent molecules, etc. Due to that the isoelectric (solvents with identical dielectric constant) protic and non-protic solvents may behave differently.⁸⁶ According to the Kirkwood-Onsagar continuum model,⁸⁷ the solvent stabilization energy of the CIP can be expressed as: $E_{CIP} = \frac{\mu^2 (\epsilon - 1)}{\rho^3 (2\epsilon - 1)}$ where μ is the dipole moment of the CIP, ρ is the radius of an equivalent spherical cavity and ϵ is the dielectric constant of the medium. The energy difference between CIP and SSIP is given by the following equation^{85,83}

$$E_{CIP} - E_{SSIP} = \frac{e^2}{2} \left(\frac{1}{r_D} + \frac{1}{r_A} \right) \left(1 - \frac{1}{\epsilon} \right) + \frac{e^2}{\epsilon d_{SSIP}} - \frac{\mu^2}{\rho^3} \left(\frac{\epsilon-1}{2\epsilon+1} \right) - \Delta E_{ex} - \frac{e^2}{d_{CIP}}$$

.....(1.3)

here e stands for the electronic charge, r_D and r_A are the radii of D and A, d_{SSIP} and d_{CIP} are the distances between D and A in SSIP and CIP respectively and ΔE_{ex} is the energy required for exciplex formation. It is evident from the equation that at the high polarity of the medium the equilibrium between SSIP and CIP shifts towards SSIP.

1.2.2 Excited State Proton Transfer (ESPT)

Besides electron transfer, excited state proton transfer and the movement of both positive and negative charge in hydrogen-bonded (HB) networks are very significant processes in chemistry and biology.⁸⁸ ESPT is the key step for the acidic and basic solutions under laser excitation, fuel-cell operation, and signal transduction. The concept of ESPT was first coined by Agmon et al., Zundel et al., Tuckerman et al. and Voth et al. and their revolutionary works are now well established by the combination of experiment, theory and simulations.^{89,90-98} Upon photoexcitation, photoacids (Photoacids are molecules which become more acidic upon absorption of light either by forming strong acids upon photodissociation or by dissociation of protons upon photoassociation (e.g., pericyclic ring closing)). For example, the triphenylsulfonium salts absorb at 233 nm, which induces the series of reactions to generate acids) increase their acidity, whereas photo bases show an increase in their basicity.^{99, 100} ESPT may be of two types, either intramolecular or intermolecular. When both (donor) acidic and basic (acceptor) moieties exist in close proximity within a molecule, intramolecular excited state proton transfer (*intra*-ESPT, time scale: 160-200~fs)¹⁰¹ is observed between them, otherwise the reaction is intermolecular (bimolecular or pseudo-unimolecular, *inter*-ESPT), such as in the case of excited state proton transfer to the solvent molecules.^{102, 103} The rate and hence the time scale of inter-ESPT could span from as low as tens of nanoseconds

for weakest photoacids to very short timescales of 100fs for the strongest photoacids synthesized so far^{104, 105}. The dependence of *inter*-ESPT time scale on the strength of photoacids ($-8.5 \pm 0.4 < pK_a < 3$) has been explained in details by Simkovitch et al.¹⁰⁴ Steps involved in excited state proton transfer in a polar or non polar solvent can easily be understood and measured by using a pump-probe spectroscopy and time correlated single photon counting fluorescence spectroscopy. Spray, D. B. et al.¹⁰⁶ have clearly shown that the excited state proton transfer dynamics shows a clear two-step process. The first thing to happen after electronic excitation is the charge redistribution occurring in tens of picoseconds time scale which is followed by proton transfer on a *pico* to *nanosecond* timescale.¹⁰⁶ After that the elementary dissociation of the proton takes place whose rate coefficient is generally denoted by k_d . The formula of dissociation rate co-efficient was first given by Marcus from the structure-reactivity correlation and later by Agmon and Levine from a mixing entropy argument.¹⁰⁷⁻¹¹⁰ The corresponding equation is:

$$k_d = k_d^0 \exp(-\Delta G^*/k_B T) \dots \dots \dots (1.4)$$

A solvated proton is produced in the solution after the dissociation. In water, the diffusion constant of a proton is $9.3 \times 10^{-5} \text{ cm}^2/\text{s}$ at room temperature and the hopping time is 1-2 ps which is at least 4.5 times larger than any other cation.^{111, 112}

1.2.3 Proton-Coupled Electron Transfer

The coupling between electrons and protons plays a pivotal role in the biological processes like respiration, photosynthesis and enzyme reactions, and also in the chemical processes like chemical sensors, fuel cells, and various electrochemical devices.¹¹³⁻¹²⁰ In proton-coupled electron transfer (PCET) reactions the electron and proton transfer processes may be stepwise or concerted. In a stepwise process, a stable intermediate is formed after a single electron or proton transfer, while in a concerted

process a single quantum-mechanical event with more than one intermediate arises from both electron and proton transfer. Because of the quantum mechanical nature of the proton, PCET reactions are termed as mixed electron-proton vibronic states rather than by purely electronic states. PCET is normally described by the non-adiabatic transitions between the reactant and product vibronic states.¹²¹

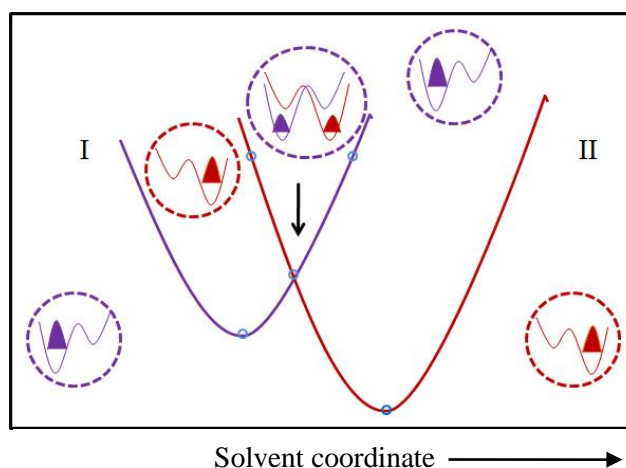


Figure 1.6: Slices of the free energy surfaces for the ground state reactant (I) and product (II) vibronic states along the solvent coordinate.¹²¹

Rate constant expression for excited state proton transfer reaction is¹²²:

$$k = \sum_{\mu} P_{\mu} \sum_{\nu} \frac{|V_{\mu\nu}|^2}{\hbar} \sqrt{\frac{\pi}{\lambda_{\mu\nu} k_B T}} \exp \left[-\frac{(\Delta G_{\mu\nu}^0 + \lambda_{\mu\nu})^2}{4\lambda_{\mu\nu} k_B T} \right] \dots \dots \dots (1.5)$$

where P_{μ} is the Boltzman probability for the reactant state μ , $V_{\mu\nu}$ is the vibronic coupling between the reactant and product vibronic state μ and ν , $\lambda_{\mu\nu}$ is the solvent reorganization energy for states μ and ν , ΔG^0 is the free energy of reaction for states μ and ν .

1.3 Magnetic Field Effect: Link between charge transfer and spin dynamics:

During photo-induced charge transfer (electron, proton or proton-coupled electron transfer), radical ion pair (RIP) or radical pair (RP) containing unpaired electrons are produced. Due to the production of species with unpaired spin, the reaction dynamics can be manipulated by applying an external magnetic field (MF).¹²³⁻

¹²⁹Generally the electronic spin multiplicity of the excited state [Singlet $(2S+1) = 1$ or

Triplet ($2S+1) = 3$] is conserved during the electron transfer and a memory of this initial spin multiplicity is maintained in the resulting RIP until the latter undergoes further reactions. The RIP is like a "spin selective microreactor" and the nature of the products formed is dependent on the initial spin states.¹³⁰The subsequent charge recombination process is also spin selective; i.e., the singlet RP recombines to produce the singlet state and the triplet RP recombines to yield the triplet state. The spin multiplicity of the RIP is however not stationary and can develop coherently between the S and T configurations. By influencing this spin evolution in the presence of an externally applied MF can thus alter the fate of a photoelectron transfer reaction without utilizing any chemical energy. The information about the magnetic properties of the intermediates; the spin multiplicity of the precursors, spin-spin exchange interactions²¹ and reaction rates for spin-dependent pathways can be obtained from the measurement of MF effects on the RIP. For a qualitative understanding of the MF effect on the photoinduced charge transfer reactions, mechanistic description of different spin states, the spin inter-conversions, and MF behaviour are given below.

1.3.1 Vectorial Representation of Singlet and Triplet RIPs

A spinning charged electron possesses a magnetic moment and in presence of an external magnetic field (MF), angular momentum component of the electron can either be parallel ($+ \frac{1}{2} \hbar$, α spin) or antiparallel ($- \frac{1}{2} \hbar$, β spin) with the direction of the external field. In a RIP, the spins of the individual electrons can interact with each other and the resultant spin states can be either triplet (spin multiplicity 3), when the two unpaired spins reorient themselves either in parallel (T_+ , $\alpha\alpha$), perpendicular (T_0 , $\frac{1}{\sqrt{2}} (\alpha\beta + \beta\alpha)$) or anti parallel (T_- , $\beta\beta$) to the axis of the magnetic field or singlet state (spin multiplicity 1) when the direction of the electronic spin are opposite (paired)

to each other ($S, 1/\sqrt{2} (\alpha\beta - \beta\alpha)$). When no external magnetic field is applied the three T states (T_0 and T_{\pm}) remain degenerate.^{126, 130, 131}

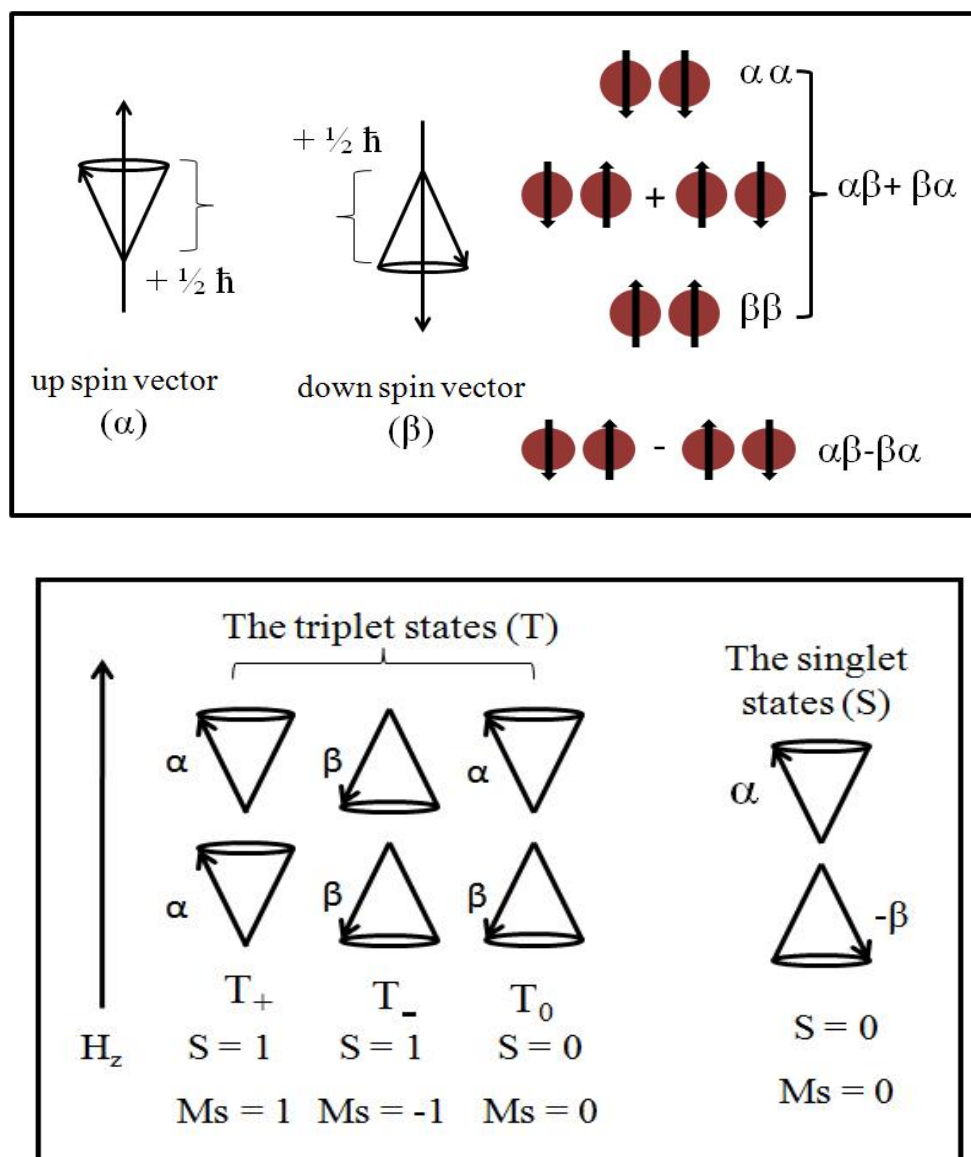


Figure 1.7: Vector representation of electron spin moment in presence of external magnetic field (up) and the Singlet and Triplet spin states (bottom) of a RIP.¹³²

The S and T state has an energy difference of $2J$ where J is the exchange integral that preserves the electron indistinguishability. J depends on the separation distance between two radical pair as,

$$2J = 2J_0 \exp(-aR) \dots \dots \dots (1.6)$$

Where R = inter radical distance, a = rate of decrease in J with R .

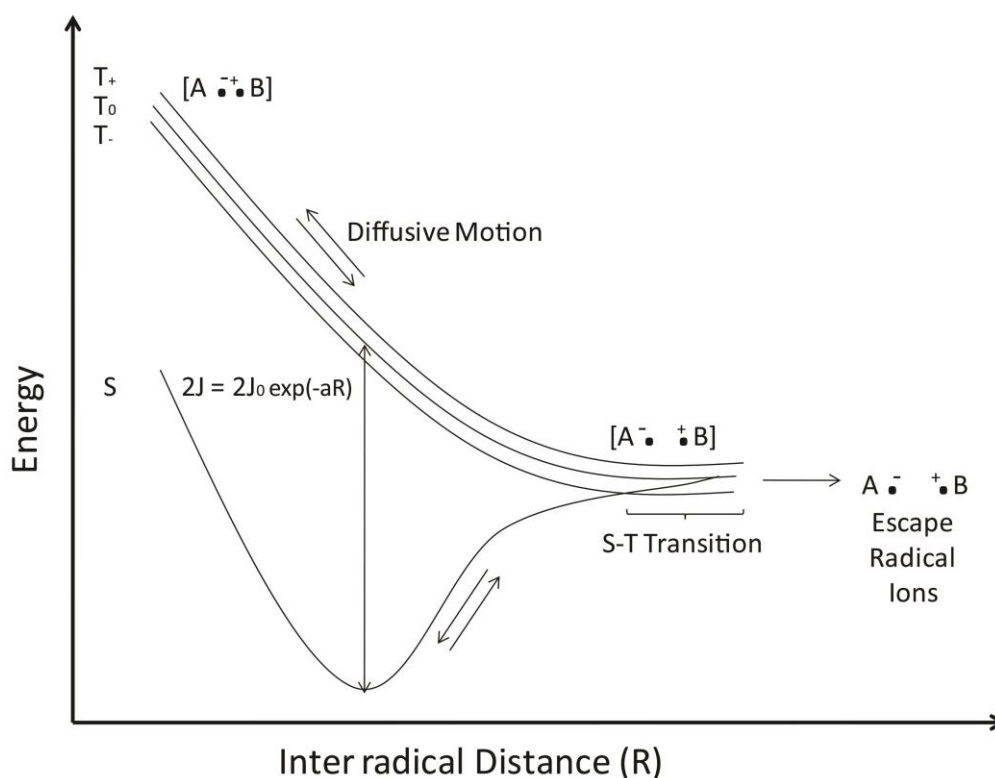


Figure 1.8: Energies of Singlet and triplet RIPs and their pathways in solution.¹³³

The energy difference between S and T is shown in the potential energy diagram. Immediately after the formation of the RIP the inter radical distance is so small that the exchange between the spin state becomes difficult due to the large energy gap. After several diffusive motions when the distance between the radical pair is infinite the term $\exp(-aR)$ becomes zero and hence $2J \sim 0$ (zero energy gap), the S-T interconversion becomes possible. However, when the separation distance between the radical pair is large enough, a spin correlation may break down. To observe the magnetic field effect, it is thus very important to maintain the separation distance between two radical pairs so that $2J$ becomes zero for a sufficiently long time and can undergo S-T interconversion. Out of three different triplet states (T_0 and T_{\pm}) of the triplet multiplicity, it is important to note that the S and T_0 (perpendicular triplet) interconversion requires a spin rephasing of the two spin vectors with respect to each other whereas interconversion between S

and T_{\pm} (parallel and antiparallel) require a spin flip or change in electronic spin momentum.

1.3.2 S-T intersystem crossing (ISC) and mechanism of MF effect

There are several pathways by which singlet-triplet ISC takes place. These are the hyperfine-coupling mechanism (HFC), spin-orbit coupling (L-S coupling), Δg mechanism, relaxation mechanism,¹³⁴⁻¹⁴¹ triplet-triplet, and triplet-doublet mechanism and level crossing mechanism.¹³⁴⁻¹⁴¹ Among all these mechanisms HFC, L-S coupling, Δg mechanism will be discussed elaborately as these are relevant to the experimental work discussed in the subsequent chapters.

1.3.2.1 The Hyperfine Coupling Mechanism

The HFC originates from the dipole-dipole interaction between electron spin and nuclear spin states. In the absence of externally applied magnetic field and at a larger inter-radical separation where $2J=0$ the four spin states S, T_+ , T_- & T_0 remain degenerate and the interconversion between S and T_0 or S and T_{\pm} becomes possible by HFC mechanism. Hyperfine coupling provides sufficient torque requires for the spin rephrasing (interconversion between S & T_0) and spin flipping (interconversion between S and T_{\pm}). Spin flipping is accompanied by a corresponding change in the nuclear spin and preserves the total spin angular momentum ($\alpha_e \beta_N - \alpha_N \beta_e = 0$, where e and N represents electron and nucleus respectively). The efficiency of ISC is governed by the extent of nuclear spin and electronic spin hyperfine coupling interaction.^{135, 138-140} The rate constant for intersystem crossing k_{ISC} depends on HFC as:

$$k_{ISC} = \frac{g\beta B_{av}}{h} \dots \dots \dots (1.7)$$

where B_{av} denotes the local magnetic field, g is the electronic g factor, β is the Bohr magneton.

When an external magnetic field is applied the T_+ and T_- sublevels differs in energy from T_0 because of Zeeman splitting, decreasing the probability of S to T_{\pm} transitions. This, in turn, leads to an increase in the population of the initial spin states. To evaluate this effect an external magnetic field in the order of 100mT (0.01T) is sufficient. In an external field beyond this range, the Zeeman interaction exceeds the magnitude of hyperfine coupling and the effect should saturate (**Figure 1.11**). The field at which half the saturation reaches is represented as $B_{1/2}$. $B_{1/2}$ is the measure of Hyperfine coupling interaction present in a system.

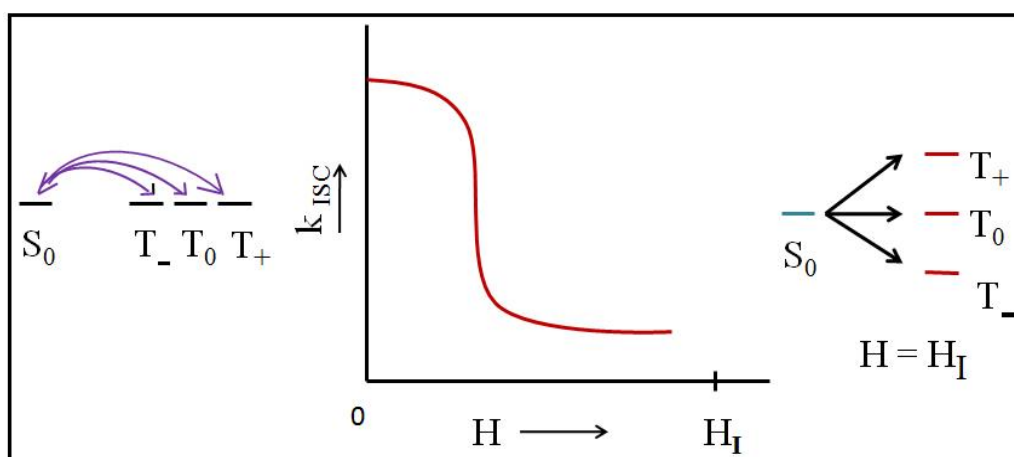


Figure.1.9: Magnetic Field effect due to hyperfine mechanism.¹³²

1.3.2.2 Spin-Orbit coupling (L-S coupling)

The role of Spin-Orbit coupling (SOC) in magnetic field effect (MFE) is unique in the sense that it can simultaneously enhance or quench the intersystem crossing (ISC) effect.^{142,143} SOC is helpful in mixing states differing in spin and orbital part of the wave function. Thus, whereas stationary states with sufficient spin-mixed character do not arise unless there is an orbital degeneracy. SOC can effectively make the excited states nonstationary by inducing ISC processes where the spin and orbital mixing occur simultaneously.¹⁴⁴ This is due to a difference between the g factors of the two electrons in the RIP. The different Larmor frequencies of the two radicals bring about a periodic dephasing and rephasing of the transverse spin components corresponding to periodic

transitions $T_0 \leftrightarrow S$ of the RP. The rate of these transitions increases linearly with the magnetic field. The difference in the g-factors arises if SOC is more efficient in one radical of RPs. i.e., the Δg mechanism is actually related to the SOC.

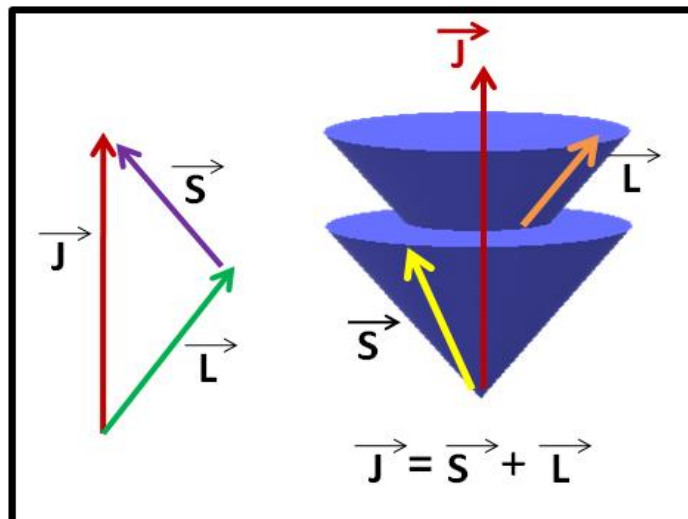


Figure 1.10: Vector cones of total angular momentum

1.3.2.3 Δg Mechanism

The Larmor precession frequency of an electronic spin vector in presence of an external magnetic field, B_0 , is given by $\omega = g\beta_e h^{-1} B_0$, where g is the lande splitting factor and β_e is the Bohr magneton. In presence of a homogeneous external magnetic field the difference in processional frequencies ($\Delta\omega$) for the electron in a radical pair is related to the g factor as:

$$\Delta\omega = \Delta g \beta_e h^{-1} B_0 \dots \dots \dots (1.8)$$

where Δg is the difference in electronic g factor and the spin evolution occurs after a time $t = \pi/\Delta\omega$. When the exchange interaction (J) is negligible in comparison to the magnetic interaction the k_{ISC} is given by $k_{ISC} = \Delta\omega/\pi$, where $\Delta\omega$ is in radian s^{-1} , $k_{ISC} = 3 \times 10^6 \Delta g B_0$, B_0 is in Gauss and k_{ISC} in s^{-1} . An effective $S-T_0$ mixing will occur when $k_{ISC} \cdot \tau \geq 1$. For $\Delta g = 10^{-3}$, $\tau = 10^{-9}$ s, the external field strength should be in the order of

10^6 G to get a significant MFE. Thus Δg mechanism is termed a high field effect and the lifetime of a RIP plays an important role in the S-T transitions. Now if by any means we can increase the Δg value then the Δg mechanism will be effective at the low external magnetic field also. In this light, we have explored the role of single domain super paramagnetic nanosurface to control the ISC rate in the latter part of this thesis.

1.4 Nanoparticles: An Overview

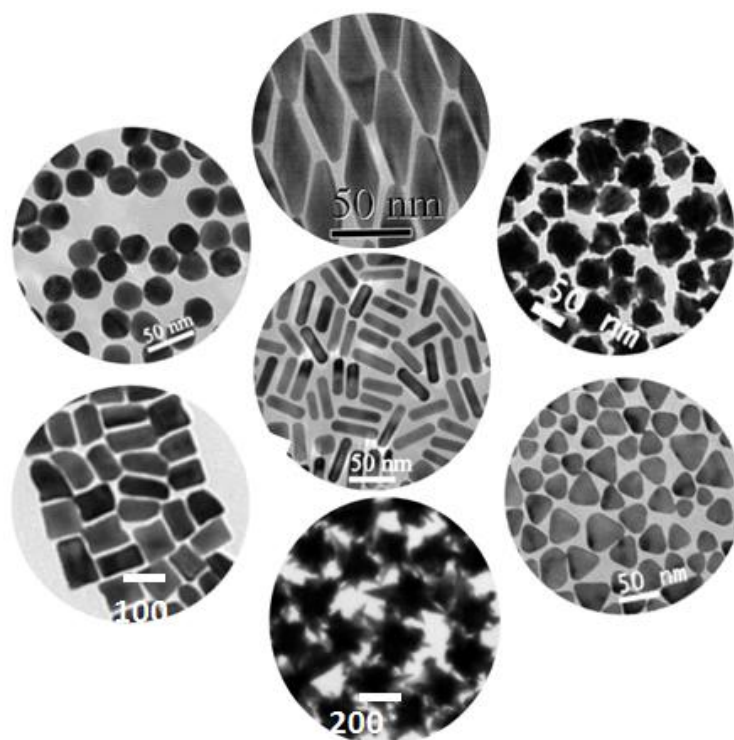


Figure 1.11: Metal nanoparticles with different shape and sizes.

‘Nano’ is a prefix used to describe ‘one billionth’ of something.¹⁴⁵ The term ‘nano’ was first introduced by Nobel laureate Richard P Feynman in 1959. It is well known that the smallest chemical entity of any matter is an atom. Atom has its dimension in Angstrom (\AA or 10^{-10} m) order i.e., below 1 nm. A molecule consists of atoms has dimension around 1 nm. On the other hand, infinite arrays of bound atoms beyond submicron range form a bulk material.¹⁴⁶ The nano regime falling in between, deals with particles of 1 nm-100 nm, represents a collection of few (about 10 to 10^6) atoms or molecules per particle¹⁴⁷. Nanomaterials can be considered to be a link between atomic scale materials

and bulk materials. Nanotechnologies are used for the development and manipulation of materials at the nanometer length scale, either by scaling up from single groups of atoms (the bottom up synthetic approach) or by reducing bulk materials to smaller sizes (the top down synthetic approach).¹⁴⁸ Nanotechnologies are now widely used in different areas as diverse as drug development, water decontamination, information and communication technologies, and the production of stronger and lighter materials^{149, 150}. When the size of the bulk materials get reduced to the nanoscale, they often exhibit novel and unpredictable characteristics such as extraordinary strength, chemical reactivity, electrical conductivity, superparamagnetic behaviour¹⁵¹ that are not common at the micro- or macro scale. The nanomaterials may be made of plasmonic, magnetic, organic, inorganic and semiconductor materials. In this thesis, I shall be discussing the plasmonic, magnetic and magnetoplasmonic nanomaterials mostly. There are many reports that have described the role of plasmonic and magnetic nanomaterials in the field of chemistry, physics, biology, and medicine.¹⁵² This thesis explores the role of plasmonic, magnetic and magnetoplasmonic nanomaterial to control the excited state dynamics of prototype anticancer drug molecules.

Depending on the particle size, nanomaterials may be classified into the following groups:

- (1) A 'Cluster' is a collection of around 150 units of atoms or molecules with a size generally below 2 nm and having a property close to their constituent atoms or molecules for atomic and molecular clusters respectively.¹⁵³
- (2) 'Quantum dot' is a particle showing a size quantization effect in at least one dimension.

(3) ‘Nanoparticles’ or ‘Nanomaterials’ are characterized to have dimensions in the range of 3-100 nm. They may be polycrystalline, noncrystalline, single crystallite or an aggregate of crystallites.¹⁴⁷

(4) ‘Nanocrystal’ is a particle which is a single crystal in the nanometer regime.

(5) ‘Nanostructured or Nanoscale materials’ are materials having at least one dimension in the nanometer range. When the material has all three dimensions in the nanometer range, it is a 3D nanoparticle e.g., nanocube, nanoflower, nanosphere, etc. If it has two dimensions in the nano-regime, it is a 2D nanoparticle e.g., nanoplate, nanofilm, etc. Materials with only one active nano-dimension are called a 1D nanoparticle e.g., nanowire, nanofibre, etc.¹⁵⁴

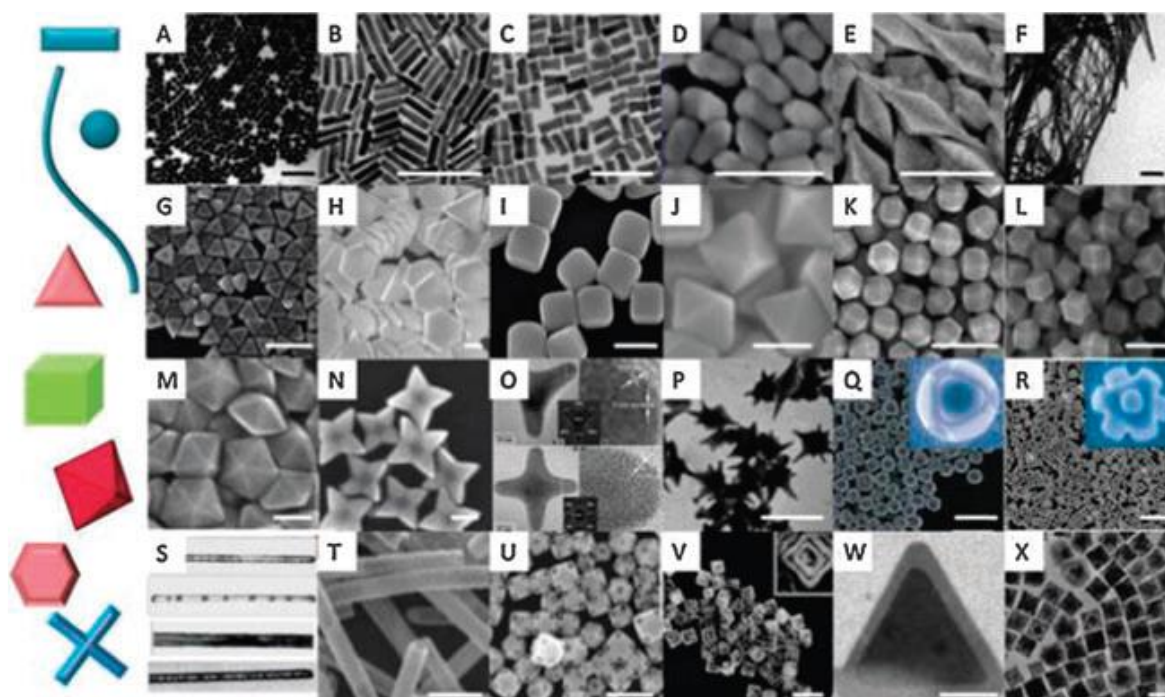


Figure1.12: Nanomaterials with different shape and size."Reprinted (adapted) with permission from Self-assembly of noble metal nanocrystals: Fabrication, optical property, and application, Nano Today (2012) 7, 564-585, DOI.org/10.1016/j.nantod.2012.10.008, Elsevier, Copyright year (2012).”

1.4.1 Plasmonic nanomaterials and their Interesting properties

Metal nanoparticles that are enriched with free moving surface electrons are called plasmonic nanomaterials. They can interact with photons through excitation of localized surface plasmon resonance (LSPR). LSPR is the coherent collective oscillation of valence electrons and is produced when an incident electromagnetic field matches with the natural frequency of surface electrons oscillating against the restoring force of positive nuclei. When the size of a particle is much smaller than the wavelength of incident light ($d_{Nano} \leq \frac{1}{10} \lambda_{Photon}$), the particle-light interaction can be described by the dipole approximation.¹⁵⁵ The resultant electron oscillation generates an oscillating dipole that radiates an electromagnetic field. This field interacts with the electric field associated with incoming photons. When the frequency of oscillation matches with that of incoming photon the electrons start resonating. At the resonance condition the intensity enhancement of the electric field is 10^2 - 10^3 times more on a single nanoparticle and 10^4 - 10^5 times more in between two nanosurfaces separated by a distance of around 1 nm, compared to that of the incoming photon flux. Due to the very high field density in between two nanosurfaces the inter-nano space is called hot spot. Such a hot spot can exhibit multiple dipole resonances with higher wavelength than that of isolated individual nanoparticles. This field might be very important for the activation and amplification of chemical transformations (especially the photochemical reactions). Due to the high field, the rate of energetic charge-carrier formation increases a lot. Plasmonic nanoparticles are the ideal platforms for many applications that require enhanced light-matter interactions due to the enhanced oscillating electromagnetic field, localized near the surface of the metal nanostructure and in the hot spot in between two nanostructures. As for example, plasmonic metal nanoparticles are useful platforms for enhancement of excited state electronic population, surface-enhanced Raman spectroscopy, molecular sensing, single-molecule spectroscopy, solar energy

conversion¹⁵⁶⁻¹⁶⁰ and surface enhanced fluorescence etc. Field localization and enhancement also play a major role to numbers of novel applications in optical imaging, nanoelectronics, biomedicine, photovoltaics, photocatalysis and many others¹⁶¹

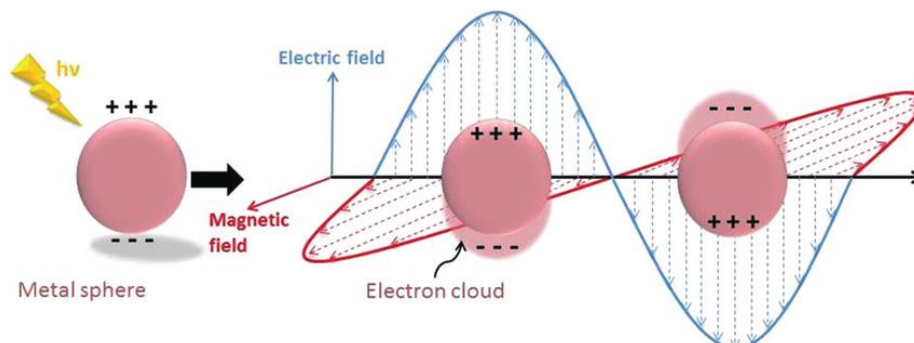


Figure 1.13: Schematic of plasmon oscillation in spherical plasmonic nanoparticle showing the displacement of the conduction electron charge cloud relative to the nuclei."Reprinted (adapted) with permission from Metal nanoparticle photocatalysts: emerging processes for green-organic synthesis, Catal. Sci. Technol., 2015, DOI: 10.1039/C5CY02048D, Copyright (2016)

1.4.2 AuNP as a drug carrier

In recent years AuNPs as Drug Delivery vehicle is an interesting field of research that has attracted the attention of innumerable researchers. For controlled and site-specific drug delivery, the release of biologically active medicament at a certain speed and at a specific location is required. Conjugates of AuNPs with drug molecules have an important role in the therapy of endocellular diseases.^{162, 163}The conjugation of the antibiotics or anticancer, antifungal, anti-inflammatory, etc. can bind to the AuNPs via ionic and covalent bonding or by physical adsorption.¹⁶⁴It is observed that the efficiency, as well as time scale for effective drug delivery for some drugs, are highly influenced by adsorbing them on the surface of nanoparticles.¹⁶⁵In addition to that for site-specific drug release, AuNP carrier plays an important role. For example, anticancer drug doxorubicin (DOX) attached to 30 nm AuNPs through a pH-sensitive linker, releases the drug only when the AuNP-DOX complex comes to an acidic environment or inside

acidic organelles. This effect enhances the therapeutic effects of drug-resistant tumour cells.¹⁶⁶ The surface of AuNPs can be modified by polyethene glycol (PEG), thiolated PEG, Polyethyleneimine (PET) etc. as a spacer to increase its stability. AuNPs attached with coumarin-PEG-thiol were found to be rapidly internalized inside the cells by the non-specific endocytosis mechanism.¹⁶⁷ Bhattacharya et al. showed that AuNPs conjugated with the PEG-amines and folic acid by noncovalent bonds can be easily targeted to the folate receptors of cancer cells.¹⁶⁸ AuNP can also be used as gene delivery, protein delivery and vaccine delivery vehicle.¹⁶⁹

1.4.3 Magnetic Materials

1.4.3.1 Magnetic property or magnetic behaviour of nanomaterials

Depending on the response to an externally applied magnetic field, the magnetism of materials is classified into five different categories and these are diamagnetic, paramagnetic, ferromagnetic, antiferromagnetic and ferrimagnetic.

Diamagnetic Materials: Diamagnetic materials are the materials which show negative magnetic susceptibility. Diamagnetic materials have a relative magnetic permeability (μ_v) less than or equal to 1 and therefore the magnetic susceptibility which is defined as $\chi_v = \mu_v - 1$ is less than or equal to 0. Diamagnetism is observed in materials with filled electronic sub-shells where the magnetic moments are paired and overall moment cancels each other. Externally applied magnetic field then deforms electron orbital motion, leading to negative magnetic susceptibility. This means that diamagnetic materials (e.g., quartz SiO_2) with negative susceptibility ($\chi < 0$) repelled by magnetic fields¹⁷⁰. Since diamagnetism is a weak property, its effects are not observable in everyday life. Common diamagnetic materials like water has a magnetic susceptibility, $\chi_v = -9.05 \times 10^{-6}$. Since χ_v is derived from the ratio of the internal magnetic field to the applied field, it is a dimensionless value. A list of notable diamagnetic materials is shown below:

Materials	Pyrolytic carbon	Bismuth	silver	Carbon (graphite)	copper
$\chi_v \times 10^{-5}$	-40.9	-16.6	-2.6	-1.6	-1.0

In that sense, the superconductors may be considered to be the perfect diamagnetic materials with $\chi_v = -1$ or $\mu_v = 0$ as they expel all magnetic fields due to the Meissner effect.¹⁷¹

Paramagnetic Materials: The materials which show a net magnetic moment and a short-range ordering of its magnetic moments under the influence of an external magnetic field are called paramagnetic materials. Constituent atoms or molecules of paramagnetic materials have permanent magnetic moments (dipoles), even in the absence of an applied field. The permanent magnetic moments attributed to the unpaired electrons in atomic (often the 3d or 4f shell electrons) or molecular electron orbitals. In the absence of an external magnetic field, these dipoles do not interact with each other and are randomly oriented due to the thermal agitation, resulting in zero net magnetic moment. In presence of an external magnetic field, the atomic or molecular dipole tend to align along the direction of the applied magnetic field and results in a net moment parallel to the externally applied field. Classically, such types of alignment can be explained by the torque exerted by an applied field on the atomic or molecular dipole which tries to align the dipoles parallel to the applied field. If there is sufficient energy exchange between neighbouring dipoles, they will interact, and may spontaneously align or anti-align and form magnetic domains, resulting in ferromagnetism (permanent magnets) or antiferromagnetism, respectively. Paramagnetic and antiferromagnetic behaviour can also be observed in ferromagnetic materials above their Curie and Néel temperature respectively and at these temperatures, the available thermal energy overcomes the interaction energy between the spins. In general, the paramagnetic susceptibility is very low and has value in the order of 10^{-3} to 10^{-5} but the susceptibility

may be as high as 10^{-1} for synthetic paramagnets such as ferrofluids.¹⁷²⁻¹⁷⁶ A list of notable paramagnetic materials is shown below:

Materials	Tungsten	Caesium	Aluminium	Lithium	Magnesium	Sodium
$\chi_v \times 10^{-5}$	6.8	5.1	2.2	1.4	1.2	0.72

Ferromagnetic Materials: Materials with aligned atomic magnetic moments of equal magnitude possess ferromagnetism and their crystalline structures allow the direct coupling interaction between the moments strongly enhances the flux density (e.g., Fe, Ni, and Co). The spontaneous magnetization is not observed in materials in the absence of an externally applied magnetic field, due to the presence of domains in the material and each of them have their own direction of magnetization. When an external magnetic field is applied, the domains in which the magnetization is more nearly parallel to the external magnetic field, grow at the expense of the domains which are in less favourable alignments. When the externally applied field is withdrawn, a part of the induced domain alignment is conserved and the material starts acting as a permanent magnet. These types of materials hold very high magnetic susceptibility.

Antiferromagnetic Material: In these materials, the uncompensated electron spins which are accompanying with the neighbouring cations orient themselves, below a temperature that is known as the Néel temperature, such that their magnetizations neutralize one another and makes the overall magnetization zero. Example of such materials is metallic manganese, chromium, and manganese oxide (MnO). The susceptibilities of these materials are low and the value is around $\sim 10^{-3}$ but when the temperature is close to Néel point the antiferromagnetic coupling breaks down and makes the materials paramagnetic.

Ferrimagnetic Materials: In these materials, the magnetic moment of one crystal sub-lattice is anti-parallel to the other. Sub-lattices of these materials contain two different

types of ions with a different magnetic moment for two types of atoms as most of these materials are made up of cations of two or more types. Due to that, the net magnetization of these materials is not equal to zero. The examples of such materials are different types of ferrite-spinel-like NiFe_2O_4 , CoFe_2O_4 , Fe_3O_4 (or $\text{FeO}\cdot\text{Fe}_2\text{O}_3$), CuFe_2O_4 etc. Magnetic behaviour of different materials and their ensemble arrangement of magnetic dipoles are shown in **Figure 1.16**.

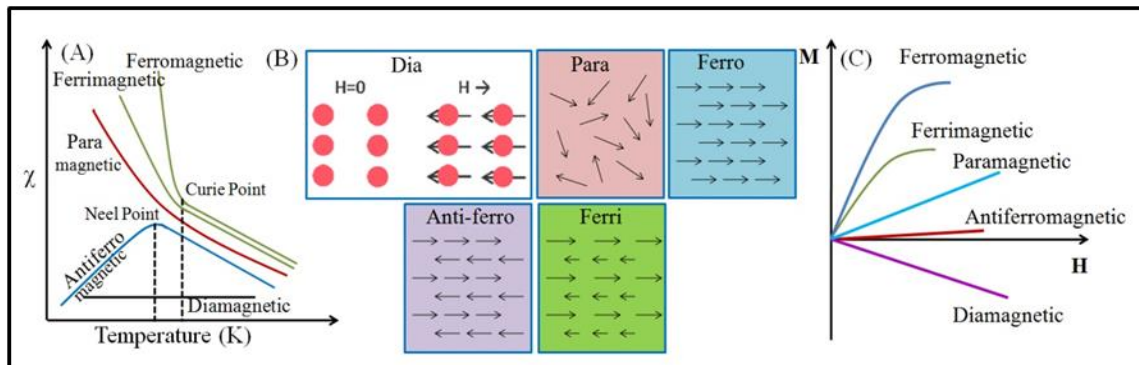


Figure 1.14: (A) Change of magnetic susceptibility with temperature for different magnetic materials (B) Ensemble orientation of the magnetic dipoles in different materials (C) Magnetization vs H plot of different types of bulk magnetic materials.

1.4.3.2 Magnetism from Bulk to nano: Superparamagnetism

Due to the movements of the charged particles like electrons, holes, protons, and ions (positive and negative), the magnetic effects are observed in materials. A spinning electric-charged particle creates a magnetic dipole, which is called magneton. In ferro or ferrimagnetic materials, magnetons are associated in groups. All magnetons are aligned in the same direction by the exchange forces inside a magnetic domain or Weiss domain. This concept of domains differentiates the ferro or ferrimagnetism from paramagnetism. The domain structure of a ferro or ferrimagnetic material determines the size dependence of their magnetic behaviour. When the size of a ferro or ferrimagnetic

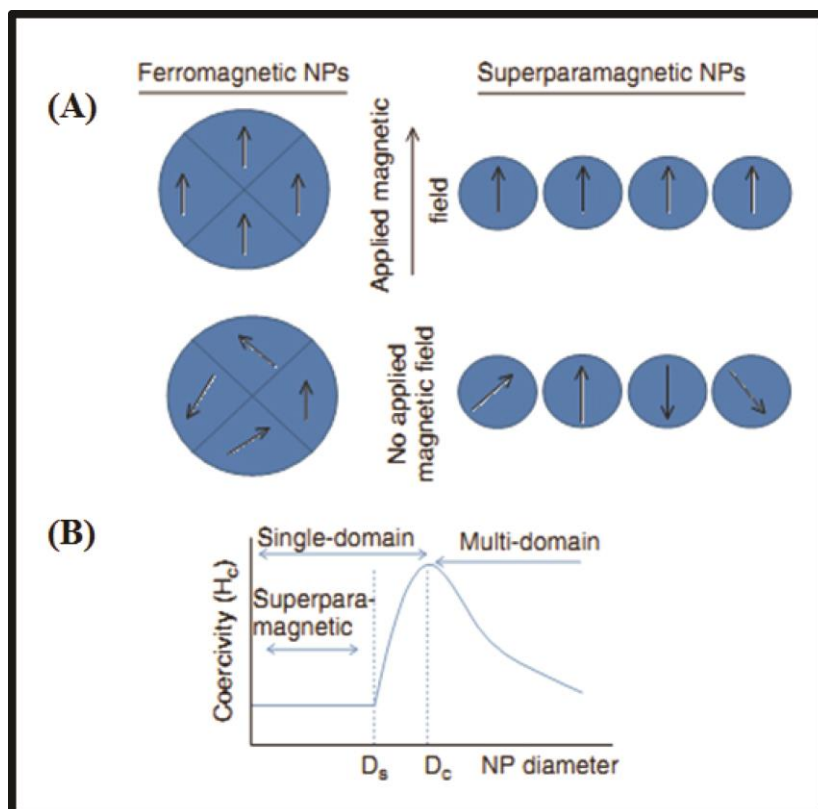


Figure 1.15: Magnetization behaviours of ferromagnetic and superparamagnetic NPs in the presence and absence of an external magnetic field (b) Relationship between nanoparticle size and the magnetic domain structures. D_s and D_c are the ‘superparamagnetism’ and ‘critical’ size thresholds.¹⁷⁷

the material is reduced below a critical value, it becomes a single domain. It can be assumed that the lowest free energy state of ferromagnetic particles has non-uniform magnetization for larger particles and has uniform magnetization for particles smaller than a certain critical size. The former ones are called multi-domain particles, while the latter is referred to as single domain particles.¹⁷⁸⁻¹⁸⁰ According to the magnetic domain theory, the critical size of the single domain is dependent on several factors including the shape of the particles, the value of the magnetic saturation, exchange forces, the strength of the crystal anisotropy and surface or domain-wall energy. The response of ferro or ferrimagnetic materials in the presence of externally applied magnetic field can be shown by a hysteresis loop, which is characterized by two main parameters:

remanence and coercivity. Both are related to the **thickness** of the hysteresis loop as well as the size of the particle. It has been found that as the particle size is reduced, the coercivity increases to a maximum and then decreases toward zero (**Figure 1.17B** and **1.18**). A particle becomes superparamagnetic when the coercivity of a single-domain particle becomes zero. Such superparamagnetism is influenced by the thermal effects too. In absence of external magnetic field even only thermal fluctuations can spontaneously demagnetize a previously saturated assembly of superparamagnetic particles. That is why these particles have zero coercivity and have no hysteresis. Nanoparticles become magnetic in the presence of an external magnet but return to a nonmagnetic state when the external magnetic field is removed. This property gives the unique advantage of working in the field where the switching on-off of the magnetic field effect needs to be observed. There are a number of crystalline materials of Fe, Co, or Ni that exhibit ferro and ferrimagnetism. The ferrite oxide-magnetite (Fe_3O_4) is widely used in the form of superparamagnetic nanoparticles as it is the most magnetic of all the naturally occurring minerals on earth.

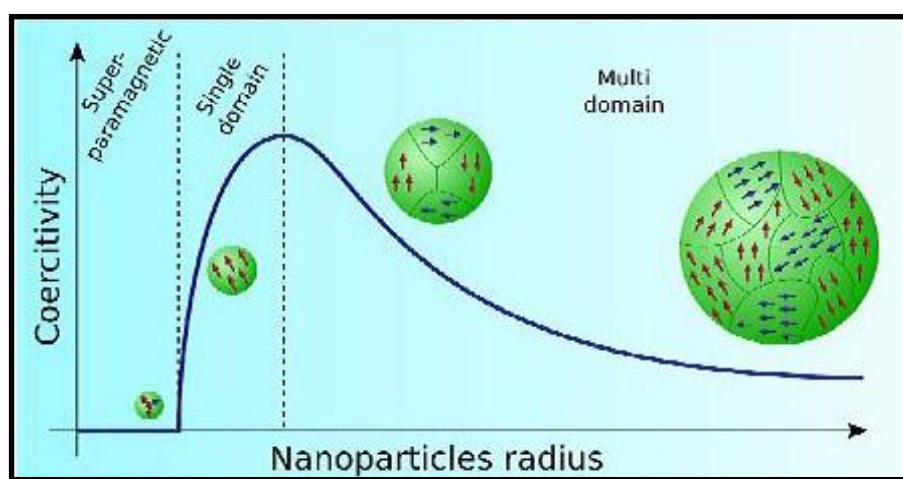


Figure1.16: Schematic illustration of the coercivity-size relations of small magnetic particles.¹⁷⁷

1.4.4 Magneto-plasmonic nanomaterials

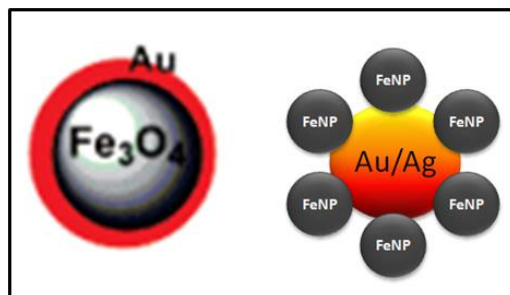


Figure 1.17: Schematic illustration of the magnetoplasmonic material

Magneto-plasmonic nanoantennas are novel nanostructures that hold the promise to meet the expectations both from plasmonic and magnetic materials in the nano-regime. In contrast to conventional plasmonic (non-magnetic) or magnetic (non-plasmonic) nanostructures, the constituents of magneto-plasmonic materials are ferro or ferrimagnetic metals such as nickel, cobalt, iron and their alloys or oxide attached with a plasmonic moiety like Au or Ag. The magneto-optical activity of such material becomes effective when we apply an external magnetic field.¹⁸¹ Magneto-optical activity is classified according to the relative orientations of the wave vector of light k and the magnetic field H , where light can either travel along the field direction ($k \parallel H$) or perpendicular to it ($k \perp H$).¹⁸² It is already reported that enhanced Faraday rotation is observed in gold-coated maghemite (γ - Fe_2O_3) nanoparticles⁵² which is not obtained in either uncoated maghemite or only in gold nanoparticles or in a mixture of Au and maghemite particles which corresponds to a near-field enhancement of the Faraday rotation due to the spectral overlap of the surface plasmon resonance in plasmonic Au with the electronic transition in maghemite. The optical response of a magneto-plasmonic nanoparticle can be manipulated by regulating the shape and size of the plasmonic moiety and the magnetic response can be tuned by changing the magnetic material as reported by several other groups.^{52, 183-185} Such metamaterials may be advantageous in optical data storage, small magneto-optic devices, as well as in optical sensing and imaging of magnetic fields and magnetic domain structures^{186, 187}. This group of material are

attractive for therapy and diagnostics (theranostics) applications too.^{188, 189} Moreover, the magnetoplasmonic behaviour may bridge the gap between nanoplasmonics and magnetic spintronics which lead to the development of new hybrid magneto-photonics nanotechnologies¹⁸⁶ The details of the relevance of such material with this thesis have been explained in details in **Chapter 6**.

1.5 Biomolecules (Ct-DNA and Chromatin):

The term biomolecule is generally used for components that are present in organisms and play an important role for some typically biological process such as cell division, morphogenesis, and development. Biomolecules include small molecules such as primary metabolites, secondary metabolites as well as large macromolecules (or polyanions) such as nucleic acids (DNA, RNA), chromosome, chromatin, proteins, carbohydrates, lipids etc¹⁹⁰. In the thesis, I have mainly worked on DNA and Chromatin.

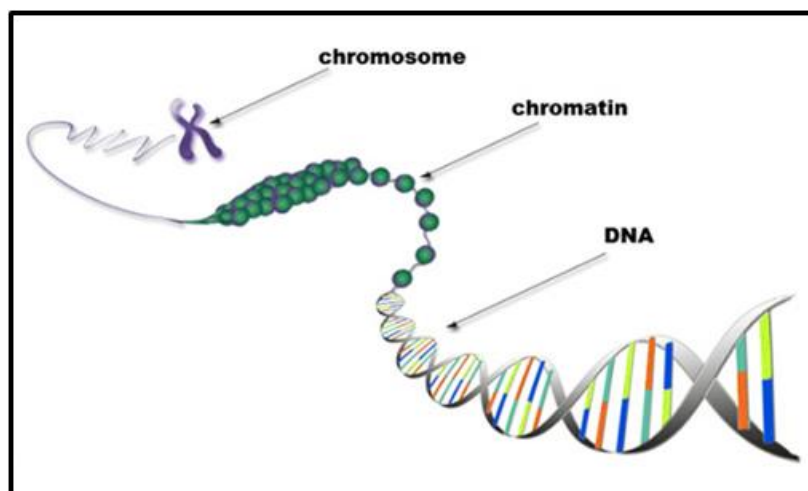


Figure 1.18: Schematic illustration of DNA and Chromatin.

1.6 Anticancer Drugs:

Anti-cancer drugs are also named as chemotherapeutic agents or anti-neoplastic agents. These drugs act upon rapidly dividing cancer cells to destroy them. When the drugs are used alone is called single-drug therapy¹⁹¹ and when several drugs are used at

once is called combination therapy.¹⁹² Anti-cancer drugs may be of different types, they can be an alkylating agents (as for example *cis*-platin, carmustine, procarbazine chlorambucil, etc.), they may be antimetabolites like methotrexate, cytarabine, gemcitabine, etc.), anti-microtubule agents (like paclitaxel, vinblastine, etc.), topoisomerase inhibitors (like etoposide, doxorubicin, etc.) or cytotoxic agents (as for example bleomycin, mitomycin, etc.).^{193, 194} The term chemotherapy is very often paralleled with the term anticancer drugs, although more accurately chemotherapy refers to the use of chemical compounds to treat the disease generally.

1.6.1 Anticancer Drug and Reactive Oxygen Species Generation

Reactive oxygen species (ROS) are a set of highly reactive molecules comprising singlet oxygen ($^1\text{O}_2$), superoxide ($\text{O}_2^{\cdot-}$), hydroxyl radical (OH^{\cdot}) etc. They have crucial roles in controlling both physiological functions and tumor.¹⁹⁵⁻¹⁹⁷ Elevated rates of reactive oxygen species (ROS) generation have been detected in almost all cancers, where they promote many aspects of tumour development and progression.

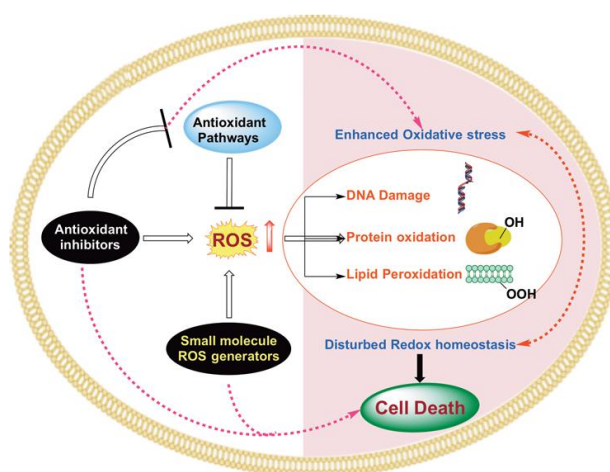


Figure1.19. Mechanism of tumour destruction by PDT. "Reprinted (adapted) with permission from (Role of Reactive Oxygen Species (ROS) in Therapeutics and Drug Resistance in Cancer and Bacteria Allimuthu T. Dharmaraja Journal of Medicinal Chemistry 2017 60 (8), 3221-3240DOI:10.1021/acs.jmedchem.6b01243).Copyright (2017)."

Production of ROS is elevated in malignant tissues compared to the benign tissues as a result of increased metabolic rate, oncogene activation, and defective vasculature. As anticancer drugs can produce species with unpaired electrons,¹⁹⁸ they can be used to detoxify the *in situ* generated radicals in carcinogenic cells¹⁹⁹. For being the source of unpaired spin, the spin dynamics of the anticancer drugs is also a very interesting phenomenon. To understand the underlying mechanism and the working principle of the drugs it is important to understand their electron transfer and spin trajectory fate in the presence of external stimuli (like light or magnetic field). The anticancer drugs can be carried by nanosurface as a selective carrier of them for controlled and selective targeting in presence of different cellular or intracellular components. So, nanosurface originated or modulated photophysics of the drug molecules are interesting as well as important for the development of modern drug modality and is worth to explore.

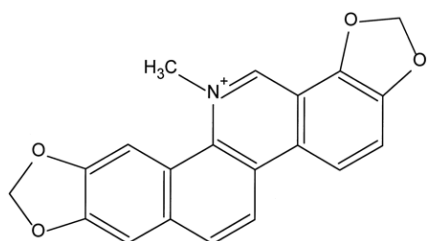
1.6.2 Sanguinarine and Chelerythrine as prototype anticancer drugs

Sanguinarine (*Pseudochelerythrine*) is a benzophenanthridine alkaloid derived from rhizomes of *Sanguinaria canadensis* L.(bloodroot) and other poppy *fumaria* species. It is a cationic molecule and it exists in two isomeric forms, one is the iminium form and other is alkanolamine form. There is an equilibrium between the two forms. The molecule converts to an iminium ion form at pH less than 6 and to an alkanolamine form at pH more than 7.²⁰⁰ Sanguinarine is a constituent of argemone oil which is responsible for the disease “epidemic dropsy”.²⁰¹ Sanguinarine shows several pharmacological effects, with outstanding antimicrobial and anti-inflammatory activities^{202,203} and is a budding compound in cancer therapy that includes apoptosis in several cancer cells via different mechanistic pathway.²⁰⁴⁻²¹⁰ Sanguinarine can also act as an effective inhibitor in the NF- κ B activation. NF- κ B is a nuclear factor, more specifically it is a pleiotropic transcription factor whose activation results in viral

replication, inflammation and growth modulation. NF- κ B is considered a major target for drug development due to its activity in pathogenesis.,²¹¹

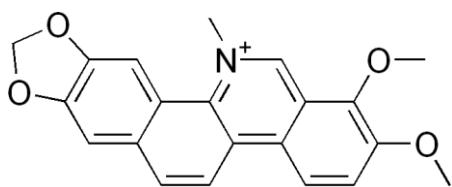
Binding of sanguinarine with different DNA and RNA structures and especially its inhibitory activity for the enzyme topoisomerase is responsible for its pronounced anticancer activity.²¹²⁻²¹⁶ At the present time, only a small number of agents are known to hold the potential for selective elimination of carcinogenic cells leaving the normal cells unaffected. By modulating the apoptotic pathway, sanguinarine may be able to affect the steady-state cell population and thus may have a potential for the development as an agent against skin cancer and perhaps against other cancer types as well.²¹⁷

Molecular Structure:



Sgr (13-Methyl-[1,3] benzodioxo [5,6-c][1,3]dioxolo[4,5-i]phenanthridin-13-ium

Chelerythrine is a natural benzophenanthridine alkaloid with strong nucleic acid binding ability.²¹⁸ Structurally, chelerythrine is very closely related to sanguinarine. Unlike sanguinarine which is found in the green biomass of *Chelidonium majus*²¹⁹, Chelerythrine mainly occurs in its roots (of *Chelidonium majus*). It has two isomeric forms, one is positively charged iminium form and another is neutral alkanolamine form. The pKa value of the molecule is 8.58.²²⁰ The iminium form or the charged form has nucleic acid binding moiety²²⁰ and the alkanolamine form or the neutral form has an affinity to functional proteins. This molecule is a selective, potent and cell-permeable protein kinase C inhibitor *in vitro*.²²¹⁻²²⁴ This small molecule has inhibitor activity towards antiapoptotic Bcl-2 family members and that has opened up new therapeutic opportunities with this molecule. It has inhibitory effects on various tumours.²²⁵⁻²²⁹ Recently this molecule has been shown to induce necroptosis in TSC₂-deficient cells via an oxidative stress-induced mechanism.²³⁰



Molecular Structure: Chelerythrine (1,2-dimethoxy-12methyl[1,3]benzodioxolo[5,6-c]phenanthridin-12-ium)

1.7 Principle of Photodynamic Therapy:

Photodynamic therapy is a therapeutic technique where the excited triplet state of a photosensitizer (PS) molecule is used to treat carcinogenic cells, tumours, acne, bacterial infection²³¹⁻²³⁴ etc. Upon laser irradiation, the PS is excited to higher energy and short-lived singlet state, $^1\text{PS}^*$. After that, the $^1\text{PS}^*$ may decay back to the ground state or it can undergo intersystem crossing to form a relatively long-lived excited triplet state ($^3\text{PS}^*$). The mechanism of tumour destruction may follow either type I or type II pathway. (Figure 1.20)

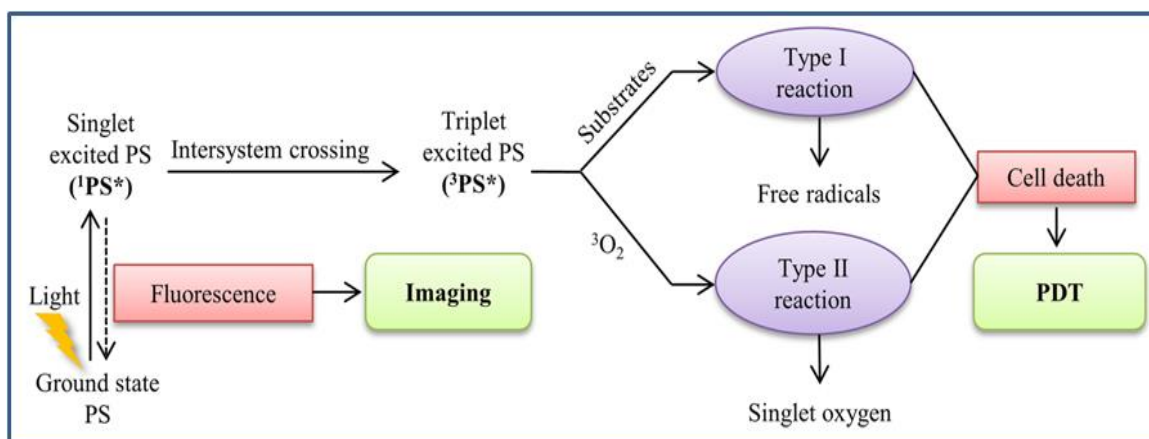


Figure 1.20: Schematic representation of photodynamic therapy

The $^3\text{PS}^*$ then directly interact with a substrate, (e.g., a molecule or cell membrane) and transfer a proton (H^+) or an electron (e^-) to form a radical anion or cation with unpaired spin which then reacts with environmental oxygen $^3\text{O}_2$ (itself a triplet in the ground state) to yield oxygenated products like hydroxyl radicals, superoxide anion radicals, and hydrogen peroxides. This pathway is called a type I reaction pathway. On the other hand, the energy of the $^3\text{PS}^*$ can be directly transferred to ground state oxygen that is

$^3\text{O}_2$, to form singlet oxygen $^1\text{O}_2$ (type II reaction). The by-products produced as a result of both type I and type II reaction pathway are responsible for the killing of toxic cells and therapeutic efficiency of PDT. As both 'type I' and 'type II' go through the formation of a triplet precursor, the therapeutic efficiency of PDT is dependent on the yield of the triplet state. There are several recent reports on the enhancement of PDT activity by nanosurface.²³⁵⁻²³⁸ In this thesis, a superparamagnetic nanosurface is used to enhance the triplet production of surface adsorbed anticancer drug sanguinarine by increasing the ISC rate. So the superparamagnetic nanosurface may be a useful tool towards the PDT.

CHAPTER-2

Methodology and Experimental Set Up

2.1 Materials:

Almost all the chemicals were purchased in purified form from Sigma Aldrich inc and used without any further purification. Milli-Q water with a resistivity of 18.2M Ω .cm is used for all the preparation steps. Name, specification and company name of the chemicals are tabulated below.

Reagent Name	Specification	Company
Ethylene glycol	EG, Anhydrous 99.8%	Sigma Aldrich
Gold(III) chloride trihydrate	HAuCl ₄ .3H ₂ O; \geq 99.9%, trace metals basis	Sigma Aldrich
Sodium citrate tribasic dihydrate	C ₆ H ₅ Na ₃ O ₇ .2H ₂ O; Bioultra, for molecular biology, \geq 99.5% (NT)	Sigma Aldrich
Spectrasol (EtOH)	Spectroscopic grade	Spectrochem
Water	Ultrapure, Milli-Q, resistivity 18.2 M Ω .cm at 25 °C	Merck Millipore
Acetonitrile	Spectroscopic grade	Spectrochem
Calf thymus DNA (ctDNA)	Type I, fibres	Sigma Aldrich
Chromatin	Separated from chicken liver	Purchased from local market.
Sanguinarine Chloride hydrate	\geq 98% (HPLC)	Sigma Aldrich
Chelerythrine Chloride	\geq 95% (TLC), powder	Sigma Aldrich
Sodium chloride	NaCl, AR, \geq 99.9%	Sigma Aldrich
Phenol	BioUltra, for molecular biology, \geq 99.5% (GC)	Sigma Aldrich
Chloroform	EMPARTA ACS 99.4%	Merck
Phenol – chloroform-isoamyl alcohol mixture	BioUltra, for molecular biology, 25:24:1	Sigma Aldrich

Isopropanol	BioReagent, for molecular biology, $\geq 99.5\%$	Sigma Aldrich
Sodium acetate	Anhydrous, for molecular biology, $\geq 99\%$	Sigma Aldrich
Hydrochloric acid	HCl, ACS reagent, 37%	Sigma Aldrich
Trizma® base	T1503 Primary Standard and Buffer, $\geq 99.9\%$	Sigma Aldrich
NH ₄ OH	ACS reagent 28-30% NH ₃ Basis	Sigma Aldrich
FeCl ₂	Reagent grade, 98%	Sigma Aldrich
FeCl ₃	Reagent grade, 97%	Sigma Aldrich

2.2 Methods:

2.2.1 Ultraviolet-Visible (UV-Vis) Absorption Spectroscopy

For UV-Vis absorption spectroscopy three different JASCO spectrometers V-650, V-730 and V-770 for the spectral range 190-900 nm, 190-1100 nm and 190-3200 nm have been used respectively by using a quartz cuvette of optical path length 10 mm.

2.2.2 Fluorescence Spectroscopy

For fluorescence spectroscopy, either FluoroMax-3 (HORIBA, Jobin-Yvon) or Horiba PTI QuantaMaster 400 fluorimeters have been used which is equipped with a xenon lamp with a quartz cuvette of 10 mm optical path length as the sample holder.

2.2.3 Time-resolved Spectra (Time-Correlated Single Photon Counting Technique)

Fluorescence lifetimes are measured using a picoseconds time-correlated single photon counting (TCSPC) set-up. The samples are excited using a picoseconds diode laser (IBH Nanoleds). Generally, 340 nm, 375 nm, and 470 nm have been used with excitation diode lasers of pulse width ~ 75 ps with a repetition rate ~ 1 MHz as a light source for our lifetime measurements. To block the exciting light during the collection of fluorescence from the sample appropriate bandpass filters are used. The liquid

samples are kept in a quartz cell of 1 cm path length. The sample fluorescence is collected at 90 degrees to the excitation beam, which is dispersed by a monochromator (IBH, model MCG-910 IB) and detected using a cooled micro-channel plate photomultiplier tube (Hamamatsu, 5000-U-09). The polarization (parallel, perpendicular and magic angle) of the fluorescence is selected by an analyzer (**Figure 2.2.1**). In this technique, a timing pulse (START) is generated in synchronization with the excitation pulse. This START pulse switches on the charging of a capacitor from a constant current source in the Time-to-Amplitude-Converter (TAC). The emitted photon from the sample generates another timing pulse (STOP) which snaps off the switch. The TAC thus maps the time-delay information which rises due to the time taken for the pulses to travel through the cables/electronics and for the excited state to relax and emit a photon, into a voltage level. The TAC output pulses are stored and displayed in a histogram in a multichannel analyzer (MCA). For statistical validity of the data and to prevent excess weightage of the early arriving pulses, the START to STOP count rate is limited to a minimum of 100:1 ratio. The decay curve then can be accurately obtained over a time zone of five lifetimes. The block diagram of the TCSPC system is shown in **Figure 2.2.1**. In practice the excitation pulse and also the system response function has finite width and the decay data on the MCA is a convolution of the excitation pulse, the actual decay, and the system response. During the experiment, first a scatterer (LUDOX solution) is placed in the sample chamber and the pump function $P(t)$ is obtained from the memory section of the MCA.

2.2.4 Femtosecond (fs) fluorescence up-conversion measurements

The fluorescence lifetime of the transient species is measured with the help of a femtosecond fluorescence up-conversion setup (FOG-100, CDP Corp).²³⁹ This is achieved using the second harmonic of a mode-locked Ti-sapphire laser (Mai Tai, Spectra-Physics) being pumped by a 5W Millennia (Spectra-Physics), the sample is

excited at 400 nm with a full excitation slit width. A nonlinear crystal (1mm BBO, $\theta = 25^\circ$, $\phi = 90^\circ$) is used to generate the second harmonic. The fluorescence emission of the sample was obtained through the magic angle configuration and was up-converted in another nonlinear crystal (0.5mm

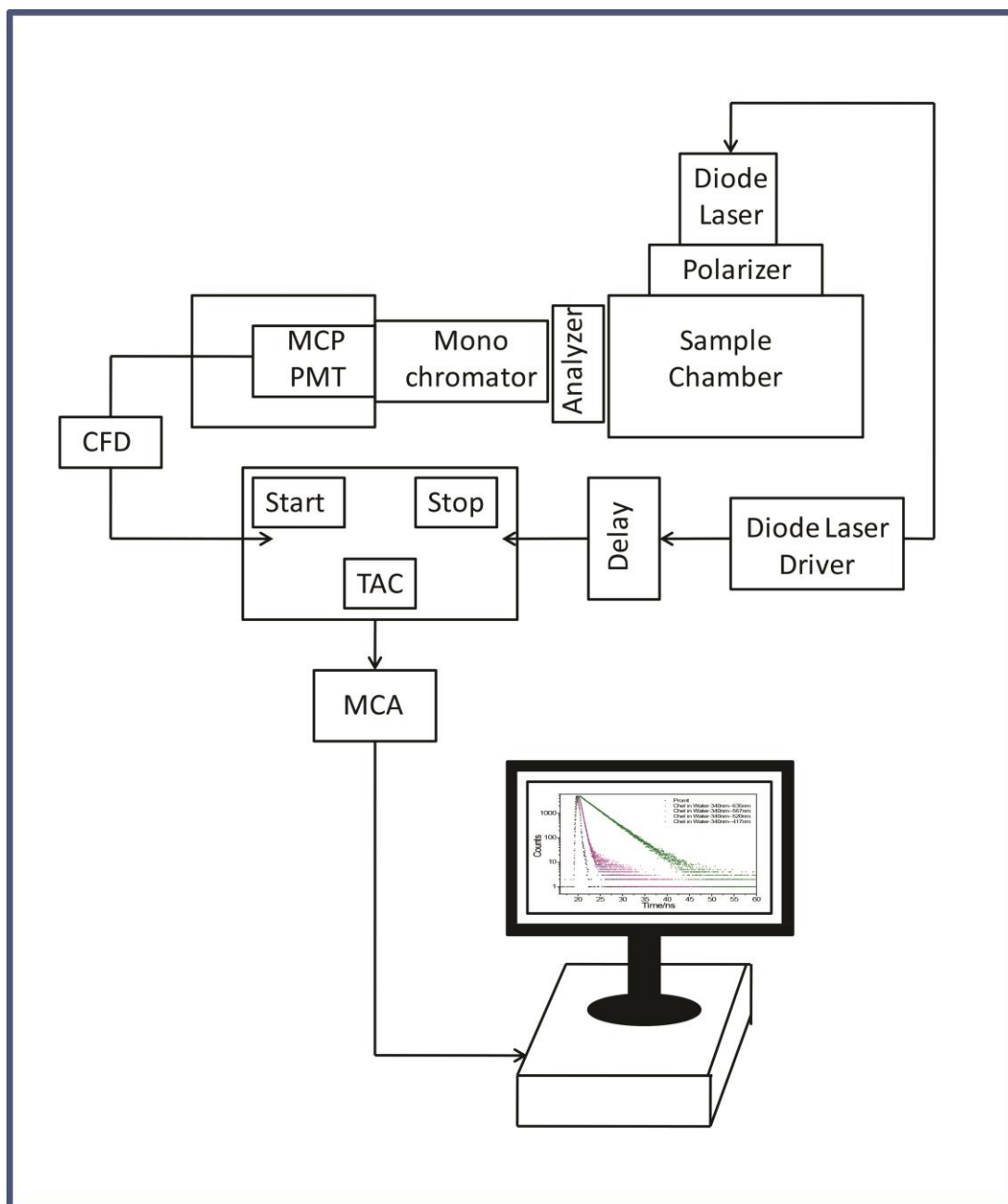


Figure 2.2.1: Block diagram of TCSPC Set up

BBO, $\theta = 38^\circ$, $\phi = 90^\circ$) by using the fundamental beam as a gate pulse. The up-converted light gets dispersed through a monochromator and is detected by photon counting electronics. A Gaussian shape for the instrument response function is used which have

an FWHM of ~ 206 fs (this is obtained through water Raman scattering) and commercial software (IGOR Pro Wave Metrics, USA), is used to deconvolute the femtosecond fluorescence decays.

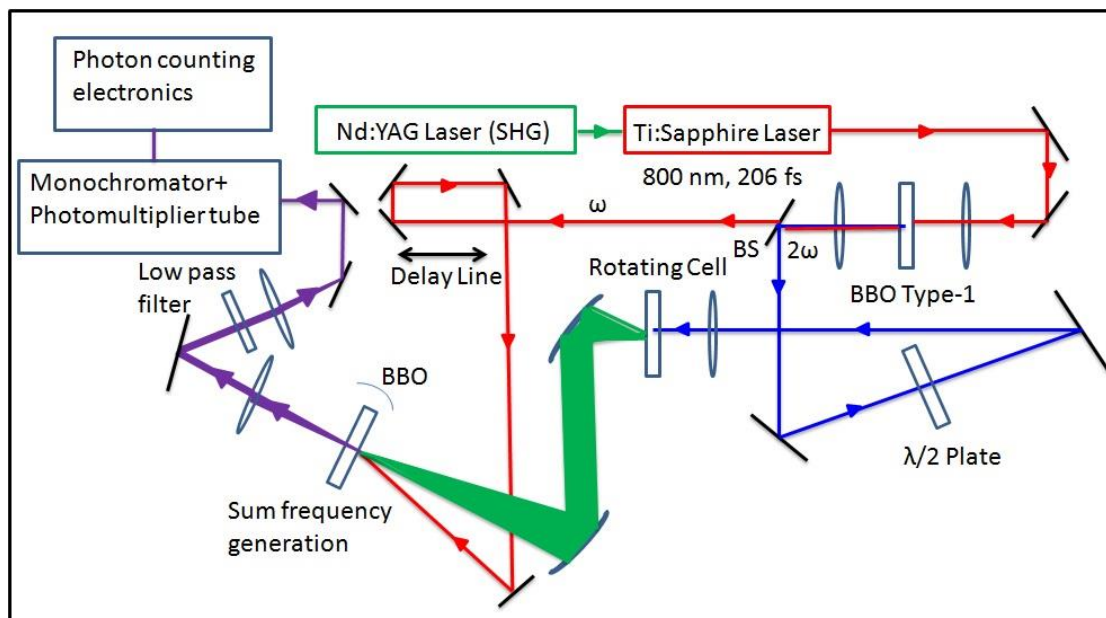


Figure 2.2.2: Block diagram of femtosecond upconversion technique.²⁴⁰

2.2.5 Laser Flash Photolysis (Excited State Transient Absorption Technique)

The laser flash photolysis technique has been used for the detection of transient, non-fluorescent species formed during photoelectron transfer (PET) and excited state proton transfer (ESPT) reactions. Transient absorption spectra have been measured using a nanosecond flash photolysis set-up (Applied Photophysics) containing a Q-switched, Neodymium-doped Yttrium Aluminium Garnet (Nd: YAG) laser (DCR-11, Spectra-Physics). The active medium is Nd^{3+} that generates a fundamental emission at 1064 nm (${}^4\text{F}_{3/2} \rightarrow {}^4\text{I}_{11/2}$). Different harmonics (**Table 2.1**) can be produced by frequency conversion in the non-linear crystal, potassium dideuterium phosphate (KD*P). In our experiments, the third harmonic, 355 nm have been used for excitation. The transients are detected by a 250 W pulsed Xe lamp. The AK-347 control unit is used to trigger the laser within the flat portion of the Xe lamp profile so that the transients are excited by absorbing an intense and steady source of light. The transmitted light is passed through a

monochromator for wavelength variation and detected by a photomultiplier, R928 (Hamamatsu Photonics). The photomultiplier output is fed into an Agilent Infiniium oscilloscope (DSO8064A, 600 MHz, 4GSa/sample rate) and the data are transferred to a computer using IYONIX software. A block diagram of the laser flash photolysis set-up is shown in **Figure 2.2.3**. The transmission changes at various wavelengths are converted to absorbance (OD) and the transient absorption spectra are obtained by plotting OD vs wavelength at a particular time delay after the laser flash. The software, Origin 8.5, is used for the analysis of the decay profiles.

2.1 Laser specification

	Fundamental	2 nd Harmonic	3 rd Harmonic	4 th Harmonic
Pulse Width (ns)	8-9	6-7	6-5	5-4
Pulse Energy (mJ/p)	275	135	60	30

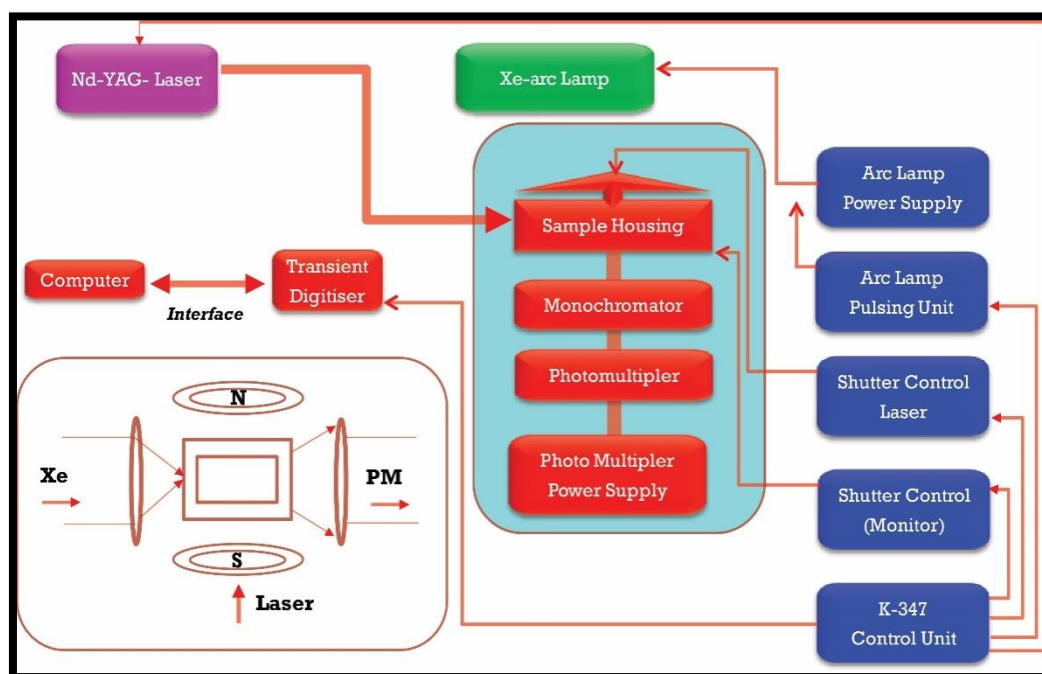


Figure 2.2.3 Schematic diagram of laser flash photolysis set-up

2.5.3 MF effect on triplet non-fluorescent species

MF effect on the transient absorption spectra is done by passing direct current (DC) through a pair of electromagnetic coils which are placed inside the sample chamber. The MF can be varied by changing the extent of current through the coils.

2.2.6 Surface Enhanced Raman Spectroscopy (SERS)

SERS experiments are done using a homemade Raman setup. A continuous-wavelength diode-pumped solid-state laser sourced from Laserglow Technologies, Canada (LRS0671-PFM-00300-03) is used, which is operating at 671 nm as an excitation light source (at fixed excitation energy, 3mW, using neutral density filters throughout the experiment). An In Photonics made 670 nm fibre optics Raman probe with a spectral range of 200–3900 cm^{-1} (Stokes) is used for sample excitation and data collection this ensures efficient focusing and filtering. The Raman probe used consists of two single fibres (105 μm excitation fibre and 200 μm collection fibre) with both filtering and steering micro-optics (numerical aperture 0.22). The excitation fibre is attached to a Thorlabs built fibre port to align the laser, whereas the collection fibre is attached to a spectrometer. A miniaturized QE65000 scientific-grade spectrometer sourced from Ocean Optics is used as the Raman detector which has a spectral response range of 220–3600 cm^{-1} . The Raman spectrometer is equipped with a TE-cooled 2048 pixel charge-coupled device and is interfaced to a computer via USB port. In the end, the Raman spectrum was recorded using the Ocean Optics data acquisition SpectraSuite spectroscopy software.¹⁹ Details picture of this SERS experimental set up has been shown in **Figure 2.2.4**.

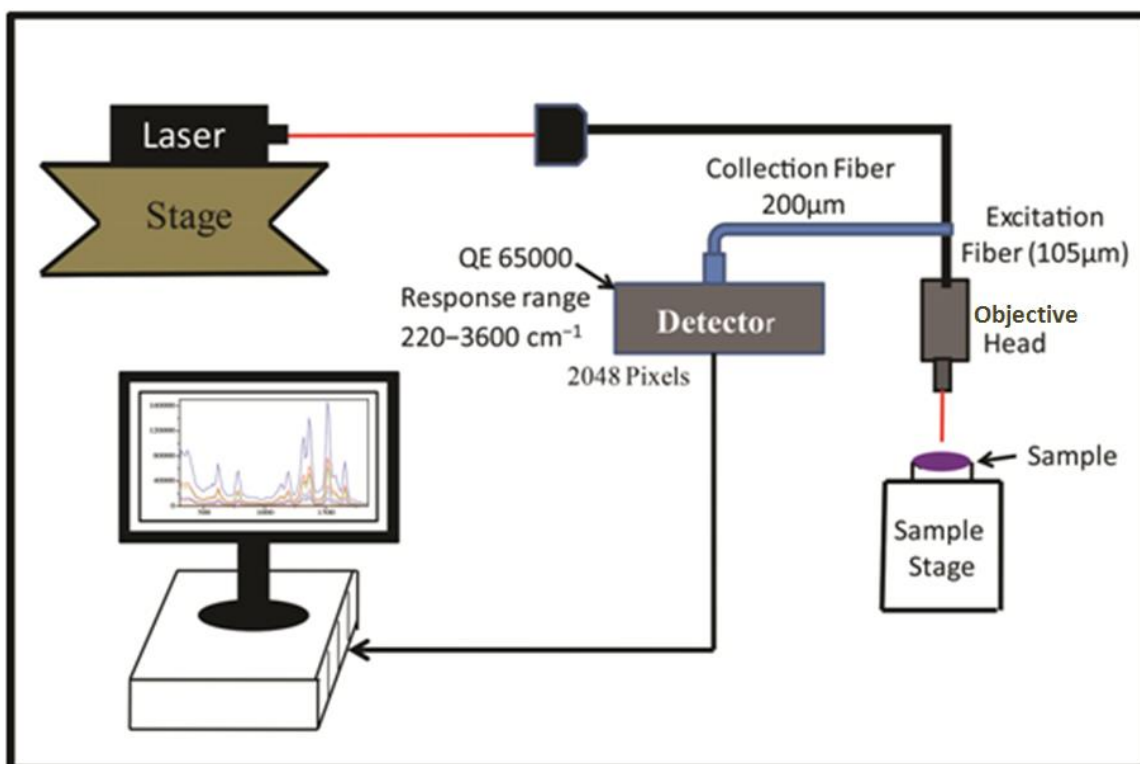


Figure 2.2.4: Schematic diagram of the experimental SERS set up.

2.2.7 Preparation of Plasmonic Spherical AuNPs

Trisodium citrate (TSC) capped spherical plasmonic AuNP is synthesized using a reported method without any further modification.²⁴¹ In short, it can be summarised as 1.25 mL of 10⁻² M aqueous solution of H₂AuCl₄·3H₂O is added to 100 mL of water taken in a three-necked bottle fitted with a cold-water-jacketed condenser. Diluted H₂AuCl₄ solution is then heated to boiling temperature, and in this condition, 0.75 mL of 1% sodium citrate dihydrate solution is added. Continued heating is carried out for the next 30 minutes in order to complete the reaction. Then, the solution is left to cool automatically up to room temperature under continuous stirring. Then, the synthesized AuNP stock solution is centrifuged at 6500 rpm for 1 h and the concentrated AuNP solution is stored.

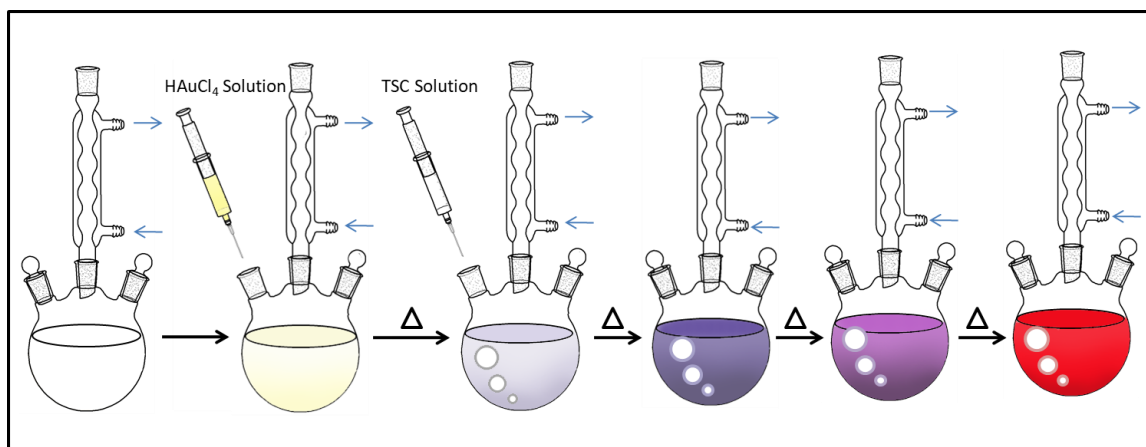


Figure 2.2.5: Schematic diagram of the AuNP synthesis set up.

2.2.8 Synthetic protocol of magnetic nanoparticle Fe_3O_4

The magnetic Fe_3O_4 nanoparticle (FeNP) is synthesized by a chemical co-precipitation procedure by reducing both Fe^{2+} and Fe^{3+} ions (1:2 molar ratio) in presence of NH_4OH this is also done using a reported protocol²⁴² of E. Cheraghipour *et al.* with minor modification. This can be summarised as a 50 mL aqueous solution of 0.10mol/L Fe^{2+} and 0.20mol/L Fe^{3+} mixture are taken in a three-necked flask and the temperature of the mixture is slowly raised to 80°C in refluxing condition in an inert Argon (Ar) atmosphere. The solution was then vigorously stirred at 1200rpm. Keeping the temperature fixed at 80°C, 10mL of NH_4OH (25 wt %) is added in order to reduce the whole reaction mixture this forms bare FeNP. Furthermore, the addition of NH_4OH base increases the pH to 10-11. The surface of the bare FeNP gets stabilized with citrate ion while incubating the above-synthesized FeNP with 0.5g/mL tri-sodium citrate and continuous stirring the mixture for 1 hour at 90°C. A black precipitate is obtained by cooling the reaction mixture up to room temperature. This suspension was washed numerous times with deionised water in order to remove excess citrate ions. TEM and XRD studies are done to characterize the synthesized nanoparticles.

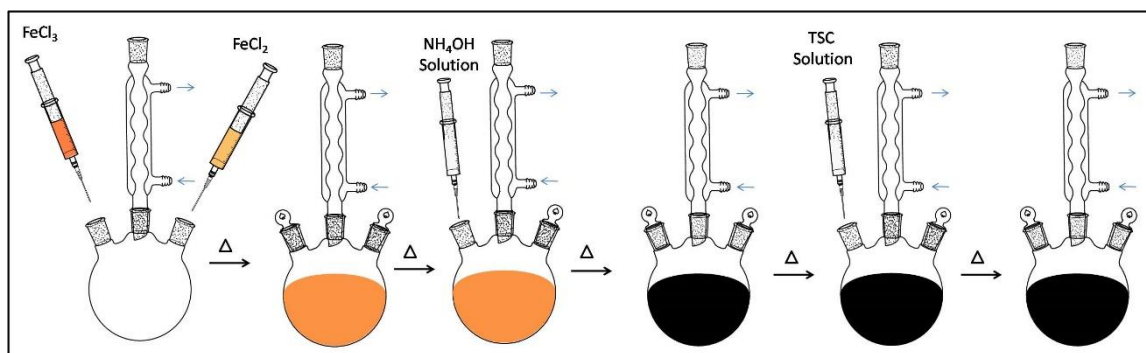


Figure 2.2.6: Schematic diagram of the FeNP synthesis set up.

2.2.9 Transmission Electron Microscopy (TEM)

Transmission electron microscopic measurements are performed through an FEI, Tecnai G²F30, S-Twin microscope which operates at 120 kV. A simple but modified technique is used for clean monolayer sample preparation on a 300 mesh copper formvar/carbon grid. A dip-and-dry technique is used to make TEM samples. In this sample preparation technique, a TEM grid is immersed into the concentrated nanomaterial sample solution using a tweezer, and the hydrophobic carbon coating is allowed to form a monolayer of the sample that sticks onto the copper mesh, which is then dried on a soft tissue paper. After complete drying, the resulting grid is used for TEM measurements. High angle annular dark-field scanning/transmission electron microscopy (STEM-HAADF) method is used here by the same microscope, which is having with a scanning unit and a HAADF detector from Fischione (model 3000). Electron energy loss spectroscopy (EELS) is carried out using a post-column Gatan Quantum SE (model 963). Energy filtered images are acquired using a Gatan Imaging Filter.

2.2.10 X-Ray Diffraction (XRD) Technique

The powder x-ray diffraction (XRD) study of FeNP and FeNP-Sgr composite has been performed at room temperature (300K) by using a RIGAKU-TTRAX-III diffractometer equipped with Copper K- α radiation of wavelength $\lambda=1.5406\text{\AA}$ in the 2θ range of 10° – 100° with step size 0.010° .

2.2.11 Magnetization Measurements

The magnetic measurements are done using SQUID-VSM (Quantum Design) having magnetic field ranges 0-7 Tesla and a temperature range of 2K- 380K.

2.2.12 Molecular Docking and Dynamics

Sgr and Chel structure (CID: 5154) are obtained from the PubChem database. Molecular dynamics (MD) simulations are performed using Desmond software²⁴³ as shown in Schrodinger Maestro (Academic version 2017-3). Sgr is placed in the centre of a simulation box and solvated with appropriate solvents. Buffer distance of 10 Å from each side of the periodic boundary box is maintained so that the solute does not see its periodic image. MD simulations are run for 1200 *ps* under optimized potentials for liquid simulations, OPLS 2005, force field²⁴⁴ in SPC (single point charge) water, ethanol and acetonitrile environments, respectively. Five step relaxation protocol is used before the production MD simulations as described earlier.²⁴⁵ Energy and hydrogen bond calculations are performed on the MD trajectory using the simulation event analysis tool as explained in Schrodinger Maestro.

2.2.13 Preparation of ctDNA

Commercial cDNA is extracted by the phenol-chloroform method so that to remove protein impurities present, if any, before use.^{246, 247} It is then dissolved in 20mM NaCl and kept overnight at 4 °C. This ctDNA solution is then sonicated for 45min, 30s pulses of 100% amplitude are given through an ultrasonic processor UP 200S sourced from Dr Hielscher GmbH, Germany. A phenol-chloroform-isoamyl alcohol mixture with a ratio of 25:24:1 is then added to this ctDNA solution and is vortexed vigorously. An emulsion is formed which is then centrifuged at 10000 rpm for 10 min at room temperature. An aqueous (top) layer is formed which is carefully removed and placed into a clean tube. This is followed by a similar extraction using an equal volume of chloroform. DNA is then precipitated by adding double the volume of pure isopropanol,

and the mixture is chilled overnight at -20°C. Before the addition of isopropanol, the pH of the DNA solution is adjusted to 5.2 by adding 1/10th the volume of 3M sodium acetate (pH 5.2). ctDNA is collected by centrifugation of the DNA solution at 12000 rpm for 15 min at 4°C. The resultant ctDNA pellet is then washed with 70% ethanol and dried in air. The dried ctDNA was dissolved in 10mM Tris buffer (pH 7.5), 50 mM NaCl buffer and dialysis were performed in the same buffer. The purity and concentration are determined spectrophotometrically using $\epsilon_{260\text{ nm}} = 6600\text{ M}^{-1}\text{ cm}^{-1}$.

2.2.14 Isolation of Chromatin from Chicken Liver

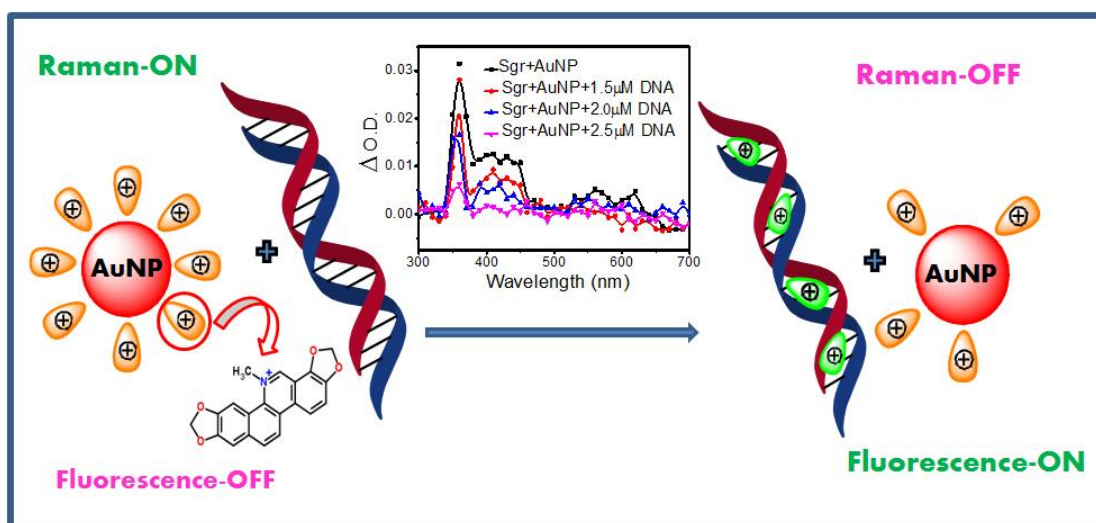
Before isolation of chromatin, chicken livers stored in sealed tubes at -80 °C are retransferred to -20 °C and kept overnight. They are then thawed at 4 °C. Nuclei are isolated following the standard protocols²⁴⁸ with minor modifications²⁴⁹ reported earlier in the literature. The obtained long chromatin was dialysed in 10 mM Tris (pH 7.5), 50 mM NaCl buffer. Agarose gel electrophoresis is used to check the purity, and the concentration is determined spectrophotometrically using $\epsilon_{260\text{ nm}} = 6600\text{ M}^{-1}\text{ cm}^{-1}$

CHAPTER-3

Development of a Triplet-Triplet Absorption Ruler: DNA and Chromatin-Mediated Drug Molecule Release from a Plasmonic Nanosurface

OUTLINE: What does the study offer?

- ❖ Quantification of the release percentage of a drug from a plasmonic nanocarrier surface in the presence of cell components like DNA and Chromatin by using the excited state transient absorption spectroscopy as the detection technique.
- ❖ The plausible explanation has been given on why the excited state spectroscopic assay could be a better sensory tool compare to the conventional fluorescence and SERS based assays for the quantification of the drug release from a plasmonic nano vehicle's surface.
- ❖ Quantification of drug release is necessary for any controlled drug delivery modality.



3.1 Introduction:

The literature is rich in the use of fluorescence and Raman based techniques and assays for highly specific and ultrasensitive detection.^{69, 250-255} Although the mentioned optical assays are universally accepted as efficient sensors, they are always limited by their inherent fluorescence and Raman cross-sections. It is not always obvious that the systems under investigation will possess a high fluorescence and Raman quantum yield so that they can be detected either in low concentration or in the early stage of a biological process. There are several molecular, cellular, and biological materials that do not offer either fluorescence or Raman scattering upon optical excitation. On the other hand, absorption of light is an intrinsic property of all materials, and it may vary only by the region of the electromagnetic spectrum. The usefulness of absorption as an ultrasensitive sensory tool has never been used in the past and remains unexplored for future applications. Over the last few decades, this absorption technique has been used either in the form of absorbance to understand the energetics of a molecule in the ground state or in flash photolysis to understand the photophysics of excited-state transient species. In most of the molecular systems, the ground state is the singlet state (S_0), and excitation by a short pulse can take them to an excited singlet state (S_n) from where it could undergo intersystem crossing to a corresponding triplet state (T_n). Because of favourable relaxation from S_n to S_0 , the lifetime of the transient state becomes too short to obtain the absorption pattern in a single shot. On the other hand, because of unfavourable relaxation from T_n to S_0 , the longer lifetime of the transient state offers sufficient time to record the absorption pattern, followed by excitation to T_{n+1} in a single shot. As a result of this, triplet-triplet (T-T) absorption could be a better tool to understand molecular pathways in great detail. The literature is rich on the use of T-T excitation spectra to study charge transfer,²⁵⁶ electron transfer,²⁵⁷ and molecular adsorption on surfaces²⁵⁸ as well as for transient photophysics.²⁵⁹ In the present set of

experiments, T-T absorption spectroscopy has been used to study the calf thymus DNA (ctDNA) and chromatin-mediated release of a small-molecule drug from a plasmonic nanosurface. Here the T excitation has been used as a ruler to estimate the efficiency of release of a drug molecule. Because T-T excitation is not limited by the fluorescence quantum yield or Raman scattering cross-section of molecules, this technique can be efficiently used for any molecule and reduce the selectivity of the spectroscopic approach. For this study, a naturally occurring alkaloid sanguinarine (Sgr) have been used as a small-molecule drug and 20-25 nm diameter plasmonic gold nanoparticles (AuNPs) as an effective vehicle for docking and undocking the drug molecule for efficient delivery to a specific site.

Over the past several years, naturally occurring alkaloids have been receiving tremendous importance²⁶⁰because of their potential pharmaceutical applications.²⁶¹⁻²⁶⁴ Among the different alkaloids, isoquinoline derivatives established themselves as one of the foremost alkaloids owing to their important contribution in biomedical research. Being a representative of the benzyloisoquinoline alkaloid family, Sgr exhibits numerous important biological activities, such as anti-inflammatory,^{265, 266} antioxidant,²⁶⁷ antifungal,²⁶⁸ anticancer²⁶⁹⁻²⁷²and antimicrobials.^{200, 273}Recent studies have revealed that Sgr can not only instigate apoptosis in various cancer cells by inducing apoptosis but also it can exhibit anticancer activity by means of inhibiting telomerase and topoisomerase enzyme activity. Thus, Sgr can act as a G-quadruplex stabilizer,²⁷⁴and hence it has high prospects as a potential anticancer drug. Because most of the biological systems in nature are highly anisotropic and restricted,²⁷⁵ a mechanistic study on effective drug delivery to these systems by an unperturbed intrinsic methodology will provide us with their actual pathways as well as a reliable way to measure their extent of delivery. Inspired by nature, researchers have invested a reasonable amount of time in understanding the relationship between the photophysical properties of small molecule

drugs (e.g., Sgr) and their interactions²⁷⁶⁻²⁸⁰ with biological components, for example, DNA, chromatin, and so forth. Moreover, to understand how Sgr is transported and finally released to its target, it is very important to establish a relationship between the environment and the photophysical properties of Sgr. In this study, T-T absorption spectroscopy has been used as a molecular ruler not only to understand the actual release process of Sgr as a drug molecule from a plasmonic gold nanoparticle surface in the presence of cell components, that is, DNA and chromatin, but also to quantify the accurate extent of the release of the drug molecule for an efficient therapeutic process. Here, gold nanospheres act as an essential microscopic drug-molecule carrier because of their inertness and nontoxic characteristics as well as their ease of synthesis. The result obtained by T-T absorption study has been verified by fluorescence and surface-enhanced Raman spectroscopy (SERS). A plausible explanation has also been put forward to account for the underestimation and overestimation of the percentage (%) of the release of drug molecules measured by fluorescence- and SERS-based techniques, respectively, over the, highlighted T-T absorption spectroscopy.

3.2 Results and Discussion:

The central theme of this report is to establish the T-T absorption technique as a ruler to quantify the site-specific release of the drug molecule (Sgr) from a nanosurface in the presence of ctDNA and chromatin. This is probably the first experimental report where the T-T absorption profile and relative OD were used as an assay to measure the extent of drug delivery. In the real experiment, Sgr and its nano complex or the transformed materials were excited at 355 nm using the third harmonics of an Nd: YAG laser with a pulse width of ~8 ns in the absence and presence of ctDNA or chromatin.

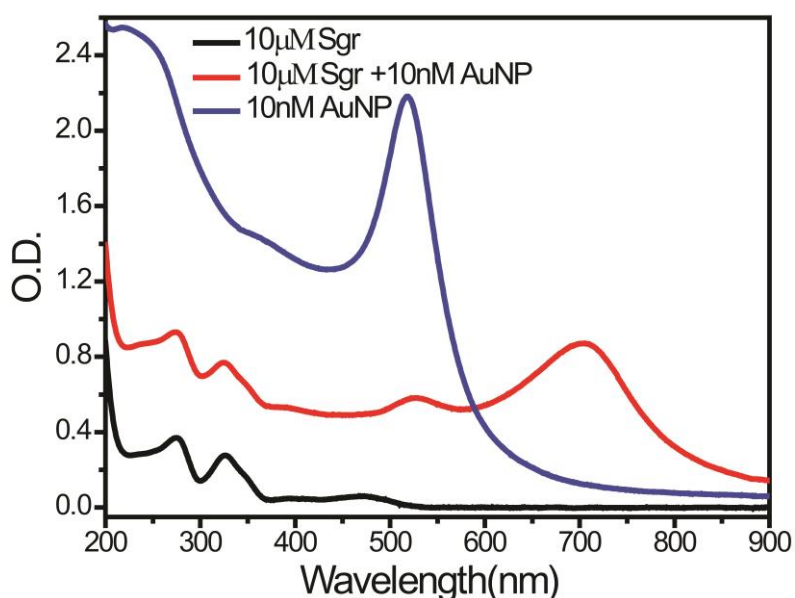


Figure 3.1: Absorption profile of Sgr (black), citrate-capped gold nanoparticle (blue) and Sgr-AuNP complex (red).

This wavelength was selected for the excitation as Sgr has its absorbance maximum at 327 nm, which is close to 355 nm. Sgr is a toxic quaternary ammonium salt from the group of benzyloquinoline alkaloids. Because of the presence of a quaternary ammonium group, Sgr has a higher affinity to the free acid groups ($-\text{COOH}$) on the surface of plasmonic spherical AuNPs made from TSC. The synthesis of plasmonic AuNP has been described in Chapter 2 Section 2.2.7. This electrostatic interaction between the quaternary ammonium group (NR^{4+}) of Sgr and the free acid group ($-\text{COO}^-$) on AuNP acts as the driving force to load Sgr drug molecules on the AuNP surface, which has been defined as the docking effect in the Introduction Section. Binding of Sgr on the surface of AuNPs can be easily observed from their absorption spectra recorded in the UV-vis region. It is clear from **Figure 3.1** that Sgr has three major absorption spectral peaks in the UV-vis region, centred on 275 nm ($\pi \rightarrow \pi^*$), 327 nm ($\pi \rightarrow \pi^*$), and 470 nm ($n \rightarrow \pi^*$). On the other hand, the TSC-based gold nanoparticle has a single strong plasmon at 519 nm. When Sgr was adsorbed on the gold nanoparticle surface, the red colour of the nanoparticle changed to blue, with a new band appearing at 704 nm at the expense of the plasmon band at 519 nm. The intensity of the

newly appeared 704 nm peak increases with an increasing amount of AuNPs. The appearance of this new peak at 704 nm along with the extended networking of AuNPs (**Figure 3.2**) in the presence of Sgr indicates that Sgr and spherical AuNPs interact to form a ground-state complex.

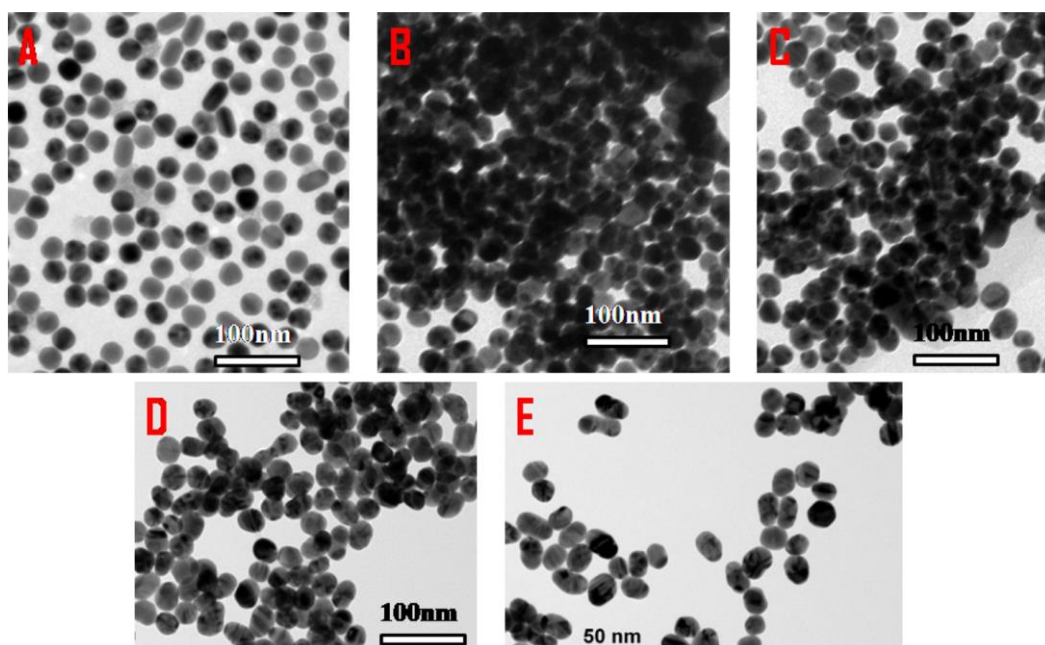


Figure 3.2: TEM images of (A) AuNP (10 nM), (B) AuNP (10 nM)-Sgr (10 μM) complex, (C) AuNP-Sgr complex, with 0.05 μM ctDNA, (D) AuNP-Sgr complex, with 0.15 μM ctDNA, and (E) AuNP-Sgr complex, with 0.25 μM ctDNA.

The same set of data can also be achieved from their T-T absorption spectra shown in **Figure 3.3**, which shows three peaks, two at 360 nm and 400 nm, respectively, and a broad peak centred at 600 nm from Sgr alone.

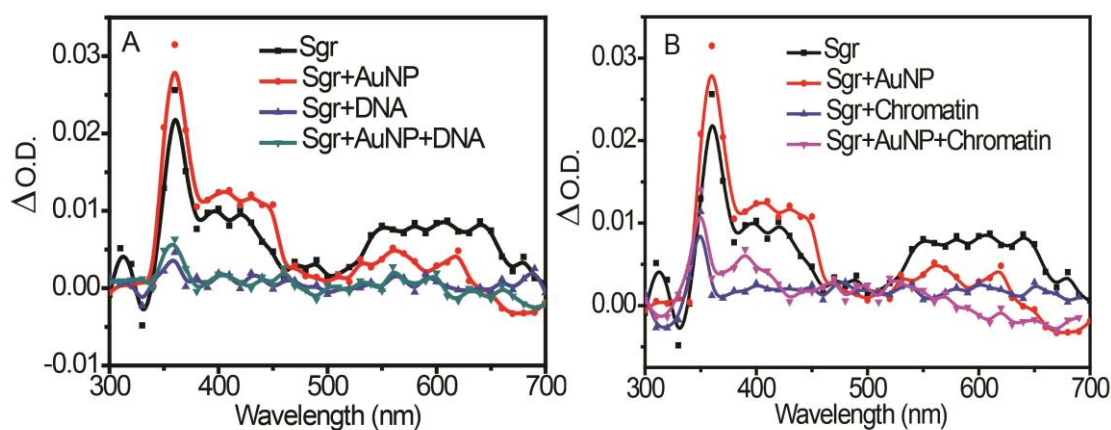


Figure 3.3. T-T absorption spectra of Sgr [100 μM] (A) with AuNP [100 nM], ctDNA [2.5 μM], and AuNP followed by ctDNA; and (B) with AuNP [100 nM], chromatin [2.5 μM], and AuNP followed by chromatin in tris-NaCl buffer (pH: 7.4 ± 0.2) after 1 μs laser flash of $\lambda_{\text{ex}} = 355$ nm.

Moreover, time-resolved T-T absorption spectra **Figure 3.4** show an overall decrease in optical density (ΔOD) from 560 to 650 nm with a gradual increase in time, which indicates that all of these peaks are of the same origin. The origin of these three T-T absorption peaks is not as straightforward as it is observed for the S-S absorption spectra (UV-Vis). Because of molecular state mixing and crossing between singlet and triplet states (intersystem crossing) to initiate a T-T transition, it is difficult to define the actual nature of the originating or destination state without knowing the actual weightage of singlet-triplet state mixing, and the excited-state molecular geometry optimization is required to infer their actual state identification, which we have not mentioned in this article.

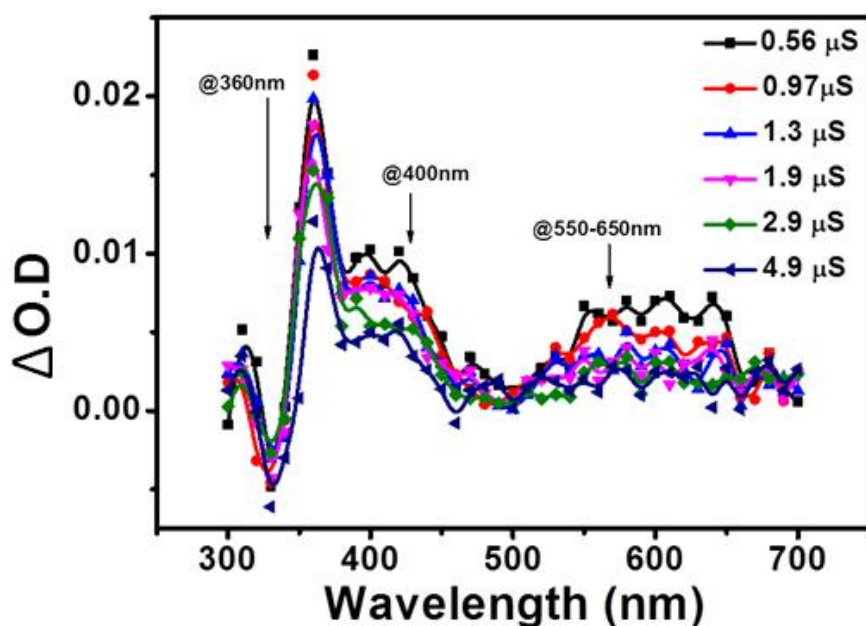


Figure 3.4: Time-resolved T-T absorption spectra of Sgr [100µM] show an overall decrease in optical density (ΔOD) from 560 to 650 nm with a gradual increase in time, which indicates that all of these peaks are of the same origin.

Upon addition of AuNPs, the peak intensities at 360 and 400 nm increase with a decrease in the peak intensity at 600 nm (**Figure 3.3**). Moreover, an isosbestic point observed at 460 nm without the generation of a new peak reveals that Sgr forms a ground-state complex with AuNP, which absorbs at 400 nm in the triplet state. Once ctDNA or chromatin is added to this gold nanoparticle-Sgr complex, the peak intensities or T-T absorbance of Sgr at 360, 400, and 600 nm decrease significantly. This phenomenon indicates that DNA or chromatin removes the Sgr molecules from the nanoparticle surface and intercalates them inside their cages, a necessary prerequisite for successful drug delivery inside a cell.^{279, 281, 282} The action of ctDNA and other DNA materials as a strong intercalator for Sgr drug molecules have been explained and well documented by Maiti et al.,^{278, 279} and this strong affinity of DNA toward Sgr acts as a driving force to undock drug molecules from the AuNP surface to intercalate them in the DNA helix for effective drug delivery into cellular components. Because of the large dimension of the Sgr-induced gold nanoparticle network, it might be difficult for the

Sgr-AuNP complex as a whole to enter the cell through a membrane pore, but the selective affinity of Sgr for DNA intercalation can put them into the nuclei for effective drug delivery. It is worth mentioning that both laser flash photolysis and UV–vis spectroscopy are absorption-based techniques, and all of the suggested complexes (Sgr-AuNP) are formed in the ground state only. As a result of this, it is logical that the latter technique that is UV–vis spectroscopy can be used to assay the extent of drug release instead of T-T absorption. As shown in **Figure 3.1**, the absorption profile of the Sgr-AuNP complex in the ground state, which is predominated by the 704 nm peak originating from plasmon coupling, cannot be used to measure the efficiency of drug release because of its nonlinear variation with intercalating components. Moreover, the $\pi-\pi^*$ peaks of Sgr near 300 nm overlapping strongly with the DNA band at 260 nm may give false-positive signalling if the $\pi-\pi^*$ band is used for fingerprinting. To avoid these problems, the T-T absorption profile has been used, which is free from the plasmon coupling band originated from AuNPs and also shows peaks at 360, 400, and 560 nm solely for Sgr avoiding any DNA band overlapping. The relative T-T absorbance at 360 nm for Sgr-AuNP-ctDNA/chromatin and Sgr-AuNP indicates the efficiency of the release of the drug molecule from the nano-vehicle (here spherical gold nanoparticle) induced by ctDNA or chromatin. Mathematically, it can be defined as

the efficiency of drug release (%) =

$$\left(\left(A_{Drug-AuNP}^{T-T} - A_{Drug-AuNP-DNA/Chromatin}^{T-T} \right) - \left(A_{Drug-AuNP}^{T-T} \right) \right) \times 100 \dots\dots\dots(3.1)$$

From **Figure 3.3** it is evident that on the addition of AuNP with Sgr, the T-T intensity at 360 nm increases from 0.022 to 0.028. On subsequent addition of ctDNA to this Sgr-AuNP adduct, the absorbance maximum falls to 0.006, which is close to that of Sgr-ctDNA. Following the above formula, the estimated drug release is 78.57%. In the case of chromatin, relative absorbances for $A_{Drug-AuNP}^{T-T}$ and $A_{Drug-AuNP-Chromatin}^{T-T}$ are 0.028

and 0.011, respectively, which gives an estimated 60.7% release of Sgr from the nanoparticle surface. To find out whether ctDNA and chromatin are efficient intercalators for Sgr, the transient absorption experiment has been performed for the Sgr-ctDNA and Sgr-chromatin complexes separately, where the concentration was fixed at 100 μ M for Sgr and at 2.5 μ M for both ctDNA and chromatin. At the above-mentioned concentrations, the Sgr-ctDNA complex shows almost zero intensity for all of the three peaks at 360, 400, and 560 nm, whereas the Sgr-chromatin complex shows a small peak at 360 nm originating from Sgr. This observation proves that ctDNA acts as a better intercalator than the chromatin molecules. Chromatin is a complex of DNA and histone tetramer proteins that form chromosomes within the nucleus of eukaryotic cells.²⁸³ DNA does not appear in free strands for chromatin, rather it is highly condensed and wrapped around histone tetramer proteins to fit compactly inside the nucleus.²⁸⁴ Therefore, DNA strands in chromatin are less accessible for intercalation of Sgr compared with free DNA strands in ctDNA, which is clearly observable from our T-T absorption results.

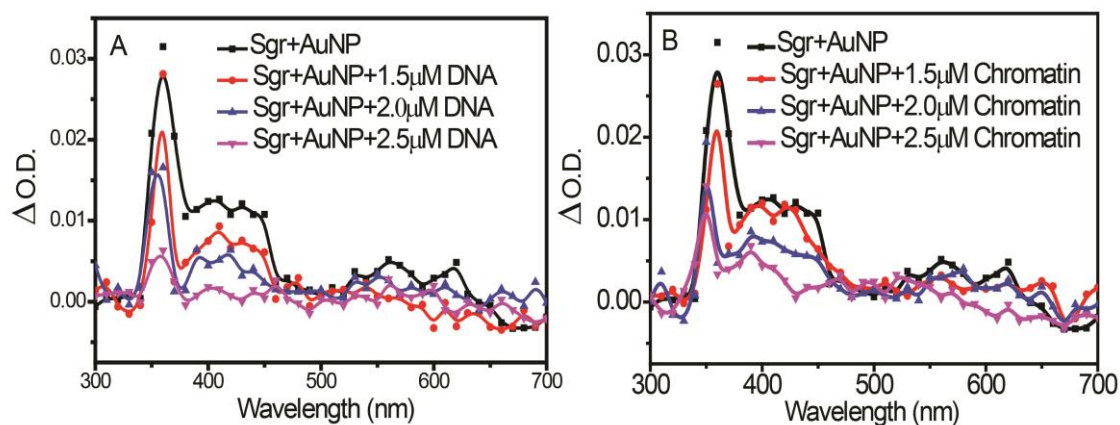


Figure 3.5: T-T absorption titration by varying the concentrations of ctDNA and chromatin and keeping the Sgr [100 μ M] concentration constant.

By varying the amount of ctDNA or chromatin and keeping the amount of Sgr on the gold nanoparticle surface constant, a T-T absorption titration has been performed to quantify the amount of Sgr released, involved in DNA/chromatin intercalation for

controlled drug delivery. From **Figure 3.5**, it is evident that on increasing the concentration of ctDNA from 1.5 to 2.5 μM , $A_{\text{Drug-AuNP-DNA}}^{T-T}$ gradually falls from 0.02 to 0.016 and to 0.0056, indicating the release of the drug Sgr and subsequent intercalation inside DNA. For chromatin, the respective absorbance ($A_{\text{Drug-AuNP-Chromatin}}^{T-T}$) also decreases gradually from 0.0206 to 0.014 and to 0.0105. As shown in **Figure 3.6**, the correlation between intercalator concentrations and efficiency of drug release (%) shows a linear plot both for ctDNA and chromatin and demonstrates that this T-T absorption assay can be used effectively as a ruler to measure the extent of drug release during a therapeutic process.

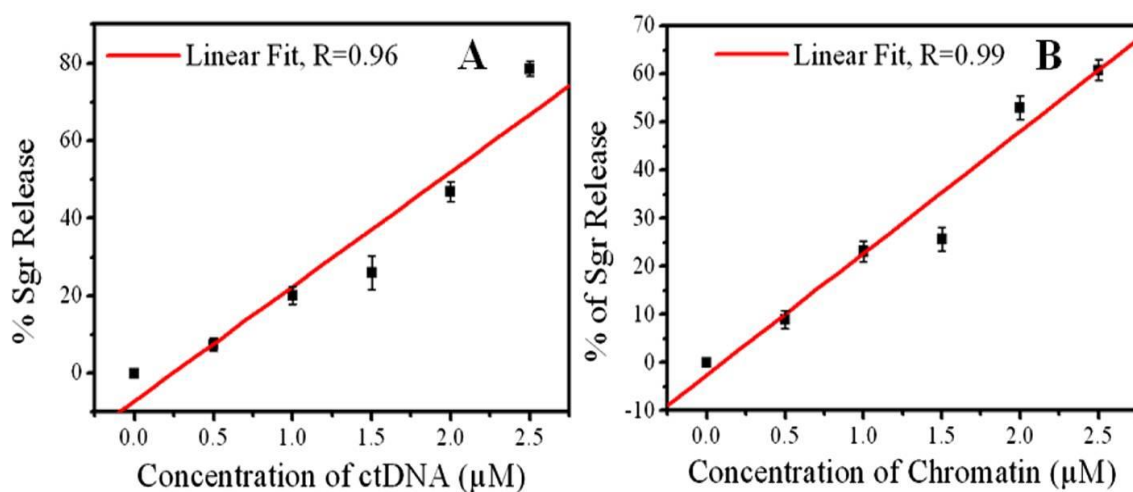


Figure 3.6: Correlation between intercalator concentration and efficiency of drug release (%) which shows a linear plot for both ctDNA (A) and chromatin (B).

The average lifetime of triplet Sgr, which is the inverse of the decay rate constant obtained from the analysis of the corresponding decay profile in **Figure 3.7**, is 2.4 μs , which increases to 2.8 μs in the presence of AuNP. This increase in a lifetime could be attributed to the formation of the Sgr-AuNP complex, which may either form in the triplet state directly or initially form in the ground singlet state followed by excitation to a higher singlet state and intersystem crossing to

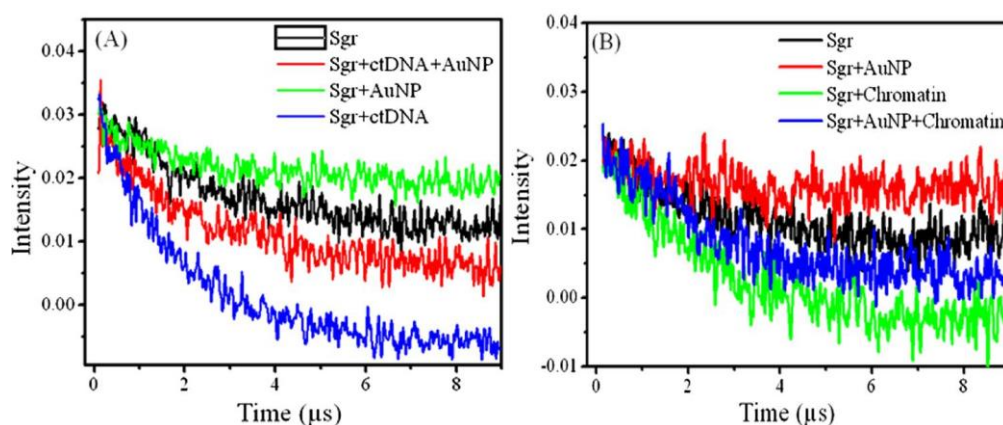


Figure 3.7: Decay profile of Sgr at 360 nm (A) with AuNP [100 nM], ctDNA [2.5 μM], and AuNP followed by ctDNA and (B) with AuNP [100 nM], chromatin [2.5 μM], and AuNP followed by chromatin in tris-NaCl (pH: 7.4 ± 0.2) buffer after 1 μs of laser flash with $\lambda_{\text{ex}} = 355 \text{ nm}$.

the corresponding triplet state, retaining its identity. After subsequent addition of ctDNA to the Sgr-AuNP complex, the lifetime becomes 2.0 μs , which is very close to the lifetime of Sgr itself inside ctDNA (1.8 μs) and indirectly indicates that the addition of ctDNA initiates the undocking process to intercalate the released Sgr drug molecules inside their helix structure. Although the change in lifetime due to the docking and undocking of Sgr molecules on or from the AuNP surface is quite small on the microsecond (μs) time scale, they are quite separated on the nanosecond (ns) time scale. There is an increment of 400 ns (0.4 μs) in lifetime due to docking (adsorption of Sgr on the AuNP surface) and a decrement of 400 ns (0.4 μs) in lifetime due to undocking (release of Sgr upon addition of ctDNA in the Sgr-AuNP adduct). However, the small discrepancy (200 ns or 0.2 μs) in lifetime between Sgr-ctDNA and Sgr-AuNP-ctDNA is due to the partial release of Sgr from the Sgr-AuNP complex (Table 3.1) in the presence of ctDNA. Similar changes in lifetime for triplet Sgr were obtained with chromatin but to a lesser extent than those with ctDNA (Table 3.1) Therefore, in this context, the lifetime of Sgr also supports the previous hypothesis obtained from its T-T absorption

that Sgr can be released from the nanocarrier (AuNP) in the presence of both DNA and chromatin.

Table 3.1: Average Lifetime of Triplet-State Sgr, Sgr-AuNP Complex, Sgr-ctDNA/Chromatin and Sgr-AuNP-ctDNA/ Chromatin, recorded at 360 nm after the Laser Flash at 355 nm.

$\tau_{\text{Sgr}} (\mu\text{s})$	$\tau_{\text{Sgr+AuNP}} (\mu\text{s})$	$\tau_{\text{Sgr+ctDNA}} (\mu\text{s})$	$\tau_{\text{Sgr+AuNP+ctDNA}} (\mu\text{s})$	$\tau_{\text{Sgr+chromatin}} (\mu\text{s})$	$\tau_{\text{Sgr+AuNP+chromatin}} (\mu\text{s})$
2.4±0.02	2.8±0.04	1.8±0.003	2.0±0.001	1.9±0.002	2.2±0.003

As standard tools, along with the above T-T absorption spectra, the fluorescence and surface-enhanced Raman scattering (SERS) experiments have been performed to prove the hypothesis as well as to measure the extent of drug release alternatively. The effect of Sgr binding on the gold nanoparticle surface was monitored by recording the fluorescence maximum at 586 nm after excitation at 470 nm. It is clear from **Figure 3.8 (A)** that the fluorescence intensity gradually reduces as the amount of AuNP is increased.

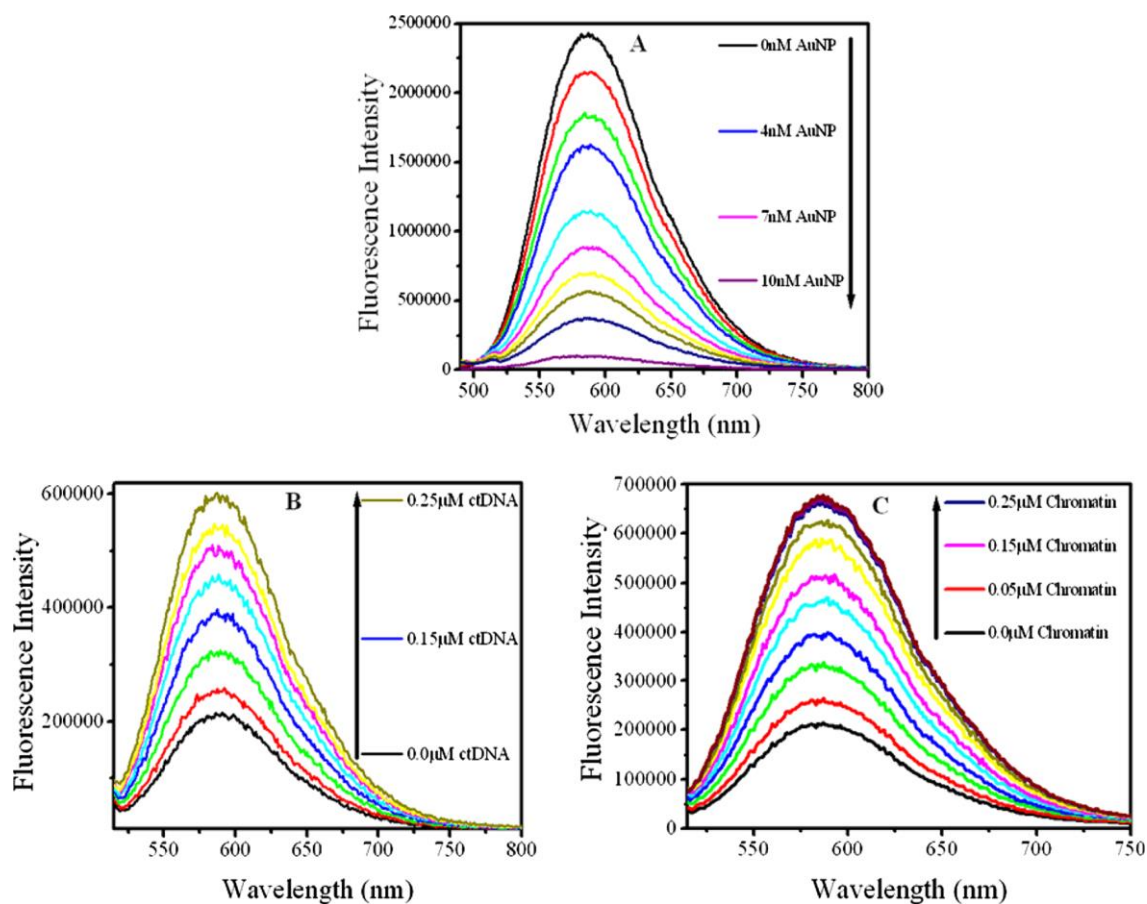


Figure 3.8: (A) Gradual reduction in fluorescence intensity as a function of the increasing amount of AuNPs for 10 μM Sgr and release of Sgr from the AuNP surface as a function of gradually increasing amount of (B) ctDNA and (C) chromatin.

By considering AuNP as an efficient fluorescence quencher, the fluorescence quenching of Sgr is analysed according to the Stern-Volmer equation where F_0 and F are the fluorescence intensities of Sgr (10 μM)

$$F_0/F = 1 + K_{sv}[Q] \dots \dots \dots (3.2)$$

in the absence and presence of AuNPs, respectively, K_{sv} is the Stern-Volmer constant, and $[Q]$ is the concentration of the quencher, that is, AuNPs. The depicted Stern-Volmer plot **Figure 3.9** shows a deviation from linearity, which indirectly proves that the quenching route is a mixture of static and dynamic processes.

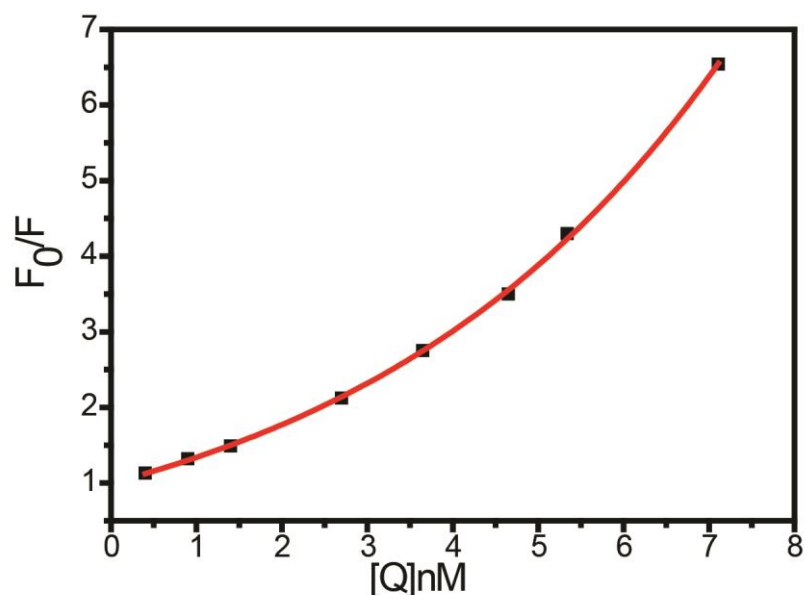


Figure 3.9: Variation of fluorescence quenching with the concentration of quencher (0.4-7.1 nM). Here 20-25 nm TSC stabilized AuNPs acts as a quencher and Sgr as the fluorophore.

Experimentally, when the AuNP-Sgr conjugate is found in the fluorescence “OFF” state, the addition of ctDNA or chromatin partially brings them back into the fluorescence “ON” state, which represents the release of Sgr from the AuNP surface, as shown clearly in **Figure 3.8(B), (C)**. After the formation of the adduct, the AuNP-Sgr complex is allowed to stand for 1 has a control experiment to check whether the release of Sgr from the AuNP surface is ctDNA/chromatin-mediated or it is released with time from the surface as a kinetically controlled process. From **Figure 3.10** it is clear that the release of the drug is purely mediated by the presence of ctDNA and chromatin as there is no substantial release in the absence of biological scaffolds.

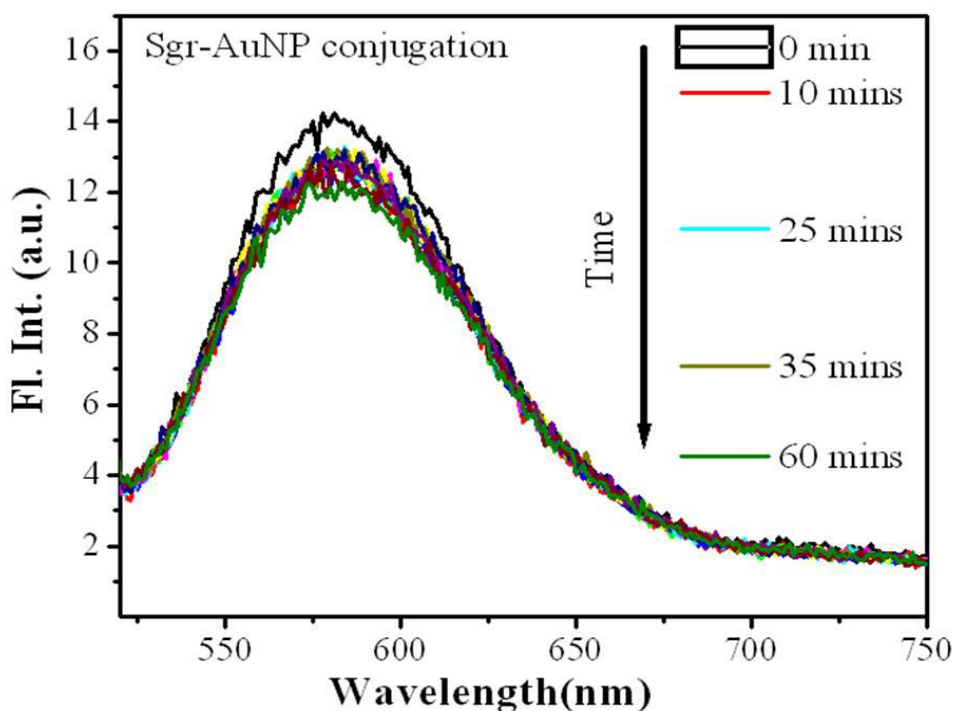


Figure 3.10: Variation of fluorescence intensity, obtained from Sgr-AuNP complex, with time without the addition of ctDNA and chromatin as active bio-scaffolds.

From the fluorescence spectral analysis, as depicted in **Figure 3.8**. The extent of fluorescence recovery can be defined as

$$\% \text{ fluorescence recovery} = (I_{\text{Sgr+AuNP+DNA}}^f / I_{\text{Sgr}}^f) \dots\dots\dots (3.3)$$

where $I_{\text{Sgr+AuNP+DNA}}^f$ is the maximum recovered fluorescence intensity after the addition of ctDNA or chromatin into the fluorescence “OFF” AuNP-Sgr conjugate and I_{Sgr}^f is the initial fluorescence intensity obtained from Sgr (10 μM). **Equation 3.3** estimates about 25 and 27% release of Sgr from the AuNP surface upon addition of ctDNA and chromatin, respectively. However, this extent of release of Sgr is quite low compared to that obtained from T-T absorption spectra. This underestimation of the release of a drug molecule compared to the measured value from the T-T absorption experiment could be attributed to either one or collective contributions from the following two effects:

(1) Intercalation of released Sgr inside the ctDNA or chromatin scaffold, which prevents the proper enhancement of fluorescence intensity. There are several reports in the literature³⁰⁻³³ in support of the explanation that the intercalation of Sgr to DNA/chromatin usually results in the decrement of the emission intensity. As a result of this intrinsic behaviour of Sgr inside the DNA/ chromatin scaffold, the measured fluorescence recovery or estimated drug delivery is far less than the actual Sgr release measured by T-T absorption spectroscopy.

(2) Alternatively, it could be due to efficient Sgr fluorescence quenching by AuNPs at a long distance. Although the Sgr molecules are not on the surface of the AuNPs but, due to their infinite surface, allow an isotropic distribution of dipole vectors to efficiently accept energy from the donor (Sgr), fluorescence quenching can occur at a much longer distance (~40 nm) compared to that at the FRET distance (3–8 nm). This nanoparticle-induced long distance quenching is generally referred to as nanoparticle surface energy transfer (NSET).²⁸⁵ Because of the complex and relatively large structure of chromatin compared to that of ctDNA, the relative distance between Sgr and the DNA scaffold in chromatin prevents efficient NSET and results in slightly more fluorescence signal recovery compared to that from ctDNA, and this has been reflected from our fluorescence quenching study. On the other hand, the T-T absorption probability does not get affected whether or not the fluorescence of the drug molecule is quenched due to its intrinsic nature, and it estimates an exact percentage of drug molecule release. Similar to fluorescence, although SERS has also been studied extensively in the past few decades²⁸⁶⁻²⁹⁰ and showed promise to be one of the most useful analytical techniques for future applications in diagnostics because of its ability to provide the chemical signature along with its enormous signal amplification ($10^8 - 10^{14}$ order),^{291, 292} its application in sensor technology is limited due to the nonlinear relation between the SERS signal intensity and the analyte concentration. The SERS intensity is a linear function of the

number of hot spots generated in the excitation volume, which is again not a linear function of the concentration of the added analyte and in general gives maximum Raman signals at a particular molar ratio between AuNP and the analyte where it generates a maximum number of hot spots along with the transformed plasmon band remaining in resonance with the excitation wavelength. As a result of this nonlinear relation between SERS intensity and Raman tag (analyte) concentration, SERS cannot be used as a standard sensory tool to estimate the release of drug molecule from the nanoparticle surface in this particular experiment. However, it is worth mentioning that by keeping the same analyte and similar system in the study, SERS could give valuable information regarding their mechanism of execution. In our experiment, Sgr is used as the analyte and AuNP as the surface to adsorb them and monitored the release of drug molecule (Sgr) upon addition of ctDNA and chromatin by measuring their SERS activity. It is clear from **Figure 3.11A** that increasing the amount of AuNPs at a particular concentration of Sgr (10 μ M)

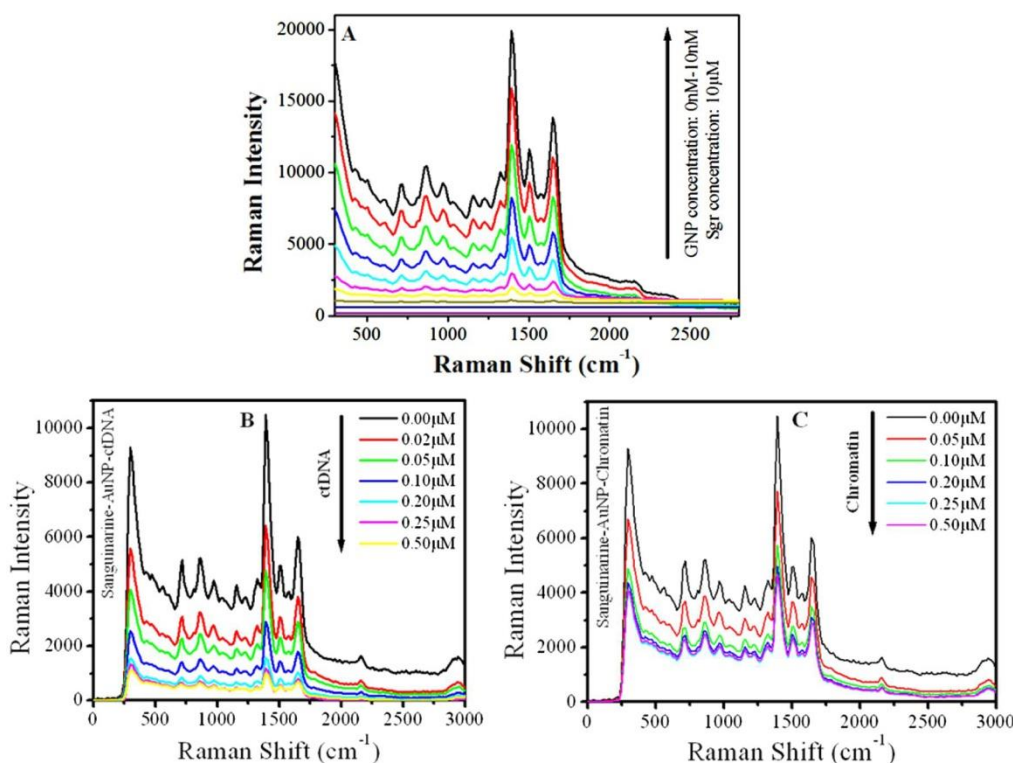


Figure 3.11: (A) The gradual increment of SERS intensity as a function of the increasing amount of AuNPs (0-10 nM) for 10 μM Sgr and release of Sgr from the AuNP surface as a function of gradually increasing amount of (B) ctDNA and (C) chromatin.

enhances the SERS intensity substantially (in the absence of AuNP, Sgr alone does not give detectable Raman signal as clearly visible from **Figure 3.11(A)** because of the formation of more number of hot spots in the excitation medium, which is further confirmed by the TEM analysis as clearly visible in **Figure 3.2**. The SERS spectra of Sgr (10 μM) have not been plotted at a higher concentration of AuNPs as it gradually reduces beyond 10 nM concentration. Unlike fluorescence study, the SERS signal gradually reduces as we increase the amount of ctDNA and chromatin to the Sgr-AuNP conjugate. SERS signal quenching as a function of the concentration of ctDNA and chromatin is shown in **Figure 3.11 (B-C)** respectively. Because of the easy intercalation

of the Sgr molecule inside ctDNA compared to that of the chromatin molecules as discussed before, more SERS quenching is expected upon addition of ctDNA compared to that of chromatin. Moreover, because of the short-range interaction pattern of SERS, the intercalated Sgr molecule does not affect the observed SERS signal after release as it has been observed for fluorescence. By comparing the SERS peak intensities for the –C–C– (in-ring) stretching mode²⁹³ at 1393 cm⁻¹ before and after the addition of cell components to the AuNP–Sgr complex, about 51% Raman quenching is observed for chromatin compared to 89% Raman quenching for ctDNA. If it is considered that this Raman quenching is solely for the release of Sgr from the nanosurface, then Raman quenching indirectly measures the extent of drug release from the nanocarrier, which corresponds well with the result obtained from our T-T absorption experiments. Mathematically, the % of Raman quenching has been defined as

$$\% \text{ Raman quenching} = \left[\left(\frac{I_{\max}^{\text{SERS}} - I_{\min}^{\text{SERS}}}{I_{\max}^{\text{SERS}}} \right) \right] \times 100 \dots\dots\dots(3.4)$$

where I_{\max}^{SERS} is the maximum SERS intensity before the addition of ctDNA or chromatin and I_{\min}^{SERS} is the minimum SERS intensity after the addition of ctDNA or chromatin.

3.3 Conclusions:

In this work, the T-T absorption spectroscopy has been used as a molecular ruler not only to understand the actual release process of Sgr as a drug molecule from a plasmonic gold nanoparticle surface in the presence of cell components, that is, DNA and chromatin, but also to measure the extent of drug release, which is necessary for any controlled drug delivery modality. The results obtained from the T-T absorption study were verified using fluorescence and SERS, and a plausible explanation has been put forward throughout the Results and Discussion section on why the T-T excitation spectroscopic assay could be a better sensory tool compared to fluorescence- and SERS-based assays. Because of the intrinsic nature of absorption, the reported T-T excitation

spectroscopic assay overpowers fluorescence- and SRES-based assays, which are limited by the long-range interaction and nonlinear dependence of analyte concentration, respectively.

CHAPTER 4

Low Magnetic Field Induced Surface Enhanced Transient Spin-Trajectory Modulation of a Prototype Anticancer Drug Sanguinarine on a Single Domain Superparamagnetic Nanosurface

OUTLINE:

- Role of Magnetic nanosurface on the intersystem crossing process.
- How a magnetic nanosurface can be used to increase the triplet yield?
- How the solvent polarity, as well as the hydrogen bonding induced solvent stabilization can influence the field effect by the magnetic nanosurface?

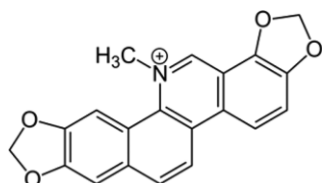


4.1 Introduction

Populating a molecule in excited states beyond its natural lifetime by spin-trajectory modulation can surprise by initiating different unusual optical, spectroscopic, photophysical, and photochemical pathways,^{83, 132, 294-303} providing new insights into molecular resources for renewable energy,^{288, 298, 304} offering flexible magneto kinetics (through radical pair mechanism),^{301, 305} commencing new dynamic trajectories,^{306, 307} crucially expanding the field of organic spintronics^{13,14} and achieving abnormal optical transition.³⁰⁸⁻³¹¹ Most of the known molecular systems remain in the singlet ground state (S_0), whereas the photochemically energized excited state could either be singlet (S_n ; $n = 1, 2, 3, \text{etc.}$) or triplet (T_n ; $n = 1, 2, 3, \text{etc.}$). There are reports on the formation of different excited spin states (singlet and triplet) when one electron from the singlet ground state (S_0) is being excited to a higher energy level (S_n or T_n) either by preserving (spin-conservation),^{312, 313} reversal (spin-flipping),^{314, 315} rephasing (spin-flopping),^{316, 317} or noncollinear spin arrangement (spin-canting)³¹⁷ of their original spin orientation.³¹⁸⁻³²⁰ Since the spin reversal process is not an allowed transition governed by the spin selection rule, optomolecular excitations are singlet-singlet ($S-S$)³²¹ type exclusively, and passage to triplet excited states is primarily governed by excited state tunnelling or conical intersection, which is generally defined as intersystem crossing (ISC).^{322, 323} In contrast, ferrimagnetic or ferromagnetic nanostructures and especially single-domain superparamagnetic nanosurfaces^{324, 325} induce several different unusual spin dynamics of electrons in surface adsorbed organic molecules by applying a small external magnetic field.³¹⁸ These spin dynamics include enhanced electronic and magnetic quantum efficiency,^{326, 327} population inversion,³²⁸ introduction of trap-sites by balancing of injection and recombination of charge carriers,³²⁹ or even unusual photochemical reaction pathways^{330, 331} to find real-life applications in organic conductors and crucial biochemical reactions along with their potential functions as molecular ruler³³² to estimate the extent of drug

release for effective therapy. The spin of an electron can be represented by a vector precessing around the laboratory Z-axis with Larmour frequency, ω (**Figure 4.1 A**).³³³ The spin vector is represented by either α or β for up (\uparrow) and down (\downarrow) spin respectively, with respect to the reference axis. The orientations of the vectors remain opposite in singlet states (S_0 and S_n are singly degenerate) with total spin angular momentum (S) as 0 and the corresponding asymmetric spin wave function can be represented as $\chi^A(1, 2) = [\alpha\beta - \beta\alpha]/2$, where 1 and 2 represent two electrons, one in highest occupied molecular orbital (HOMO) and the other in lowest unoccupied molecular orbital (LUMO). From the S_1 state, the molecule can undergo radiative internal conversion (IC) or radiative fluorescence, which again brings the molecules to the S_0 state. On the other hand, the nonradiative ISC which is effective through intramolecular and intermolecular spin-modulation to produce the T_1 state (triply degenerate) with total spin angular momentum (S) as 1 and the corresponding three symmetric spin wave functions can be represented as $\chi^S(1, 2) = \alpha\alpha, \beta\beta$, and $[\alpha\beta + \beta\alpha]/2$. Therefore, the conversion of S_1 to T_1 is possible if spins are flipped or rephased by xy and z component of L-S coupling, respectively. The L-S coupling is responsible not only to change the precessional frequency but also their direction due to the generated torque (Γ).^{334, 335} Precessional motion of the magnetization vector, which controls both the precessional frequency as well as their direction, directly enhances the S_1 to T_1 spin trajectory population through spin rephasing or flipping mechanism.^{336, 337} In the present set of experiments, a large magnetic field (in the order of Tesla (T)) antenna has been generated by low external magnetic-field (0.08 T)-induced single-domain magnetic moment alignment of individual constituent atoms arranged in a superparamagnetic nanosurface to enforce the programmable transient spin-trajectory modulation through $S_1 \rightarrow T_1$ conversion of the surface adsorbed sanguinarine (Sgr) molecule. Sgr is a known small molecule, which is a naturally occurring alkaloid and has gained tremendous importance in the pharmaceutical industry for the last several decades.³³⁸⁻³⁴⁰ Along with its

proven anti-inflammatory, antioxidant, antifungal, and antimicrobial activities, it shows potential application as an anticancer drug.^{265-268, 272, 274, 341-345} Sgr is a toxic quaternary ammonium salt, and the presence of this quaternary ammonium group helps to bind with a free acid group ($-\text{COO}^-$) on the surface of spherical FeNPs capped by trisodium citrate (TSC).



The molecular structure: Sanguinarine ((13-Methyl-[1,3] benzodioxo [5,6-c][1,3]- dioxolo[4,5-

The mechanism of single-domain (with a surface area less than 10^{-12} m^2) magnetic moment aligned large-field super-paramagnetic field-driven spin interconversion has been cross-checked by using the diamagnetic nanosurface in presence of low external magnetic field (0.08 T). The generated torque as a result of L-S coupling tends to align the magnetic dipole with the external magnetic field. In the present set of experiments, this externally applied low magnetic field (0.08 T) could be scaled up several orders on the surface of a small (10 nm) superparamagnetic Fe_3O_4 nanoparticle. In presence of this induced gigantic magnetic field, the magnetic dipole of the surface adsorbed Sgr will be aligned perpendicular to the superparamagnetic moment to achieve the lowest potential energy compared to the random angle between Sgr and Fe_3O_4 nanoparticle. For

$$\begin{aligned} \theta = 90^0, \sin\theta = 1; \text{Torque}(\Gamma) &= \mu \times B = \mu B \sin\theta \\ &= \mu B \text{ or the torque } (\Gamma) \text{ becomes maximum at } \theta = 90^0 \end{aligned}$$

where μ is the magnetic dipole moment of surface adsorbed Sgr and B = induced magnetic field on the Fe_3O_4 nanoparticle.

As a result of this induced gigantic magnetic field, L-S coupling for Sgr in the perpendicular orientation with the Fe₃O₄ nanoparticle is the most favourable orientation to assist the projected spin interconversion. Along with this high-field-induced intramolecular spin-interconversion, there is another mechanism that prevails in the presence of a low magnetic field even on the order of 0.01 T and that is known as radical pair mechanism. Perhaps this could be the first experimental observation of the theory for the modulation of radical pair dynamics by magnetic nanoparticles originally developed by Cohen,³¹⁸ for the specific case of a superparamagnetic system.⁶³⁻⁶⁵ There the molecule itself on photoexcitation can generate a “radical pair with the surrounding molecules including solvent” either by donating electrons from its LUMO or accepting electrons to its HOMO. Therefore, in water in the presence of citrate ion H-abstraction may be facilitated, which will produce an intermolecular geminate radical pair (Sgr-H)·(-H-solvent). If the radical pair is formed involving excited singlet Sgr, then the orientation of two spins of the radical electrons will be of singlet type that is antiparallel. On the other hand, if the radical pair is formed through triplet Sgr, then the orientation of the spins of two electrons will be of triplet type. In radical pairs, two molecules are loosely bound by intervening or surrounding solvent molecules and undergo diffusion within the solvent cage. During diffusion either they can recombine (more with singlet pair) or they can form free radicals escaping from the solvent cage (more with triplet pair since there two free electrons are with similar spin orientation). However, they can also undergo singlet-triplet interconversion ($S \leftrightarrow T$) at an interrational distance where exchange interaction between the two free electrons becomes negligible through a hyperfine interaction present in the system. The $S \leftrightarrow T$ phenomenon can be suppressed by application of an external magnetic field on the order of hyperfine interaction, generated through nuclear spin-electron spin coupling (I.S., on the order of 0.01-0.02 T, low field effect) making T_{\pm} energetically non-degenerate with respect to S and T_0 through Zeeman splitting. Therefore, if initially a

singlet radical pair is formed, in the presence of a magnetic field the singlet yield will increase, and hence the recombination of the geminate radical pair will increase. On the other hand, if initially triplet radical pair is formed, in the presence of a magnetic field the triplet yield will increase; that is, the free radical formation will increase.

4.2 Results and Discussion:

The experiments are done by taking sanguinarine (Sgr) as a model molecule and iron oxide nanoparticle as the model magnetic nanosurface. The synthesis of the Fe₃O₄ nanoparticle has been discussed in Chapter 2 Section 2.2.8

4.2.1 Portrayal of the nanoparticle by Transmission Electron Microscopy (TEM)

The above-mentioned nanomaterial has been characterized by both TEM and XRD study. The bright field TEM imaging of the sample is shown in **Figure 4.1B**. The average size of the nanoparticles is 10 nm in diameter range. **Figure 4.1B** shows the HRTEM image of the nanoparticles, which confirms the crystalline nature of the magnetic nanoparticles. The plane spacing in different directions is calculated from the HRTEM image and has been shown in **Figure 4.1B1**. **Figure 4.1B2** shows the selected area diffraction pattern of the nanoparticles and the different planes present in the nanoparticles. **Figure 4.1C** shows the EDX spectra attained in STEM mode from TEM study. From the spectra, it is observed that the elements present in the sample are Fe and O. To know the exact chemical composition of the material, the electron energy loss spectra of our sample is done (**Figure 4.1D**). The composition of the material is found through the white-line ratio method. The respective maxima of L₃ and L₂ peaks for Fe are located at 709 eV and 722 eV. Using the white- line ratio method, area under the L₃ and L₂ peak of 2 eV window around the maxima is calculated, also the measured ratio is 4.29, which shows the composition of the nanoparticle as Fe₃O₄.³⁴⁶

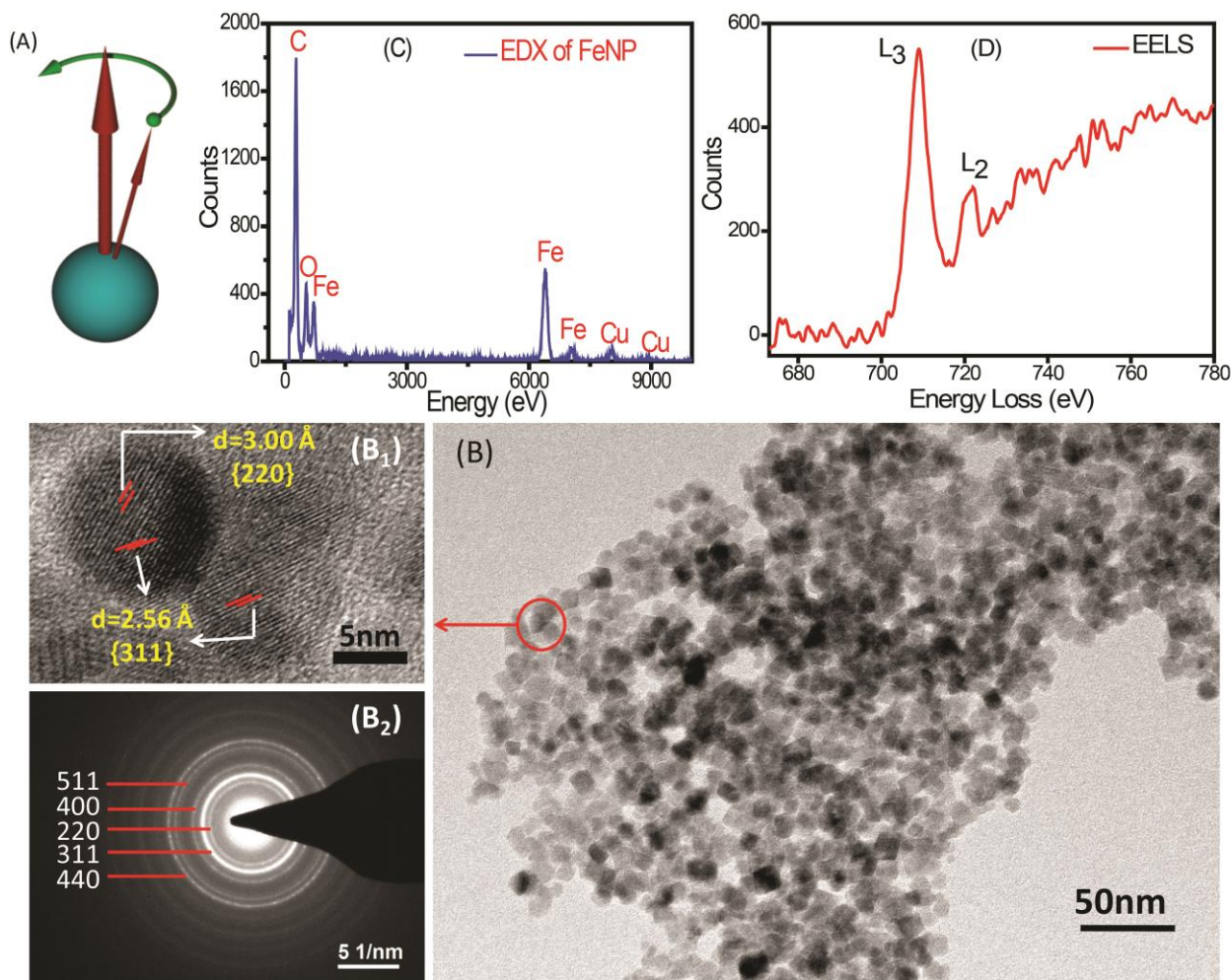


Figure 4.1: (A) Direction of precession of an electron, with the large arrow indicating the external magnetic field and the small arrow showing the spin angular momentum of the electron; (B) synthesized FeNP (TEM images); (B₁) Individual FeNP (HRTEM image) ; (B₂) Diffraction Pattern (Acquired Selected Area) of the nanoparticles and the different crystal planes present in the nanoparticles; (C) EDX spectra of nanoparticles acquired in STEM mode from TEM. (D) Electron energy loss spectra (EELS) of the nanoparticles.

4.2.2 The measurement of magnetization of the nanoparticle (Isothermal Magnetization and the Equivalent Langevin Function Fit.)

To study the magnetic property of the synthesized Fe₃O₄ nanoparticles, isothermal magnetization measurements are performed at 200 K and 300 K as depicted in **(Figure 4.2A)**. Both of the M-H curves show negligible hysteresis (coercivity-free or remanence-

free magnetic hysteresis)¹⁷³ with enormous saturation magnetization of 50.6 emu/g and 47.3 emu/g at 200 K and 300 K respectively. It is known that on reducing the size of the ferrimagnetic particle to the nanometer scale, they may act like individual ferrimagnetic entity, i.e., like superparamagnetic materials.³⁴⁷ Therefore, in order to verify the nature of the prepared 10 nm Fe₃O₄ nanoparticles, normalized magnetization (M/M_s) is being plotted with H/T and is shown in **Figure 4.2A**. It is evident from the figure that both the curves merge on to a single curve, which signifies the superparamagnetic nature of the particles. The nature of the sample can also be explained using the Langevin theory of paramagnetism in which the magnetization can be expressed as

$$M(H, T) = M_S \left[\coth(\mu_p H / K_B T) - \frac{K_B T}{\mu_p H} \right]$$

where μ_p is the average magnetic moment of the nanoparticle, T is the temperature, and H is the applied magnetic field. **Figure 4.2B** depicts that the measured M-H data at 300 K which fully fits with Langevin's theory of paramagnetism for the Fe₃O₄ nanosystem, and also again explains the superparamagnetic nature of the nanoparticles.

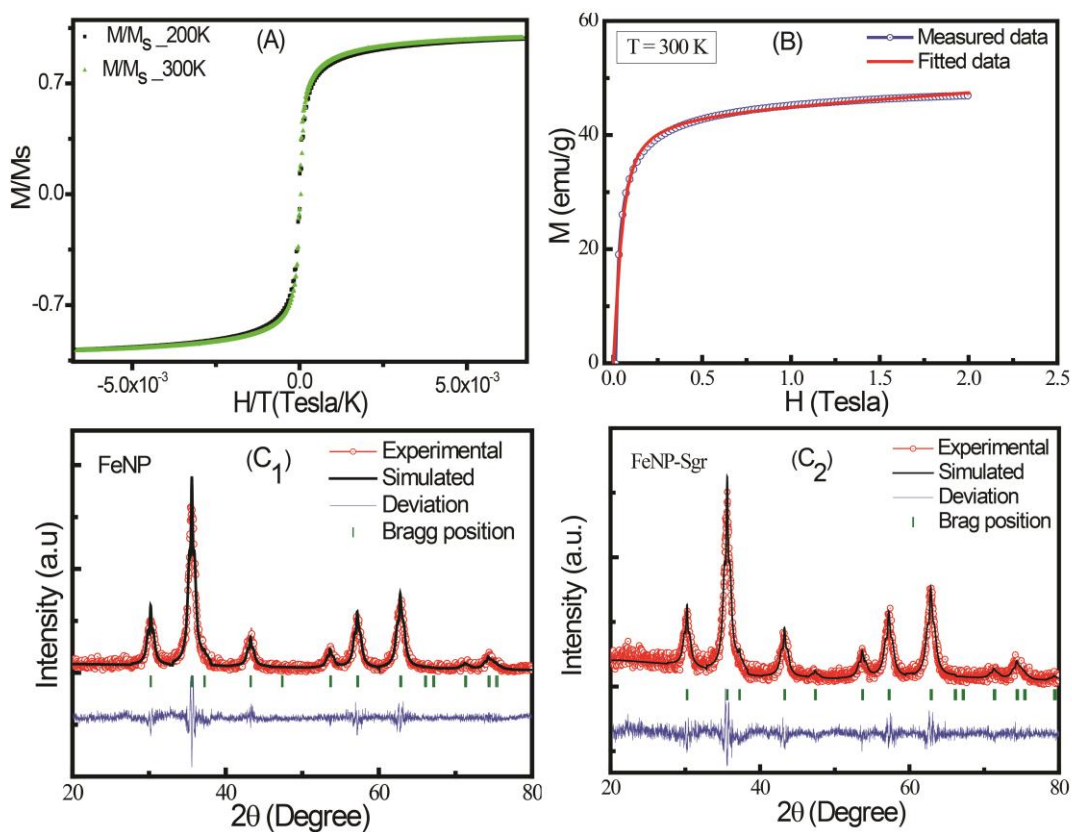


Figure 4.2: (A) The plot of Normalized magnetization (M/M_s) as a function of H/T at 200K and 300K; (B) Magnetization vs applied magnetic field dependence at 300K. The red line depicts the Langevin function fit on to the M-H data, and (C₁& C₂) shows XRD pattern of FeNP and FeNP-Sgr complex respectively.

4.2.3 Structural Characterization by XRD method.

The crystal structure of the nanoparticle and the effect of drug adsorption on the nanosurface has been studied by X-ray diffraction (XRD). The XRD patterns obtained for both the FeNP and FeNP-Sgr complex are depicted in **Figure 4.2**, C₁ and C₂ respectively. Obtained XRD patterns again prove the magnetite (Fe_3O_4) nature of the nanoparticle. Also, the unaffected XRD pattern confirms that the association of FeNP with Sgr does not affect the redox state of the superparamagnetic nanoparticles.

4.2.4 The Ground State Complex Formation between Sgr and Superparamagnetic FeNPs and its Stability to Govern the Transient Spin-Trajectory Followed by Photoexcitation

There exists a known tendency to form ground state complex between superparamagnetic nanosurface (iron nanoparticles; FeNP) and the fluorophore (Sgr). It is also important to know about their relative population in the excited state. In order to verify the formation of any ground state complex between Sgr and FeNP, a differential absorption spectroscopy is carried out (**Figure 4.3 A, B**); i.e., same volume of FeNP solution in CH₃CN and H₂O was added in both sample (Sgr) solution and in reference (CH₃CN or H₂O) cells, which helps to eliminate the individual cause of FeNP (**Figure 4.3 C**) in the overall absorbance. Surprisingly on progressive addition of FeNP in Sgr solution, an isosbestic point is achieved at 343.5 nm in CH₃CN and 267 nm in H₂O, this signifies that there exists an equilibrium between Sgr and Sgr-FeNP complex. Moreover, the appearance of the isosbestic point for CH₃CN at higher wavelength also implies that the ground state complex is much more stable in CH₃CN solvent compared to H₂O. The water molecules stabilize the individual Sgr or FeNP much more than their complex (Sgr-FeNP), which is also apparent from their time-resolved fluorescence experiments (**Figure 4.4A₁, B₁**) described later in the subsequent headings.

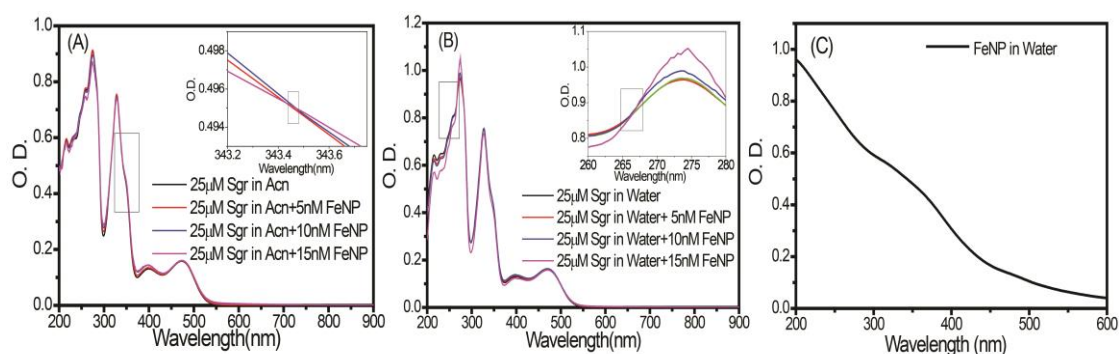


Figure 4.3: (A and B) The plot of differential absorption spectra of Sgr in the presence of superparamagnetic FeNP in CH₃CN and H₂O respectively (insets shows their respective isosbestic points); (C) Plot of UV-vis absorption spectra of the synthesized FeNP.

4.2.5 The Influence of Nanosurface, Donor-Acceptor Proximity, Surface Charge and Hydration Dynamics for Transient Spin-Trajectory Modulation

After the excitation of the ground state complex which regulates the spin-trajectory modulated excited state, the triplet-triplet absorption spectra along with their extent of fluorescence quenching are measured, separately in CH₃CN, H₂O, and ethanol (C₂H₅OH). It is observable from **Figure 4.4A₂ & A₃** that both the triplet (T₁) yield of Sgr as a whole, and its fluorescence intensity decreases on subsequently increasing the concentration of FeNPs (5-75 nM) in CH₃CN medium. There is also a decrease in fluorescence intensity which is a direct measure of the drop of excited singlet species (S₁) population on the addition of FeNP. The corresponding Stern-Volmer plot, i.e., the plot of relative Sgr fluorescence intensity vs FeNP (**Figure 4.4A₄**), is almost a linear fit in the lower concentration range of the quencher (FeNP) with which time-resolved studies are performed. There is quenching due to the formation of a ground state complex is also evident from absorption spectra of Sgr in the presence of FeNP (**Figure 4.3A, B**) this phenomenon is reconfirmed from their corresponding lifetime measurements where the measured lifetime stays unchanged with a variable concentration of FeNP in CH₃CN (**Figure 4.4A₁ and Table 4.1A**). hence it is proven that both the excited singlet and corresponding triplet yields of Sgr are reduced in the presence of FeNP in CH₃CN solution due to the ground state complex formation.

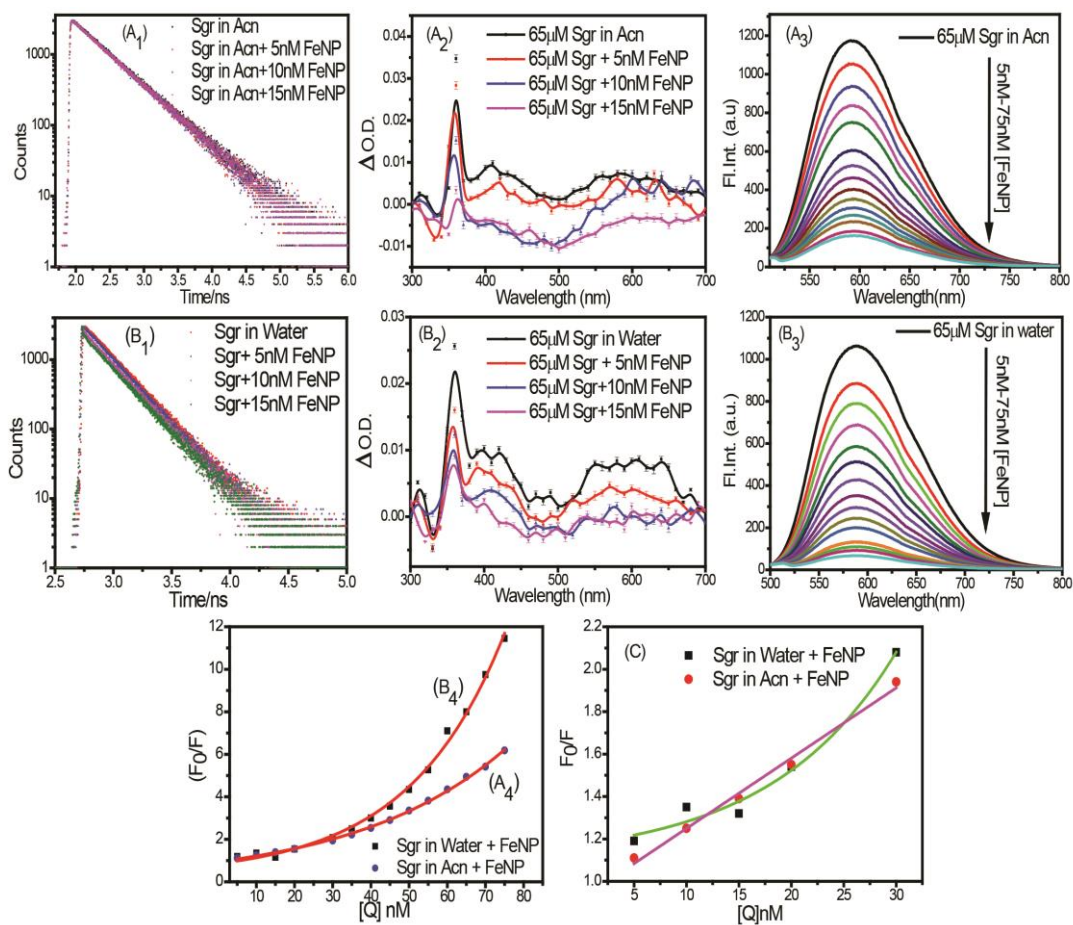


Figure 4.4: (A₁ and B₁) Plot of fluorescence decay profile of surface adsorbed Sgr on increasing concentrations of FeNP in CH₃CN and H₂O respectively; (A₂ and B₂) Plot of FeNP concentration-dependent T-T absorption spectra of surface adsorbed Sgr in CH₃CN and H₂O respectively; (A₃ and B₃) Plot showing the Trend and extent of fluorescence quenching from S1 state of Sgr in presence of varying concentrations of FeNP in CH₃CN and H₂O respectively; (A₄ and B₄) Stern-Volmer plot of Sgr-FeNP complex as a function of increasing concentration of FeNP for CH₃CN and H₂O respectively; (C) Linear and nonlinear Stern-Volmer plot of Sgr-FeNP complex as a function of low concentration FeNP in CH₃CN and H₂O respectively.

It is clearly evident from the **Figure 4.4B₂& B₃** that both the triplet (T_1) yield of Sgr molecule as a whole and the excited singlet (S_1) (which is measured by the fluorescence quenching experiment) population in H_2O medium decreases with rising concentrations of FeNP as it is also observed in CH_3CN medium also. If **Figure 4.4A₂** and **B₂**, are compared it is clear that the excited Sgr bears a signature of H abstraction as also evident from earlier reports³³², this leads to the generation of H-abstracted Sgr, (Sgr-H) \cdot , by producing two significant humps near 400 nm (395 and 420 nm) in the transient T-T absorption spectra in H_2O medium. As the significant absorption strength near 400 nm appears in absence of FeNP, it can be considered that the excited Sgr abstracts one $H\cdot$ from the H_2O matrix in order to generate an intermolecular geminate radical pair (Sgr-H) \cdot \cdot OH, and the quantity of this radical pair formation reduces with increasing concentration of FeNP because of the intramolecular (Sgr-FeNP-NaOOC-Cyt) hydrogen transfer between the citrate ion and the geminate radical pair [(Sgr-H) \cdot \cdot (OOC-Cyt)] on the same FeNP-surface. Though it cannot be disregarded that there is a possibility of formation of a geminate radical pair (Sgr-H) \cdot \cdot (N=C=CH₂) in CH_3CN as clearly evident from the weak humps near 400 nm in the excited state transient T-T absorption spectra, the formed ion pair shall recombine very fast because of the absence of solvent stabilization. Furthermore, the extent of H abstraction is comparatively low in the case of CH_3CN due to the lower stability of the solvent separated radical pair in absence of hydrogen bonding. Lack of the geminate radical pair (Sgr-H) \cdot \cdot (N=C=CH₂) stability along with the unchanged intramolecular (Sgr-FeNP-COONa-Cyt) hydrogen transfer decreases the 400 nm humps in a comparatively fast rate as clearly evident from **Figure 4.4A₂**, which further supports our mechanistic explanation. Moreover, twice high average fluorescence lifetime, τ , of Sgr in CH_3CN compared to H_2O (**Table 4.1A, B**) signifies a more stable nature of the excited singlet state of Sgr in an aprotic solvent.

Table 4.1: (A and B) Represents the details about the lifetime components of Sgr as a result of adsorption on magnetic nanosurface in CH₃CN and H₂O medium respectively.

(A) Sample in CH ₃ CN	τ (ns)	χ^2
65 μ M Sgr	4.99	1.09
Sgr +5 nM FeNP	4.97	1.01
Sgr +10 nM FeNP	4.93	1.00
Sgr +15 nM FeNP	4.91	1.01

Sample in H ₂ O	τ_1 (ns)	τ_2 (ns)	B ₁	B ₂	χ^2	Average Lifetime (ns) $\langle\tau\rangle$
65 μ M Sgr	-	2.36	-	-	1.01	2.36
(B) Sgr +5 nM FeNP	0.08	2.33	1.50	98.50	1.00	2.33
Sgr +10 nM FeNP	0.05	2.34	4.33	95.67	1.04	2.34
Sgr +15 nM FeNP	0.04	2.34	5.77	94.23	1.04	2.34

The nonlinear Stern–Volmer plot and the biexponential decay profiles of fluorescence lifetime (**Figure 4.4B₁,B₄**) in H₂O medium generate two-lifetime values, τ_1 and τ_2 . That supports the H-abstraction followed by geminate recombination with static fluorescence quenching of Sgr in the lower concentration range of FeNPs (**Table 4.1B**) at which we have done our time-resolved studies. The τ_2 component is of a longer-lifetime with higher percentage contribution and it does not change substantially with the addition of FeNPs. Therefore it bears the signature of static quenching. Whereas, the τ_1 component in the order of several picoseconds as well as with a very low percentage contribution possibly depicts the dynamic quenching due to the fluctuation between the molecule Sgr and the geminate

recombined form. Sgr-(H·OOC-)Cyt, in S_1 states and the contribution of geminate radical pair, (Sgr-H)·OH, in the T_1 state is negligible due to its expected longer lifetime. The relative contribution of dynamic part with respect to the static part of total fluorescence quenching increases when concentration of FeNPs is increased (as quencher) as clearly observable from **Figure 4.4B4**, which indirectly shows the increased rate of conversion from the geminate radical pair, (Sgr-H)·OH, in the T_1 state to the geminate recombined state, Sgr-(H·OOC-)Cyt, in the S_1 state. Because of a favourable transition from S_1 to S_0 in presence of a higher amount of FeNPs, a gradual reduction of the faster component (τ_1) of the excited state lifetime is observed. Kinetics of geminate radical recombination (S_1) is much faster compared to the corresponding internal conversion (IC)-based relaxation³⁴⁸. τ_1 is dependent heavily on the close proximity between donor [D: (Sgr-H)·] and acceptor [A: ·(OOC-Cyt)]. As the amount of FeNPs is increased, proximity between D and A also increases to increase the extent of geminate recombined S_1 state (increased from 1.5% to 5.8%) to relax the energy in a faster rate (allowed S-S transition), which is in good agreement³⁴⁹ with the reduction in fluorescence lifetime data shown in **Table 4.1B**. To substantiate this phenomenon, the experiments were cross-checked using a femtosecond fluorescence upconversion technique. The fluorescence decay profiles for Sgr in absence and presence of a variable concentration of FeNP in CH_3CN and H_2O medium are shown in **Figure 4.5**, panels **A1** and **B1** and the corresponding fluorescence lifetime components in CH_3CN and H_2O medium are listed in **Table 4.2**, **A1** and **B1** respectively. It is evident from **Table 4.2A1, B1** that the fluorescence lifetime of Sgr molecule in the femtosecond (τ_1) and picosecond (τ_2) time scale decreases drastically on the addition of FeNPs in H_2O medium. Then again, when the experiments were carried out in CH_3CN medium those components are hardly affected on the addition of FeNPs. Thus, it may be said that the prevailing H_2O molecules by faster hydration dynamics³⁵⁰ can stabilize the individual geminate

recombined S_1 energy state by the intramolecular hydrogen transfer between the geminate radical pair [(Sgr-H) $\cdot\cdot$ (OOC-Cyt)] and citrate ion on same FeNPs surface.

Table 4.2: (A and B) The lifetime components of Sgr due to the adsorption on nanosurface in CH_3CN and H_2O respectively.

(A ₁) τ	65 μ M Sgr in Acn	65 μ M Sgr in Acn+ 5nM FeNP	65 μ M Sgr in Acn+ 15nM FeNP	(A ₂) Acn	τ_1 (μ s)	τ_2 (μ s)	(A ₃) Acn	τ_1 (μ s)	τ_2 (μ s)
τ_1 (fs)	202.82	217	232	Decay@360nm without MF	5.59	0.059	Decay@410nm without MF	1.56	0.053
τ_2 (ps)	1.13	1.01	1.17	Decay@360nm with MF	8.42	0.36	Decay@410nm with MF	2.76	0.07

(B ₁) τ	65 μ M Sgr in Water	65 μ M Sgr in Water+ 5nM FeNP	65 μ M Sgr in Water+ 15nM FeNP	(B ₂) Water	τ_1 (μ s)	τ_2 (μ s)	(B ₃) Water	τ_1 (μ s)	τ_2 (μ s)
τ_1 (fs)	886.43	490.48	178	Decay@360nm without MF	1.96	-	Decay@410nm without MF	9.05	0.059
τ_2 (ps)	31.223	3.201	1.34	Decay@360nm with MF	2.04	-	Decay@410nm with MF	6.72	6.72

Figure 4.5A₂, A₃ and **Figure 4.5B₂, B₃** represents the decay profiles of Sgr molecule in presence of FeNPs in absence and presence of an external magnetic field at 360 nm and 410 nm in CH_3CN and H_2O respectively. Likewise, **Table 4.2A₂, A₃** and **Table 4.2B₂, B₃** show the triplet lifetime of Sgr in the presence of FeNPs in the absence and presence of an external magnetic field at 360 and 410 nm in CH_3CN and H_2O medium respectively. In CH_3CN , there are two components of lifetime at 5.59 and 0.059 μ s and 0.053 and 1.56 μ s at 360 nm and 410 nm respectively in the absence of an external magnetic field. In presence of an external magnetic field, an overall increase in a lifetime is found for all the components. The overall increase in lifetime may be due to the L-S coupling, which induces $S \leftrightarrow T$ interconversion. Though it is very fast (i.e in the ps timescale), the final effect is the increase in lifetime of triplet species in presence of external magnetic field as

the triplet (with microsecond lifetime scale) is much more energetically stable than the corresponding excited singlet state (with ns lifetime scale).

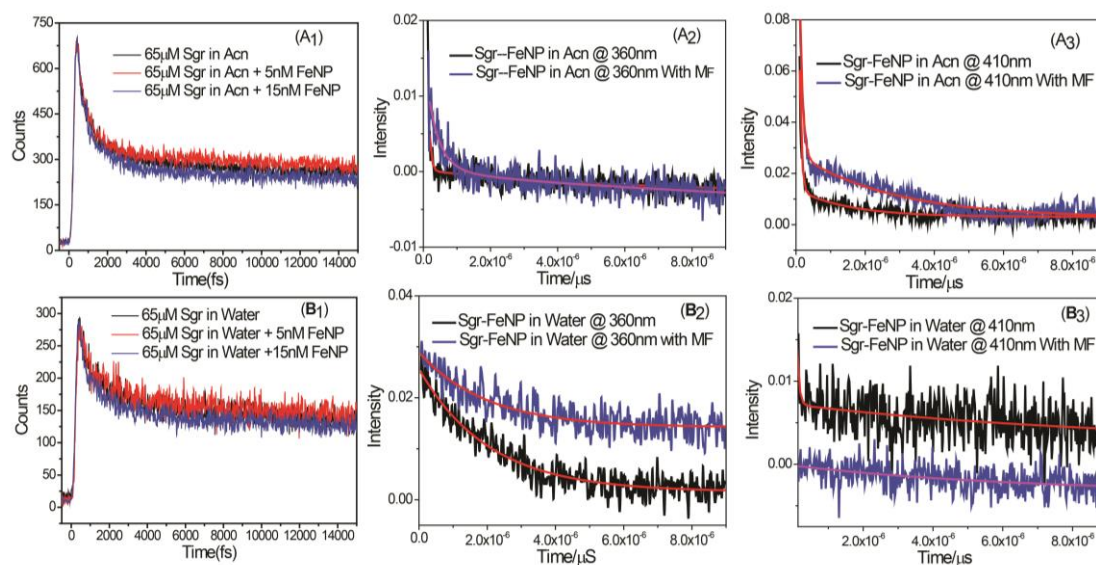


Figure 4.5: (A₁ and B₁) Decay profile of fluorescence lifetime of Sgr molecule in absence and presence of increasing concentration of the FeNPs in CH₃CN and H₂O medium respectively; (A₂ and A₃) biexponential decay profile of the excited triplet state of Sgr-FeNPs complex in the absence and presence of an external magnetic field in CH₃CN and (B₂ and B₃) in H₂O medium respectively.

Alternatively, in case of H₂O medium, one of the lifetime components at 410 nm reduces in presence of an external magnetic field and that is due to the reduction in the generation of free radicals (as discussed previously) following the radical pair mechanism. Though, the lifetime of the species at 360 nm (It is the signature of triplet Sgr) remains almost unchanged in the low concentration range of FeNPs, where radical pair mechanism dominates over L-S coupling based mechanism. The magnetic field effect on the geminate radical pair is the interplay among diffusion dynamics (which makes exchange interaction negligible), spin dynamics and geminate recombination (for the singlet radical pair) or free ion formation (for the triplet radical pair) as discussed in detail in the subsequent section of discussion. Though this is a nanosecond phenomenon, homogeneous recombination of

radicals takes place in the microsecond time scale that is being observed in the laser flash photolysis experiments.

Because of the lack of stability of the magnetic FeNP linked with Sgr, it is not feasible to carry out the experiments with different nonpolar organic solvents. Moreover, due to the big difference in dielectric constant of H₂O and CH₃CN solvents, which accounts for the effect of polarity in all possible polar solvents, but the discussion here has been limited within these two solvents to keep it coherent. In order to take away the ambiguity related to solvent effect, similar experiments are carried out with another protic polar solvent, i.e., ethanol (C₂H₅OH), C₂H₅OH solvent is having a dielectric constant very close to CH₃CN medium ($\epsilon_{\text{CH}_3\text{CN}}$: 37.5, $\epsilon_{\text{C}_2\text{H}_5\text{OH}}$: 24.5, $\epsilon_{\text{H}_2\text{O}}$: 80.0) but it exhibits hydrogen bonding ability similar to that of H₂O. The biexponential decay profile of the excited triplet state of Sgr-FeNP complex both in absence and presence of an externally applied magnetic field in C₂H₅OH medium is shown in **Figure 4.6 A, B**. It is clear from the excited triplet state decay profile of Sgr-FeNP composite in C₂H₅OH (**Table 4.3**) that there is the whole increment of lifetime both for 360 nm as well as 410 nm in presence of an external magnetic field. This indicates that the triplet yield is increased with the presence of an externally applied magnetic field as observed both for CH₃CN and H₂O medium (**Figure 4.7A, B**). This however directly proves that irrespective of the solvent polarity, an induced magnetic field can cause the S \leftrightarrow T conversion.

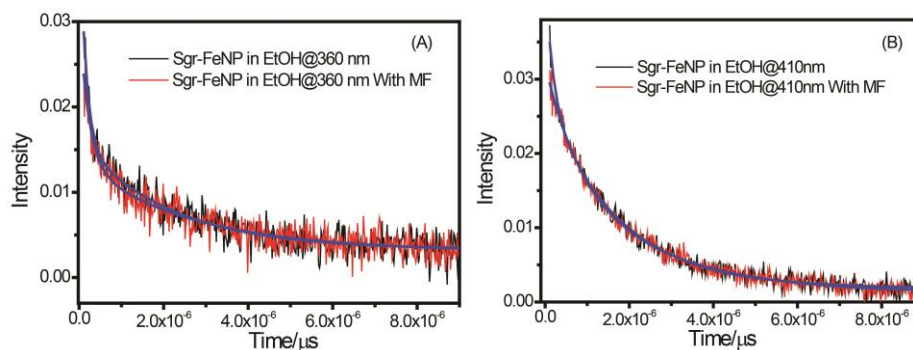


Figure 4.6: The plot of biexponential decay profiles of the excited triplet state of Sgr-FeNP in absence and presence of magnetic field (0.08T) at 360 nm (A) and 410 nm (B).

Table 4.3: Components of the biexponential decay profiles at (A) 360 nm and (B) 400 nm in C₂H₅OH medium.

(A)	τ_1 (μ s)	τ_2 (μ s)	(B)	τ_1 (μ s)	τ_2 (μ s)
Decay@360nm without MF	2.15	0.14	Decay@410nm without MF	1.7	0.04
Decay@360nm with MF	0.22	2.63	Decay@410nm with MF	2.32	0.3

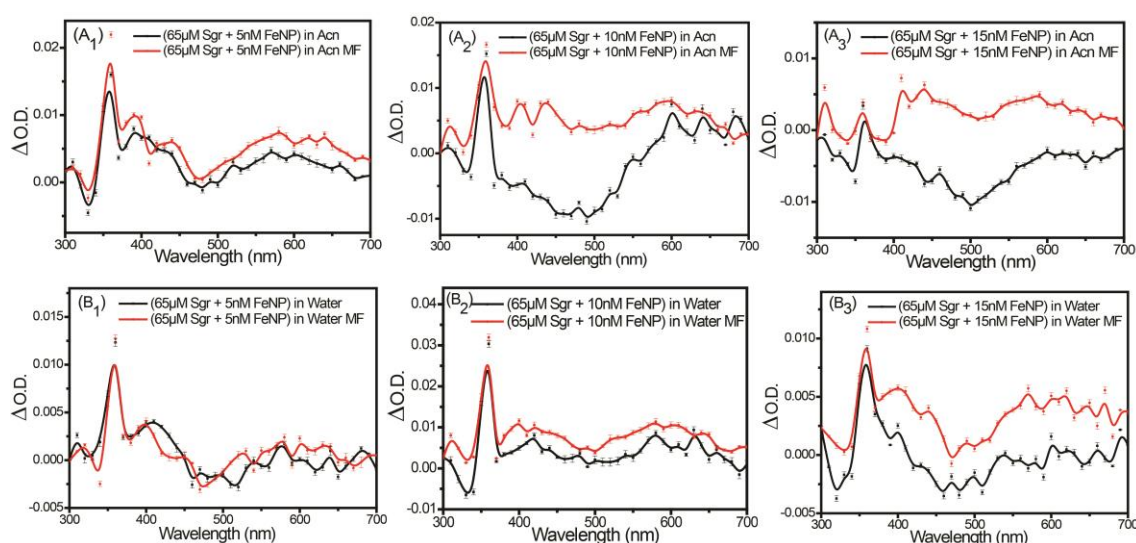


Figure 4.7: (A and C) The plot of T-T absorption spectra and the respective modulation of the transient spin state of Sgr molecule in presence of variable FeNPs concentration in presence of constant low external magnetic field (0.08T) in CH₃CN and H₂O respectively;

4.2.6 Efficient Transient Spin-Trajectory Modulation by Single-Domain Superparamagnetic Moment-Driven Spin Interconversion

To reduce the internal energy,³⁵¹ magnetic alignment of individual constituent atoms gets randomized in a single domain ferrimagnetic nanomaterial to behave like a paramagnetic particle rather than a ferrimagnetic particle where the resultant magnetic moment of individual domains are aligned in a particular direction. Due to this random

orientation of the magnetic moments of the individual atoms in a boundary-less single-domain crystalline paramagnetic material, the resulting magnetic moments for both the paramagnetic and diamagnetic nanomaterial are comparable in the absence of an externally applied magnetic field. The ultimate trajectorial fate of the transient excited state mainly dependent upon the surface charge of the matrix on which the molecule of interest is adsorbed and the polarity of the medium in which the photoexcitation is performed. On the contrary, low external magnetic-field-induced, magnetic moment alignment of individual constituent atoms arranged inside a single-domain on a superparamagnetic nanosurface makes them much different from the diamagnetic materials to produce a large-field magnetic moment on the magnetic nanosurface which in turn makes the effective intramolecular (through L-S coupling) spin-trajectory modulation. The gradual increase of triplet optical density ($\Delta O.D.$) in the presence of an externally applied magnetic field (0–0.08 T) as observed in **Figure 4.8A** gives indication of the larger contribution of the L-S coupling to transfer efficiently the excited state population from S_1 to T_1 energy state in presence of an induced high magnetic field by magnetic nanosurface.

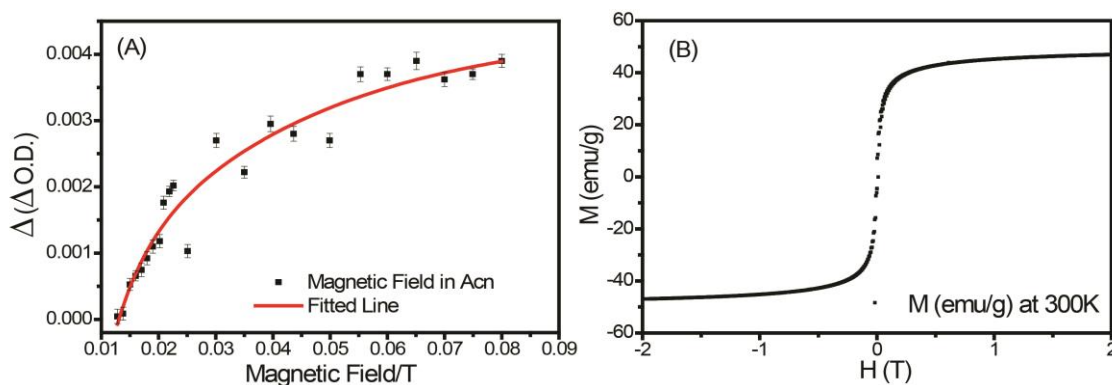


Figure 4.8: Plot of (A) Triplet absorbance (O.D.) as a function of externally applied low magnetic field (in Tesla unit) in CH_3CN and (B) Induced magnetic moment vs external magnetic field (in Tesla unit) in vacuum at 300K.

Efficient $S \leftrightarrow T$ trajectory modulation has again been verified by a gradual enhancement of Sgr triplet yield (**Figure 4.7 A1–A3**) in CH_3CN medium with increasing the concentration of FeNPs in the presence of an external low magnetic field (0.08 T) and that is monitored by using laser flash photolysis through triplet-triplet (T-T) absorption. Similar sets of experiments have also been done using a 25 nm diameter TSC-capped plasmonic gold nanoparticle (AuNP) which is a single crystal diamagnetic nanomaterial and it does not show a considerable extent of increment of triplet yield for comparable concentration (15 nM) of AuNPs under the influence of the same magnitude (0.08 T) of external low magnetic field (**Figure 4.9**).

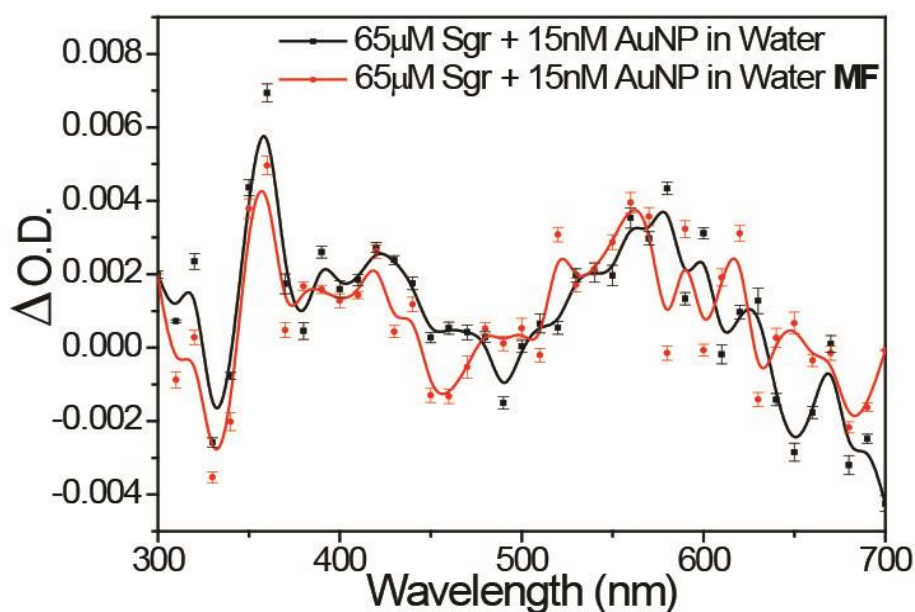


Figure 4.9. The plot of excited state T-T absorption spectra of Sgr-AuNP composite in the presence (red-line) and absence (black-line) of a magnetic field of magnitude 0.08T.

The comparable surface adsorption property of Sgr on both FeNPs and AuNPs can be substantiated from their fluorescence quenching properties by monitoring their fluorescence intensity. Both Fe and Au nanoparticle show almost a similar pattern of quenching in fluorescence with comparable quenching constant as the concentration of nanoparticles is increased. That indirectly verifies that both FeNP and AuNP show a similar adsorption property toward the surface attached Sgr molecule (**Figure 4.10**).

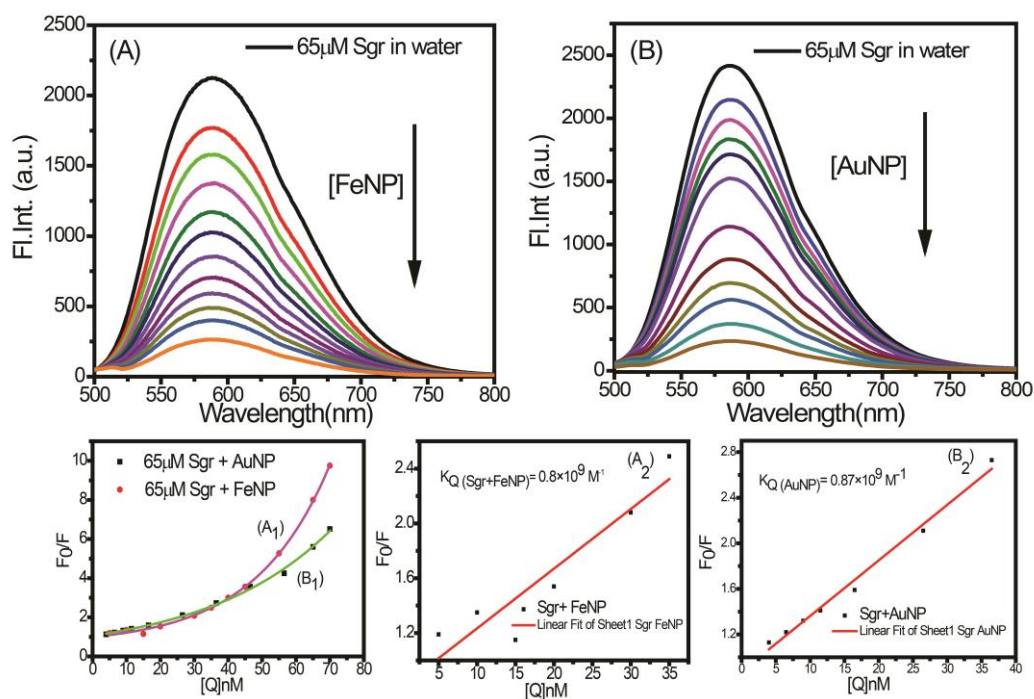


Figure 4.10: Fluorescence quenching trend and extent from the S_1 state of Sgr molecule with variable concentration of (A) FeNPs and (B) AuNPs in H_2O medium. (A₁ and B₁) The corresponding Stern-Volmer plot of Sgr-FeNP complex (red) and Sgr-AuNP (black) complex with the concentration of FeNPs and AuNPs. (A₂ and B₂) Shows the corresponding quenching constants in presence of a lower concentration of FeNPs and AuNPs respectively.

To figure out the effect of an external magnetic field on Sgr in absence of magnetic nanoparticle FeNP, the T-T absorption experiments have been carried out both in CH_3CN and H_2O media and presented as **Figure 4.11 (A) and (B)** which show no considerable effect on the triplet yield of Sgr in absence of FeNPs but in presence of the same external magnetic field. This indirectly verifies the excellence of the hypothetical large magnetic moment induced enhanced triplet spin trajectory population.

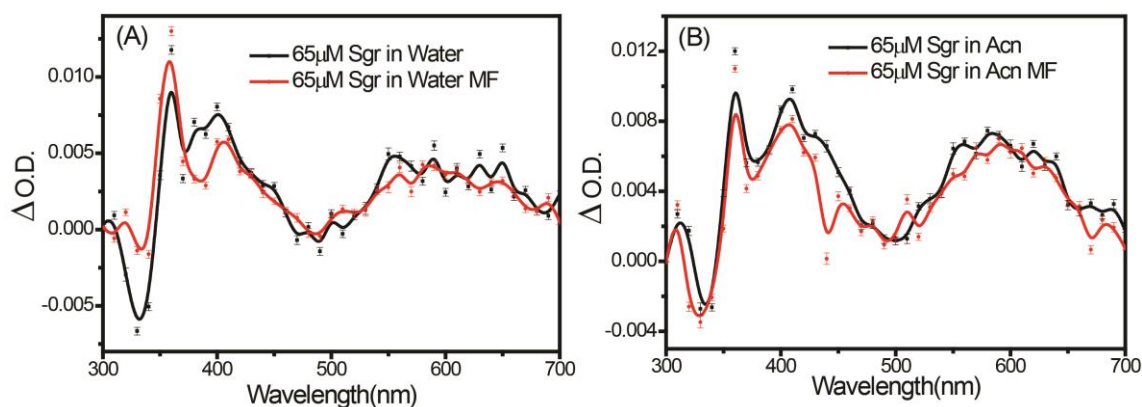


Figure 4.11: The plot of excited state T-T absorption spectra of Sgr molecule in (A) H₂O and (B) CH₃CN medium in the presence (**red-line**) and absence (**black-line**) of an external magnetic field of 0.08T.

Experimentally it is observed that the presence of 0.08 T external magnetic field can produce a considerable enhancement in induced magnetization within the ferrimagnetic nanoparticles (**Figure 4.8B**). Besides its induced large magnetic field, the absence of domain boundary permits these single-domain ferrimagnetic nanoparticles to develop a very strong internal magnetization due to the exchange coupling of electrons within the magnetic domain in presence of an external magnetic field and thus it becomes superparamagnetic. Superparamagnetic materials do not retain any net magnetization once the external field is removed, so these single-domain ferrimagnetic materials act as superparamagnetic particles without any magnetic memory. Hence, these types of materials are beneficial for switching ON-OFF of a magnetic field effect.

As a continuation with the previous section, when similar type of experiments are done in H₂O medium, the above phenomenon will also exist; i.e., the S₁ state to T₁ state transition of Sgr is enhanced due to a large induced magnetic field of the order of Tesla on the superparamagnetic FeNP surface which will enhance the T-T absorbance of Sgr molecule and it is clearly observable from **Figure 4.7B₁–B₃**. Comparison of **Figure 4.7A, B** clearly shows that at a lower concentration of FeNPs in the presence of a low external

magnetic field the relative triplet yield of Sgr molecule in CH_3CN medium is much higher than that in H_2O medium.

As described in the earlier section, the H-abstraction of Sgr molecule in H_2O medium from the matrix, without or with the addition of FeNPs produce a T-T absorption hump at 400 nm and that is supported well by the transient absorption spectra of Sgr molecule. That is not identical with those obtained in CH_3CN medium where the Sgr molecule undergoes H- abstraction from the CH_3CN medium in a more difficult way because of lack of stability of the geminate radical pair in absence of hydrogen bonding. Additional support in favour of hydrogen abstraction mechanism for the presence of two significant humps near 400 nm (individually at 395 and 420 nm) is in the T-T transient spectra as apparent from the recorded time delayed transient spectra (**Figure 4.12**). It is also evident from **Figure 4.12** that as the delay time between pump and probe pulse is increased between 0.5 to 4.9 μs , the corresponding intensity of humps responsible for the radical formation through H-abstraction also decay progressively.

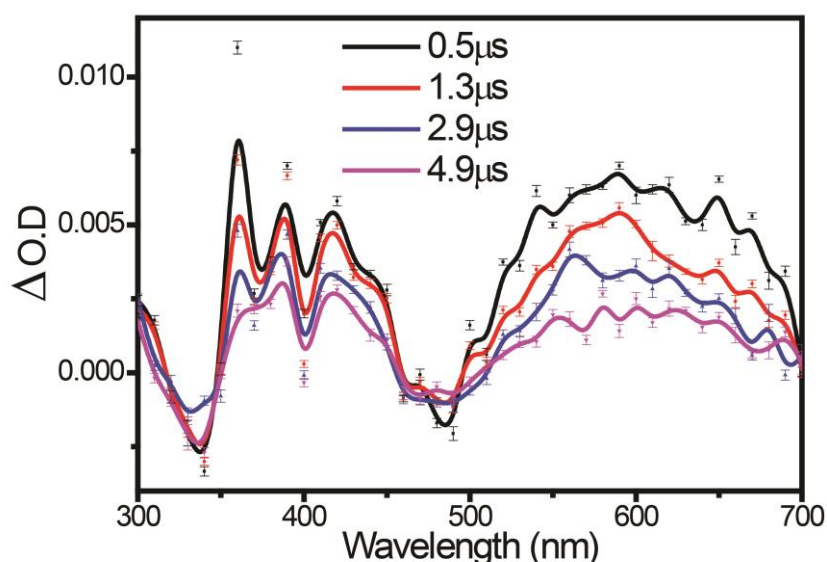


Figure 4.12: The plot of time-delayed transient (excited triplet state) absorption spectra of Sgr. The time delay between pump and probe pulse ranges between 0.5 to 4.9 μs .

To show the origin of two humps near 400 nm really come from effective H abstraction and not from the signal fluctuation, the T-T absorption spectra of Sgr have further been recorded in the absence of external magnetic field in H₂O medium at a higher resolution i.e 5 nm data point and that has been compared with the same, obtained at low-resolution, i.e 10 nm data point in the transient spectra, shown in **Figure 4.13 (A) and (B)**. The decrement of hump intensity with the increase of delay time and the persistence of humps near 400 nm at high-resolution T-T spectra directly shows that the obtained significant humps near 400 nm are the proof of transient species not initiated from noise; then they might have revealed the fluctuating nature instead of a gradual reduction.

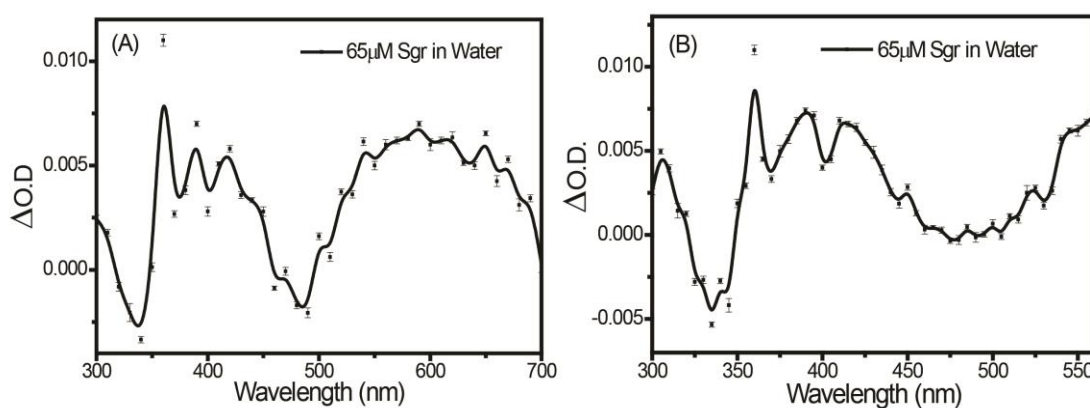


Figure 4.13: (A) The plot of low-resolution, i.e 10 nm data point and (B) high-resolution, i.e 5 nm data point, T-T absorption spectra of Sgr molecule in absence of magnetic field in H₂O medium with noticeable humps in the 400 nm region.

The solvent polarity and the hydrogen bonding ability of the neighbouring solvents show a key role in regulating the ultimate products. To find out the role of excited state and the corresponding lifetime for the photo-induced therapeutic activity, these experiments have been performed in H₂O as the solvent medium. Furthermore, to explore the importance of solvent polarity and the hydrogen bonding ability for effective spin-trajectory modulation, it has been compared with the results with three solvents: one is polar aprotic, i.e., acetonitrile (CH₃CN), one polar protic solvent, i.e., H₂O and another

solvent is ethanol. The polarity of EtOH is comparable with H₂O whereas the dielectric constant is comparable with CH₃CN. It has been observed that the radical formation is negligible in CH₃CN medium (**Figure 4.4.A₂**), moderate in EtOH medium (**Figure 4.14.**), and maximum with H₂O medium (**Figure 4.4.B₂**). The T-T absorption spectra of surface adsorbed Sgr molecules in C₂H₅OH medium in **Figure 4.14** explain the role of radical formation. To clarify the role of solvents with different polarity on a radical formation, MD calculations are done which showed that water can make a solvent cage surrounding Sgr molecule, which causes maximum hydrogen abstraction due to the formation of stable free radicals.

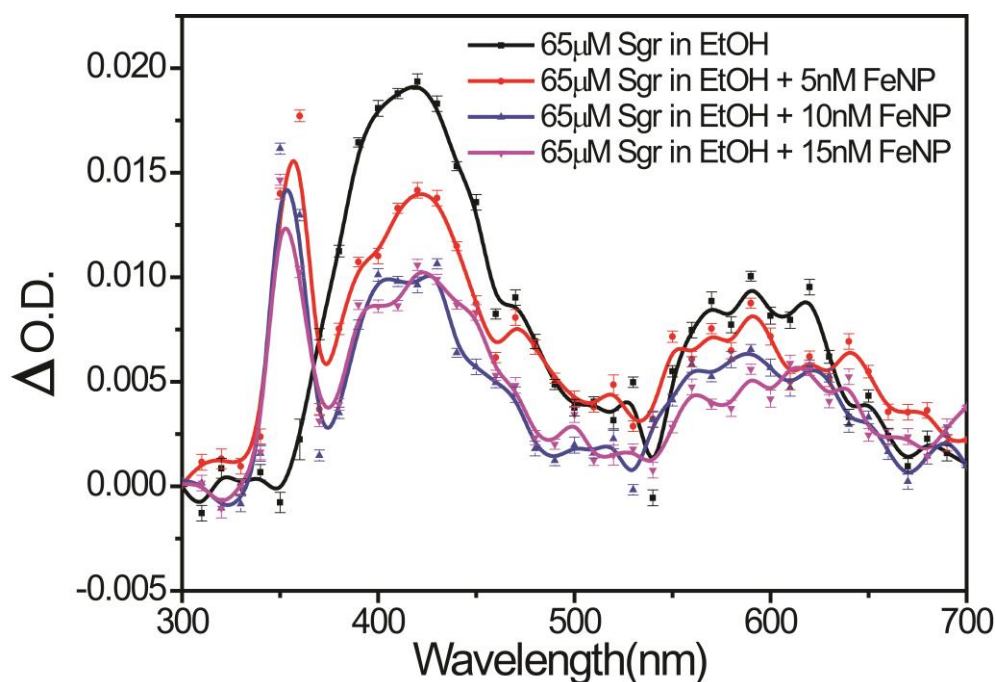


Figure 4.14: The plot of FeNP concentration-dependent T-T absorption spectra of surface adsorbed Sgr molecule in Ethanol medium.

Alternatively, in CH₃CN medium, the force developed due to Coulomb interaction is maximum, that favours the recombination of the geminate radical pair. In ethanol medium, although the van der Waals force is maximum, even then due to the lesser hydrogen bonding ability the stability of the individual radicals reduces, as the solvent cage

formed surrounding Sgr molecule is not as rigid like that formed by H₂O molecules. The contribution of both the van der Waals and Coulombic forces in the solvation of the Sgr molecule has been tried to be predicted by the MD simulation results. **Figure 4.15. A₁** displays the van der Waals interaction energy of the Sgr molecule with the solvents over the simulation time in a statistical ensemble. **Figure 4.15.A₂** illustrates the contribution of Coulombic energy in the solvation of the Sgr molecule. The time average data of both the van der Waals and Coulombic forces are plotted in **Figure 4.15.A₃** and enlisted in **Table 4.4**. The MD simulations results could highlight these dominant non-electrostatic forces in Sgr molecules solvation. The van der Waals interaction energy has been found to change significantly from solvent to solvent. Solvent cage formation has been observed in the trajectory shown in **figure 4.16**. H₂O molecules can form stable hydrogen bonded solvent cage surrounding the Sgr molecule but no significant caging is observed in the case of solvent EtOH. In contrast to that, CH₃CN being aprotic, solvent cage formation is not present. Such a solvent cage formed as a result of hydrogen bonding may further stabilize the aggregates of Sgr molecule. **Table 4.4.B** shows the H bonding tendencies of Sgr molecule with the solvents. It shows a significant number of H bonds formation with solvent H₂O. For most of the simulation time, Sgr molecule remains H bonded with H₂O whereas EtOH shows only a slight amount of hydrogen bonding transiently.

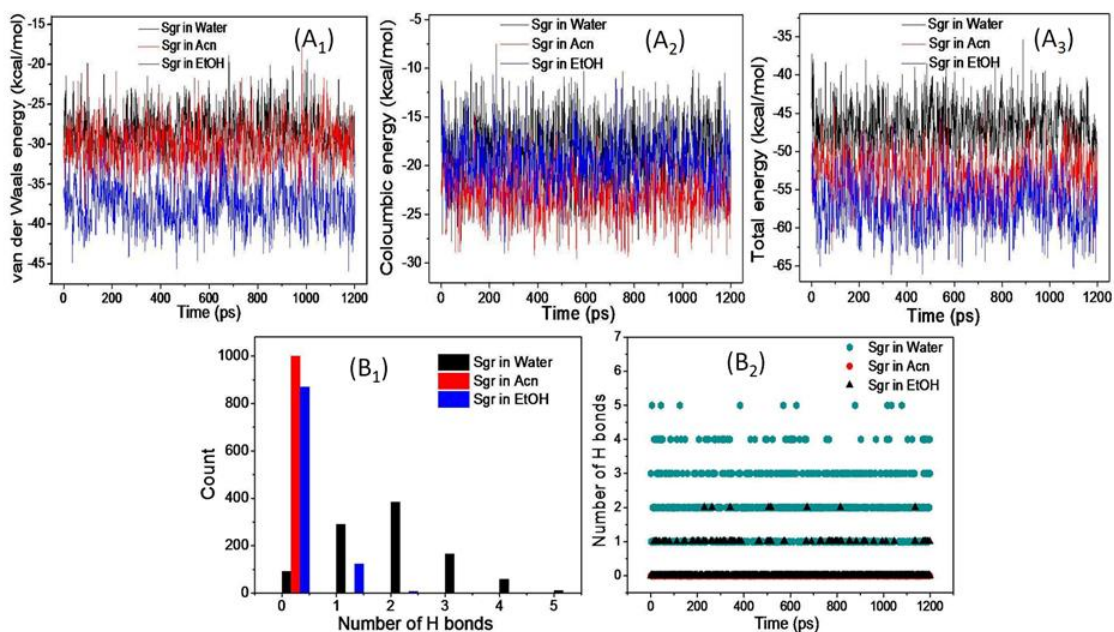


Figure 4.15: The plot of MD simulation to know the contribution from (A₁) van der Waals, (A₂) Coulombic, (A₃) total electrostatic and non-electrostatic forces in the solvation of Sgr molecule in different solvents, (B) Hydrogen bonding tendencies of Sgr molecule with the different solvents.

Table 4.4: Table showing the time-averaged energetics for different electrostatic and non-electrostatic forces in different solvents.

Solvents	van der Waals (kcal/mol) Mean SEM	Coulombic (kcal/mol) Mean SEM	Total (kcal/mol) Mean SEM
H ₂ O	-28.410.08	-18.39 0.11	-46.80 0.10
CH ₃ CN	-30.27 0.09	-22.89 0.08	-53.16 0.10
EtOH	-37.62 0.09	-19.62 0.09	-57.24 0.11

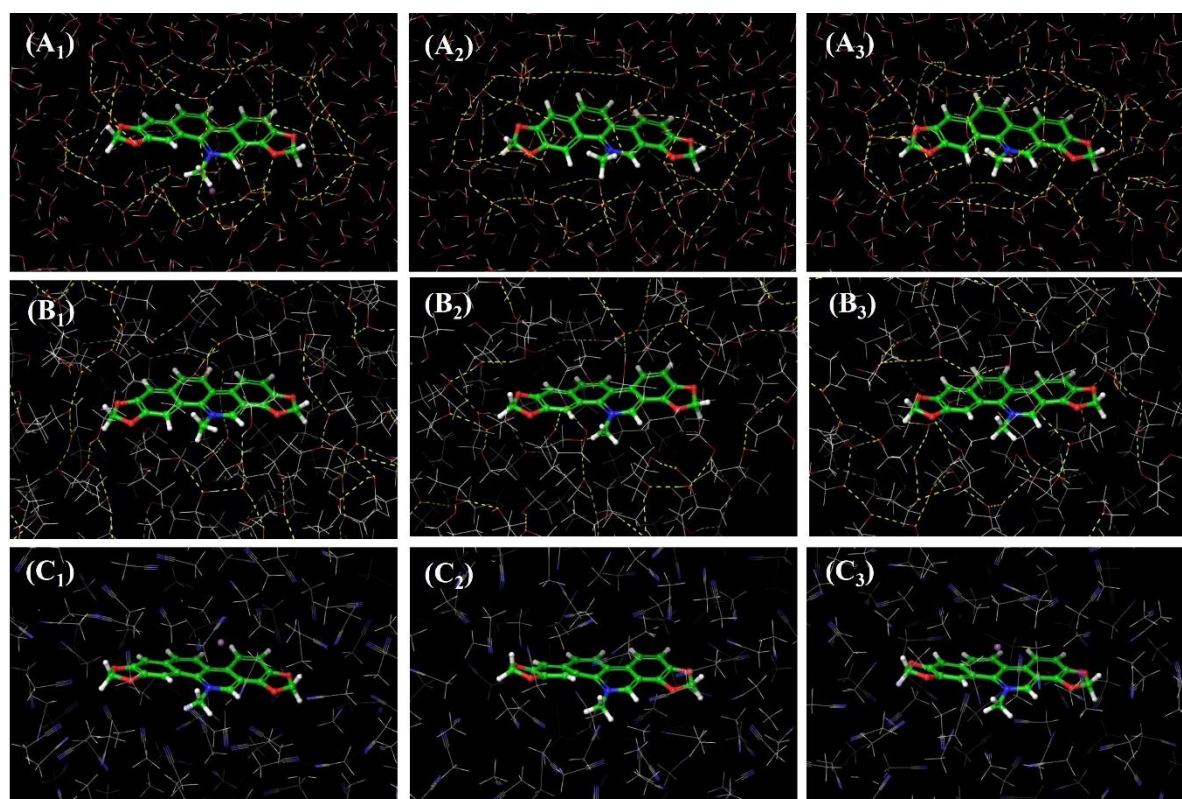


Figure 4.16: Solvent cage formation around Sgr in (A₁-A₃) H₂O, (B₁-B₃) EtOH and (C₁-C₃) CH₃CN medium 0, 600 and 1200 ps time frame.

The experimental observation supports facile hydrogen abstraction by Sgr from the protic solvent like H₂O (two significant humps near 400 nm (395 and 420 nm)) and moderate hydrogen abstraction from C₂H₅OH (humps with moderate intensity) while negligible abstraction from CH₃CN (humps with diminished intensity). In presence of lower concentration of FeNPs in H₂O medium under the influence of low external magnetic field (0.08T) it is observed that the absorbance around 400nm decreases, however there prevails the signature of overall increase in triplet yield throughout other wavelength regions as obtained in CH₃CN medium. As the stability of geminate radical (Sgr-H)··OH recombined state (S₁) is much more in H₂O medium, production of geminate radical pair (T₁) in the triplet state and the corresponding T-T transient absorbance at 400 nm shall always be low compared to that of CH₃CN medium as clearly seen from the experimental results (**Figure 4.7 A, B**). The decay profile for the radicals (by exciting them at 360 and

400 nm, that is close to the radical extinction maximum) of the excited triplet state of Sgr-FeNP complex in **Figure 4.6 A₂-A₃** and **Figure 4.6 B₂-B₃** shows marked reduction in energy relaxation (i.e. increment in triplet lifetime) in the presence of an magnetic field in CH₃CN medium. In other words, the applied external magnetic field can change the spin trajectorial fate of the solvent dynamics by selectively stabilizing either the geminate radical pair or the geminate recombinant. When Compared to CH₃CN medium, in the presence of lower concentration of FeNP, the decay profile in H₂O medium exhibits no significant change in triplet lifetime on application of a magnetic field perhaps due to the greater stability of the geminate recombined state in H₂O which helps the magnetic field induced singlet-triplet interconversion ($S \leftrightarrow T$) following the radical pair mechanism, this indicates that if the spin correlation of the geminate radical pair is of singlet type, then on application of a magnetic field the corresponding triplet yield, i.e., formation of free radical, will decrease. However, in the presence of an excess quantity of FeNP, enhancement of triplet yield of Sgr through the L-S coupling outweighs over the decrease in free radical formation by a radical pair mechanism. Therefore, an overall increase in triplet-triplet absorption of Sgr is seen in the presence of FeNP as depicted in **Figure 4.7B₃**. Also a high magnetic field induction within the single domain ferrimagnetic nanoparticle (or boundary-less paramagnetic nanoparticle) shall act as a superparamagnetic nanosurface under the influence the switchable on-off spin rephasing of the surface adsorbed molecules by highly efficient spin-orbit (L-S) coupling to control their overall transient spin trajectory distribution with a significantly measurable contribution from solvent polarity. This high throughput spin-trajectory modulation can find several useful applications such as electron-hole recombination in organic conductors,^{352, 353} molecular state lifetime to control the drug release efficiency, radical reactions and their separation even their stability which controls crucial biochemical reactions.

4.3. Conclusions:

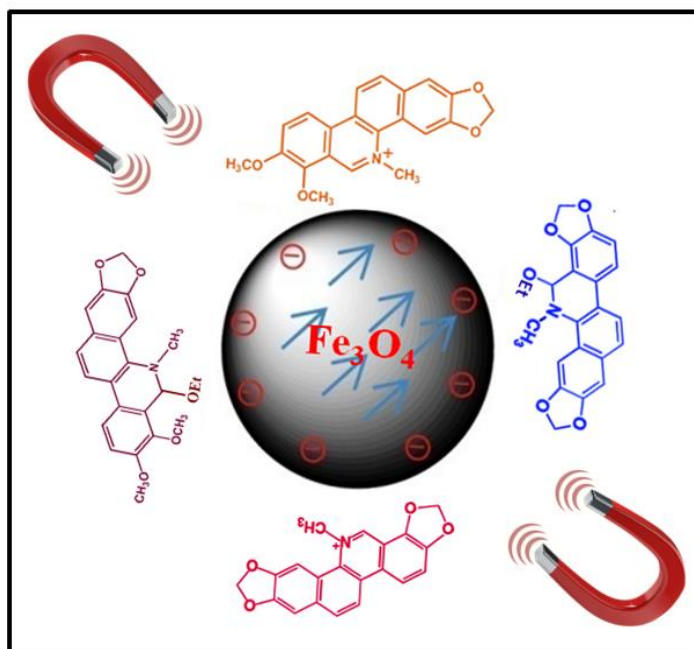
The effective manipulation of the excited state transient spin trajectory of a surface adsorbed molecular (here Sgr) system can easily be done by utilizing a low external magnetic field (less than 0.1 T) induced single-domain magnetic moment alignment of the constituent atoms on a ferrimagnetic single crystalline nanoparticle surface that will act like a magnetic memory-less superparamagnetic particle which is programmable with ability of magnetic field ON-OFF switching. Found results clearly show that the high-field-induced L-S coupling with a significantly measurable contribution from solvent polarity can control the overall transient spin trajectory distribution. Relative spin trajectory distribution and its resultant modulation not only depend on the localized large magnetic field strength but can also be fine-tuned by controlling the solvent polarity and the hydrogen bonding induced solvent stabilization. Obtained results also provide one of the rare experimental observations of transient spin trajectory modulation in differential magnetic field strengths in a nearfield configuration.

CHAPTER-5

Differential Photophysical Behaviour of the Iminium and Alkanolamine form of Chelerythrine and Sanguinarine on Superparamagnetic Nano surface

Outline: Points to be discussed

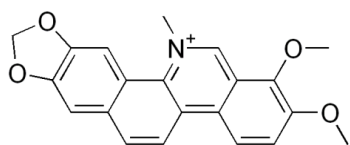
- ❖ Superparamagnetic nanosurface modulated photophysics of the iminium and alkanolamine form of chelerythrine.
- ❖ The comparative excited state photophysical study of the iminium and alkanolamine form of chelerythrine and sanguinarine.
- ❖ Theoretical explanation of the obtained result.



5.1 Introduction:

In the previous chapter (**Chapter-4**) an interesting excited state photophysical pathway modulation have been shown of the prototype anticancer drug sanguinarine (Sgr) in presence of the Fe_3O_4 nanosurface. There it has been shown that a large magnetic field antenna can be generated by a single domain superparamagnetic Fe_3O_4 nanosurface in presence of a low external magnetic-field (0.08T) on the nanosurface adsorbed molecules. The magnetic nanosurface can enforce the transient spin-trajectory modulation through $S_1 \rightarrow T_1$ interconversion of surface adsorbed sanguinarine (Sgr) molecule, through the enhanced population of the spin-rephased component in the triplet nondegenerate state. The superparamagnetic moment helps to achieve the lowest potential energy between Sgr and Fe_3O_4 nanoparticle by orienting their magnetic moment in the same direction instead of the random angle in presence of external low (0.08T) magnetic field for the favourable orientation to assist the projected spin interconversion.²³⁹

In this chapter, the photophysics of another anticancer drug chelerythrine (Chel) has been studied. Chel and Sgr are very much similar in their structure and a functional group, but Chel differs from Sgr in its structural rigidity. Chel is more flexible than Sgr due to its open alkyl chain, unlike Sgr which has closed five-membered group at the end.



Molecular Structure: Chelerythrine (1,2-dimethoxy-12methyl[1,3]benzodioxolo[5,6-c]phenanthridin-12-ium)

Chel is also a natural benzophenanthridine alkaloid like Sgr and it has a strong nucleic acid binding ability.^{230, 354, 355} It can exist as a positively charged iminium form and neutral alkanolamine form.³⁵⁴ The charged iminium form is the nucleic acid binding moiety³⁵⁴ and

the neutral alkanolamine form has the affinity to functional proteins.³⁵⁴ Chel has anticancer activity³⁵⁶⁻³⁵⁸ and it is a potent, selective and cell-permeable protein kinase C inhibitor *in vitro*.^{225, 359, 360} Along with these, it has inhibitory effects on various tumours.^{361, 362} It has been shown to induce necroptosis in TSC₂-deficient cells through a novel oxidative stress-dependent mechanism or via formation of free radicals with unpaired spin.³⁶³

In recent time with the advent of nanotechnology, nanoparticles are extensively used as a smart carrier of several important molecules or drugs. The nanoparticle-based drug delivery systems are used to alter drug distribution, target desired cells and control the release of chemotherapeutic drugs. The nanoparticles can be effectively designed to be either passive or active targeting agent.³⁶⁴⁻³⁶⁶ The magnetic nanoparticles (FeNPs), especially superparamagnetic iron oxide nanoparticles (Fe₃O₄), can offer a favourable platform for drug targeting under the effect of external magnetic field and have shown great potential applications as drug carrier in cancer therapeutics towards the improvement of their therapeutic efficacy.³⁶⁷⁻³⁷² Cao, L. *et al.* have used Fe₃O₄@OCMCS-Chel as an active tumour-targeting system where magnetic Fe₃O₄@OCMCS nanoparticles act as the carrier and Chel as the model anti-tumour drug.³⁷³ It is also reported that the Chel and Fe₃O₄ loaded multi-walled carbon nanotubes (Fe₃O₄/MWNTs-Chel nanocomposites) can target hepatocytes when treating malignant tumours.³⁷⁴ In addition to that the *in vitro* cytotoxicity studies of Chel revealed that the Fe₃O₄/MWNTs-Chel nanocomposites showed an efficient inhibition rate to HepG₂ cell line and exhibited lower cytotoxicity to LO₂ cell line in comparison to the native Chel.³⁷⁵ Therefore, the multifunctional Fe₃O₄-Chel nanocomposites should be a useful and promising candidate for the treatment of malignant tumours.³⁷⁶

Now to understand the action of a drug attached with a nanosurface it is very important to know the actual mechanistic pathways. In this chapter, the main target is the

excited state photophysical pathway of Chel upon laser irradiation on magnetic nanomaterial Fe_3O_4 surface. It is very interesting to observe that the two isomeric forms i.e., the iminium and the alkanolamine form of Chel differ much in their drug activity. Moreover, despite being similar in structure and functionality between Chel and Sgr, they differ much in their drug activity.^{220, 375-379} As they are anticancer drugs and well known to work via reactive oxygen species (ROS) generation³⁸⁰⁻³⁸³ and ROS are the species with unpaired spin, therefore, the spin dynamical study of the molecules becomes very important for developing knowledge on the working principle of the drug on nanocarrier surface upon laser irradiation. In this chapter, I have discussed the difference between the excited state photophysical pathways of the iminium and alkanol amine forms of Chel on Fe_3O_4 surface in water and ethanol medium. Moreover, a comparative study supported by DFT calculations has been attempted to find out the role of structural rigidity of molecules on their photophysical pathways.

5.2 Results and Discussion:

It has been mentioned earlier that Chel exists in two forms, the iminium form and the alkanolamine form. The iminium form predominates over the alkanolamine form in water (H_2O) whereas the reverse is true in ethanol (EtOH) (**Fig 5.1**).³⁸⁴

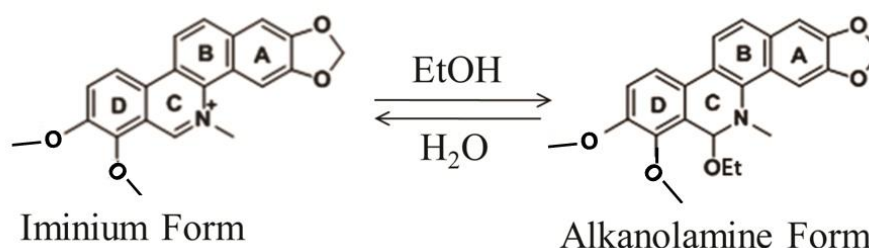


Figure 5.1: The iminium and alkanolamine form of Chel in H_2O and EtOH medium respectively.

H_2O and EtOH both are polar and protic solvents. However the dielectric constant of H_2O ($\epsilon=80.1$) is quite higher than EtOH ($\epsilon=24.5$). On the other hand, the hydrophobicity of

ethanol is greater than water. **Figure 5.2** depicts the UV-Vis absorption spectra of Chel in H₂O and EtOH respectively which support the predominance of iminium or alkanolamine form in the respective solvent. For the presence of iminium form in water, the absorption maxima come around 267 nm, 316 nm, and 338 nm along with a broad peak centred on 420 nm. On the other hand, the absorption spectrum of alkanolamine form, which predominates in ethanol, lacks the small hump at 338 nm. With a lower concentration of Chel (below 5 μ M) the broad hump around 410 nm appears, however with an increase in concentration a broad hump centred around 420 nm and grows up subsequently. The broad hump near 420 nm is from the aggregation or dimer formation of the molecules at higher concentration. It is reported earlier that these group of molecules can form dimer.³⁸⁵

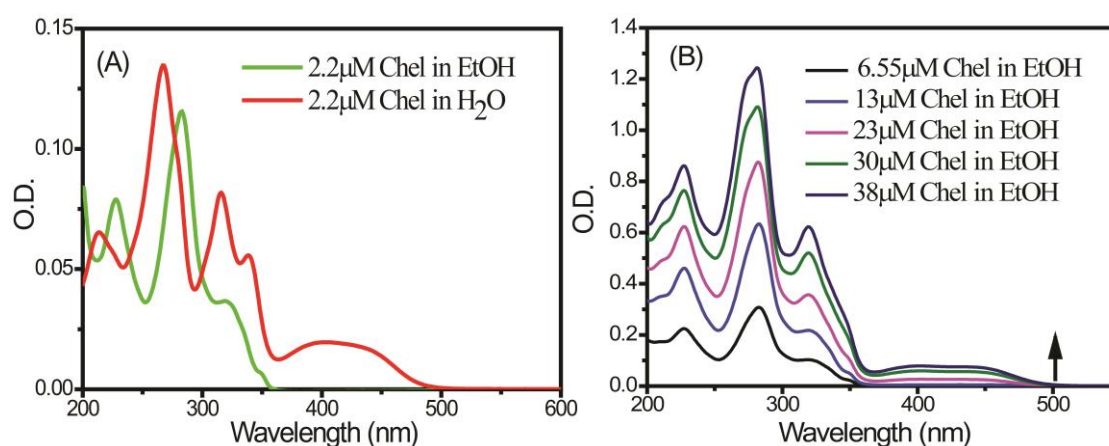


Figure 5.2: UV-Vis absorption spectra (A) of the iminium and the alkanolamine form of Chelerythrine (Chel) in H₂O and EtOH medium (B) with increasing concentration of the drug in EtOH medium.

Figure 5.3 shows the fluorescence spectra of Chel in H₂O and EtOH with a low concentration of Chel (5.0 μ M) where excitation wavelength is 340 nm. With a lower concentration of Chel, a single fluorescence peak appears around 440 nm and 586 nm for the alkanolamine and the iminium form in the EtOH and H₂O medium respectively.

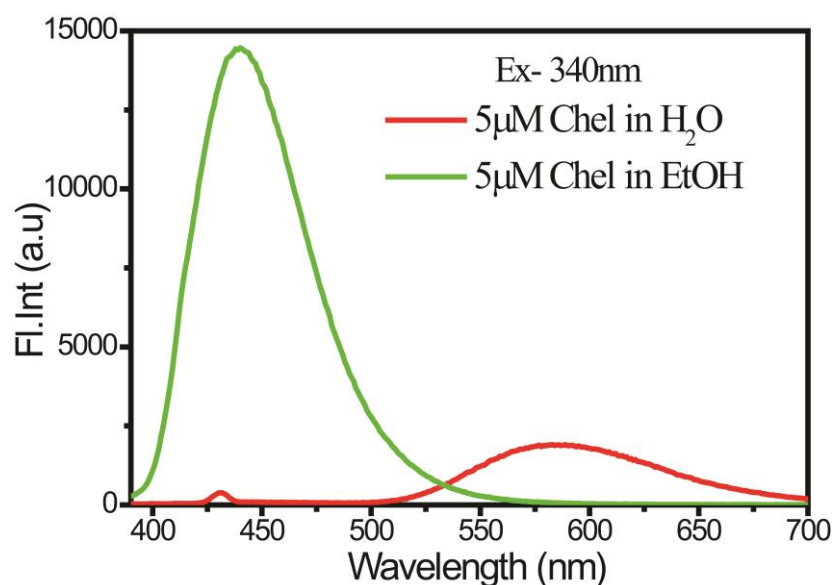


Figure 5.3: The fluorescence spectra of Chel in H₂O and EtOH medium at lower concentration (5 μM).

However, with the increase in the concentration of Chel (after 14.5 μM) in ethanol, the rising peak around 440 nm starts diminishing with the generation of a new peak around 560 nm and an isoemissive point at 495 nm. The fluorescent species at 560 nm also supports the dimer formation of Chel and the isoemissive point is representing the equilibrium between the two forms. However extensive spectroscopic work has not been reported earlier on this aspect.

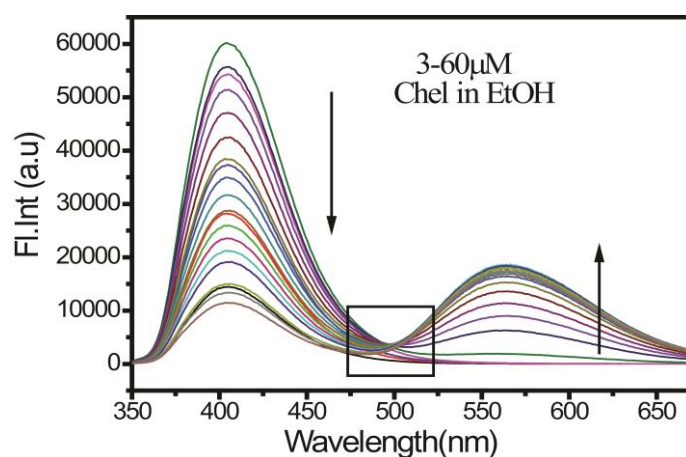


Figure 5.4: Change of fluorescence spectra on increasing the concentration of Chel from 5 μM to 60 μM in EtOH medium.

Therefore, for clarification, the corresponding fluorescence lifetime has been measured of Chel in ethanol medium with increasing concentration. However, **Table 5.1** depicts that the fluorescence lifetime of Chel does not change with its increasing concentration.

Table 5.1: Fluorescence lifetime of Chel on increasing the concentration of the drug in EtOH medium.

Chelerythrine	τ_1 (ns)	τ_2 (ns)
11 μ M	2.77	-
22 μ M	2.77	4.12
33 μ M	2.77	4.113
50 μ M	2.74	4.119

Therefore, it is inferred that the dimerization of Chel occurs in its ground state and not in the excited state.

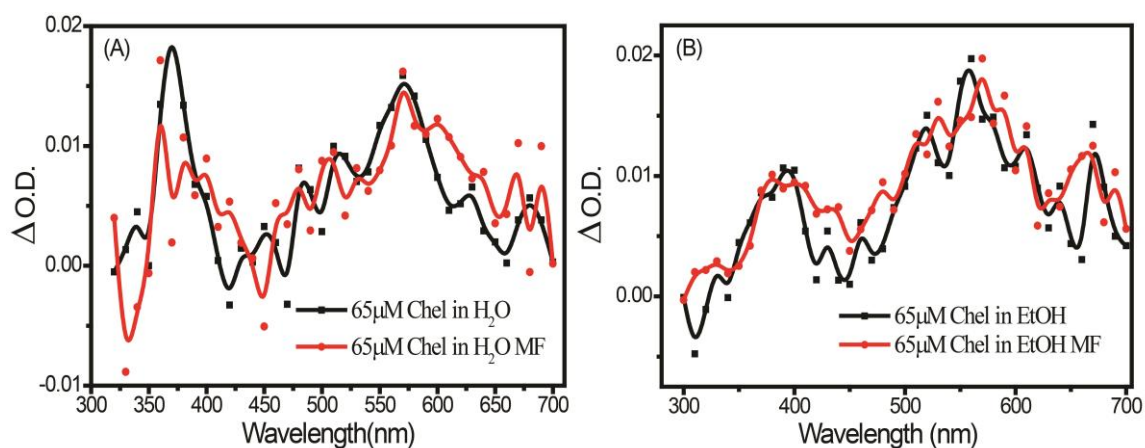


Figure 5.5: The triplet-triplet absorption spectra of Chel in (A) H₂O and (B) EtOH medium respectively in presence and absence of external magnetic field.

Now it has been reported that the Chel type of molecules (e.g., Sgr) can undergo hydrogen or hydroxyl radical abstraction from H₂O or EtOH forming a geminate radical pair²³⁹ with

triplet spin configuration ($\text{ChlOH}\bullet\uparrow\uparrow\bullet\text{H}(-\text{OH})$) or ($\text{ChlOEt}\bullet\uparrow\uparrow\bullet\text{H}(-\text{OEt})$). Formation of triplet radical pair is supported by its transient absorption spectrum (**Figure 5.5**) where the absorbance around 420 nm and 620 nm increases in presence of a low magnetic field (~ 0.08 Tesla), compared to that in absence of magnetic field. In the previous chapter it has been reported that the stability of the radical pair is lesser in ethanol compared to water for benzyloquinoline group of alkaloids, e.g., sanguinarine, etc. due to the difference in hydrogen bonding ability and solvent cage formation to stabilize the produced radicals. The same is true for Chel also as obtained from the theoretical observation (**Fig 5.6**).

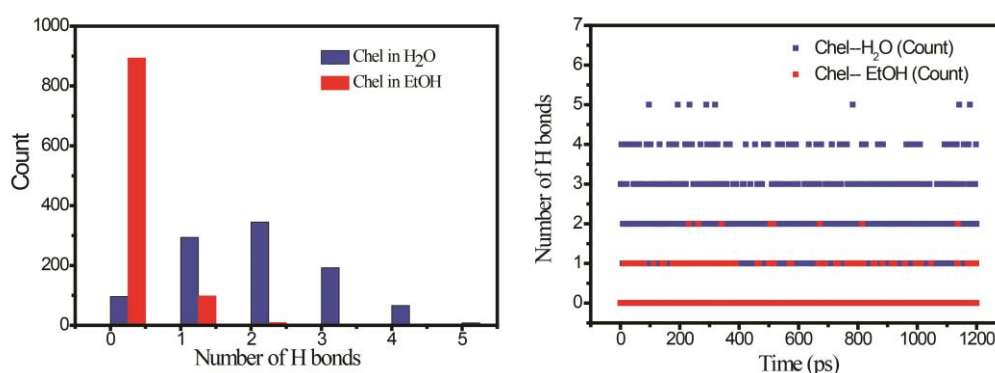


Figure 5.6: Changes in the number of H bonds with solvents (H₂O and EtOH) over time.

5.2.1 Complex formation between Chel and superparamagnetic Fe₃O₄ nanosurface and its stability to govern the transient spin-trajectory followed by photoexcitation

On addition of 10 nm sized citrate-capped superparamagnetic Fe₃O₄ nanoparticle, as synthesized using a reported protocol²⁴², the fluorescence intensity of Chel quenches but without any change in fluorescence lifetime in both the solvent, which depicts (**Figure 5.7**) that both the iminium and alkanolamine form of Chel becomes associated with FeNPs in the ground state.

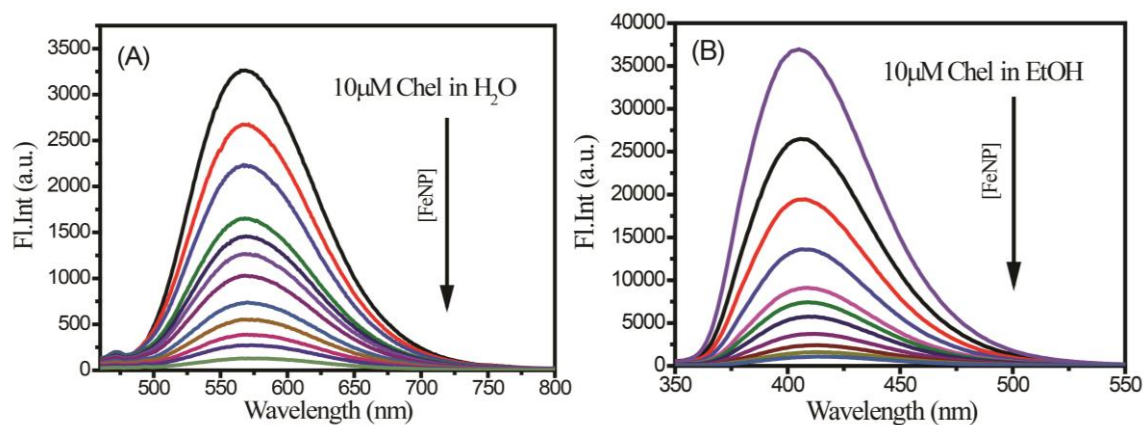


Figure 5.7: Quenching of fluorescence intensity on gradual addition of FeNP in (A) H₂O and (B) EtOH medium respectively.

Quenching of fluorescence intensity indicates the reduction of singlet yield in presence of FeNP which in turn decreases the triplet yield. Like singlet fluorescence yield the triplet yield of Chel also reduces in presence of FeNPs in both the solvents (**Figure 5.8**).

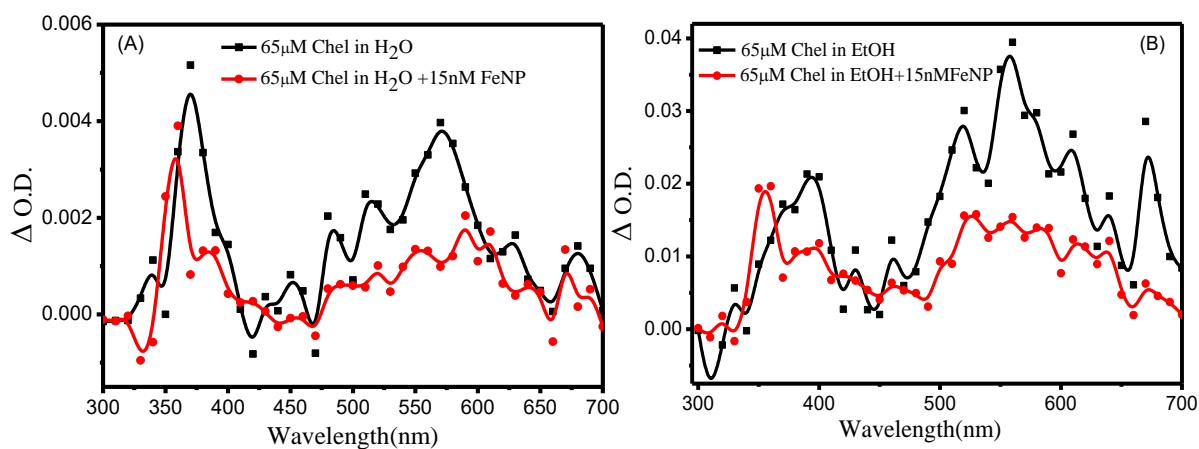


Figure 5.8: FeNP concentration-dependent T–T absorption spectra of surface adsorbed Chel in (A) H₂O and (B) EtOH respectively.

However, on the application of an external magnetic field, the triplet yield of Chel attached with Fe₃O₄ increases, but only in H₂O and not in EtOH (**Figure 5.9**). There is no significant change in triplet yield of Chel on Fe₃O₄ surface in presence of magnetic field when it is dissolved in ethanol. In presence of the external magnetic field, the magnetic moment aligned large-field superparamagnetic field on FeNPs can orient Chel molecules attached

on nanosurface towards the direction which favours singlet-triplet interconversion ($S \leftrightarrow T$) preferably while Chel is caged by water molecules. Therefore, the transition from ground singlet to excited singlet state followed by intersystem crossing to a corresponding triplet state is enhanced which increases the triplet-triplet absorption of Chel associated with FeNPs in presence of an external magnetic field. But if the competition between the radical pair mechanism and L.S coupling based mechanism is considered then the iminium form is expected to show lesser triplet yield than the alkanolamine form.

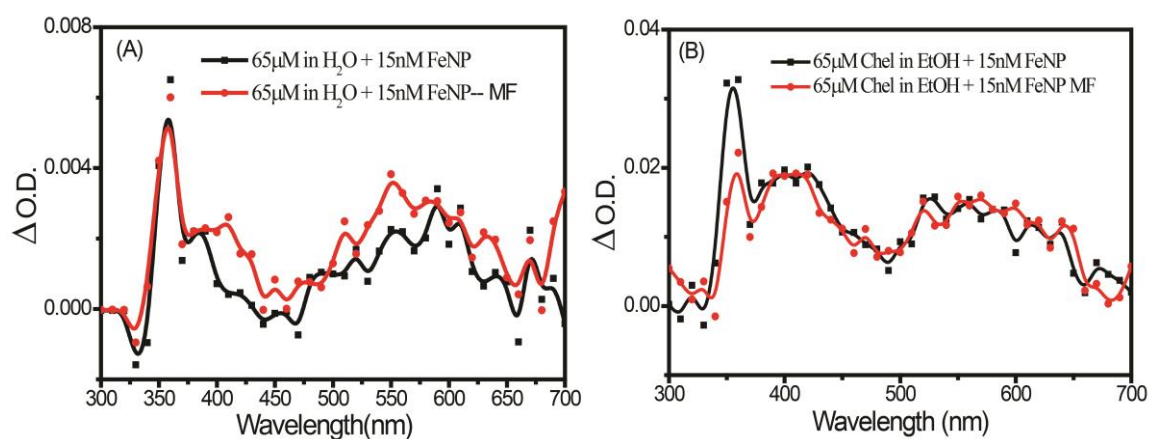


Figure 5.9: Excited state transient absorption spectra of Chel on FeNP nanosurface in (A) H_2O and (B) EtOH medium respectively.

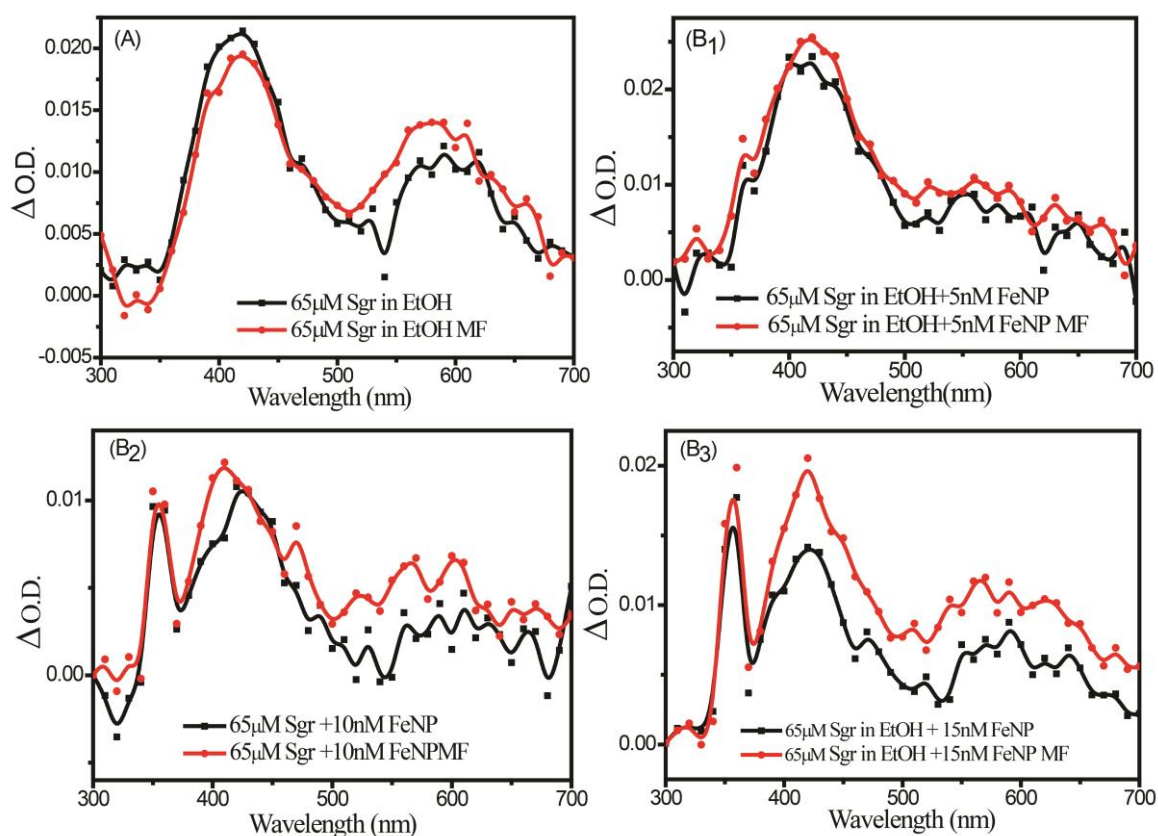


Figure 5.10: Excited state transient absorption spectra of (A) Sgr in ethanol medium, Sgr on FeNP surface at (B₁) 5nM (B₂) 10nM and (B₃) 15nM concentration.

It is also quite surprising to note that although sanguinarine (Sgr) belongs to the same group of Chel, i.e. benzyloquinoline, however in the presence of external magnetic field the extent of $S \leftrightarrow T$ interconversion, hence the increase in overall triplet yield, is lesser for Chel compared to Sgr attached on the FeNP surface in EtOH medium (**Figure 5.10**). The DFT calculations are carried out to find out whether the difference in geometry between the molecules is responsible for such discrepancy.

5.2.2 MD Simulation to understand the role of difference in geometry between the molecules on the extent of $S \leftrightarrow T$ interconversion

Radical formation in different solvents optimized geometries of Chel (iminium) and Sgr (iminium) along with their dipole orientation is shown in **Figure 5.11** and **Figure 5.12**.

The dipole moment vectors are shown with a red arrow. In Chel, the dipole vector is out of the plane whereas, in Sgr, dipole vector is in the plane of the molecule.

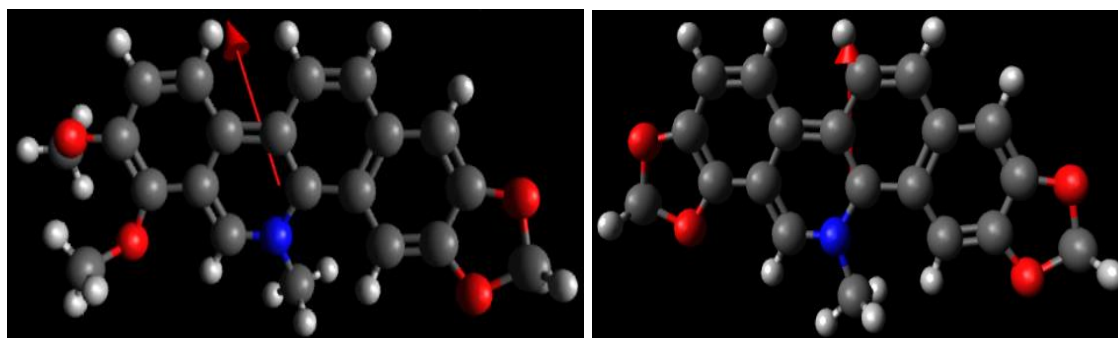


Figure 5.11: Optimized geometries of Chel (left) and Sgr (right).

In the alkanolamine forms, the dipole vector was found to be projected out of the plane (Figure 5.11).

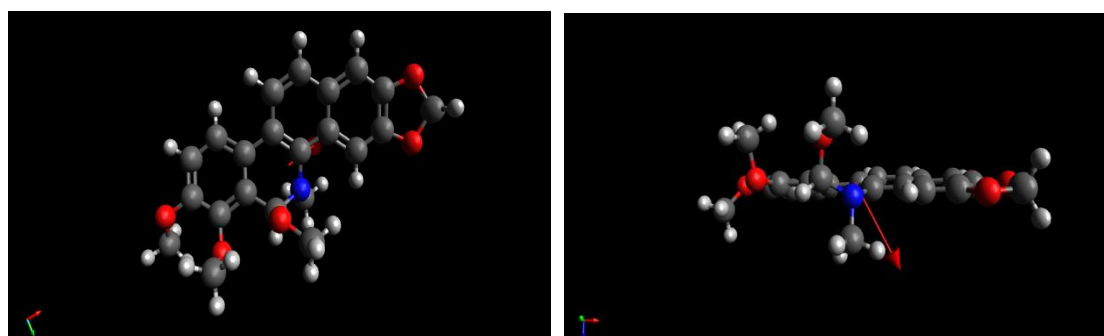


Figure 5.12. Optimized geometry of the alkanolamine form of Chel (top view in the left and side view in the right). The dipole vector is shown with the red arrow.

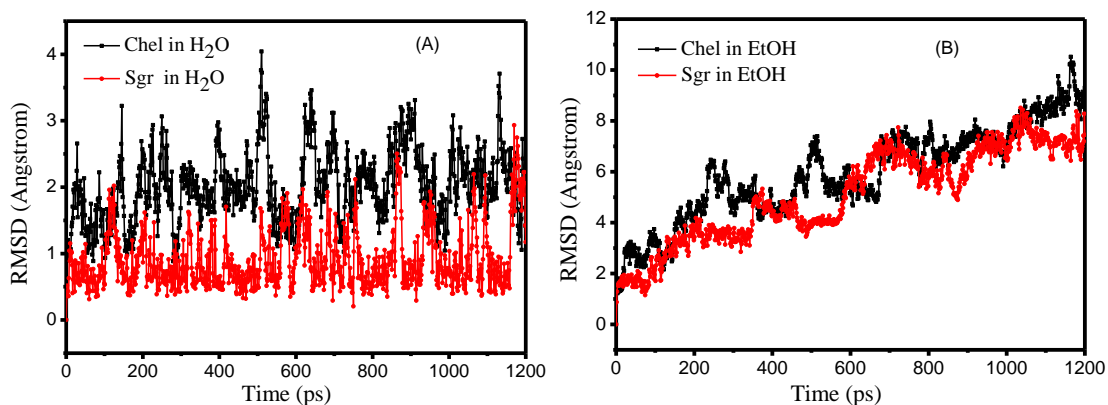


Figure 5.13. Root mean square deviations of Chel (black) and Sgr (red) dimers in H₂O (A) and EtOH (B) during MD simulation. In H₂O Chel and Sgr is in iminium form whereas, in EtOH, Chel and Sgr are in alkanolamine form.

Based on the dipole orientation, dimers of the molecules were constructed in Maestro and subjected to molecular dynamics simulation in H₂O and EtOH medium. **Figure 5.13** shows the structural fluctuations of Chel and Sgr dimers in the solvents. Structural changes of the Chel (iminium) and Sgr (iminium) dimers in H₂O medium with time may also be visualized in **Figure 5.14**. From this result, it is evident that both Sgr and Chel form a dimer in a ground state. Therefore, in presence of FeNP, a monomer, as well as dimer forms of both the molecules, may reside on the FeNP surface.

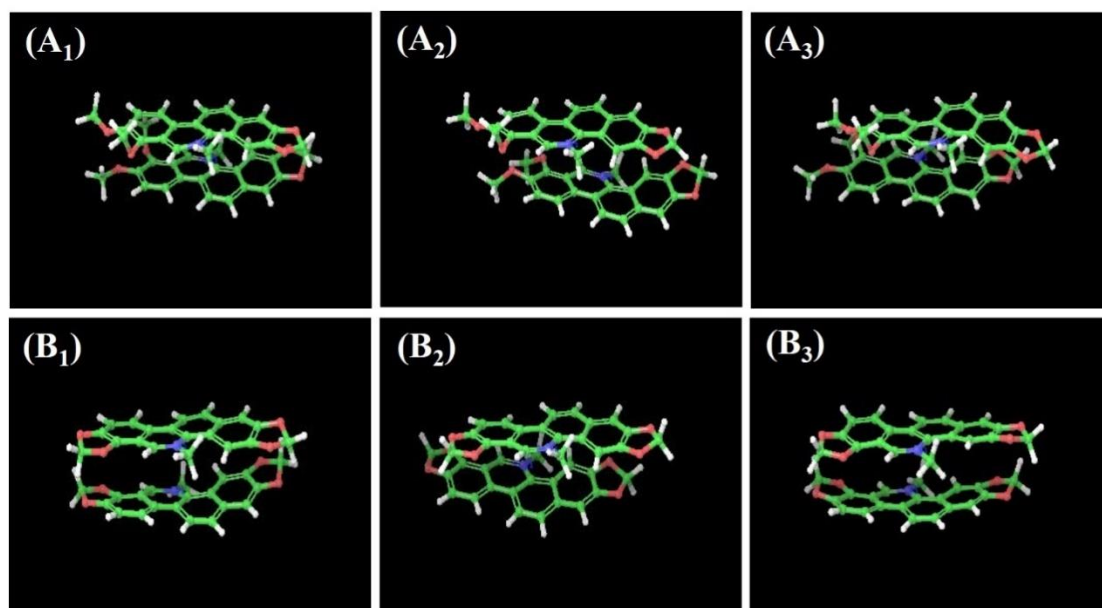


Figure 5.14. Structural changes of the Chel iminium dimer (A₁-A₃) and Sgr iminium dimer (B₁-B₃) in H₂O medium at 0, 600 and 1200 ps time frame.

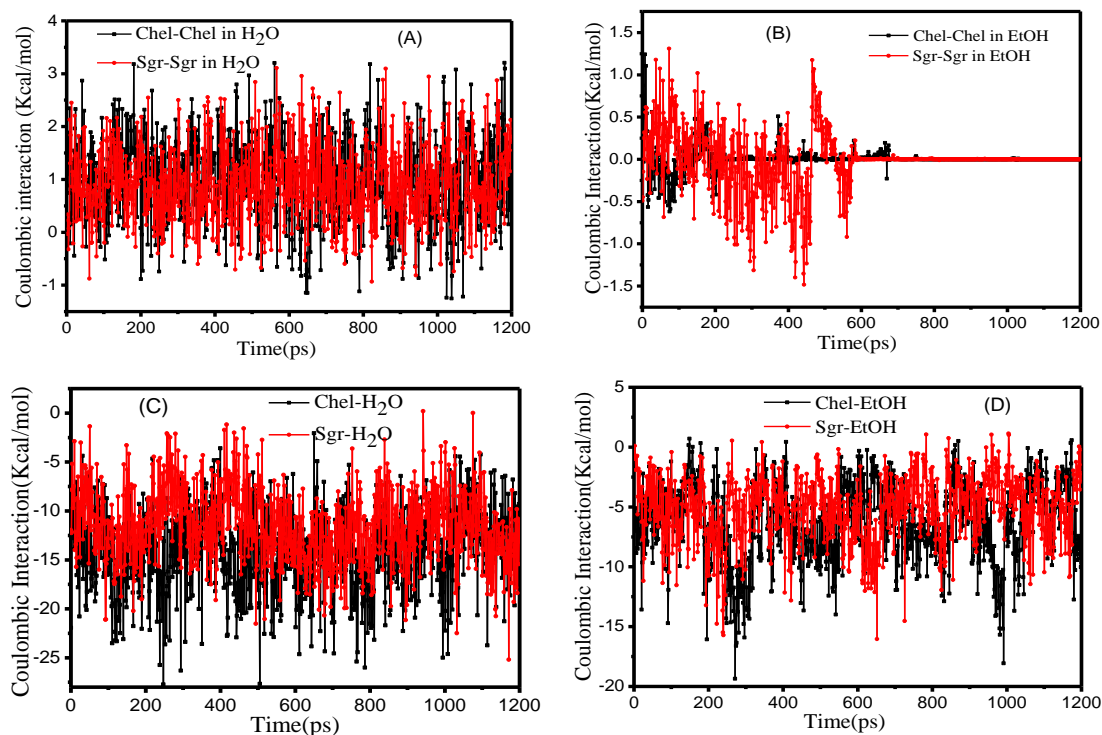


Figure 5.15. (A) Coulombic energy for Chel and Sgr (iminium) dimer formation in H₂O medium, (B) Coulombic energy for Chel and Sgr (alkanolamine) dimer formation in EtOH medium. Energy converges to zero as the dimer eventually breaks down. (C) Coulombic energy for the interaction of Chel and Sgr (iminium) with solvent H₂O, (D) Coulombic energy for the interaction of Chel and Sgr (iminium) with solvent EtOH.

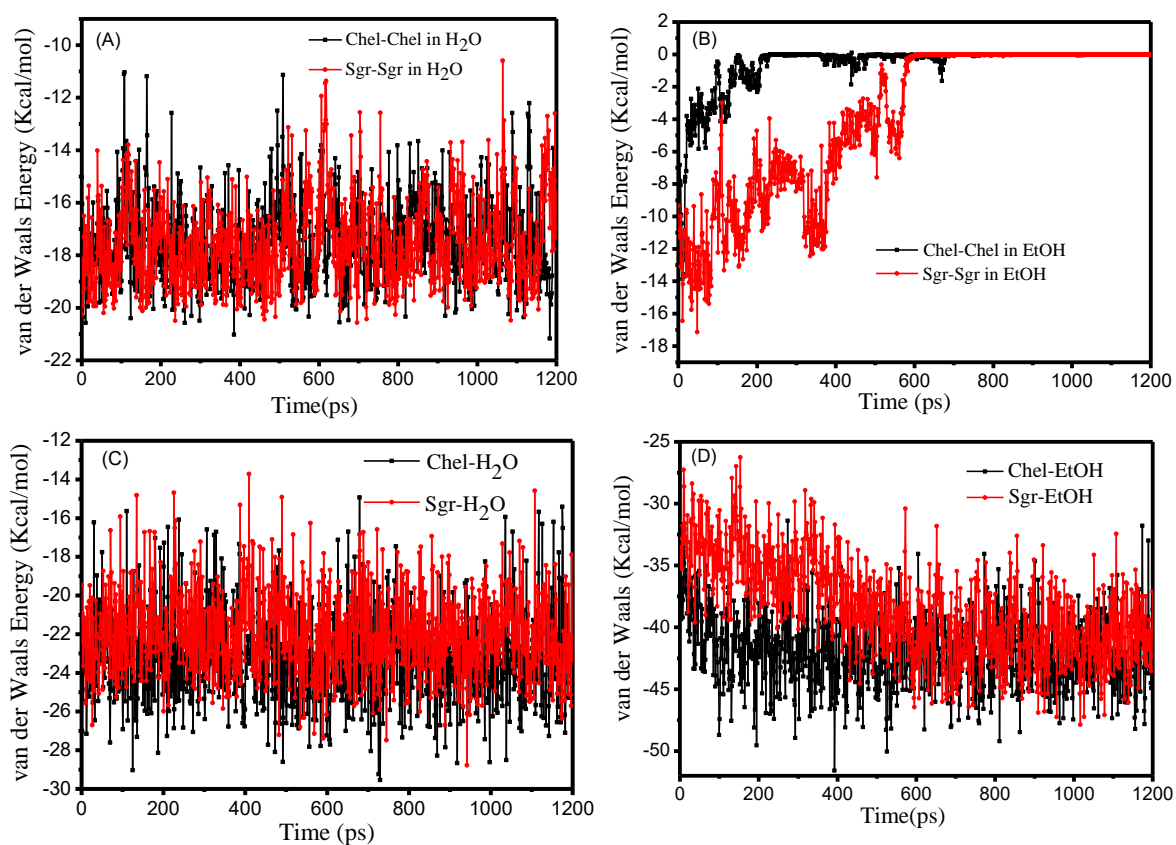


Figure 5.16: (A) van der Waals energy for Chel and Sgr (iminium) dimer formation in H₂O medium. (B) van der Waals energy for Chel and Sgr (alkanolamine) dimer formation in EtOH medium, Energy converges to zero as the dimer eventually breaks down. (C) van der Waals energy for the interaction of Chel and Sgr (iminium) with solvent H₂O. (D) van der Waals energy for the interaction of Chel and Sgr (iminium) with solvent EtOH.

Mean energy and standard deviation and significance of mean differences are given in the table:

Table 5.2: Solute-solute and solute-solvent interaction energies for Chel and Sgr in H₂O (iminium forms).

Interaction with	Chel (Energy in Kcal/mol)	Sgr (Energy in Kcal/mol)	T-test (p-value) (Energy in Kcal/mol)	Remarks
Solute (Coulombic)	0.98±0.09	0.92±0.08	0.04	Significant
Solute (vdW)	17.47±0.12	17.54±0.10	0.34	Not significant
Solute (total)	16.49±0.11	16.62±0.09	0.08	May not be significant
Solvent (Coulombic)	15.39±0.12	13.63±0.14	2.80E-27	Very Significant
Solvent (vdW)	23.78±0.11	22.82±0.12	8.42E-21	Very Significant
Solvent (total)	39.17±0.09	36.45±0.11	2.42E-63	Very Significant

Table 5.3: Solute-solute and solute-solvent interaction energies for Chel and Sgr in EtOH (alkanolamine forms).

Interaction with	Chel (Energy in Kcal/mol)	Sgr (Energy in Kcal/mol)	T-test (p- value) (Energy in Kcal/mol)	Remarks
Solvent (Coulombic)	-6.30±0.11	-4.50±0.08	5.45E-17	Very Significant
Solvent (vdW)	-42.30±0.09	-40.74±0.07	2.89E-14	Very Significant
Solvent (total)	-48.60±0.10	-45.24±0.11	9.65E-27	Very Significant

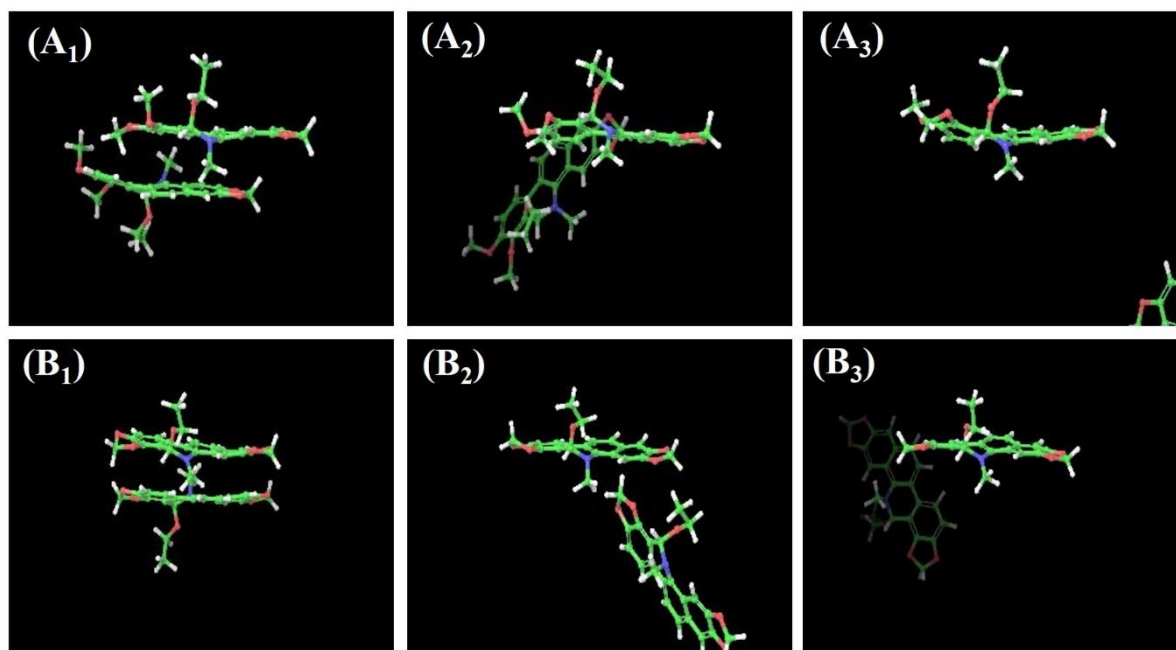


Figure 5.17. Chel alkanolamine (A₁-A₃) dimers and Sgr alkanolamine (B₁-B₃) dimer in ethanol medium at 0, 600 and 1200 ps time frame.

The dissolution and dimer formation energies (solute-solute and solvent-solute interaction energies) for Chel (iminium) and Sgr (iminium) are shown in **Figure 5.15**, **Figure 5.16**, **Figure 5.17** and **Table 5.2 & 5.3**. Although the solute-solute interactions in both the dimers are almost comparable, however, the solute-solvent interaction of Chel dimer, which predominates over Sgr dimer as well as the flexibility of Chel which is greater compared to that of Sgr, make Chel unstable on the FeNP surface in presence of a solvent. That is why the triplet yield of Chel is less compared to that of Sgr (described in **Chapter 4**) in water medium also for the same concentration (15 nM) of FeNP. On the other hand, although the dimer of the alkanolamine form of both the molecules is not very stable in ethanol (**Figure 5.17**), in the comparison between the two, Sgr dimer remains stable longer than Chel dimer in ethanol. Therefore, in presence of an external magnetic field, the orientation of Sgr molecule towards magnetic moment remains aligned for a longer time than Chel. This

phenomenon leads to much more singlet to triplet transitions for Sgr molecule compared to Chel.

5.3 Conclusion:

In conclusion from the above study it can be inferred that the orientation of molecular dipole, flexibility in the molecular structure, dimerization type of phenomena can influence the overall field effect exerted by a superparamagnetic nanosurface on its surface adsorbed molecule and can manipulate the excited state photophysical pathway and hence the extent of the $S \leftrightarrow T$ interconversion.

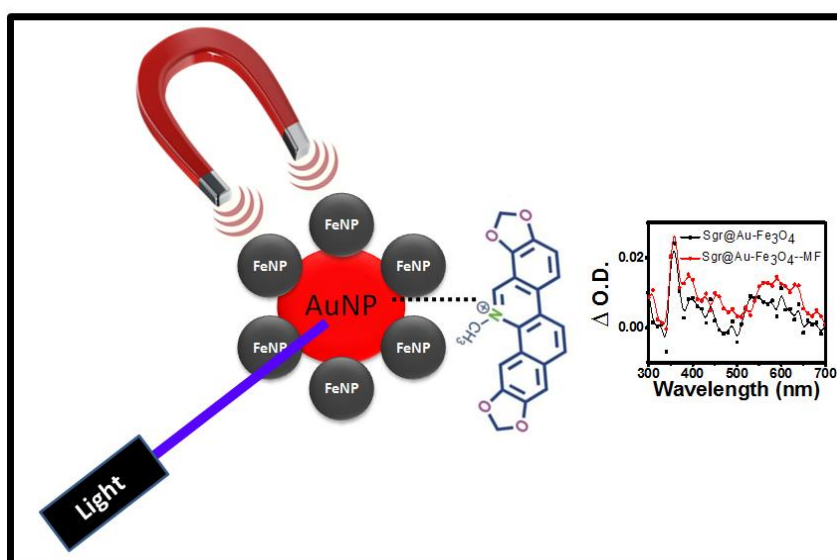
CHAPTER-6

Exploration of the Role of a Magnetoplasmonic Field on the Excited State

Photophysical Pathways of Sanguinarine

Outline: Point to be discussed

- ❖ Role of magnetic and plasmonic nanosurface on the excited state photophysical pathway of the drug molecule, sanguinarine.
- ❖ How do both plasmonic and magnetic surface simultaneously influence the overall spin dynamics of the drug?
- ❖ Magnetoplasmonic material is more efficient compared to the individual plasmonic or magnetic nanoparticle to enhance the singlet-triplet interconversion—a case study.
- ❖ Future direction.



6.1 Introduction:

Nanosystems combined with both magnetic and plasmonic functionalities are called a magnetoplasmonic nanomaterial which is now an active topic of cutting-edge research areas. In photonics, the polarization of light is used as an information carrier for optical communications³⁸⁶⁻³⁸⁸ sensing³⁸⁹ and imaging.³⁹⁰⁻³⁹² The state of polarization has a significant role in the photonic transfer of quantum information.^{393, 394} This leads to the implementation of an extensive and growing effort to design efficient polarization control of propagating optical modes with plasmonic metasurface. With the invention of magneto-optic materials, such as metallic ferri and ferromagnets which combine the concepts obtained from plasmonics and magnetism, an understanding of unexpected and extraordinary phenomena by the manipulation of light at the nanoscale becomes possible.³⁹⁵⁻⁴⁰⁶ Plasmon resonances are light-induced collective electron oscillations which assist energy confinement at the nanoscale⁴⁰⁷ by enhancing the electromagnetic field at the resonant wavelength. Because of the strong localized field, plasmon resonance undergoes enhanced interaction with the external magnetic field and that gives rise to an enhanced value of the magneto-optical Kerr signal in magnetoplasmonic materials.¹⁸¹ These characteristics of the materials help to explore the nonreciprocal propagation of light by designing suitable nanoscopic magnetoplasmonic elements.³⁹⁸ Due to the internal architecture of the constituting components, the magneto-optical activity of such nanosystem is greatly enhanced as the electromagnetic field enhancement is associated with the plasmon resonance. Moreover, in presence of an external magnetic field, the magnetic functionality permits the control of the plasmonic properties and helps to develop active photonic devices.⁴⁰⁸ As the novel magneto-plasmonic nanoantennas are sensitive not only by light but also by external magnetic fields, they can introduce additional degrees of freedom in controlling light at the nano-scale. This property can be used to frame new devices such as

magneto-plasmonic rulers, ultra-sensitive biosensors, one-way sub-wavelength waveguides¹⁸¹ and extraordinary optical transmission structures in integrated photonic devices for telecommunications⁴⁰⁹ as well as in astonishing biomedical imaging modalities.¹⁸¹ In such nanosystems the ‘non-optical’ ferro or ferrimagnetic nanostructures may operate as magneto-plasmonic nanoantennas which offer extra functionality to launch optical characterization techniques of magnetic nanomaterials and that may be beneficial for the integration of nanophotonics and nanomagnetism on a single chip.¹⁸¹

In the previous chapters, I have discussed the influence of a magnetic nanosurface on the excited state spin dynamics and the modulation of photophysical pathways for the anticancer drug molecules such as sanguinarine and chelerythrine in the different solvent environment. There I have discussed that a magnetic nanosurface can alter the overall spin statistics of the surface adsorbed molecules by changing the extent of singlet-triplet interconversion in presence of a low external magnetic field. As the magnetoplasmonic materials lead to show various interesting and unusual characteristics, I have directed my thesis work in this track to find out the influence of magnetoplasmonic nanomaterials on the excited state photophysical pathway modulation of the Sanguinarine (Sgr) molecule as a case study. A part of the work is described in this chapter where the photophysics and spin dynamics of the Sgr molecule on a frosted (like differentially ice-covered) magnetoplasmonic nanomaterials with plasmonic material at the core and assembly of Fe₃O₄ nanoparticles in the shell has been studied. The whole work has not yet been finished and I am planning to extend the work simply by varying the plasmonic and magnetic nature of the core and shell respectively. Where the plasmonic nature of the core can be varied by changing the shape and size of the Au core and the magnetic nature can be varied or changing the thickness as well as the magnetic material as the shell.

6.2 Result and Discussion:

Literature is not very affluent with well synthesized magnetoplasmonic materials dispersible in a water medium. Here a magnetoplasmonic material has been attempted to synthesize with noble metal spherical Au nanoparticles as the core and ferrimagnetic Fe₃O₄ crystals as a magnetic shell in order to find out the role of both plasmonic and magnetic behaviour of the composite nanoparticles. Here, a simple yet innovative sonochemical method have been adopted to avoid of very high temperature and pressure conditions to synthesize these materials in a seedless single step synthetic modality.

6.2.1 Sonochemical Synthesis of Magneto-plasmonic material

In a 50mL conical flask, 45mL of ethylene glycol (EG) have been taken. To this, 40μL seed (concentration: 0.1gm Fe₃O₄/1mL EG) of synthesized Fe₃O₄ nanoparticle (synthesis of Fe₃O₄ nanoparticle has been described in Chapter 2) followed by 25μL of 10⁻¹M HAuCl₄ and then purged with Ar and mixed properly under constant stirring. The resultant mixture was then sonicated at 100 Hz for 2h at room temperature. The colour of the solution changes to brown. Due to the viscous nature of EG, it is difficult to separate the resultant magnetoplasmonic materials by using magnetic force. To separate the generated magnetoplasmonic nanoparticles out of the solution the reaction mixture have been centrifuged at 4500 rpm for 2h and then redispersed in water or ethanol medium. The centrifuged particles then easily get attracted by the magnet to separate them out.

6.2.1.1 Ground state UV-vis absorption spectra

Since magnetic nanomaterials do not show any strong plasmonic behaviour, resultant magnetoplasmonic nanoparticles bear the optical signature of the plasmonic core only which shows a single absorption peak around 570.nm (**Figure 6.1**).

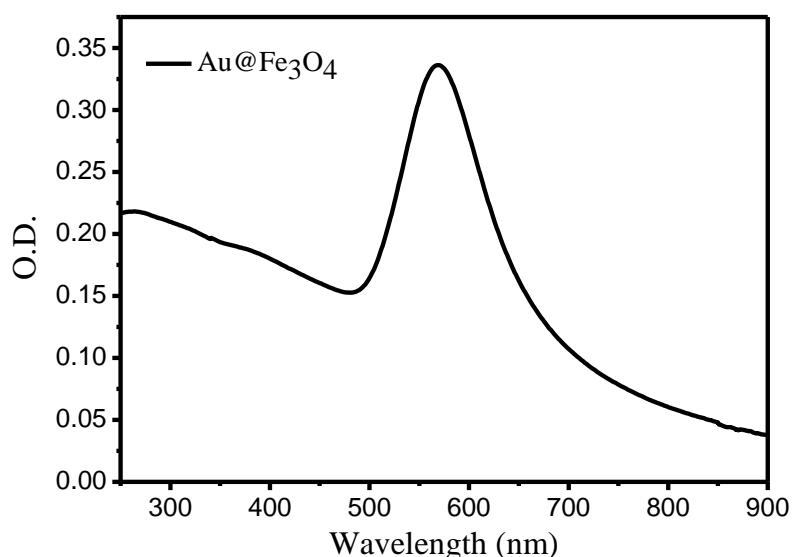


Figure 6.1. The ground state absorption spectra of the Au@Fe₃O₄ nanoparticle

6.2.2 Characterization of magnetoplasmonic nanomaterial

The synthesized material was characterized by TEM study. The TEM results (**Figure 6.2**) show that a plasmonic core frosted with magnetic Fe₃O₄ has been synthesized. The HRTEM study is showing the magnetoplasmonic interface of the Au (111) and Fe₃O₄ (220) crystal facets along with the highly crystalline nature of the individual magnetic and plasmonic nanoparticles (**Figure 6.3**). Due to the crystal mismatch, a high strain is generated at the interface (**Figure 6.3 D**). The elemental mapping analysis is showing the presence of Au and Fe (**Figure 6.4**) where an abundance of Au is at the core and abundance of Fe is at the surface (**Figure 6.5**).

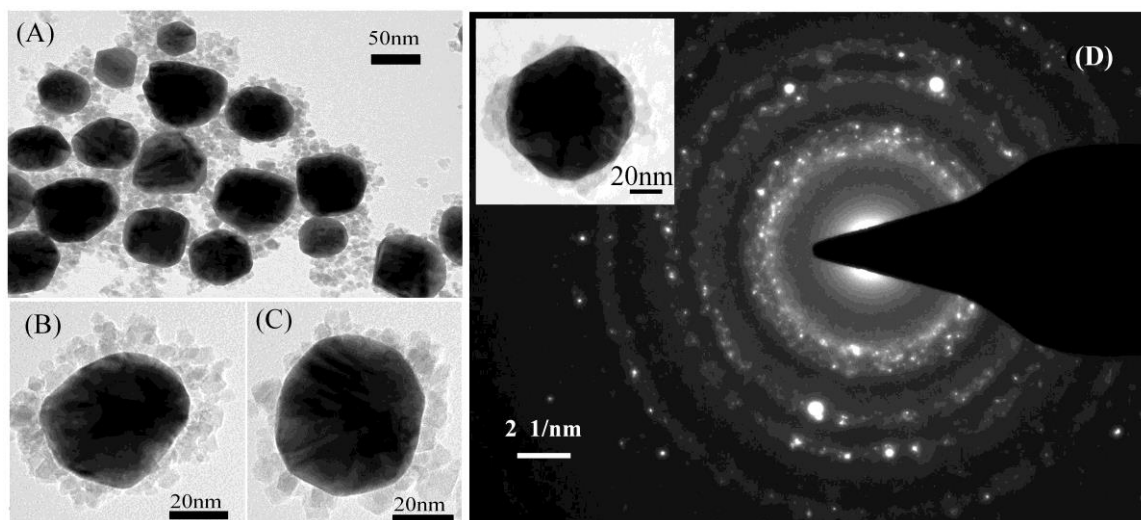


Figure 6.2.(A), (B), (C) Bright field TEM images of Au@Fe₃O₄nanoparticle(D) Selected area electron diffraction (SAED) image from the nanoparticlespresented at the inset.

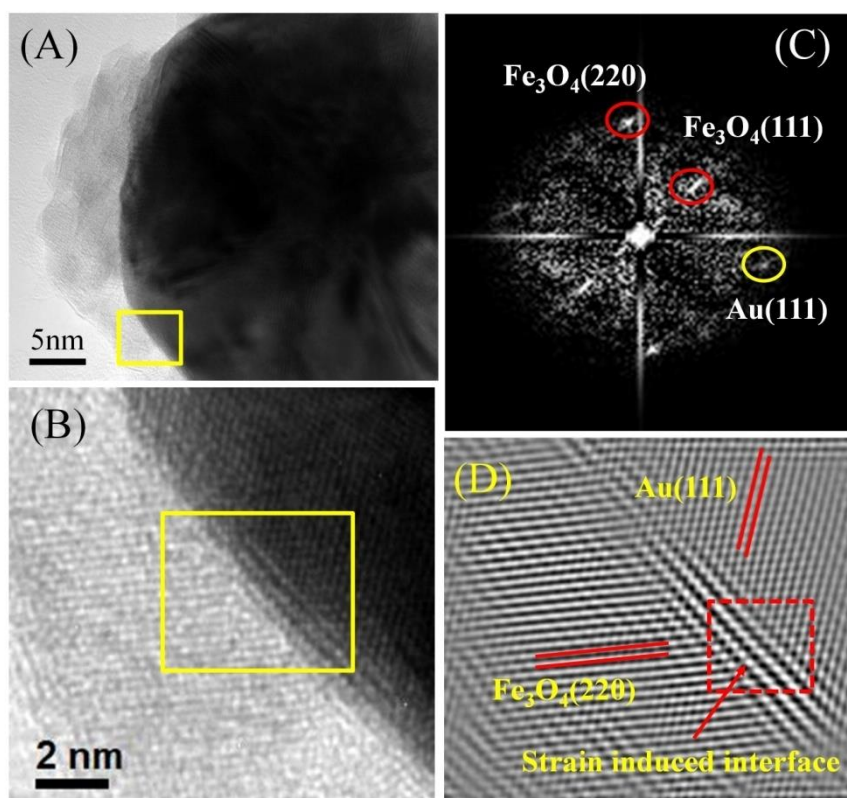


Figure 6.3. (A), (B) High-resolution TEM (HRTEM) images of Au@Fe₃O₄ (C) FFT image from the area shown in Fig (B), (D) Fourier filtered image of Fig (C)

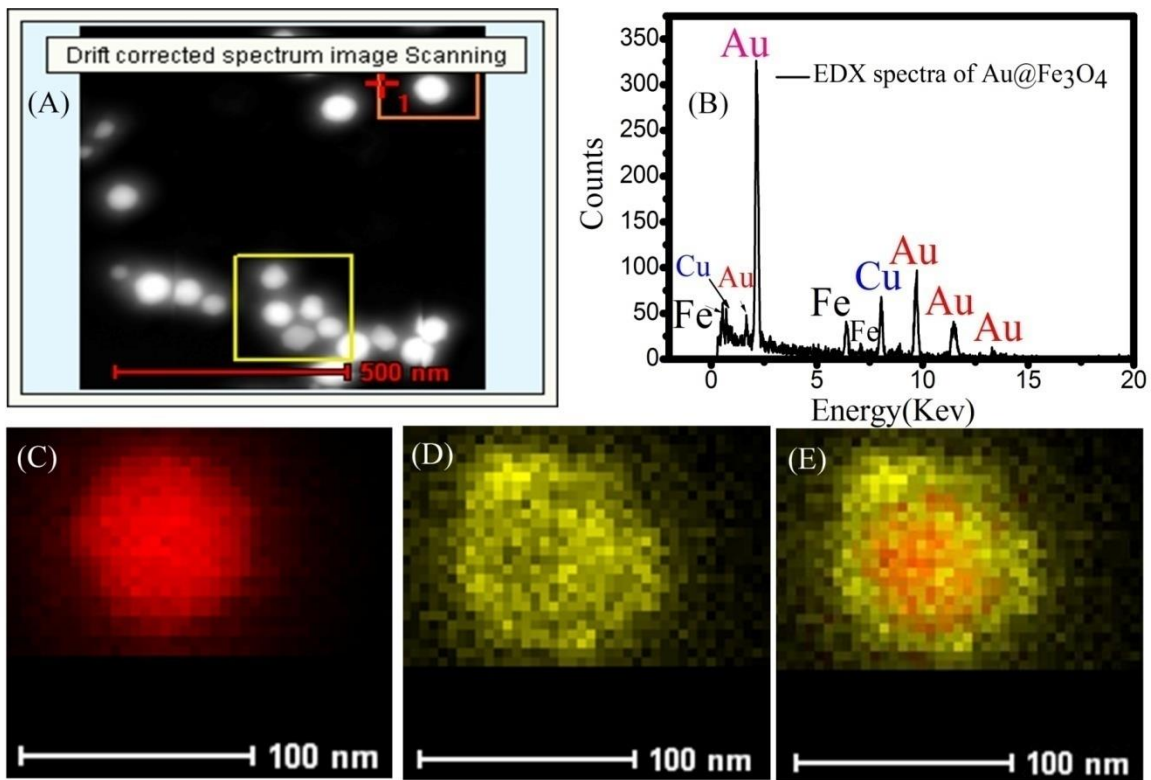


Figure 6.4. (A) STEM-HAADF image of the Au@Fe₃O₄, (B) EDX spectra acquired from the selected area 1 in Fig (A), (C) Au-L map, (D) Fe-K map, (E) Composite map.

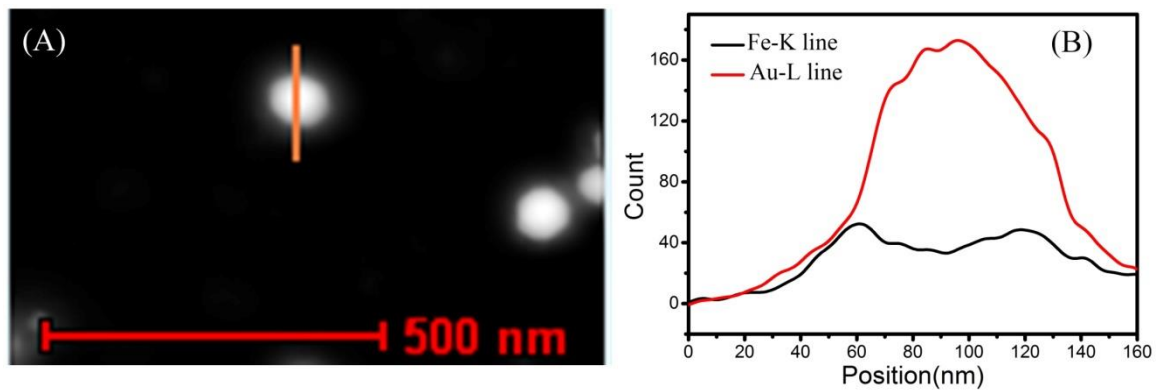


Figure 6.5.(A) STEM-HAADF image of the Au@Fe₃O₄, (B) Line scan profile of the NP along the line shown in Fig (A).

6.2.3 Magnetization of the magnetoplasmonic material in presence of an external magnetic field

The M-H plot is showing the coercivity-free or remanence-free magnetic hysteresis of the material. The measured saturation magnetization for the Au@Fe₃O₄ is 28.4 emu/g. **Figure 6.3A** shows the M-H nature of Au@Fe₃O₄ and **Figure 6.3B** shows the magnetization behaviour comparison between Au@Fe₃O₄ and Fe₃O₄.

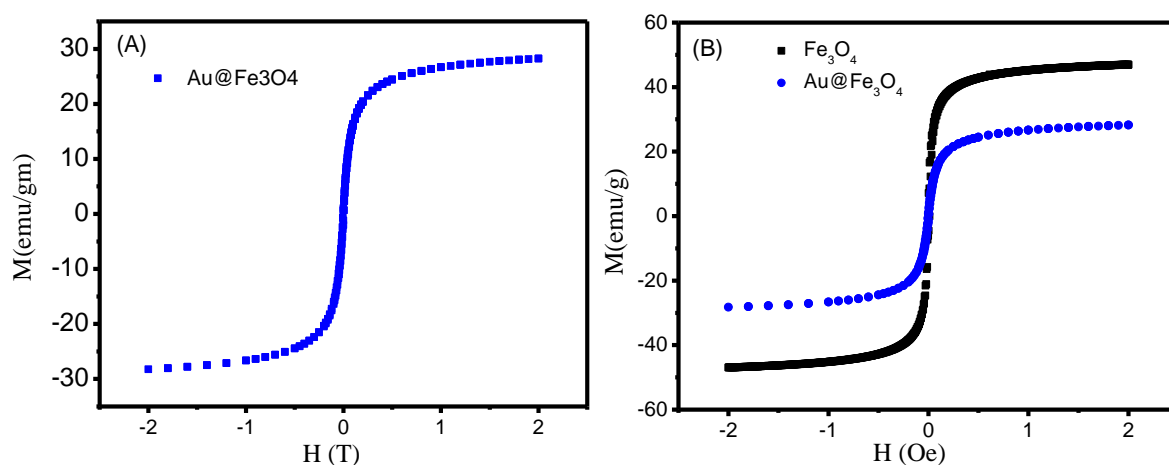


Figure 6.6: Magnetic field dependent magnetization at 300 K for (A) Au@Fe₃O₄ and (B) comparison of the extent of magnetization between Fe₃O₄ and Au@Fe₃O₄.

6.2.4 The complex formation between Sgr and Au@Fe₃O₄

The surface attachment of the Sgr molecule with Au@Fe₃O₄ has been analyzed from their observed UV-vis spectroscopy (**Figure 6.4**). A new broad peak centred at 700 nm indicates the ground state complex formation between Sgr and the Au@Fe₃O₄ nanosurface.

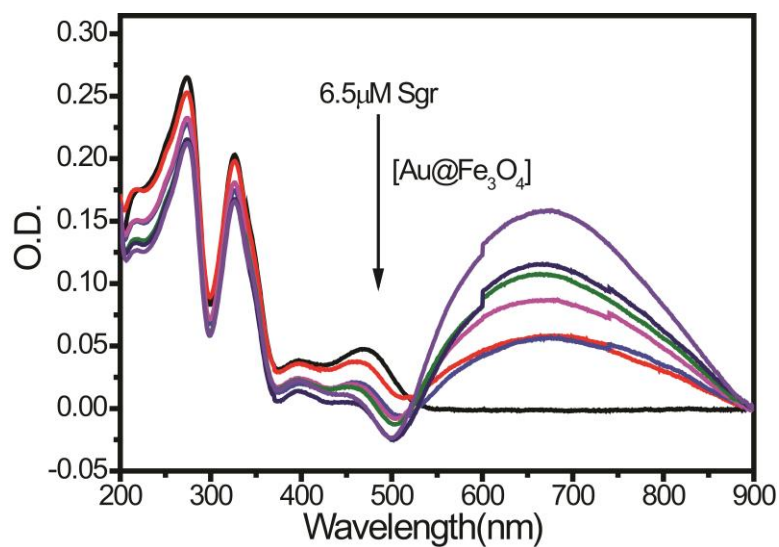


Figure 6.7. UV-vis absorption spectra of Sgr on gradual addition of Au@Fe₃O₄

The surface attachment is again confirmed from the fluorescence experiment where we observed the quenching of Sgr fluorescence intensity on the gradual addition of Au@Fe₃O₄ (**Figure 6.5**). Reduction of fluorescence intensity of Sgr directly measures the drop of excited singlet species (S₁) population as a result of the attachment with the Au@Fe₃O₄.

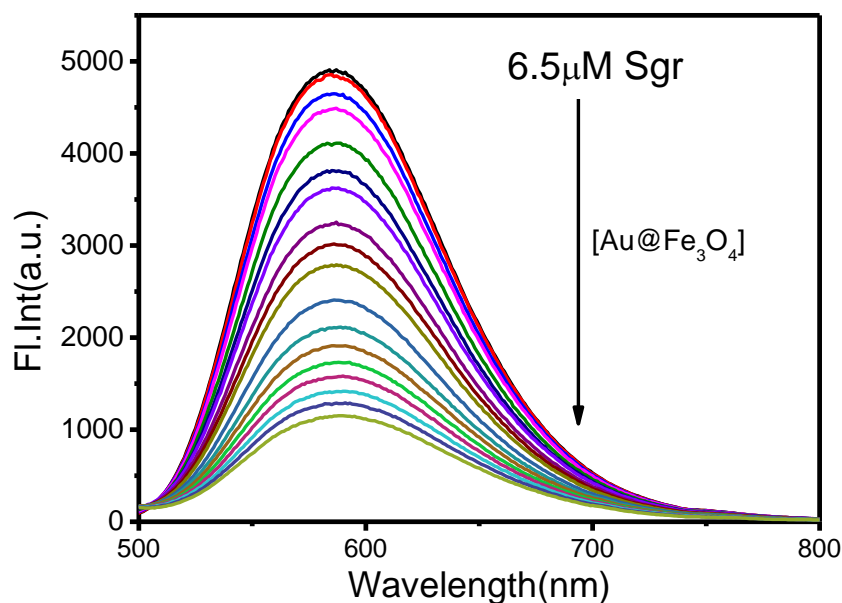


Figure 6.8. Trend and extent of fluorescence quenching from the S_1 state of Sgr in presence of a variable concentration of $Au@Fe_3O_4$.

Though the corresponding stern Volmer plot of fluorescence quenching has shown an overall nonlinearity (**Figure 6.6 A**), linearity was maintained upto the 80 nM concentration of $Au@Fe_3O_4$ as shown in **Figure 6.6 A**. This supports the ground state complexation between Sgr and $Au@Fe_3O_4$ below 80 nM concentration of $Au@Fe_3O_4$. The non-linearity at high concentration may arise (above 80 nM) due to the collisional quenching.

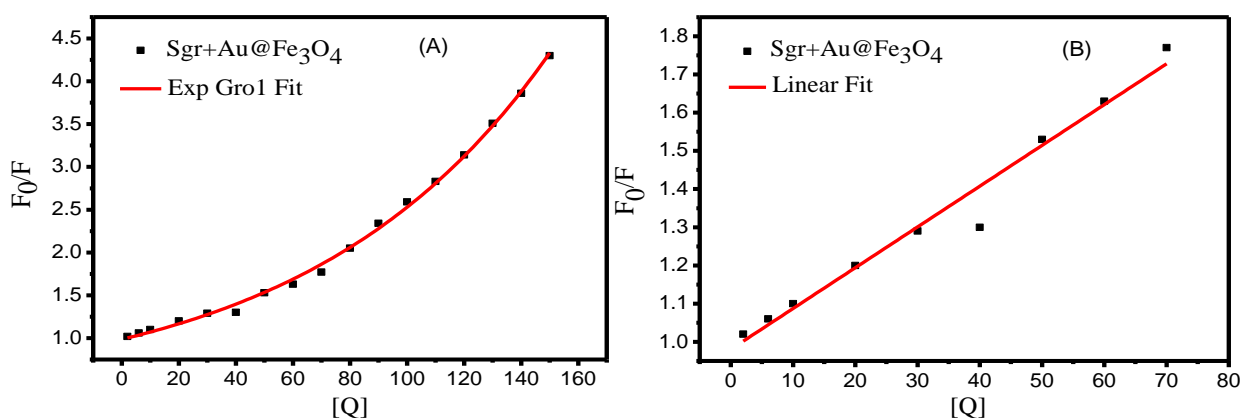


Figure 6.9. (A) The stern-volmer plot of Sgr- $Au@Fe_3O_4$ complex as a function of increasing concentration of $Au@Fe_3O_4$. (B) Linear Stern-Volmer plot of Sgr- $Au@Fe_3O_4$ complex at low concentration $Au@Fe_3O_4$.

The major fluorescence lifetime component (**Table 6.1**) of Sgr remains unchanged on the addition of variable concentration of Au@Fe₃O₄ which again proves that the excited singlet population of Sgr is reduced in presence of Au@Fe₃O₄ due to the ground state complex formation.

Table 6.1. The Lifetime Components of Sgr as a result of adsorption on Nanosurface.

Sample	τ_1	τ_2	%	
			B ₁	B ₂
65 μ M Sgr	2.06	2.84	61	38
Sgr+10 nM Au@Fe ₃ O ₄	2.18	3.59	85	14
Sgr+20 nM Au@Fe ₃ O ₄	2.07	3.26	73	26
Sgr+40 nM Au@Fe ₃ O ₄	1.98	2.77	50	49
Sgr+80 nM Au@Fe ₃ O ₄	2.37	0.1	96	4

6.2.5: Influence of Au@Fe₃O₄ Nanosurface on the Transient Spin-Trajectory Modulation of surface adsorbed Sgr

The complex formation is also observed in the triplet-triplet (T-T) absorption spectra with an isosbestic point around 500 nm. It has been shown in **Chapter 4** that on the addition of FeNP, there is a reduction in Sgr triplet population, however, on the addition of Au@Fe₃O₄, there is no such significant reduction in triplet population. It is already reported that ⁵⁰ AuNP surface can enhance the triplet population via transmitter-receiver antenna interaction.⁵⁰It has also been shown in **Chapter 3** that due to the attachment of Sgr on plasmonic AuNP surface, the T-T absorption around 360 to 500 nm increases. Therefore, it can be inferred that in case of Au@Fe₃O₄, the surface adsorbed Sgr shows a compromising

T-T absorption due to the simultaneous occurrence of the two-opposing type of interactions which uphold the overall triplet population almost unchanged.

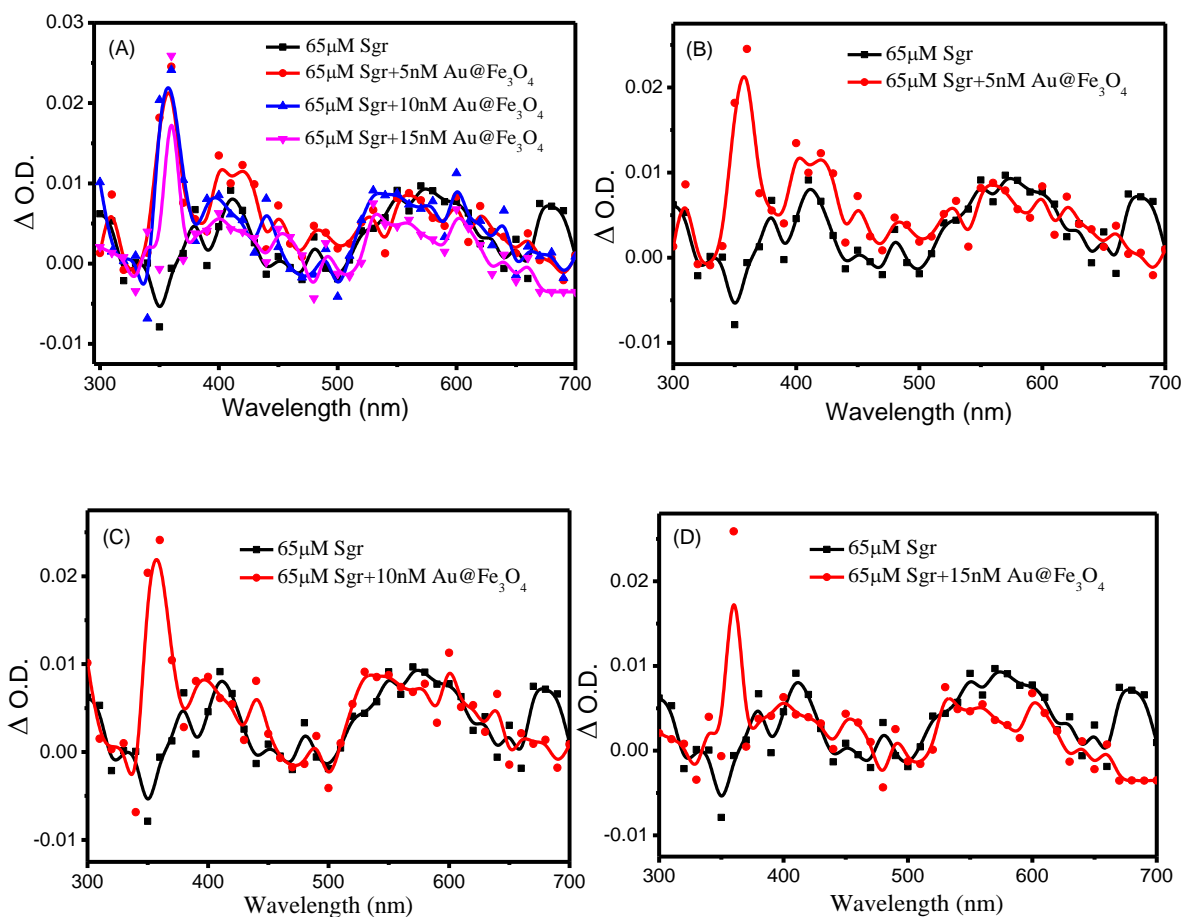


Figure 6.10. T-T absorption spectra of Sgr upon the addition of different concentration of $\text{Au@Fe}_3\text{O}_4$.

6.2.6: Transient Spin-Trajectory Modulation by $\text{Au@Fe}_3\text{O}_4$ surface with ultra-high efficiency in presence of a low external magnetic field

On application of an external magnetic field of 0.08 T, an overall increment in the T-T absorption is observed. The triplet decay profile and the corresponding enhancement of lifetime support the increase of the triplet population. A detail of triplet lifetime for Sgr- $\text{Au@Fe}_3\text{O}_4$ in presence of external magnetic field has been described in **Table 6.2**. Previously (described in **Chapter 4**) the role of superparamagnetic nanosurface

on controlling the ISC process to enhance the triplet population by directing the surface adsorbed molecule and making the transition dipole moment (μ) favourable for $S \leftrightarrow T$ interconversion in presence of an externally applied magnetic field have been observed. Since the magnetoplasmonic nanomaterial contains both the functionalities of plasmonic and magnetic nanoparticles, the overall triplet lifetime for such a material increases immensely compared to that of bare FeNP as well as bare AuNP. Here the plasmonic moiety raises the triplet yield through enhancing S_1 state population whereas in presence of an external magnetic field its magnetic moiety helps to augment the triplet intensity via increasing $S_1 \leftrightarrow T_1$ interconversion. Therefore, in presence of MF, T_1 yield will increase for the increased S_1 population by AuNP alongwith for the favourable alignment of the molecular dipole towards the $S_1 \leftrightarrow T_1$ interconversion by the magnetic moiety. Thus in presence of magnetic field due to these two driving forces, the overall triplet lifetime is increasing enormously. The overall effect is observable from the concentration vs lifetime plot.

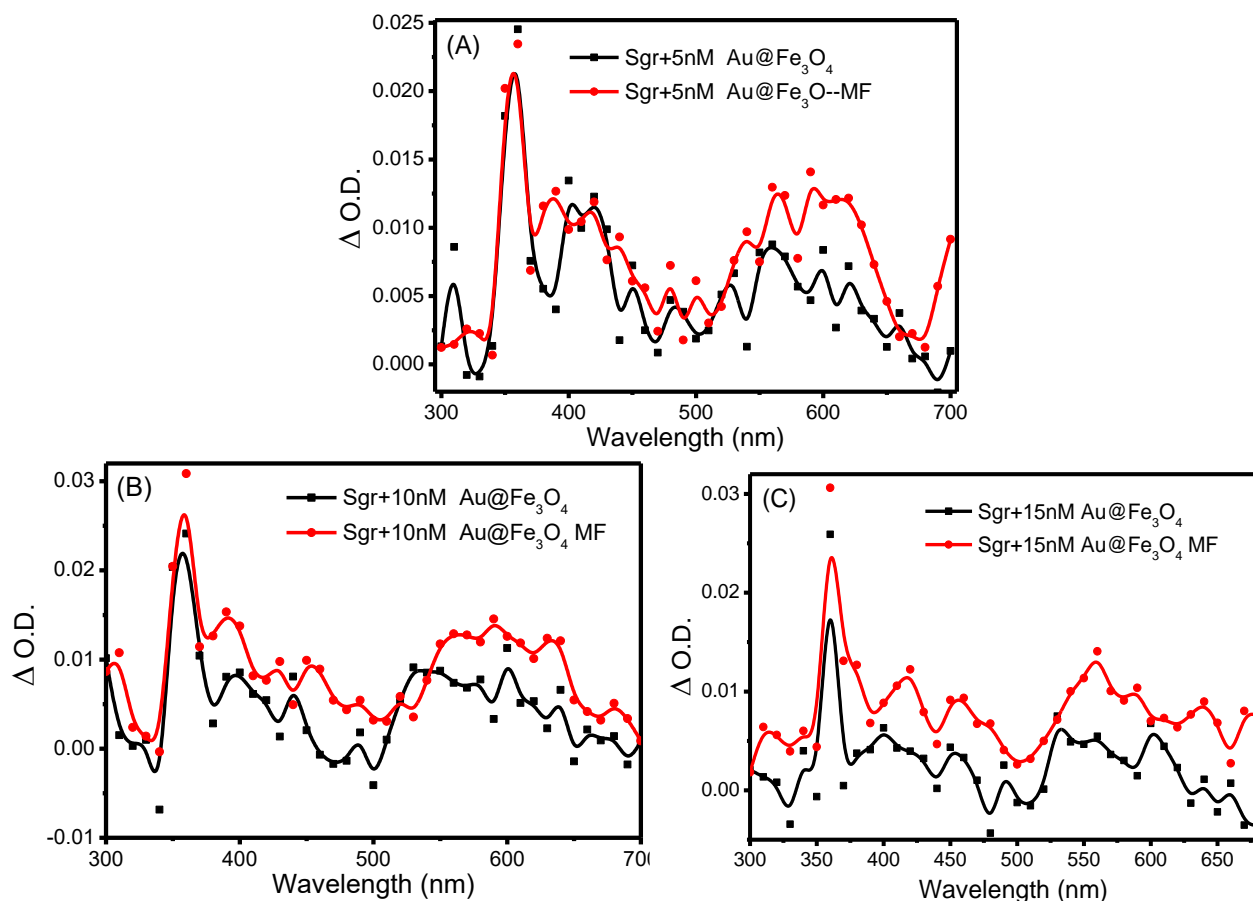


Figure 6.11. T-T absorption spectra and the corresponding modulation of the transient spin state of Sgr in presence of variable FeNP concentration under the influence of a constant low external magnetic field (0.08 T).

6.2.7: Triplet lifetime of Sgr in presence of Au@Fe₃O₄ nanosurface

It is very interesting to observe that the slope of the excited state triplet lifetime of Sgr with varying concentration of Au@Fe₃O₄ is much steeper in presence of magnetic field compared to that in absence of magnetic field (**Figure 6.7**). This proves that the magnetoplasmonic material is much more efficient to enhance the S \leftrightarrow T interconversion rate in presence of magnetic field.

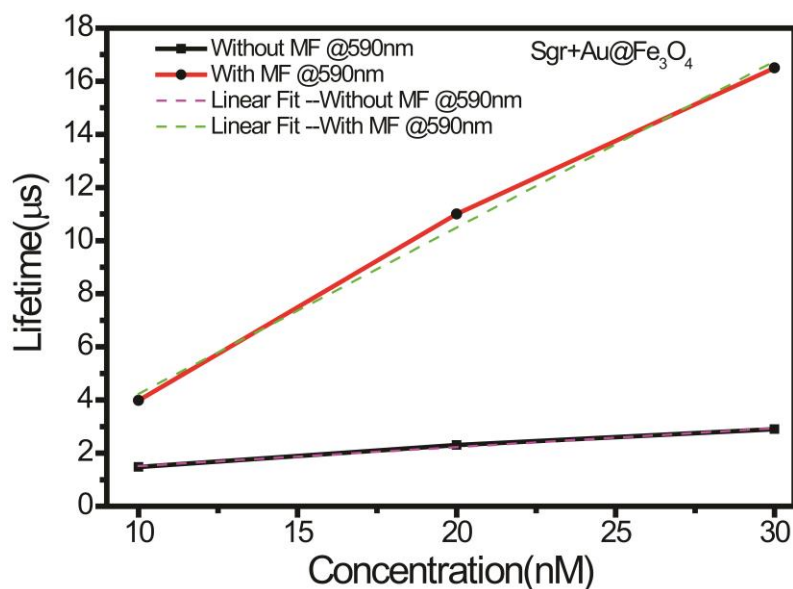


Figure 6.12. Change of excited state triplet lifetime with Au@Fe₃O₄ concentration in the presence (red line) and absence (black line) of the magnetic field.

Table 6.2. Excited state triplet lifetime of Sgr on plasmonic (AuNP), magnetic (FeNP) and magnetoplasmonic (Au@Fe₃O₄) nanosurface in presence and absence of magnetic field.

Sample name	Without Field	With Field (us)
Sgr@590	2.63393E-6	2.72393E-6
Sgr+AuNP@590	3.17101 E-6	6.82772E-8
Sgr+FeNP@590	1.41797E-8	4.47923E-8
Sgr@ Au@Fe ₃ O ₄ @590	2.93393E-6	2.21836E-5

It is also evident from the excited state lifetime table (**Table 6.2**) that a magnetoplasmonic nanosurface can enhance the excited state triplet lifetime in presence of externally applied low (0.08T) magnetic field compared to that of a plasmonic and magnetic nanosurface. Enhancement of triplet lifetime is intern related to the enhancement of triplet yield.

6.3 Future Direction and Conclusion: The above study gives us an indication that a magnetoplasmonic nanosurface can undergo better transmitter-receiver antenna interaction towards excited-state molecular dynamics. In recent days, photodynamic therapy is a useful and developing field of research for the treatment of a malignant tumour, carcinogenesis, acne, etc. where a triplet sensitizer is used to destroy the toxic cells. As an anticancer drug, Sgr is showing better triplet lifetime as well as triplet yield on a magnetoplasmonic nanosurface in presence of external magnetic field, the Sgr@Au@Fe₃O₄ can be a useful tool towards the betterment of such therapeutic technique. Though the work has not yet been completed, supporting data as control experiments along with the effect of the variation of the plasmonic and magnetic moiety on the effective triplet yield will enormously improve the quality of this study.

References

1. Aly, S. M.; Carraher J.R., C. E.; Harvey, P. D. J. M. C. M.; Photophysics, M. L. E.; Polymers, P. o. M. C. Introduction to Photophysics and Photochemistry. 2010.
2. Rohatgi-Mukherjee, K., *Fundamentals of photochemistry*. New Age International: 1978.
3. Macdonell, A. A., *The Brhad-Devata: attributed to Saunaka; a summary of the deities and myths of the Rgveda*. Motilal Banarsidass Published: 1994.
4. Butler, W. L. J. A. o. C. R., Primary photochemistry of photosystem II of photosynthesis. **1973**,*6* (6), 177-184.
5. Hirano, T.; Hasumi, Y.; Ohtsuka, K.; Maki, S.; Niwa, H.; Yamaji, M.; Hashizume, D. J. J. o. t. A. C. S., Spectroscopic studies of the light-color modulation mechanism of firefly (beetle) bioluminescence. **2009**,*131* (6), 2385-2396.
6. Rubasinghege, G.; Elzey, S.; Baltrusaitis, J.; Jayaweera, P. M.; Grassian, V. H. J. T. J. o. P. C. L., Reactions on atmospheric dust particles: surface photochemistry and size-dependent nanoscale redox chemistry. **2010**,*1* (11), 1729-1737.
7. Weltmann, K. D.; Kindel, E.; von Woedtke, T.; Hähnel, M.; Stieber, M.; Brandenburg, R. J. P.; Chemistry, A., Atmospheric-pressure plasma sources: Prospective tools for plasma medicine. **2010**, *82* (6), 1223-1237.
8. Holick, M. F.; MacLaughlin, J.; Clark, M.; Holick, S.; Potts, J.; Anderson, R.; Blank, I.; Parrish, J.; Elias, P. J. S., Photosynthesis of previtamin D3 in human skin and the physiologic consequences. **1980**, *210* (4466), 203-205.
9. Riveros, O. J.; Diestler, D. J. J. o. t. A. C. S., Dynamics of proton translocation in the primary process of vision. **1988**, *110* (21), 7206-7208.
10. Babino, D.; Golczak, M.; Kiser, P. D.; Wyss, A.; Palczewski, K.; Von Lintig, J. J. A. c. b., The biochemical basis of vitamin A3 production in arthropod vision. **2016**,*11* (4), 1049-1057.
11. Asghar, M. I.; Halme, J.; Kaukonen, S.; Humalamäki, N.; Lund, P.; Korppi-Tommola, J. J. T. J. o. P. C. C., Intriguing photochemistry of the additives in the dye-sensitized solar cells. **2016**,*120* (49), 27768-27781.
12. Maeda, K.; Domen, K. J. T. J. o. P. C. L., Photocatalytic water splitting: recent progress and future challenges. **2010**,*1* (18), 2655-2661.
13. Urbain, P.; Jakobsen, J. J. J. o. a.; chemistry, f., Dose–response effect of sunlight on vitamin D2 production in *Agaricus bisporus* mushrooms. **2015**,*63* (37), 8156-8161.
14. Calegari, G. C.; Santos, V. A.; Teixeira, S. D.; Barbosa-Dekker, A. M. J. J. o. P.; Pharmacology, Sulfonation of (1→6)-β-D-Glucan (Lasiodiplodan) and Its Antioxidant and Antimicrobial Potential. **2017**,*5*, 850-863.
15. Rene, O.; Stepek, I. A.; Gobbi, A.; Fauber, B. P.; Gaines, S. J. T. J. o. o. c., Palladium-catalyzed ring expansion of spirocyclopropanes to form caprolactams and azepanes. **2015**,*80* (20), 10218-10225.
16. Haaf, F.; Sanner, A.; Straub, F. J. P. J., Polymers of N-vinylpyrrolidone: synthesis, characterization and uses. **1985**,*17* (1), 143.
17. Dong, N.-N.; Pedroni, M.; Piccinelli, F.; Conti, G.; Sbarbati, A.; Ramírez-Hernández, J. E.; Maestro, L. M.; Iglesias-de la Cruz, M. C.; Sanz-Rodríguez, F.; Juarranz, A. J. A. n., NIR-to-NIR two-photon excited CaF2: Tm³⁺, Yb³⁺ nanoparticles: multifunctional nanoprobes for highly penetrating fluorescence bio-imaging. **2011**,*5* (11), 8665-8671.
18. Woo, H.; Cho, S.; Han, Y.; Chae, W.-S.; Ahn, D.-R.; You, Y.; Nam, W. J. J. o. t. A. C. S., Synthetic control over photoinduced electron transfer in phosphorescence zinc sensors. **2013**,*135* (12), 4771-4787.

19. Chakraborty, S. D.; Sau, A.; Kuznetsov, D. V.; Banerjee, A.; Bardhan, M.; Bhattacharya, M.; Dasgupta, D.; Basu, S.; Senapati, D. J. *T. J. o. P. C. B.*, Development of a Triplet–Triplet Absorption Ruler: DNA-and Chromatin-Mediated Drug Molecule Release from a Nanosurface. **2016**, *120* (27), 6872-6881.
20. Valeur, B.; Berberan-Santos, M. N., *Molecular fluorescence: principles and applications*. John Wiley & Sons: 2012.
21. Jackson, J. D. *J. C. e.*, Plane electromagnetic waves and wave propagation. **1975**, 273-278.
22. Bolton, J. R.; Hall, D. O. *J. A. R. o. E.*, Photochemical conversion and storage of solar energy. **1979**, *4* (1), 353-401.
23. Han, K.; Wang, S.-B.; Lei, Q.; Zhu, J.-Y.; Zhang, X.-Z. *J. A. n.*, Ratiometric biosensor for aggregation-induced emission-guided precise photodynamic therapy. **2015**, *9* (10), 10268-10277.
24. Dhar, S.; Senapati, D.; Das, P. K.; Chattopadhyay, P.; Nethaji, M.; Chakravarty, A. R. *J. J. o. t. A. C. S.*, Ternary copper complexes for photocleavage of DNA by red light: Direct Evidence for sulfur-to-copper charge transfer and d– d band involvement. **2003**, *125* (40), 12118-12124.
25. Steiner, U. E., Fundamentals of Photophysics, Photochemistry, and Photobiology. In *Photodynamic Therapy*, Springer: 2014; pp 25-58.
26. Zimmermann, J.; Zeug, A.; Röder, B. *J. P. C. C. P.*, A generalization of the Jablonski diagram to account for polarization and anisotropy effects in time-resolved experiments. **2003**, *5* (14), 2964-2969.
27. Leermakers, P. A.; Vesley, G. F. *J. J. o. C. E.*, Organic photochemistry and the excited state. **1964**, *41* (10), 535.
28. Bixon, M.; Jortner, J.; Cortes, J.; Heitele, H.; Michel-Beyerle, M. *J. T. J. o. P. C.*, Energy gap law for nonradiative and radiative charge transfer in isolated and in solvated supermolecules. **1994**, *98* (30), 7289-7299.
29. Gould, I. R.; Noukakis, D.; Gomez-Jahn, L.; Young, R. H.; Goodman, J. L.; Farid, S. *J. C. p.*, Radiative and nonradiative electron transfer in contact radical-ion pairs. **1993**, *176* (2-3), 439-456.
30. Nafie, L. A.; Freedman, T. B. *J. T. J. o. C. P.*, Vibronic coupling theory of infrared vibrational transitions. **1983**, *78* (12), 7108-7116.
31. Halstead, J. A. *J. J. o. C. E.*, Teaching the Spin Selection Rule: An Inductive Approach. **2012**, *90* (1), 70-75.
32. Song, Q.; Zhang, Z. *J. J. T. J. o. P. C. B.*, Correlation between spin– orbital coupling and the superparamagnetic properties in magnetite and cobalt ferrite spinel nanocrystals. **2006**, *110* (23), 11205-11209.
33. Aich, S.; Basu, S. *J. T. J. o. P. C. A.*, Magnetic field effect: A tool for identification of spin state in a photoinduced electron-transfer reaction. **1998**, *102* (4), 722-729.
34. Lower, S.; El-Sayed, M. *J. C. R.*, The triplet state and molecular electronic processes in organic molecules. **1966**, *66* (2), 199-241.
35. Ward, M. D. *J. C. S. R.*, Photo-induced electron and energy transfer in non-covalently bonded supramolecular assemblies. **1997**, *26* (5), 365-375.
36. Levanon, H.; Norris, J. R. *J. C. R.*, The photoexcited triplet state and photosynthesis. **1978**, *78* (3), 185-198.
37. Yago, T.; Ishikawa, K.; Katoh, R.; Wakasa, M. *J. T. J. o. P. C. C.*, Magnetic field effects on triplet pair generated by singlet fission in an organic crystal: application of radical pair model to triplet pair. **2016**, *120* (49), 27858-27870.
38. Wang, Z.; Zhao, J.; Barbon, A.; Toffoletti, A.; Liu, Y.; An, Y.; Xu, L.; Karatay, A.; Yaglioglu, H. G.; Yildiz, E. *A. s. J. J. o. t. A. C. S.*, Radical-Enhanced Intersystem

- Crossing in New Bodipy Derivatives and Application for Efficient Triplet–Triplet Annihilation Upconversion. **2017**,*139* (23), 7831-7842.
39. Lee, T. S.; Lin, Y. L.; Kim, H.; Pensack, R. D.; Rand, B. P.; Scholes, G. D. J. T. j. o. p. c. l., Triplet Energy Transfer Governs the Dissociation of the Correlated Triplet Pair in Exothermic Singlet Fission. **2018**,*9* (14), 4087-4095.
40. Chesta, C. A.; Mohanty, J.; Nau, W. M.; Bhattacharjee, U.; Weiss, R. G. J. J. o. t. A. C. S., New insights into the mechanism of triplet radical-pair combinations. The persistent radical effect masks the distinction between in-cage and out-of-cage processes. **2007**,*129* (16), 5012-5022.
41. Sanders, S. N.; Kumarasamy, E.; Pun, A. B.; Trinh, M. T.; Choi, B.; Xia, J.; Taffet, E. J.; Low, J. Z.; Miller, J. R.; Roy, X. J. J. o. t. A. C. S., Quantitative intramolecular singlet fission in bipentacenes. **2015**,*137* (28), 8965-8972.
42. Roduner, E. J. C. S. R., Size matters: why nanomaterials are different. **2006**,*35* (7), 583-592.
43. Zhang, A.; Lieber, C. M. J. C. r., Nano-bioelectronics. **2015**,*116* (1), 215-257.
44. Michaudel, Q.; Ishihara, Y.; Baran, P. S. J. A. o. c. r., Academia–industry symbiosis in organic chemistry. **2015**,*48* (3), 712-721.
45. Liou, Y.; Lee, M.; You, K. J. A. P. L., Magnetic coupling in Ge nanoparticles. **2007**,*91* (8), 082505.
46. Koole, R.; Groeneveld, E.; Vanmaekelbergh, D.; Meijerink, A.; de Mello Donegá, C., Size effects on semiconductor nanoparticles. In *Nanoparticles*, Springer: 2014; pp 13-51.
47. Watermann, A.; Brieger, J. J. N., Mesoporous silica nanoparticles as drug delivery vehicles in cancer. **2017**,*7* (7), 189.
48. Senapati, S.; Mahanta, A. K.; Kumar, S.; Maiti, P. J. S. t.; therapy, t., Controlled drug delivery vehicles for cancer treatment and their performance. **2018**,*3* (1), 7.
49. Chowdhury, S.; Yusof, F.; Salim, W. W. A. W.; Sulaiman, N.; Faruck, M. O. J. J. o. P.; Biology, P. B., An overview of drug delivery vehicles for cancer treatment: nanocarriers and nanoparticles including photovoltaic nanoparticles. **2016**,*164*, 151-159.
50. Pacioni, N. L.; González-Béjar, M. a.; Alarcón, E.; McGilvray, K. L.; Scaiano, J. J. J. o. t. A. C. S., Surface plasmons control the dynamics of excited triplet states in the presence of gold nanoparticles. **2010**,*132* (18), 6298-6299.
51. Baumberg, J. J.; Kelf, T. A.; Sugawara, Y.; Cintra, S.; Abdelsalam, M. E.; Bartlett, P. N.; Russell, A. E. J. N. l., Angle-resolved surface-enhanced Raman scattering on metallic nanostructured plasmonic crystals. **2005**,*5* (11), 2262-2267.
52. Jain, P. K.; Xiao, Y.; Walsworth, R.; Cohen, A. E. J. N. l., Surface plasmon resonance enhanced magneto-optics (SuPREMO): Faraday rotation enhancement in gold-coated iron oxide nanocrystals. **2009**,*9* (4), 1644-1650.
53. Lim, D.-K.; Barhoumi, A.; Wylie, R. G.; Reznor, G.; Langer, R. S.; Kohane, D. S. J. N. l., Enhanced photothermal effect of plasmonic nanoparticles coated with reduced graphene oxide. **2013**,*13* (9), 4075-4079.
54. Huang, Y. Y.; Sharma, S. K.; Dai, T.; Chung, H.; Yaroslavsky, A.; Garcia-Diaz, M.; Chang, J.; Chiang, L. Y.; Hamblin, M. R., Can nanotechnology potentiate photodynamic therapy? *Nanotechnology reviews* **2012**,*1* (2), 111-146.
55. Karam, T. E.; Smith, H. T.; Haber, L. H. J. T. J. o. P. C. C., Enhanced photothermal effects and excited-state dynamics of plasmonic size-controlled gold–silver–gold core–shell–shell nanoparticles. **2015**,*119* (32), 18573-18580.
56. Yang, W.; Liu, K.; Song, D.; Du, Q.; Wang, R.; Su, H. J. T. J. o. P. C. C., Aggregation-induced enhancement effect of gold nanoparticles on triplet excited state. **2013**,*117* (51), 27088-27095.

57. Zhou, M.; Yao, C.; Sfeir, M. Y.; Higaki, T.; Wu, Z.; Jin, R. J. T. J. o. P. C. C., Excited-State Behaviors of M1Au24 (SR) 18 Nanoclusters: The Number of Valence Electrons Matters. **2018**.
58. Zhou, M.; Zeng, C.; Sfeir, M. Y.; Cotlet, M.; Iida, K.; Nobusada, K.; Jin, R. J. T. j. o. p. c. l., Evolution of Excited-State Dynamics in Periodic Au28, Au36, Au44, and Au52 Nanoclusters. **2017**,8 (17), 4023-4030.
59. Anger, P.; Bharadwaj, P.; Novotny, L. J. P. r. l., Enhancement and quenching of single-molecule fluorescence. **2006**,96 (11), 113002.
60. Bharadwaj, P.; Novotny, L. J. O. E., Spectral dependence of single molecule fluorescence enhancement. **2007**,15 (21), 14266-14274.
61. Cohen, A. E. J. T. J. o. P. C. A., Nanomagnetic control of intersystem crossing. **2009**,113 (41), 11084-11092.
62. Zhao, Z.; Rinaldi, C. J. T. J. o. P. C. C., Magnetization Dynamics and Energy Dissipation of Interacting Magnetic Nanoparticles in Alternating Magnetic Fields with and without a Static Bias Field. **2018**,122 (36), 21018-21030.
63. Werner, H. J.; Schulten, Z.; Schulten, K., Theory of the magnetic field modulated geminate recombination of radical ion pairs in polar solvents: Application to the pyrene–N, N-dimethylaniline system. *The Journal of Chemical Physics* **1977**,67 (2), 646-663.
64. Osintsev, A.; Popov, A.; Fuhs, M.; Möbius, K., Spin dynamics in strongly coupled spin-correlated radical pairs: Stochastic modulation of the exchange interaction and ST– 1 mixing in different magnetic fields. *Applied Magnetic Resonance* **2001**,20 (1-2), 111-135.
65. Montoya, R. D., Magnetic fields, radicals and cellular activity. *Electromagnetic biology and medicine* **2017**,36 (1), 102-113.
66. Werner, H. J.; Schulten, Z.; Schulten, K. J. T. J. o. C. P., Theory of the magnetic field modulated geminate recombination of radical ion pairs in polar solvents: Application to the pyrene–N, N-dimethylaniline system. **1977**,67 (2), 646-663.
67. Osintsev, A.; Popov, A.; Fuhs, M.; Möbius, K. J. A. M. R., Spin dynamics in strongly coupled spin-correlated radical pairs: Stochastic modulation of the exchange interaction and ST– 1 mixing in different magnetic fields. **2001**,20 (1-2), 111-135.
68. Montoya, R. D. J. E. b.; medicine, Magnetic fields, radicals and cellular activity. **2017**,36 (1), 102-113.
69. Dasary, S. S. R.; Singh, A. K.; Senapati, D.; Yu, H.; Ray, P. C., Gold Nanoparticle Based Label-Free SERS Probe for Ultrasensitive and Selective Detection of Trinitrotoluene. *Journal of the American Chemical Society* **2009**,131 (38), 13806-13812.
70. Camden, J. P.; Dieringer, J. A.; Zhao, J.; Van Duyne, R. P. J. A. o. c. r., Controlled plasmonic nanostructures for surface-enhanced spectroscopy and sensing. **2008**,41 (12), 1653-1661.
71. Barhoumi, A.; Zhang, D.; Tam, F.; Halas, N. J. J. J. o. t. A. C. S., Surface-enhanced Raman spectroscopy of DNA. **2008**,130 (16), 5523-5529.
72. Bonham, A. J.; Braun, G.; Pavel, I.; Moskovits, M.; Reich, N. O. J. J. o. t. A. C. S., Detection of sequence-specific protein-DNA interactions via surface enhanced resonance Raman scattering. **2007**,129 (47), 14572-14573.
73. Liu, D.; Huang, X.; Wang, Z.; Jin, A.; Sun, X.; Zhu, L.; Wang, F.; Ma, Y.; Niu, G.; Hight Walker, A. R. J. A. n., Gold nanoparticle-based activatable probe for sensing ultralow levels of prostate-specific antigen. **2013**,7 (6), 5568-5576.
74. Kang, B.; Afifi, M. M.; Austin, L. A.; El-Sayed, M. A. J. A. n., Exploiting the nanoparticle plasmon effect: observing drug delivery dynamics in single cells via Raman/fluorescence imaging spectroscopy. **2013**,7 (8), 7420-7427.
75. Qiu, L.; Chen, T.; Öçsoy, I.; Yasun, E.; Wu, C.; Zhu, G.; You, M.; Han, D.; Jiang, J.; Yu, R. J. N. l., A cell-targeted, size-photocontrollable, nuclear-uptake nanodrug delivery system for drug-resistant cancer therapy. **2014**,15 (1), 457-463.

76. Meyer, T. J. J. A. o. C. R., Chemical approaches to artificial photosynthesis. **1989**,22 (5), 163-170.
77. Ceroni, P., *The exploration of supramolecular systems and nanostructures by photochemical techniques*. Springer Science & Business Media: 2011; Vol. 78.
78. Nelson, J.; Chandler, R. E., Random walk models of charge transfer and transport in dye sensitized systems. *Coordination Chemistry Reviews* **2004**,248 (13-14), 1181-1194.
79. Ceroni, P.; Balzani, V., Photoinduced energy and electron transfer processes. In *The exploration of supramolecular systems and nanostructures by photochemical techniques*, Springer: 2012; pp 21-38.
80. Barbara, P. F.; Walker, G. C.; Smith, T. P., Vibrational modes and the dynamic solvent effect in electron and proton transfer. *Science* **1992**,256 (5059), 975-981.
81. Fumino, K.; Stange, P.; Fossog, V.; Hempelmann, R.; Ludwig, R., Equilibrium of Contact and Solvent-Separated Ion Pairs in Mixtures of Protic Ionic Liquids and Molecular Solvents Controlled by Polarity. *Angewandte Chemie International Edition* **2013**,52 (47), 12439-12442.
82. Gould, I. R.; Young, R. H.; Moody, R. E.; Farid, S. J. T. J. o. P. C., Contact and solvent-separated geminate radical ion pairs in electron-transfer photochemistry. **1991**,95 (5), 2068-2080.
83. Bhattacharyya, K.; Chowdhury, M., Environmental and magnetic field effects on exciplex and twisted charge transfer emission. *Chemical Reviews* **1993**,93 (1), 507-535.
84. Zachariasse, K. A.; Busse, R.; Schrader, U.; Kühnle, W., Intramolecular siglet and triplet excimers with diphenanthrylpropanes. *Chemical Physics Letters* **1982**,89 (4), 303-308.
85. Kavarnos, G. J.; Turro, N. J., Photosensitization by reversible electron transfer: theories, experimental evidence, and examples. *Chemical Reviews* **1986**,86 (2), 401-449.
86. Nath, D. N.; Chowdhury, M. J. P., Effect of variation of dielectric constant on the magnetic field modulation of exciplex luminescence. **1990**,34 (1), 51-66.
87. Basilevsky, M.; Chudinov, G. J. C. p., Dynamics of charge transfer chemical reactions in a polar medium within the scope of the Born-Kirkwood-Onsager model. **1991**,157 (3), 327-344.
88. Liu, X.; Wei, X.; Zhou, H.; Meng, S.; Zhao, Y.; Xue, J.; Zheng, X. J. T. J. o. P. C. A., UV and Resonance Raman Spectroscopic and Theoretical Studies on the Solvent-Dependent Ground and Excited-State Thione→Thiol Tautomerization of 4, 6-Dimethyl-2-mercaptoprimidine (DMMP). **2018**,122 (26), 5710-5720.
89. Agmon, N. J. T. J. o. c. p., Geminate recombination in proton-transfer reactions. III. Kinetics and equilibrium inside a finite sphere. **1988**,88 (9), 5639-5642.
90. Agmon, N. J. T. J. o. P. C. A., Elementary steps in excited-state proton transfer. **2005**,109 (1), 13-35.
91. Berkelbach, T. C.; Lee, H.-S.; Tuckerman, M. E. J. P. r. l., Concerted hydrogen-bond dynamics in the transport mechanism of the hydrated proton: A first-principles molecular dynamics study. **2009**,103 (23), 238302.
92. Chandra, A.; Tuckerman, M. E.; Marx, D. J. P. r. l., Connecting Solvation Shell Structure to Proton Transport Kinetics in Hydrogen-Bonded Networks via Population Correlation Functions. **2007**,99 (14), 145901.
93. Chen, H.; Voth, G. A.; Agmon, N. J. T. J. o. P. C. B., Kinetics of proton migration in liquid water. **2009**,114 (1), 333-339.
94. Cox, M. J.; Timmer, R. L.; Bakker, H. J.; Park, S.; Agmon, N. J. T. J. o. P. C. A., Distance-Dependent Proton Transfer along Water Wires Connecting Acid-Base Pairs. **2009**,113 (24), 6599-6606.
95. Feng, S.; Voth, G. A. J. T. J. o. P. C. B., Proton solvation and transport in hydrated nafion. **2011**,115 (19), 5903-5912.

96. Markovitch, O.; Agmon, N. *J. Phys. Chem. A* **2008**, *112* (8), 084505.
97. Marx, D.; Tuckerman, M. E.; Hutter, J.; Parrinello, M. *J. Chem. Phys.* **1999**, *111* (6), 601.
98. Maupin, C. M.; McKenna, R.; Silverman, D. N.; Voth, G. A. *J. Phys. Chem. B* **2009**, *113* (22), 7598-7608.
99. Förster, T. *Z. Naturforsch.* **1949**, *36* (1949) 186; *Z. Naturforsch.* **1950**, *54*, 531.
100. Weller, A. *J. Phys. Chem.* **1956**, *60* (1956) 1144; *J. Phys. Chem.* **1961**, *65*, 187.
101. Chou, P.-T.; Chen, Y.-C.; Yu, W.-S.; Chou, Y.-H.; Wei, C.-Y.; Cheng, Y.-M. *J. Phys. Chem. A* **2001**, *105* (10), 1731-1740.
102. Douhal, A.; Lahmani, F.; Zewail, A. H. *J. Phys. Chem. B* **1996**, *100* (2-3), 477-498.
103. Formosinho, S. J.; Arnaut, L. G. *J. Phys. Chem. B* **1993**, *97* (1), 21-48.
104. Simkovitch, R.; Karton-Lifshin, N.; Shomer, S.; Shabat, D.; Huppert, D. *J. Phys. Chem. A* **2013**, *117* (16), 3405-3413.
105. Simkovitch, R.; Shomer, S.; Gepshtein, R.; Huppert, D. *J. Phys. Chem. B* **2014**, *118* (6), 2253-2262.
106. Spry, D.; Fayer, M. *J. Phys. Chem. A* **2007**, *111* (20), 204501.
107. Agmon, N.; Levine, R. *J. Chem. Phys.* **1977**, *66* (2), 197-201.
108. Agmon, N.; Levine, R. *J. Chem. Phys.* **1980**, *72* (1-4), 330-336.
109. Agmon, N. *J. Chem. Phys.* **1981**, *75* (4), 333-365.
110. Marcus, R. In *Energetic and dynamical aspects of proton transfer reactions in solution*, Faraday Symposia of the Chemical Society, Royal Society of Chemistry: 1975; pp 60-68.
111. Franck, E. U., *Electrolyte Solutions*, von R. A. Robinson und R. H. Stokes. — *The Measurement and Interpretation of Conductance, Chemical Potential and Diffusion in Solutions of Simple Electrolytes*. Butterworths Scientific Publication, London 1959. **1960**, *72* (12), 426-426.
112. Luz, Z.; Meiboom, S. *J. Phys. Chem. B* **1964**, *68* (22), 4768-4769.
113. Belevich, I.; Verkhovskiy, M. I.; Wikström, M. *J. Phys. Chem. B* **2006**, *110* (7085), 829.
114. Cukier, R. I.; Nocera, D. G. *J. Am. Chem. Soc.* **1998**, *120* (1), 337-369.
115. Hammes-Schiffer, S. *J. Am. Chem. Soc.* **2001**, *123* (4), 273-281.
116. Huynh, M. H. V.; Meyer, T. *J. Phys. Chem. B* **2007**, *111* (11), 5004-5064.
117. Knight, C.; Voth, G. A. *J. Phys. Chem. A* **2011**, *115* (1), 101-109.
118. Mayer, J. M. *J. Am. Chem. Soc.* **2004**, *126*, 363-390.

119. Sjödin, M.; Styring, S.; Åkermark, B.; Sun, L.; Hammarström, L. J. J. o. t. A. C. S., Proton-coupled electron transfer from tyrosine in a tyrosine– ruthenium– tris-bipyridine complex: comparison with tyrosine oxidation in photosystem II. **2000**, *122* (16), 3932-3936.
120. Weatherly, S. C.; Yang, I. V.; Thorp, H. H. J. J. o. t. A. C. S., Proton-coupled electron transfer in duplex DNA: driving force dependence and isotope effects on electrocatalytic oxidation of guanine. **2001**, *123* (6), 1236-1237.
121. Hammes-Schiffer, S.; Soudackov, A. V. J. T. J. o. P. C. B., Proton-coupled electron transfer in solution, proteins, and electrochemistry. **2008**, *112* (45), 14108-14123.
122. Hammes-Schiffer, S., Theoretical perspectives on proton-coupled electron transfer reactions. *Accounts of Chemical Research* **2001**, *34* (4), 273-281.
123. Bhattacharyya, K.; Chowdhury, M. J. C. r., Environmental and magnetic field effects on exciplex and twisted charge transfer emission. **1993**, *93* (1), 507-535.
124. Breslin, D. T.; Schuster, G. B. J. J. o. t. A. C. S., Anthraquinone photonucleases: mechanisms for GG-selective and nonselective cleavage of double-stranded DNA. **1996**, *118* (10), 2311-2319.
125. Fox, M. A.; Chanon, M., *Photoinduced Electron Transfer: Photoinduced electron transfer reactions, inorganic substrates and applications*. Elsevier Science Limited: 1988.
126. Gould, I. R.; Turro, N. J.; Zimmt, M. B. J. A. i. p. o. c., Magnetic field and magnetic isotope effects on the products of organic reactions. **1984**, *20*, 1.
127. Pan, Y.; Fu, Y.; Liu, S.; Yu, H.; Gao, Y.; Guo, Q.; Yu, S. J. T. J. o. P. C. A., Studies on photoinduced H-atom and electron transfer reactions of o-naphthoquinones by laser flash photolysis. **2006**, *110* (23), 7316-7322.
128. Rogers, J. E.; Kelly, L. A. J. J. o. t. A. C. S., Nucleic acid oxidation mediated by naphthalene and benzophenone imide and diimide derivatives: consequences for DNA redox chemistry. **1999**, *121* (16), 3854-3861.
129. Steiner, U. E.; Ulrich, T. J. C. R., Magnetic field effects in chemical kinetics and related phenomena. **1989**, *89* (1), 51-147.
130. Turro, N. J. J. P. o. t. N. A. o. S., Influence of nuclear spin on chemical reactions: magnetic isotope and magnetic field effects (a review). **1983**, *80* (2), 609-621.
131. Nagakura, S.; Hayashi, H.; Azumi, T., *Dynamic spin chemistry*. Kodansha: 1998.
132. Gould, I. R.; Turro, N. J.; Zimmt, M. B., Magnetic field and magnetic isotope effects on the products of organic reactions. *Advances in physical organic chemistry* **1984**, *20*, 1-53.
133. Tanimoto, Y.; Fujiwara, Y., Handbook of Photochemistry and Photobiology. *Inorganic Photochemistry* **2003**, *1*, 413.
134. Hayashi, H.; Sakaguchi, Y. J. J. o. P.; Reviews, P. C. P., Magnetic field effects and CIDEP due to the d-type triplet mechanism in intra-molecular reactions. **2005**, *6* (1), 25-36.
135. Karogodina, T. Y.; Dranov, I. G.; Sergeeva, S. V.; Stass, D. V.; Steiner, U. E. J. C., Kinetic Magnetic-Field Effect Involving the Small Biologically Relevant Inorganic Radicals NO and O₂-. **2011**, *12* (9), 1714-1728.
136. Mori, Y.; Sakaguchi, Y.; Hayashi, H. J. T. J. o. P. C. A., Magnetic field effects on chemical reactions of biradical radical ion pairs in homogeneous fluid solvents. **2000**, *104* (21), 4896-4905.
137. Scaiano, J.; Jovanovic, S. V.; Morris, D. G. J. J. o. P.; Chemistry, P. A., Magnetic field effects on radical pairs photochemically derived from 2, 3, 6, 7-dibenzofluorenone. **1998**, *113* (3), 197-201.
138. Sengupta, T.; Dutta Choudhury, S.; Basu, S. J. J. o. t. A. C. S., Medium-dependent electron and H atom transfer between 2'-deoxyadenosine and menadione: a magnetic field effect study. **2004**, *126* (34), 10589-10593.

139. Tanimoto, Y.; Shimizu, K.; Udagawa, H.; Itoh, M. *J. C. L.*, Magnetic field effect on the photoinduced electron transfer reaction between duroquinone and aromatic amines in SDS micellar solution. **1983**,*12* (3), 353-356.
140. Tanimoto, Y.; Takayama, M.; Itoh, M.; Nakagaki, R.; Nagakura, S. *J. C. p. l.*, Magnetic field effects on the photoinduced electron-transfer reaction of 1-acetonaphthone and diphenylamine in micellar solution. **1986**,*129* (4), 414-418.
141. Turro, N. J.; Weed, G. C. *J. J. o. t. A. C. S.*, Micellar systems as supercages for reactions of geminate radical pairs. Magnetic effects. **1983**,*105* (7), 1861-1868.
142. Khudyakov, I. V.; Serebrennikov, Y. A.; Turro, N. J. *J. C. r.*, Spin-orbit coupling in free-radical reactions: on the way to heavy elements. **1993**,*93* (1), 537-570.
143. Steiner, U. E.; Haas, W. J. T. *J. o. P. C.*, Spin-orbit coupling induced magnetic field effects in electron-transfer reactions with excited triplets: the role of triplet exciplexes and radical pairs in geminate recombination. **1991**,*95* (5), 1880-1890.
144. McGlynn, S. P.; Azumi, T.; Kinoshita, M., Molecular spectroscopy of the triplet state. **1969**.
145. Benelmekki, M., An introduction to nanoparticles and nanotechnology. In *Designing Hybrid Nanoparticles*, Morgan & Claypool Publishers: 2015; pp 1-1-1-14.
146. Drexler, K. J. A. B. N. Y., NY. Elimelech, M.,; CR O'Melia, E. o. p. s. o. c. e. i. t. d. o. b. p. w. e. e. b. L., Engines of destruction, in engines of creation: The Coming Era of Nanotechnology. 1986. **1990**,*6*, 1153-1163.
147. Klabunde, K. J., Nanoscale materials in chemistry/Edited by Kenneth J. Klabunde.
148. Roco, M. C., The long view of nanotechnology development: the National Nanotechnology Initiative at 10 years. Springer: 2011.
149. Patra, J. K.; Das, G.; Fraceto, L. F.; Campos, E. V. R.; del Pilar Rodriguez-Torres, M.; Acosta-Torres, L. S.; Diaz-Torres, L. A.; Grillo, R.; Swamy, M. K.; Sharma, S. J. *J. o. n.*, Nano based drug delivery systems: recent developments and future prospects. **2018**,*16* (1), 71.
150. Santhosh, C.; Velmurugan, V.; Jacob, G.; Jeong, S. K.; Grace, A. N.; Bhatnagar, A. J. C. E. J., Role of nanomaterials in water treatment applications: a review. **2016**,*306*, 1116-1137.
151. Bean, C.; Livingston, u. D. *J. J. o. A. P.*, Superparamagnetism. **1959**,*30* (4), S120-S129.
152. Pankhurst, Q.; Thanh, N.; Jones, S.; Dobson, J. J. *J. o. P. D. A. P.*, Progress in applications of magnetic nanoparticles in biomedicine. **2009**,*42* (22), 224001.
153. Kelsall, R.; Hamley, I. W.; Geoghegan, M., *Nanoscale science and technology*. John Wiley & Sons: 2005.
154. Centi, G.; Perathoner, S. J. C., Nano-architecture and reactivity of titania catalytic materials. Quasi-1D nanostructures. **2007**,*19*, 367.
155. Jain, P. K.; El-Sayed, M. A. J. C. P. L., Plasmonic coupling in noble metal nanostructures. **2010**,*487* (4-6), 153-164.
156. Akbay, N.; Lakowicz, J. R.; Ray, K. J. T. *J. o. P. C. C.*, Distance-dependent metal-enhanced intrinsic fluorescence of proteins using polyelectrolyte layer-by-layer assembly and aluminum nanoparticles. **2012**,*116* (19), 10766-10773.
157. Hayden, S. C.; Austin, L. A.; Near, R. D.; Ozturk, R.; El-Sayed, M. A. J. *J. o. P.*; Chemistry, P. A., Plasmonic enhancement of photodynamic cancer therapy. **2013**,*269*, 34-41.
158. Jain, P. K.; El-Sayed, M. A. J. N. I., Noble metal nanoparticle pairs: effect of medium for enhanced nanosensing. **2008**,*8* (12), 4347-4352.
159. Linic, S.; Aslam, U.; Boerigter, C.; Morabito, M. J. N. m., Photochemical transformations on plasmonic metal nanoparticles. **2015**,*14* (6), 567.

160. Linic, S.; Christopher, P.; Xin, H.; Marimuthu, A. J. A. o. c. r., Catalytic and photocatalytic transformations on metal nanoparticles with targeted geometric and plasmonic properties. **2013**,*46* (8), 1890-1899.
161. Hu, E. L.; Brongersma, M.; Baca, A., Applications: nanophotonics and plasmonics. In *Nanotechnology Research Directions for Societal Needs in 2020*, Springer: 2011; pp 417-444.
162. Saha, B.; Bhattacharya, J.; Mukherjee, A.; Ghosh, A.; Santra, C.; Dasgupta, A. K.; Karmakar, P., In Vitro Structural and Functional Evaluation of Gold Nanoparticles Conjugated Antibiotics. *Nanoscale Research Letters* **2007**,*2* (12), 614.
163. Gu, H.; Ho, P. L.; Tong, E.; Wang, L.; Xu, B., Presenting Vancomycin on Nanoparticles to Enhance Antimicrobial Activities. *Nano Letters* **2003**,*3* (9), 1261-1263.
164. Chen, Y.-H.; Tsai, C.-Y.; Huang, P.-Y.; Chang, M.-Y.; Cheng, P.-C.; Chou, C.-H.; Chen, D.-H.; Wang, C.-R.; Shiau, A.-L.; Wu, C.-L., Methotrexate Conjugated to Gold Nanoparticles Inhibits Tumor Growth in a Syngeneic Lung Tumor Model. *Molecular Pharmaceutics* **2007**,*4* (5), 713-722.
165. Cheng, Y.; Samia, A. C.; Meyers, J. D.; Panagopoulos, I.; Fei, B.; Burda, C. J. J. o. t. A. C. S., Highly efficient drug delivery with gold nanoparticle vectors for in vivo photodynamic therapy of cancer. **2008**,*130* (32), 10643-10647.
166. Wang, F.; Wang, Y.-C.; Dou, S.; Xiong, M.-H.; Sun, T.-M.; Wang, J., Doxorubicin-Tethered Responsive Gold Nanoparticles Facilitate Intracellular Drug Delivery for Overcoming Multidrug Resistance in Cancer Cells. *ACS Nano* **2011**,*5* (5), 3679-3692.
167. Shenoy, D.; Fu, W.; Li, J.; Crasto, C.; Jones, G.; DiMarzio, C.; Sridhar, S.; Amiji, M. J. I. j. o. n., Surface functionalization of gold nanoparticles using hetero-bifunctional poly (ethylene glycol) spacer for intracellular tracking and delivery. **2006**,*1* (1), 51.
168. Bhattacharya, R.; Patra, C. R.; Earl, A.; Wang, S.; Katarya, A.; Lu, L.; Kizhakkedathu, J. N.; Yaszemski, M. J.; Greipp, P. R.; Mukhopadhyay, D.; Mukherjee, P., Attaching folic acid on gold nanoparticles using noncovalent interaction via different polyethylene glycol backbones and targeting of cancer cells. *Nanomedicine: Nanotechnology, Biology and Medicine* **2007**,*3* (3), 224-238.
169. Rana, S.; Bajaj, A.; Mout, R.; Rotello, V. M. J. A. d. d. r., Monolayer coated gold nanoparticles for delivery applications. **2012**,*64* (2), 200-216.
170. Jiles, D., *Introduction to magnetism and magnetic materials*. CRC press: 2015.
171. Charles, P. J. F.; Richard J. creswick, s., Pool JR, Ruslan prozorov, Horacio A. 3.
172. Abu-Dief, A. M.; Hamdan, S. K. J. A. J. o. N., Functionalization of magnetic nanoparticles: synthesis, characterization and their application in water purification. **2016**,*2* (3), 26-40.
173. Akbarzadeh, A.; Samiei, M.; Davaran, S. J. N. r. l., Magnetic nanoparticles: preparation, physical properties, and applications in biomedicine. **2012**,*7* (1), 144.
174. Alhakeim, H.; M. Redha, M. a.; Dawook, A. H., Synthesis of New Magnetic Nanoparticles and Study their Effect on Prolactin Structure. **2014**.
175. Mathew, D. S.; Juang, R.-S. J. C. E. J., An overview of the structure and magnetism of spinel ferrite nanoparticles and their synthesis in microemulsions. **2007**,*129* (1-3), 51-65.
176. Ramesh, C.; Selvanandan, S. In *An overview of magnetism of spinel nanoferrite particles and A study of chromium substituted Zn-Mn ferrites nanostructures via sol-gel method*, Nanoscience, Engineering and Technology (ICONSET), 2011 International Conference on, IEEE: 2011; pp 119-124.
177. Akbarzadeh, A.; Samiei, M.; Davaran, S., Magnetic nanoparticles: preparation, physical properties, and applications in biomedicine. *Nanoscale research letters* **2012**,*7* (1), 144.

178. Heidsieck, A. *Magnetic Nanoparticles-Characterization and Modeling for Drug Targeting Applications*. Technische Universität München, 2014.
179. Tauxe, L., *Essentials of paleomagnetism*. Univ of California Press: 2010.
180. Westwood, S. M. *The physics of magnetic particle inspection*. Durham University, 1993.
181. Maksymov, I. S. J. R. i. P., Magneto-plasmonic nanoantennas: Basics and applications. **2016**,*1*, 36-51.
182. Armelles, G.; Cebollada, A.; García-Martín, A.; González, M. U. J. A. O. M., Magnetoplasmonics: combining magnetic and plasmonic functionalities. **2013**,*1* (1), 10-35.
183. Adeyeye, A.; Singh, N. J. J. o. P. D. A. P., Large area patterned magnetic nanostructures. **2008**,*41* (15), 153001.
184. Feng, H. Y.; Luo, F.; Kekesi, R.; Granados, D.; Meneses-Rodríguez, D.; García, J. M.; García-Martín, A.; Armelles, G.; Cebollada, A. J. A. O. M., Magnetoplasmonic Nanorings as Novel Architectures with Tunable Magneto-optical Activity in Wide Wavelength Ranges. **2014**,*2* (7), 612-617.
185. Xu, Z.; Hou, Y.; Sun, S., Magnetic core/shell Fe₃O₄/Au and Fe₃O₄/Au/Ag nanoparticles with tunable plasmonic properties. *Journal of the American Chemical Society* **2007**,*129* (28), 8698-8699.
186. Maksymov, I. J. N., Magneto-plasmonics and resonant interaction of light with dynamic magnetisation in metallic and all-magneto-dielectric nanostructures. **2015**,*5* (2), 577-613.
187. Baron, C.; Elezzabi, A. J. O. E., Active plasmonic devices via electron spin. **2009**,*17* (9), 7117-7129.
188. Bardhan, R.; Lal, S.; Joshi, A.; Halas, N. J. J. A. o. c. r., Theranostic nanoshells: from probe design to imaging and treatment of cancer. **2011**,*44* (10), 936-946.
189. Larson, T. A.; Bankson, J.; Aaron, J.; Sokolov, K. J. N., Hybrid plasmonic magnetic nanoparticles as molecular specific agents for MRI/optical imaging and photothermal therapy of cancer cells. **2007**,*18* (32), 325101.
190. Tsai, C. S., *Biomacromolecules: Introduction to structure, function and informatics*. John Wiley & Sons: 2007.
191. Maubec, E.; Petrow, P.; Scheer-Senyarich, I.; Duvillard, P.; Lacroix, L.; Gelly, J.; Certain, A.; Duval, X.; Crickx, B.; Buffard, V. J. J. C. O., Phase II study of cetuximab as first-line single-drug therapy in patients with unresectable squamous cell carcinoma of the skin. **2011**,*29* (25), 3419-3426.
192. Wilson, W. R., Combination therapy for cancer. Google Patents: 2003.
193. Harrison, T. R.; Adams, R. D.; Bennett Jr, I. L.; Resnik, W. H.; Thorn, G. W.; Wintrobe, M. M. J. A. M., Principles of internal medicine. **1962**,*37* (11), 1246.
194. Katzung, B. G.; Masters, S. B.; Trevor, A. J., *Basic and Clinical Pharmacology (LANGE Basic Science)*. McGraw-Hill Education: 2012.
195. Bouayed, J.; Bohn, T. J. O. m.; longevity, c., Exogenous antioxidants—double-edged swords in cellular redox state: health beneficial effects at physiologic doses versus deleterious effects at high doses. **2010**,*3* (4), 228-237.
196. Liou, G.-Y.; Storz, P. J. F. r. r., Reactive oxygen species in cancer. **2010**,*44* (5), 479-496.
197. Poljsak, B.; Šuput, D.; Milisav, I. J. O. m.; longevity, c., Achieving the balance between ROS and antioxidants: when to use the synthetic antioxidants. **2013**,*2013*.
198. Karihtala, P.; Soini, Y. J. A., Reactive oxygen species and antioxidant mechanisms in human tissues and their relation to malignancies. **2007**,*115* (2), 81-103.
199. Steiling, H.; Munz, B.; Werner, S.; Brauchle, M. J. E. c. r., Different types of ROS-scavenging enzymes are expressed during cutaneous wound repair. **1999**,*247* (2), 484-494.

200. Godowski, K. J. T. J. o. c. d., Antimicrobial action of sanguinarine. **1989**,*1* (4), 96-101.
201. Dalvi, R. R., Sanguinarine: its potential as a liver toxic alkaloid present in the seeds of *Argemone mexicana*. *Experientia* **1985**,*41* (1), 77-8.
202. Godowski, K. C., Antimicrobial action of sanguinarine. *The Journal of clinical dentistry* **1989**,*1* (4), 96-101.
203. Lenfeld, J.; Kroutil, M.; Maršálek, E.; Slavik, J.; Preininger, V.; Šimánek, V. J. P. m., Antiinflammatory activity of quaternary benzophenanthridine alkaloids from *Chelidonium majus*. **1981**,*43* (10), 161-165.
204. Adhami, V. M.; Aziz, M. H.; Reagan-Shaw, S. R.; Nihal, M.; Mukhtar, H.; Ahmad, N. J. M. C. T., Sanguinarine causes cell cycle blockade and apoptosis of human prostate carcinoma cells via modulation of cyclin kinase inhibitor-cyclin-cyclin-dependent kinase machinery. **2004**,*3* (8), 933-940.
205. Ahsan, H.; Reagan-Shaw, S.; Breur, J.; Ahmad, N. J. C. l., Sanguinarine induces apoptosis of human pancreatic carcinoma AsPC-1 and BxPC-3 cells via modulations in Bcl-2 family proteins. **2007**,*249* (2), 198-208.
206. Debiton, E.; Madelmont, J.-C.; Legault, J.; Barthomeuf, C. J. C. c.; pharmacology, Sanguinarine-induced apoptosis is associated with an early and severe cellular glutathione depletion. **2003**,*51* (6), 474-482.
207. Han, M. H.; Kim, S. O.; Kim, G. Y.; Kwon, T. K.; Choi, B. T.; Lee, W. H.; Choi, Y. H. J. A.-c. d., Induction of apoptosis by sanguinarine in C6 rat glioblastoma cells is associated with the modulation of the Bcl-2 family and activation of caspases through downregulation of extracellular signal-regulated kinase and Akt. **2007**,*18* (8), 913-921.
208. Hussain, A. R.; Al-Jomah, N. A.; Siraj, A. K.; Manogaran, P.; Al-Hussein, K.; Abubaker, J.; Plataniias, L. C.; Al-Kuraya, K. S.; Uddin, S. J. C. r., Sanguinarine-dependent induction of apoptosis in primary effusion lymphoma cells. **2007**,*67* (8), 3888-3897.
209. Kim, S.; Lee, T. J.; Leem, J.; Choi, K. S.; Park, J. W.; Kwon, T. K. J. J. o. c. b., Sanguinarine-induced apoptosis: Generation of ROS, down-regulation of Bcl-2, c-FLIP, and synergy with TRAIL. **2008**,*104* (3), 895-907.
210. Sun, M.; Lou, W.; Chun, J. Y.; Cho, D. S.; Nadiminty, N.; Evans, C. P.; Chen, J.; Yue, J.; Zhou, Q.; Gao, A. C. J. G.; cancer, Sanguinarine suppresses prostate tumor growth and inhibits survivin expression. **2010**,*1* (3), 283-292.
211. Chaturvedi, M. M.; Kumar, A.; Darnay, B. G.; Chainy, G. B.; Agarwal, S.; Aggarwal, B. B. J. J. o. B. C., Sanguinarine (pseudochelethrine) is a potent inhibitor of NF- κ B activation, I κ B α phosphorylation, and degradation. **1997**,*272* (48), 30129-30134.
212. Bhadra, K.; Kumar, G. S. J. B. e. B. A.-G. S., Interaction of berberine, palmatine, coralyne, and sanguinarine to quadruplex DNA: a comparative spectroscopic and calorimetric study. **2011**,*1810* (4), 485-496.
213. Bhadra, K.; Kumar, G. S. J. M. r. r., Therapeutic potential of nucleic acid-binding isoquinoline alkaloids: Binding aspects and implications for drug design. **2011**,*31* (6), 821-862.
214. Maiti, M.; Kumar, G. S., Protoberberine alkaloids: physicochemical and nucleic acid binding properties. In *Bioactive Heterocycles IV*, Springer: 2007; pp 155-209.
215. Maiti, M.; Kumar, G. S. J. B. r., Biophysical aspects and biological implications of the interaction of benzophenanthridine alkaloids with DNA. **2009**,*1* (3), 119-129.
216. Maiti, M.; Kumar, G. S. J. M. R. R., Molecular aspects on the interaction of protoberberine, benzophenanthridine, and aristolochia group of alkaloids with nucleic acid structures and biological perspectives. **2007**,*27* (5), 649-695.
217. Ahmad, N.; Gupta, S.; Husain, M. M.; Heiskanen, K. M.; Mukhtar, H. J. C. C. R., Differential antiproliferative and apoptotic response of sanguinarine for cancer cells versus normal cells. **2000**,*6* (4), 1524-1528.

218. Haque, L.; Pradhan, A. B.; Bhuiya, S.; Das, S. J. P. C. C. P., Exploring the comparative binding aspects of benzophenanthridine plant alkaloid chelerythrine with RNA triple and double helices: a spectroscopic and calorimetric approach. **2015**,*17* (26), 17202-17213.
219. Bennett, M.; AHG, H. W.; Mimi Hernandez, M.; Snow, J.; MA, A. V., An Appalachian Plant Monograph.
220. Bhuiya, S.; Pradhan, A. B.; Haque, L.; Das, S. J. T. J. o. P. C. B., Molecular aspects of the interaction of iminium and alkanolamine forms of the anticancer alkaloid chelerythrine with plasma protein bovine serum albumin. **2015**,*120* (1), 5-17.
221. Chmura, S. J.; Nodzinski, E.; Weichselbaum, R. R.; Quintans, J. J. C. r., Protein kinase C inhibition induces apoptosis and ceramide production through activation of a neutral sphingomyelinase. **1996**,*56* (12), 2711-2714.
222. Varga, A.; Bölcskei, K.; Szöke, E.; Almasi, R.; Czeh, G.; Szolcsanyi, J.; Pethö, G. J. N., Relative roles of protein kinase A and protein kinase C in modulation of transient receptor potential vanilloid type 1 receptor responsiveness in rat sensory neurons in vitro and peripheral nociceptors in vivo. **2006**,*140* (2), 645-657.
223. Wang, J.-L.; Liu, D.; Zhang, Z.-J.; Shan, S.; Han, X.; Srinivasula, S. M.; Croce, C. M.; Alnemri, E. S.; Huang, Z. J. P. o. t. N. A. o. S., Structure-based discovery of an organic compound that binds Bcl-2 protein and induces apoptosis of tumor cells. **2000**,*97* (13), 7124-7129.
224. Wu-Zhang, A. X.; Newton, A. C. J. B. J., Protein kinase C pharmacology: refining the toolbox. **2013**,*452* (2), 195-209.
225. Chmura, S. J.; Dolan, M. E.; Cha, A.; Mauceri, H. J.; Kufe, D. W.; Weichselbaum, R. R. J. C. C. R., In vitro and in vivo activity of protein kinase C inhibitor chelerythrine chloride induces tumor cell toxicity and growth delay in vivo. **2000**,*6* (2), 737-742.
226. Colombo, M. L.; Bosisio, E. J. P. r., Pharmacological activities of chelidonium majusl.(papaveraceae). **1996**,*33* (2), 127-134.
227. Herbert, J.; Augereau, J.; Gleye, J.; Maffrand, J. J. B.; communications, b. r., Chelerythrine is a potent and specific inhibitor of protein kinase C. **1990**,*172* (3), 993-999.
228. Kemény-Beke, Á.; Aradi, J.; Damjanovich, J.; Beck, Z.; Facskó, A.; Berta, A.; Bodnár, A. J. C. l., Apoptotic response of uveal melanoma cells upon treatment with chelidonine, sanguinarine and chelerythrine. **2006**,*237* (1), 67-75.
229. Vogler, M.; Weber, K.; Dinsdale, D.; Schmitz, I.; Schulze-Osthoff, K.; Dyer, M.; Cohen, G. J. C. d.; differentiation, Different forms of cell death induced by putative BCL2 inhibitors. **2009**,*16* (7), 1030.
230. Basu, P.; Basu, A.; Kumar, G. S. J. T. J. o. C. T., Binding of the putative anticancer agent chelerythrine to double stranded poly (A): Calorimetry and spectral characterization studies. **2016**,*103*, 228-233.
231. Tegos, G.; Dai, T.; Fuchs, B. B.; Coleman, J. J.; Prates, R. A.; Astrakas, C.; St Denis, T. G.; Ribeiro, M. S.; Mylonakis, E.; Hamblin, M. R., Concepts and principles of photodynamic therapy as an alternative antifungal discovery platform. *Frontiers in microbiology* **2012**,*3*, 120.
232. Dobson, J.; de Queiroz, G. F.; Golding, J. P., Photodynamic therapy and diagnosis: Principles and comparative aspects. *The Veterinary Journal* **2017**.
233. Ni, D.; Ferreira, C. A.; Barnhart, T. E.; Quach, V.; Yu, B.; Jiang, D.; Wei, W.; Liu, H.; Engle, J. W.; Hu, P., Magnetic Targeting of Nanotheranostics Enhances Cerenkov Radiation-Induced Photodynamic Therapy. *Journal of the American Chemical Society* **2018**.
234. Song, R.; Hu, D.; Chung, H. Y.; Sheng, Z.; Yao, S., Lipid-polymer bilaminar oxygen nanobubbles for enhanced photodynamic therapy of cancer. *ACS applied materials & interfaces* **2018**.

235. Nag, O. K.; Naciri, J.; Erickson, J. S.; Oh, E.; Delehanty, J. B., Hybrid Liquid Crystal Nanocarriers for Enhanced Zinc Phthalocyanine-Mediated Photodynamic Therapy. *Bioconjugate chemistry* **2018**,*29* (8), 2701-2714.
236. Bai, J.; Jia, X.; Ruan, Y.; Wang, C.; Jiang, X., Photosensitizer-Conjugated Bi₂Te₃ Nanosheets as Theranostic Agent for Synergistic Photothermal and Photodynamic Therapy. *Inorganic chemistry* **2018**,*57* (16), 10180-10188.
237. Li, F.; Chen, C.; Yang, X.; He, X.; Zhao, Z.; Li, J.; Yu, Y.; Yang, X.; Wang, J., Acetal-Linked Hyperbranched Polyphosphoester Nanocarriers Loaded with Chlorin e6 for pH-Activatable Photodynamic Therapy. *ACS applied materials & interfaces* **2018**.
238. Wang, H.; Lv, B.; Tang, Z.; Zhang, M.; Ge, W.; Liu, Y.; He, X.; Zhao, K.; Zheng, X.; He, M., Scintillator-Based Nanohybrids with Sacrificial Electron Prodrug for Enhanced X-ray-Induced Photodynamic Therapy. *Nano letters* **2018**,*18* (9), 5768-5774.
239. Chakraborty, S. D.; Sau, A.; Maity, A.; Pal, U.; Sengupta, C.; Bhattacharya, M.; Bhattacharjee, G.; Banik, S.; Satpati, B.; Basu, S. J. T. J. o. P. C. C., Low Magnetic Field Induced Surface Enhanced Transient Spin-Trajectory Modulation of a Prototype Anticancer Drug Sanguinarine on a Single Domain Superparamagnetic Nanosurface. **2018**,*122* (36), 20619-20631.
240. Ganguly, B. N. In *Nanomaterials in Bio-Medical Applications: A Novel approach*, Materials Research Forum LLC: 2018.
241. Griffin, J.; Singh, A. K.; Senapati, D.; Rhodes, P.; Mitchell, K.; Robinson, B.; Yu, E.; Ray, P. C. J. C. A. E. J., Size-and distance-dependent nanoparticle surface-energy transfer (NSET) method for selective sensing of hepatitis C virus RNA. **2009**,*15* (2), 342-351.
242. Cheraghipour, E.; Javadpour, S.; Mehdizadeh, A. R. J. J. o. B. S.; Engineering, Citrate capped superparamagnetic iron oxide nanoparticles used for hyperthermia therapy. **2012**,*5* (12), 715.
243. Bowers, K. J.; Chow, D. E.; Xu, H.; Dror, R. O.; Eastwood, M. P.; Gregersen, B. A.; Klepeis, J. L.; Kolossvary, I.; Moraes, M. A.; Sacerdoti, F. D. In *Scalable algorithms for molecular dynamics simulations on commodity clusters*, SC 2006 conference, proceedings of the ACM/IEEE, IEEE: 2006; pp 43-43.
244. Banks, J. L.; Beard, H. S.; Cao, Y.; Cho, A. E.; Damm, W.; Farid, R.; Felts, A. K.; Halgren, T. A.; Mainz, D. T.; Maple, J. R., Integrated modeling program, applied chemical theory (IMPACT). *Journal of computational chemistry* **2005**,*26* (16), 1752-1780.
245. Pal, U.; Pramanik, S. K.; Bhattacharya, B.; Banerji, B.; Maiti, N. C., Binding interaction of a gamma-aminobutyric acid derivative with serum albumin: an insight by fluorescence and molecular modeling analysis. *SpringerPlus* **2016**,*5* (1), 1121.
246. Fasman, G. D., *Handbook of Biochemistry: Section D Physical Chemical Data, Volume I*. CRC Press: 2018.
247. Sambrook, J.; Fritsch, E. F.; Maniatis, T., *Molecular cloning: a laboratory manual*. Cold spring harbor laboratory press: 1989.
248. Blobel, G.; Potter, V. R., Nuclei from rat liver: isolation method that combines purity with high yield. *Science* **1966**,*154* (3757), 1662-1665.
249. Majumder, P.; Dasgupta, D., Effect of DNA groove binder distamycin A upon chromatin structure. *PLoS One* **2011**,*6* (10), e26486.
250. Barhoumi, A.; Zhang, D.; Tam, F.; Halas, N. J., Surface-Enhanced Raman Spectroscopy of DNA. *Journal of the American Chemical Society* **2008**,*130* (16), 5523-5529.
251. Bonham, A. J.; Braun, G.; Pavel, I.; Moskovits, M.; Reich, N. O., Detection of Sequence-Specific Protein-DNA Interactions via Surface Enhanced Resonance Raman Scattering. *Journal of the American Chemical Society* **2007**,*129* (47), 14572-14573.

252. Camden, J. P.; Dieringer, J. A.; Zhao, J.; Van Duyne, R. P., Controlled Plasmonic Nanostructures for Surface-Enhanced Spectroscopy and Sensing. *Accounts of Chemical Research* **2008**,*41* (12), 1653-1661.
253. Kang, B.; Afifi, M. M.; Austin, L. A.; El-Sayed, M. A., Exploiting the Nanoparticle Plasmon Effect: Observing Drug Delivery Dynamics in Single Cells via Raman/Fluorescence Imaging Spectroscopy. *ACS Nano* **2013**,*7* (8), 7420-7427.
254. Liu, D.; Huang, X.; Wang, Z.; Jin, A.; Sun, X.; Zhu, L.; Wang, F.; Ma, Y.; Niu, G.; Hight Walker, A. R.; Chen, X., Gold Nanoparticle-Based Activatable Probe for Sensing Ultralow Levels of Prostate-Specific Antigen. *ACS Nano* **2013**,*7* (6), 5568-5576.
255. Qiu, L.; Chen, T.; Öçsoy, I.; Yasun, E.; Wu, C.; Zhu, G.; You, M.; Han, D.; Jiang, J.; Yu, R.; Tan, W., A Cell-Targeted, Size-Photocontrollable, Nuclear-Uptake Nanodrug Delivery System for Drug-Resistant Cancer Therapy. *Nano Letters* **2015**,*15* (1), 457-463.
256. Sengupta, T.; Dutta Choudhury, S.; Basu, S., Medium-Dependent Electron and H Atom Transfer between 2'-Deoxyadenosine and Menadione: A Magnetic Field Effect Study. *Journal of the American Chemical Society* **2004**,*126* (34), 10589-10593.
257. Dey, D.; Bose, A.; Chakraborty, M.; Basu, S., Magnetic Field Effect on Photoinduced Electron Transfer between Dibenzo[a,c]phenazine and Different Amines in Acetonitrile–Water Mixture. *The Journal of Physical Chemistry A* **2007**,*111* (5), 878-884.
258. Negrón-Encarnación, I.; Arce, R.; Jiménez, M. J. T. J. o. P. C. A., Characterization of acridine species adsorbed on (NH₄)₂SO₄, SiO₂, Al₂O₃, and MgO by steady-state and time-resolved fluorescence and diffuse reflectance techniques. **2005**,*109* (5), 787-797.
259. Grodowski, M.; Veyret, B.; Weiss, K. J. P.; Photobiology, Photochemistry of flavins. II. Photophysical properties of alloxazines and isoalloxazines. **1977**,*26* (4), 341-352.
260. Wink, M.; Roberts, M. F., *Alkaloids: biochemistry, ecology, and medicinal applications*. Plenum Press: 1998.
261. Cushnie, T. P. T.; Cushnie, B.; Lamb, A. J., Alkaloids: An overview of their antibacterial, antibiotic-enhancing and antivirulence activities. *International Journal of Antimicrobial Agents* **2014**,*44* (5), 377-386.
262. Kittakoop, P.; Mahidol, C.; Ruchirawat, S., Alkaloids as Important Scaffolds in Therapeutic Drugs for the Treatments of Cancer, Tuberculosis, and Smoking Cessation. *Current Topics in Medicinal Chemistry* **2013**,*14* (2), 239-252.
263. Qiu, S.; Sun, H.; Zhang, A.-H.; Xu, H.-Y.; Yan, G.-L.; Han, Y.; Wang, X.-J., Natural alkaloids: basic aspects, biological roles, and future perspectives. *Chinese Journal of Natural Medicines* **2014**,*12* (6), 401-406.
264. Russo, P.; Frustaci, A.; Del Bufalo, A.; Fini, M.; Cesario, A., Multitarget Drugs of Plants Origin Acting on Alzheimer's Disease. *Current Medicinal Chemistry* **2013**,*20* (13), 1686-1693.
265. Li, W.; Li, H.; Yao, H.; Mu, Q.; Zhao, G.; Li, Y.; Hu, H.; Niu, X., Pharmacokinetic and anti-inflammatory effects of sanguinarine solid lipid nanoparticles. *Inflammation* **2014**,*37* (2), 632-638.
266. Niu, X.; Fan, T.; Li, W.; Xing, W.; Huang, H., The anti-inflammatory effects of sanguinarine and its modulation of inflammatory mediators from peritoneal macrophages. *European journal of pharmacology* **2012**,*689* (1-3), 262-269.
267. Vrba, J.; Hrbáč, J.; Ulrichová, J.; Modrianský, M., Sanguinarine is a potent inhibitor of oxidative burst in DMSO-differentiated HL-60 cells by a non-redox mechanism. *Chemico-biological interactions* **2004**,*147* (1), 35-47.
268. Yang, X.-J.; Miao, F.; Yao, Y.; Cao, F.-J.; Yang, R.; Ma, Y.-N.; Qin, B.-F.; Zhou, L., In vitro antifungal activity of sanguinarine and chelerythrine derivatives against phytopathogenic fungi. *Molecules* **2012**,*17* (11), 13026-13035.

269. Adhami, V. M.; Aziz, M. H.; Mukhtar, H.; Ahmad, N. J. C. C. R., Activation of prodeath Bcl-2 family proteins and mitochondrial apoptosis pathway by sanguinarine in immortalized human HaCaT keratinocytes. *2003*,**9** (8), 3176-3182.
270. Holy, J.; Lamont, G.; Perkins, E. *BMC Cell Biology* **2006**,**7** (1), 13.
271. Pica, F.; Balestrieri, E.; Serafino, A.; Sorrentino, R.; Gaziano, R.; Moroni, G.; Moroni, N.; Palmieri, G.; Mattei, M.; Garaci, E.; Sinibaldi-Vallebona, P., Antitumor effects of the benzophenanthridine alkaloid sanguinarine in a rat syngeneic model of colorectal cancer. *Anti-Cancer Drugs* **2012**,**23** (1), 32-42.
272. Sun, M.; Lou, W.; Chun, J. Y.; Cho, D. S.; Nadiminty, N.; Evans, C. P.; Chen, J.; Yue, J.; Zhou, Q.; Gao, A. C., Sanguinarine Suppresses Prostate Tumor Growth and Inhibits Survivin Expression. *Genes & Cancer* **2010**,**1** (3), 283-292.
273. Obiang-Obounou, B. W.; Kang, O.-H.; Choi, J.-G.; Keum, J.-H.; Kim, S.-B.; Mun, S.-H.; Shin, D.-W.; Kim, K. W.; Park, C.-B.; Kim, Y.-G. J. T. J. o. t. s., The mechanism of action of sanguinarine against methicillin-resistant *Staphylococcus aureus*. **2011**,**36** (3), 277-283.
274. Ji, X.; Sun, H.; Zhou, H.; Xiang, J.; Tang, Y.; Zhao, C., The interaction of telomeric DNA and C-myc22 G-quadruplex with 11 natural alkaloids. *Nucleic acid therapeutics* **2012**,**22** (2), 127-136.
275. Satpathi, S.; Gavvala, K.; Hazra, P., Fluorescence switching of sanguinarine in micellar environments. *Physical Chemistry Chemical Physics* **2015**,**17** (32), 20725-20732.
276. Banerjee, A.; Sanyal, S.; Kulkarni, K. K.; Jana, K.; Roy, S.; Das, C.; Dasgupta, D., Anticancer drug mithramycin interacts with core histones: An additional mode of action of the DNA groove binder. *FEBS Open Bio* **2014**,**4** (1), 987-995.
277. Gumenyuk, V.; Bashmakova, N.; Kutovyy, S. Y.; Yashchuk, V.; Zaika, L. J. a. p. a., Binding parameters of alkaloids Berberine and sanguinarine with DNA. **2012**.
278. Maiti, M.; Das, S.; Sen, A.; Das, A.; Kumar, G. S.; Nandi, R., Influence of DNA Structures on the Conversion of Sanguinarine Alkanolamine Form to Iminium Form. *Journal of Biomolecular Structure and Dynamics* **2002**,**20** (3), 455-464.
279. Saran, A.; Srivastava, S.; Coutinho, E.; Maiti, M. J. I. j. o. b.; biophysics, ¹H NMR investigation of the interaction of berberine and sanguinarine with DNA. **1995**,**32** (2), 74-77.
280. Selvi, R.; Pradhan, S. K.; Shandilya, J.; Das, C.; Sailaja, B. S.; Gadad, S. S.; Reddy, A.; Dasgupta, D.; Kundu, T. K. J. C.; biology, Sanguinarine interacts with chromatin, modulates epigenetic modifications, and transcription in the context of chromatin. **2009**,**16** (2), 203-216.
281. Bai, L.-P.; Zhao, Z.-Z.; Cai, Z.; Jiang, Z.-H., DNA-binding affinities and sequence selectivity of quaternary benzophenanthridine alkaloids sanguinarine, chelerythrine, and nitidine. *Bioorganic & Medicinal Chemistry* **2006**,**14** (16), 5439-5445.
282. Hossain, M.; Kumar, G. S., DNA binding of benzophenanthridine compounds sanguinarine versus ethidium: Comparative binding and thermodynamic profile of intercalation. *The Journal of Chemical Thermodynamics* **2009**,**41** (6), 764-774.
283. Luger, K.; Mäder, A. W.; Richmond, R. K.; Sargent, D. F.; Richmond, T. J., Crystal structure of the nucleosome core particle at 2.8 Å resolution. *Nature* **1997**,**389** (6648), 251-260.
284. Biswas, M.; Voltz, K.; Smith, J. C.; Langowski, J., Role of Histone Tails in Structural Stability of the Nucleosome. *PLoS Computational Biology* **2011**,**7** (12), e1002279.
285. Griffin, J.; Singh, A. K.; Senapati, D.; Rhodes, P.; Mitchell, K.; Robinson, B.; Yu, E.; Ray, P. C., Size- and Distance-Dependent Nanoparticle Surface-Energy Transfer (NSET) Method for Selective Sensing of Hepatitis C Virus RNA. *Chemistry - A European Journal* **2009**,**15** (2), 342-351.

286. Haynes, C. L.; Yonzon, C. R.; Zhang, X.; Van Duyne, R. P., Surface-enhanced Raman sensors: early history and the development of sensors for quantitative biowarfare agent and glucose detection. *Journal of Raman Spectroscopy* **2005**,*36* (6-7), 471-484.
287. Lu, W.; Singh, A. K.; Khan, S. A.; Senapati, D.; Yu, H.; Ray, P. C., Gold Nano-Popcorn-Based Targeted Diagnosis, Nanotherapy Treatment, and In Situ Monitoring of Photothermal Therapy Response of Prostate Cancer Cells Using Surface-Enhanced Raman Spectroscopy. *Journal of the American Chemical Society* **2010**,*132* (51), 18103-18114.
288. Quang, L. X.; Lim, C.; Seong, G. H.; Choo, J.; Do, K. J.; Yoo, S.-K., A portable surface-enhanced Raman scattering sensor integrated with a lab-on-a-chip for field analysis. *Lab on a Chip* **2008**,*8* (12), 2214.
289. Senapati, D.; Dasary, S. S. R.; Singh, A. K.; Senapati, T.; Yu, H.; Ray, P. C., A Label-Free Gold-Nanoparticle-Based SERS Assay for Direct Cyanide Detection at the Parts-per-Trillion Level. *Chemistry - A European Journal* **2011**,*17* (30), 8445-8451.
290. Vo-Dinh, T.; Yan, F.; Wabuyele, M. B., Surface-enhanced Raman scattering for medical diagnostics and biological imaging. *Journal of Raman Spectroscopy* **2005**,*36* (6-7), 640-647.
291. Alvarez-Puebla, R. A.; Liz-Marzán, L. M., SERS-Based Diagnosis and Biodetection. *Small* **2010**,*6* (5), 604-610.
292. Vikesland, P. J.; Wigginton, K. R., Nanomaterial Enabled Biosensors for Pathogen Monitoring - A Review. *Environmental Science & Technology* **2010**,*44* (10), 3656-3669.
293. Motevich, I. G.; Strelak', N. D.; Nowicky, J. W.; Maskevich, S. A., Absorption, fluorescence, and SERS spectra of sanguinarine at different pH values. *Journal of Applied Spectroscopy* **2007**,*74* (5), 666-672.
294. Aich, S.; Basu, S., Magnetic field effect: A tool for identification of spin state in a photoinduced electron-transfer reaction. *The Journal of Physical Chemistry A* **1998**,*102* (4), 722-729.
295. Atkins, P.; Evans, G., Magnetic field effects on chemiluminescent fluid solutions. *Molecular Physics* **1975**,*29* (3), 921-935.
296. Atkins, P.; Lambert, T., . The effect of a magnetic field on chemical reactions. *Annual Reports on the Progress of Chemistry, Section A: Physical and Inorganic Chemistry* **1975**,*72*, 67-88.
297. Bera, K.; Sau, A.; Mondal, P.; Mukherjee, R.; Mookherjee, D.; Metya, A.; Kundu, A. K.; Mandal, D.; Satpati, B.; Chakrabarti, O., Metamorphosis of Ruthenium-Doped Carbon Dots: In Search of the Origin of Photoluminescence and Beyond. *Chemistry of Materials* **2016**,*28* (20), 7404-7413.
298. Klein, M.; Pankiewicz, R.; Zalas, M.; Stampor, W., Magnetic field effects in dye-sensitized solar cells controlled by different cell architecture. *Scientific reports* **2016**,*6*, 30077.
299. Lim, Y. T.; Kim, S.; Nakayama, A.; Stott, N. E.; Bawendi, M. G.; Frangioni, J. V., Selection of quantum dot wavelengths for biomedical assays and imaging. *Molecular imaging* **2003**,*2* (1), 15353500200302163.
300. Sako, Y.; Minoghchi, S.; Yanagida, T., Single-molecule imaging of EGFR signalling on the surface of living cells. *Nature cell biology* **2000**,*2* (3), 168.
301. Sengupta, T.; Dutta Choudhury, S.; Basu, S., Medium-dependent electron and H atom transfer between 2'-deoxyadenosine and menadione: a magnetic field effect study. *Journal of the American Chemical Society* **2004**,*126* (34), 10589-10593.
302. Steiner, U. E.; Ulrich, T., Magnetic field effects in chemical kinetics and related phenomena. *Chemical Reviews* **1989**,*89* (1), 51-147.
303. Tokunaga, M.; Imamoto, N.; Sakata-Sogawa, K., Highly inclined thin illumination enables clear single-molecule imaging in cells. *Nature methods* **2008**,*5* (2), 159.

304. McCamey, D.; Seipel, H.; Paik, S.; Walter, M.; Borys, N.; Lupton, J.; Boehme, C., Spin Rabi flopping in the photocurrent of a polymer light-emitting diode. *Nature materials* **2008**,*7* (9), 723.
305. Chen, C.-p.; J. Heinsohn, R.; N. Mulay, L., Effect of electrical and magnetic fields on chemical equilibrium. *Journal of the Physical Society of Japan* **1968**,*25* (2), 319-322.
306. Elf, J.; Li, G.-W.; Xie, X. S., Probing transcription factor dynamics at the single-molecule level in a living cell. *Science* **2007**,*316* (5828), 1191-1194.
307. Kural, C.; Kim, H.; Syed, S.; Goshima, G.; Gelfand, V. I.; Selvin, P. R., Kinesin and dynein move a peroxisome in vivo: a tug-of-war or coordinated movement? *Science* **2005**,*308* (5727), 1469-1472.
308. Bates, M.; Huang, B.; Dempsey, G. T.; Zhuang, X., Multicolor super-resolution imaging with photo-switchable fluorescent probes. *Science* **2007**,*317* (5845), 1749-1753.
309. Betzig, E.; Patterson, G. H.; Sougrat, R.; Lindwasser, O. W.; Olenych, S.; Bonifacino, J. S.; Davidson, M. W.; Lippincott-Schwartz, J.; Hess, H. F., Imaging intracellular fluorescent proteins at nanometer resolution. *Science* **2006**,*313* (5793), 1642-1645.
310. Goswami, N.; Lin, F.; Liu, Y.; Leong, D. T.; Xie, J., Highly luminescent thiolated gold nanoclusters impregnated in nanogel. *Chemistry of Materials* **2016**,*28* (11), 4009-4016.
311. Richards, C. I.; Hsiang, J.-C.; Senapati, D.; Patel, S.; Yu, J.; Vosch, T.; Dickson, R. M., Optically modulated fluorophores for selective fluorescence signal recovery. *Journal of the American Chemical Society* **2009**,*131* (13), 4619-4621.
312. Jin, W.; Liu, C., Luminescence rule of polycyclic aromatic hydrocarbons in micelle-stabilized room-temperature phosphorescence. *Analytical Chemistry* **1993**,*65* (7), 863-865.
313. Powell, B., Conservation laws, radiative decay rates, and excited state localization in organometallic complexes with strong spin-orbit coupling. *Scientific reports* **2015**,*5*.
314. Nehrkorn, J.; Schnegg, A.; Holldack, K.; Stoll, S., General magnetic transition dipole moments for electron paramagnetic resonance. *Physical review letters* **2015**,*114* (1), 010801.
315. Sugimoto, T.; Fukutani, K., Electric-field-induced nuclear-spin flips mediated by enhanced spin-orbit coupling. *Nature Physics* **2011**,*7* (4), 307.
316. Eremenko, V.; Kaner, N.; Litvinenko, Y. G.; Shapiro, V., Spin-flopping in MnF₂ in a tilted magnetic field: Spin-noncollinearity of photoexcited and ground-state Mn²⁺ ions. *Solid state communications* **1983**,*45* (11), 975-976.
317. Wang, X.-Y.; Wang, L.; Wang, Z.-M.; Su, G.; Gao, S., Coexistence of spin-canting, metamagnetism, and spin-flop in a (4, 4) layered manganese azide polymer. *Chemistry of materials* **2005**,*17* (25), 6369-6380.
318. Cohen, A. E., Nanomagnetic control of intersystem crossing. *The Journal of Physical Chemistry A* **2009**,*113* (41), 11084-11092.
319. Dollinger, T.; Kammermeier, M.; Scholz, A.; Wenk, P.; Schliemann, J.; Richter, K.; Winkler, R., Signatures of spin-preserving symmetries in two-dimensional hole gases. *Physical Review B* **2014**,*90* (11), 115306.
320. Krzykowski, M.; Gawęlczyk, M.; Machnikowski, P., Carrier Spin Dephasing during Spin-Preserving Tunneling in Coupled Quantum Dots. *Acta Physica Polonica A* **2016**,*130* (5), 1165-1168.
321. Chakraborty, B.; Bose, A.; Basu, S., 4. Electron transfer and hydrogen abstraction in biologically relevant systems.
322. Musser, A. J.; Liebel, M.; Schnedermann, C.; Wende, T.; Kehoe, T. B.; Rao, A.; Kukura, P., Evidence for conical intersection dynamics mediating ultrafast singlet exciton fission. *Nature Physics* **2015**,*11* (4), 352.

323. Zaari, R. R.; Varganov, S. A., Nonadiabatic transition state theory and trajectory surface hopping dynamics: intersystem crossing between 3B1 and 1A1 states of SiH₂. *The Journal of Physical Chemistry A* **2015**,*119* (8), 1332-1338.
324. Carey, R.; Isaac, E. D., Magnetic domains and techniques for their observation. **1966**.
325. Chou, S. Y., Patterned magnetic nanostructures and quantized magnetic disks. *Proceedings of the IEEE* **1997**,*85* (4), 652-671.
326. Hu, B.; Wu, Y.; Zhang, Z.; Dai, S.; Shen, J., Effects of ferromagnetic nanowires on singlet and triplet exciton fractions in fluorescent and phosphorescent organic semiconductors. *Applied physics letters* **2006**,*88* (2), 022114.
327. Sun, C.-J.; Wu, Y.; Xu, Z.; Hu, B.; Bai, J.; Wang, J.-P.; Shen, J., Enhancement of quantum efficiency of organic light emitting devices by doping magnetic nanoparticles. *Applied physics letters* **2007**,*90* (23), 232110.
328. Bassett, L. C.; Heremans, F. J.; Christle, D. J.; Yale, C. G.; Burkard, G.; Buckley, B. B.; Awschalom, D. D., Ultrafast optical control of orbital and spin dynamics in a solid-state defect. *Science* **2014**,*345* (6202), 1333-1337.
329. Kumar, P.; Kumar, H.; Chand, S.; Jain, S.; Kumar, V.; Kumar, V.; Pant, R.; Tandon, R., Effect of CoFe magnetic nanoparticles on the hole transport in poly (2-methoxy, 5-(2-ethylhexyloxy) 1, 4-phenylenevinylene). *Journal of Physics D: Applied Physics* **2008**,*41* (18), 185104.
330. Herve, P.; Nome, F.; Fendler, J. H., Magnetic effects on chemical reactions in the absence of magnets. Effects of surfactant vesicle entrapped magnetite particles on benzophenone photochemistry. *Journal of the American Chemical Society* **1984**,*106* (26), 8291-8292.
331. Scaiano, J.; Monahan, S.; Renaud, J., Dramatic effect of magnetite particles on the dynamics of photogenerated free radicals. *Photochemistry and photobiology* **1997**,*65* (4), 759-762.
332. Chakraborty, S. D.; Sau, A.; Kuznetsov, D. V.; Banerjee, A.; Bardhan, M.; Bhattacharya, M.; Dasgupta, D.; Basu, S.; Senapati, D., Development of a Triplet–Triplet Absorption Ruler: DNA-and Chromatin-Mediated Drug Molecule Release from a Nanosurface. *The Journal of Physical Chemistry B* **2016**,*120* (27), 6872-6881.
333. Keeler, J., *Understanding NMR spectroscopy*. John Wiley & Sons: 2011.
334. Thiaville, A.; Nakatani, Y.; Miltat, J.; Suzuki, Y., Micromagnetic understanding of current-driven domain wall motion in patterned nanowires. *EPL (Europhysics Letters)* **2005**,*69* (6), 990.
335. Zhang, S.; Li, Z., Roles of nonequilibrium conduction electrons on the magnetization dynamics of ferromagnets. *Physical Review Letters* **2004**,*93* (12), 127204.
336. Munowitz, M.; Pines, A., Multiple-Quantum NMR. *Adv. Chem. Phys* **1987**,*66*, 1.
337. Placidi, G., *MRI: essentials for innovative technologies*. CRC Press: 2012.
338. Leeson, P. D.; Springthorpe, B., The influence of drug-like concepts on decision-making in medicinal chemistry. *Nature Reviews Drug Discovery* **2007**,*6* (11), 881.
339. Lipinski, C. A., Lead-and drug-like compounds: the rule-of-five revolution. *Drug Discovery Today: Technologies* **2004**,*1* (4), 337-341.
340. Roberts, M. F., *Alkaloids: biochemistry, ecology, and medicinal applications*. Springer Science & Business Media: 2013.
341. Adhami, V. M.; Aziz, M. H.; Mukhtar, H.; Ahmad, N., Activation of prodeath Bcl-2 family proteins and mitochondrial apoptosis pathway by sanguinarine in immortalized human HaCaT keratinocytes. *Clinical Cancer Research* **2003**,*9* (8), 3176-3182.
342. Godowski, K., Antimicrobial action of sanguinarine. *The Journal of clinical dentistry* **1989**,*1* (4), 96-101.

343. Holy, J.; Lamont, G.; Perkins, E., Disruption of nucleocytoplasmic trafficking of cyclin D1 and topoisomerase II by sanguinarine. *BMC cell biology* **2006**,*7* (1), 13.
344. Obiang-Obounou, B. W.; Kang, O.-H.; Choi, J.-G.; Keum, J.-H.; Kim, S.-B.; Mun, S.-H.; Shin, D.-W.; Kim, K. W.; Park, C.-B.; Kim, Y.-G., The mechanism of action of sanguinarine against methicillin-resistant *Staphylococcus aureus*. *The Journal of toxicological sciences* **2011**,*36* (3), 277-283.
345. Pica, F.; Balestrieri, E.; Serafino, A.; Sorrentino, R.; Gaziano, R.; Moroni, G.; Moroni, N.; Palmieri, G.; Mattei, M.; Garaci, E., Antitumor effects of the benzophenanthridine alkaloid sanguinarine in a rat syngeneic model of colorectal cancer. *Anti-cancer drugs* **2012**,*23* (1), 32-42.
346. Cho, S.-J.; Idrobo, J.-C.; Olamit, J.; Liu, K.; Browning, N. D.; Kauzlarich, S. M., Growth mechanisms and oxidation resistance of gold-coated iron nanoparticles. *Chemistry of materials* **2005**,*17* (12), 3181-3186.
347. Sheng-Nan, S.; Chao, W.; Zan-Zan, Z.; Yang-Long, H.; Venkatraman, S. S.; Zhi-Chuan, X., Magnetic iron oxide nanoparticles: Synthesis and surface coating techniques for biomedical applications. *Chinese Physics B* **2014**,*23* (3), 037503.
348. Vilchiz, V. H.; Kloefer, J. A.; Germaine, A. C.; Lenchenkov, V. A.; Bradforth, S. E., Map for the relaxation dynamics of hot photoelectrons injected into liquid water via anion threshold photodetachment and above threshold solvent ionization. *The Journal of Physical Chemistry A* **2001**,*105* (10), 1711-1723.
349. Van Dijk, B.; Carpenter, J.; Hoff, A.; Hore, P., Magnetic field effects on the recombination kinetics of radical pairs. *The Journal of Physical Chemistry B* **1998**,*102* (2), 464-472.
350. Pal, S. K.; Peon, J.; Bagchi, B.; Zewail, A. H., Biological water: femtosecond dynamics of macromolecular hydration. ACS Publications: 2002.
351. Feynman, R. P.; Leighton, R. B.; Sands, M., The Feynman Lectures in Physics, Vol. II. Addison-Wesley: 2002.
352. Birnbaum, M.; Stocker, T. L., Effect of electron-hole recombination processes on semiconductor reflectivity modulation. *British Journal of Applied Physics* **1966**,*17* (4), 461.
353. Van der Holst, J.; Van Oost, F.; Coehoorn, R.; Bobbert, P., Electron-hole recombination in disordered organic semiconductors: Validity of the Langevin formula. *Physical Review B* **2009**,*80* (23), 235202.
354. Basu, P.; Bhowmik, D.; Kumar, G. S. J. J. o. P.; Biology, P. B., The benzophenanthridine alkaloid chelerythrine binds to DNA by intercalation: Photophysical aspects and thermodynamic results of iminium versus alkanolamine interaction. **2013**,*129*, 57-68.
355. Basu, P.; Kumar, G. S. J. R. A., Structural and thermodynamic basis of interaction of the putative anticancer agent chelerythrine with single, double and triple-stranded RNAs. **2015**,*5* (38), 29953-29964.
356. Basu, P.; Payghan, P. V.; Ghoshal, N.; Kumar, G. S. J. J. o. P.; Biology, P. B., Structural and thermodynamic analysis of the binding of tRNA^{Phe} by the putative anticancer alkaloid chelerythrine: Spectroscopy, calorimetry and molecular docking studies. **2016**,*161*, 335-344.
357. Jash, C.; Basu, P.; Payghan, P. V.; Ghoshal, N.; Kumar, G. S. J. P. C. C. P., Chelerythrine-lysozyme interaction: spectroscopic studies, thermodynamics and molecular modeling exploration. **2015**,*17* (25), 16630-16645.
358. Malikova, J.; Zdarilova, A.; Hlobilkova, A. J. B. p., Effects of sanguinarine and chelerythrine on the cell cycle and apoptosis. **2006**,*150* (1), 5-12.

359. Herbert, J. M.; Augereau, J. M.; Gleye, J.; Maffrand, J. P., Chelerythrine is a potent and specific inhibitor of protein kinase C. *Biochemical and biophysical research communications* **1990**,*172* (3), 993-9.
360. Yu, R.; Mandlekar, S.; Tan, T.-H.; Kong, A.-N. T. J. J. o. B. C., Activation of p38 and c-Jun N-terminal kinase pathways and induction of apoptosis by chelerythrine do not require inhibition of protein kinase C. **2000**,*275* (13), 9612-9619.
361. Hoffmann, T. K.; Leenen, K.; Hafner, D.; Balz, V.; Gerharz, C. D.; Grund, A.; Balló, H.; Hauser, U.; Bier, H. J. A.-c. d., Antitumor activity of protein kinase C inhibitors and cisplatin in human head and neck squamous cell carcinoma lines. **2002**,*13* (1), 93-100.
362. Zhang, Z.-f.; Guo, Y.; Zhang, J.-b.; Wei, X.-h. J. A. o. p. r., Induction of apoptosis by chelerythrine chloride through mitochondrial pathway and Bcl-2 family proteins in human hepatoma SMMC-7721 cell. **2011**,*34* (5), 791-800.
363. Medvetz, D.; Sun, Y.; Li, C.; Khabibullin, D.; Balan, M.; Parkhitko, A.; Priolo, C.; Asara, J. M.; Pal, S.; Yu, J. J. M. C. R., High-throughput drug screen identifies chelerythrine as a selective inducer of death in a TSC2-null setting. **2015**,*13* (1), 50-62.
364. Jiang, H.; Wu, H.; Xu, Y.-l.; Wang, J.-z.; Zeng, Y. J. J. o. b.; bioengineering, Preparation of galactosylated chitosan/tripolyphosphate nanoparticles and application as a gene carrier for targeting SMMC7721 cells. **2011**,*111* (6), 719-724.
365. Lee, C.-M.; Jeong, H.-J.; Kim, S.-L.; Kim, E.-M.; Kim, D. W.; Lim, S. T.; Jang, K. Y.; Jeong, Y. Y.; Nah, J.-W.; Sohn, M.-H. J. I. j. o. p., SPION-loaded chitosan–linoleic acid nanoparticles to target hepatocytes. **2009**,*371* (1-2), 163-169.
366. Wang, L.; Li, M.; Zhang, N. J. I. j. o. n., Folate-targeted docetaxel-lipid-based-nanosuspensions for active-targeted cancer therapy. **2012**,*7*, 3281.
367. Ling, Y.; Wei, K.; Luo, Y.; Gao, X.; Zhong, S. J. B., Dual docetaxel/superparamagnetic iron oxide loaded nanoparticles for both targeting magnetic resonance imaging and cancer therapy. **2011**,*32* (29), 7139-7150.
368. Liu, J.; Qiao, S. Z.; Hu, Q. H.; Lu, G. Q. J. s., Magnetic nanocomposites with mesoporous structures: synthesis and applications. **2011**,*7* (4), 425-443.
369. Mahmoudi, M.; Sant, S.; Wang, B.; Laurent, S.; Sen, T. J. A. d. d. r., Superparamagnetic iron oxide nanoparticles (SPIONs): development, surface modification and applications in chemotherapy. **2011**,*63* (1-2), 24-46.
370. Quan, Q.; Xie, J.; Gao, H.; Yang, M.; Zhang, F.; Liu, G.; Lin, X.; Wang, A.; Eden, H. S.; Lee, S. J. M. p., HSA coated iron oxide nanoparticles as drug delivery vehicles for cancer therapy. **2011**,*8* (5), 1669-1676.
371. Shen, L.; Li, B.; Qiao, Y. J. M., Fe₃O₄ nanoparticles in targeted drug/gene delivery systems. **2018**,*11* (2), 324.
372. Wu, M.; Huang, S. J. M.; oncology, c., Magnetic nanoparticles in cancer diagnosis, drug delivery and treatment. **2017**,*7* (5), 738-746.
373. Tietze, R.; Lyer, S.; Durr, S.; Alexiou, C., Nanoparticles for cancer therapy using magnetic forces. *Nanomedicine (London, England)* **2012**,*7* (3), 447-57.
374. Hamidi Malayeri, F.; Sohrabi, M.; Ghourchian, H. J. I. J. o. N.; Nanotechnology, Magnetic multi-walled carbon nanotube as an adsorbent for toluidine blue o removal from aqueous solution. **2012**,*8* (2), 79-86.
375. Cao, L.; Liang, Y.; Zhao, F.; Zhao, X.; Chen, Z. J. J. o. b. n., Chelerythrine and Fe₃O₄ loaded multi-walled carbon nanotubes for targeted cancer therapy. **2016**,*12* (6), 1312-1322.
376. Huang, Y.; Zhou, Z.; Liang, J.; Ding, P.; Cao, L.; Chen, Z.; Li, G. J. J. o. E. N., Preparation, characterisation and in vitro cytotoxicity studies of chelerythrine-loaded magnetic Fe₃O₄@ O-carboxymethylchitosan nanoparticles. **2015**,*10* (7), 483-498.

377. Kaminsky, V.; Lin, K. W.; Filyak, Y.; Stoika, R. J. C. B. I., Differential effect of sanguinarine, chelerythrine and chelidonine on DNA damage and cell viability in primary mouse spleen cells and mouse leukemic cells. **2008**,*32* (2), 271-277.
378. Tian, Y.; Zhang, C.; Guo, M. J. B. c.; medicine, a., Comparative study on alkaloids and their anti-proliferative activities from three *Zanthoxylum* species. **2017**,*17* (1), 460.
379. Wianowska, D.; Garbaczewska, S.; Cieniecka–Roslonkiewicz, A.; Typek, R.; Dawidowicz, A. J. C.; Ecology, Chemical composition and antifungal activity of *Chelidonium majus* extracts–antagonistic action of chelerythrine and sanguinarine against *Botrytis cinerea*. **2018**, 1-13.
380. Kovacic, P.; Ames, J. R.; Lumme, P.; Elo, H.; Cox, O.; Ryan, M. D. J. A.-c. d. d., Charge transfer-oxy radical mechanism for anti-cancer agents. **1986**.
381. Tavares, L. d. C.; Zanon, G.; Weber, A. D.; Neto, A. T.; Mostardeiro, C. P.; Da Cruz, I. B.; Oliveira, R. M.; Ilha, V.; Dalcol, I. I.; Morel, A. F. J. P. o., Structure-activity relationship of benzophenanthridine alkaloids from *Zanthoxylum rhoifolium* having antimicrobial activity. **2014**,*9* (5), e97000.
382. Yamamoto, S.; Seta, K.; Morisco, C.; Vatner, S. F.; Sadoshima, J. J. J. o. m.; cardiology, c., Chelerythrine rapidly induces apoptosis through generation of reactive oxygen species in cardiac myocytes. **2001**,*33* (10), 1829-1848.
383. Yokoyama, C.; Sueyoshi, Y.; Ema, M.; Mori, Y.; Takaishi, K.; Hisatomi, H. J. O. l., Induction of oxidative stress by anticancer drugs in the presence and absence of cells. **2017**,*14* (5), 6066-6070.
384. Lei, Y.; Liu, L.; Tang, X.; Yang, D.; Yang, X.; He, F. J. R. A., Sanguinarine and chelerythrine: two natural products for mitochondria-imaging with aggregation-induced emission enhancement and pH-sensitive characteristics. **2018**,*8* (8), 3919-3927.
385. Dostál, J.; Bochořáková, H.; Táborská, E.; Slavík, J.; Potáček, M.; Buděšínský, M.; de Hoffmann, E. J. J. o. n. p., Structure of sanguinarine base. **1996**,*59* (6), 599-602.
386. Bull, J. D.; Jaeger, N. A.; Kato, H.; Fairburn, M.; Reid, A.; Ghanipour, P. In *40-GHz electro-optic polarization modulator for fiber optic communications systems*, Photonics North 2004: Optical Components and Devices, International Society for Optics and Photonics: 2004; pp 133-144.
387. Pan, S.; Yao, J. J. J. o. L. T., UWB-over-fiber communications: modulation and transmission. **2010**,*28* (16), 2445-2455.
388. Willner, A. E.; Huang, H.; Yan, Y.; Ren, Y.; Ahmed, N.; Xie, G.; Bao, C.; Li, L.; Cao, Y.; Zhao, Z. J. A. i. O.; Photonics, Optical communications using orbital angular momentum beams. **2015**,*7* (1), 66-106.
389. Sepúlveda, B.; Calle, A.; Lechuga, L. M.; Armelles, G. J. O. l., Highly sensitive detection of biomolecules with the magneto-optic surface-plasmon-resonance sensor. **2006**,*31* (8), 1085-1087.
390. Maehara, A.; Mintz, G. S.; Weissman, N. J. J. C. C. I., Advances in intravascular imaging. **2009**,*2* (5), 482-490.
391. Wang, B.; Su, J. L.; Karpiouk, A. B.; Sokolov, K. V.; Smalling, R. W.; Emelianov, S. Y. J. I. J. o. s. t. i. Q. E., Intravascular photoacoustic imaging. **2010**,*16* (3), 588-599.
392. Weissleder, R.; Nahrendorf, M.; Pittet, M. J. J. N. m., Imaging macrophages with nanoparticles. **2014**,*13* (2), 125.
393. Northup, T.; Blatt, R. J. N. p., Quantum information transfer using photons. **2014**,*8* (5), 356.
394. Peyronel, T.; Firstenberg, O.; Liang, Q.-Y.; Hofferberth, S.; Gorshkov, A. V.; Pohl, T.; Lukin, M. D.; Vuletić, V. J. N., Quantum nonlinear optics with single photons enabled by strongly interacting atoms. **2012**,*488* (7409), 57.

395. Armelles, G.; Cebollada, A.; García-Martín, A.; García-Martín, J. M.; González, M. U.; González-Díaz, J. B.; Ferreira-Vila, E.; Torrado, J. F., Magnetoplasmonic nanostructures: systems supporting both plasmonic and magnetic properties. *Journal of Optics A: Pure and Applied Optics* **2009**,*11* (11), 114023.
396. Belotelov, V. I.; Akimov, I. A.; Pohl, M.; Kotov, V. A.; Kasture, S.; Vengurlekar, A. S.; Gopal, A. V.; Yakovlev, D. R.; Zvezdin, A. K.; Bayer, M., Enhanced magneto-optical effects in magnetoplasmonic crystals. *Nature Nanotechnology* **2011**,*6* (6), 370-376.
397. Belotelov, V. I.; Kreilkamp, L. E.; Akimov, I. A.; Kalish, A. N.; Bykov, D. A.; Kasture, S.; Yallapragada, V. J.; Venu Gopal, A.; Grishin, A. M.; Khartsev, S. I.; Nur-E-Alam, M.; Vasiliev, M.; Doskolovich, L. L.; Yakovlev, D. R.; Alameh, K.; Zvezdin, A. K.; Bayer, M., Plasmon-mediated magneto-optical transparency. *Nature Communications* **2013**,*4* (1).
398. Chin, J. Y.; Steinle, T.; Wehler, T.; Dregely, D.; Weiss, T.; Belotelov, V. I.; Stritzker, B.; Giessen, H., Nonreciprocal plasmonics enables giant enhancement of thin-film Faraday rotation. *Nature Communications* **2013**,*4* (1).
399. Ctistis, G.; Papaioannou, E.; Patoka, P.; Gutek, J.; Fumagalli, P.; Giersig, M., Optical and Magnetic Properties of Hexagonal Arrays of Subwavelength Holes in Optically Thin Cobalt Films. *Nano Letters* **2009**,*9* (1), 1-6.
400. González-Díaz, J. B.; García-Martín, A.; García-Martín, J. M.; Cebollada, A.; Armelles, G.; Sepúlveda, B.; Alaverdyan, Y.; Käll, M., Plasmonic Au/Co/Au Nanosandwiches with Enhanced Magneto-optical Activity. *Small* **2008**,*4* (2), 202-205.
401. Papaioannou, E. T.; Kapaklis, V.; Melander, E.; Hjörvarsson, B.; Pappas, S. D.; Patoka, P.; Giersig, M.; Fumagalli, P.; Garcia-Martin, A.; Ctistis, G., Surface plasmons and magneto-optic activity in hexagonal Ni anti-dot arrays. *Optics Express* **2011**,*19* (24), 23867.
402. Razdolski, I.; Gheorghe, D. G.; Melander, E.; Hjörvarsson, B.; Patoka, P.; Kimel, A. V.; Kirilyuk, A.; Papaioannou, E. T.; Rasing, T., Nonlocal nonlinear magneto-optical response of a magnetoplasmonic crystal. *Physical Review B* **2013**,*88* (7).
403. Temnov, V. V., Ultrafast acousto-magneto-plasmonics. *Nature Photonics* **2012**,*6* (11), 728-736.
404. Temnov, V. V.; Armelles, G.; Woggon, U.; Guzatov, D.; Cebollada, A.; Garcia-Martin, A.; Garcia-Martin, J.-M.; Thomay, T.; Leitenstorfer, A.; Bratschitsch, R., Active magneto-plasmonics in hybrid metal-ferromagnet structures. *Nature Photonics* **2010**,*4* (2), 107-111.
405. Temnov, V. V.; Klieber, C.; Nelson, K. A.; Thomay, T.; Knittel, V.; Leitenstorfer, A.; Makarov, D.; Albrecht, M.; Bratschitsch, R., Femtosecond nonlinear ultrasonics in gold probed with ultrashort surface plasmons. *Nature Communications* **2013**,*4* (1).
406. Valev, V. K.; Silhanek, A. V.; Gillijns, W.; Jeyaram, Y.; Paddubrouskaya, H.; Volodin, A.; Biris, C. G.; Panoiu, N. C.; De Clercq, B.; Ameloot, M.; Aktsipetrov, O. A.; Moshchalkov, V. V.; Verbiest, T., Plasmons Reveal the Direction of Magnetization in Nickel Nanostructures. *ACS Nano* **2011**,*5* (1), 91-96.
407. Schuller, J. A.; Barnard, E. S.; Cai, W.; Jun, Y. C.; White, J. S.; Brongersma, M. L. J. N. m., Plasmonics for extreme light concentration and manipulation. **2010**,*9* (3), 193.
408. Armelles, G.; Cebollada, A.; García-Martín, A.; González, M. U., Magnetoplasmonics: Combining Magnetic and Plasmonic Functionalities. **2013**,*1* (1), 10-35.
409. Ignatyeva, D. O.; Knyazev, G. A.; Kapralov, P. O.; Dietler, G.; Sekatskii, S. K.; Belotelov, V. I., Magneto-optical plasmonic heterostructure with ultranarrow resonance for sensing applications. *Scientific Reports* **2016**,*6*, 28077.

